SECONDARY ORGANIC AEROSOLS: DEVELOPMENT AND APPLICATION OF NEW TECHNIQUES IN CHAMBER AND FIELD EXPERIMENTS

by

JORDAN EDWARD KRECHMER

A.B., Bowdoin College, 2007

A thesis submitted to the
Faculty of the Graduate School of the
University of Colorado in partial fulfillment
of the requirement for the degree of
Doctor of Philosophy
Department of Chemistry and Biochemistry
2017

This thesis entitled:

Secondary Organic Aerosols: Development and Application of New Techniques in Chamber and Field Experiments

written by Jordan Edward Krechmer

has been approved for the Department of Chemistry and Biochemistry

Professor Jose-Luis Jimenez

Professor Paul J. Ziemann

Date

The final copy of this thesis has been examined by the signatories, and we find that both the content and the form meet acceptable presentation standards of scholarly work in the above mentioned discipline.

Krechmer, Jordan Edward (Ph.D., Chemistry, Department of Chemistry and Biochemistry)

Secondary Organic Aerosols: Development and Application of New Techniques in Chamber and Field Experiments

Thesis directed by Professor Jose-Luis Jimenez

Secondary organic aerosols (SOA) have detrimental effects on human health and can influence the Earth's climate by altering radiative forcing. Their sources, fates, and chemical composition across the globe, however, remain poorly constrained. A better understanding is necessary to improve predictive air quality models and enable effective mitigation strategies. This thesis presents advances in instrumentation and technique for the analysis of secondary organic aerosols, and applies them to laboratory and field studies.

First, this work describes a new SOA formation pathway in which isoprene formed low volatility gas-phase compounds that condensed onto preexisting aerosol. Results from environmental chamber experiments and a field measurement campaign identified product elemental formulas from chemical ionization mass spectrometry measurements (CIMS). It also produced SOA mass yields for the new pathway and estimated its importance in the atmosphere.

The development of a method to quantify the loss of gaseous compounds to the Teflon walls of chambers using real-time measurements is described. The method used short bursts of light to produce oxidants *in situ*, which in turn produced a several gas-phase products with differing volatilities. In the subsequent absence of aerosol and oxidants, the gas-phase products were observed to decay, with the only possible fate being absorption by the chamber walls. The time scale of this process was short (< 700 s) enough to be on the order of other processes in SOA chamber experiments and is thus important enough to necessitate accounting for.

Additional experiments are described in which the above method is used with different aerosol seed surface areas to quantify the effect of wall losses on aerosol mass yield.

Finally, we demonstrate the application of ion mobility spectrometry-mass spectrometry (IMS–MS) to the simultaneous characterization of the elemental composition and collision cross section of organic species in the gas and particulate phases. Time-resolved measurements (5 min) of oxidized organic molecules were obtained with IMS–MS during the 2013 Southern Oxidant and Aerosol Study (SOAS) ambient field campaign in rural Alabama. The ambient IMS–MS signals are consistent with laboratory spectra obtained from single-component carboxylic acids and multicomponent mixtures of isoprene and monoterpene oxidation products.

Acknowledgements:

First and foremost I would like to thank Professor Jose-Luis Jimenez for his guidance throughout this process. Several years ago when I debated returning to graduate school many of my scientist colleagues told me I would not be disappointed if I chose to work for Jose. That was an understatement. Jose has taught me so much about how to think scientifically, how to work, and how to solve problems. None of this would have been possible without him.

It has been a pleasure working with the rest of the Jimenez group staff scientists, postdocs, and graduate students on field studies and in the office. I am grateful to Doug Day for many useful conversations and additional supervision as the group's Staff Scientist. The warm and collaborative atmosphere made all of this work possible. I am lucky to have worked with three excellent laboratory managers in Michael Lechner, Philip Handley, and Anne Hanschy who gracefully handled so many problems I ran away from.

I am grateful to many of the excellent scientists at Aerodyne Research who provided me with countless hours of assistance in the field and lab. My special gratitude is due to Manjula Canagaratna with whom I spent years of work trying to get the IMS instrument to run properly and who taught me a great deal about the writing process.

I am grateful to have entered CU in a fantastic five-person analytical chemistry cohort. They have made graduate school a pleasure during the day and after hours.

I am grateful to Brian D. Musselman, my former mentor, who introduced me to the world of mass spectrometry and gave my career a direction I never imagined.

All of us are the sum of our experiences and I am thankful to my friends and family who made me who I am, especially my parents.

I am very grateful to the EPA for providing me with a STAR graduate fellowship over the past two years. Additional fellowships from CIRES and the CU Graduate School provided timely and vital support of my work.

Contents:

Chapter 4:

Chapter 5:

Chapter 6:

List of Tables:

List of Figures:

List of Publications:

First author:

Krechmer, J. E., Groessl, M., Zhang, X., Junninen, H., Massoli, P., Lambe, A. T., Kimmel, J. R., Cubison, M. J., Graf, S., Lin, Y.-H., Budisulistiorini, S. H., Zhang, H., Surratt, J. D., Knochenmuss, R., Jayne, J. T., Worsnop, D. R., Jimenez, J.-L. and Canagaratna, M. R.: Ion mobility spectrometry–mass spectrometry (IMS–MS) for on- and offline analysis of atmospheric gas and aerosol species, Atmos. Meas. Tech., 9(7), 3245–3262, doi:10.5194/amt-9-3245-2016, 2016.

Krechmer, J. E., Pagonis, D., Ziemann, P. J. and Jimenez, J. L.: Quantification of Gas-Wall Partitioning in Teflon Environmental Chambers Using Rapid Bursts of Low-Volatility Oxidized Species Generated in Situ, Environ. Sci. Technol., 50(11), 5757–5765, doi:10.1021/acs.est.6b00606, 2016.

Krechmer, J. E., Coggon, M. M., Massoli, P., Nguyen, T. B., Crounse, J. D., Hu, W., Day, D. A., Tyndall, G. S., Henze, D. K., Rivera-Rios, J. C., Nowak, J. B., Kimmel, J. R., Mauldin, R. L., Stark, H., Jayne, J. T., Sipilä, M., Junninen, H., Clair, J. M. St., Zhang, X., Feiner, P. A., Zhang, L., Miller, D. O., Brune, W. H., Keutsch, F. N., Wennberg, P. O., Seinfeld, J. H., Worsnop, D. R., Jimenez, J. L. and Canagaratna, M. R.: Formation of low volatility organic compounds and secondary organic aerosol from isoprene hydroxyhydroperoxide low-NO oxidation, Environ. Sci. Technol., 49(17), 10330–10339, doi:10.1021/acs.est.5b02031, 2015.

Co-author:

Thompson, S. L., Yatavelli, R. L. N., Stark, H., Kimmel, J. R., Krechmer, J. E., Day, D. A., Hu, W., Isaacman-VanWertz, G., Yee, L., Goldstein, A. H., Khan, M. A. H., Holzinger, R., Kreisberg, N., Lopez-Hilfiker, F. D., Mohr, C., Thornton, J. A., Jayne, J. T., Canagaratna, M., Worsnop, D. R. and Jimenez, J. L.: Field intercomparison of the gas/particle partitioning of oxygenated organics during the Southern Oxidant and Aerosol Study (SOAS) in 2013, Aerosol Sci. Technol., (0), 1–27, doi:10.1080/02786826.2016.1254719, 2016.

Hu, W., Palm, B. B., Day, D. A., Campuzano-Jost, P., Krechmer, J. E., Peng, Z., de Sá, S. S., Martin, S. T., Alexander, M. L., Baumann, K., Hacker, L., Kiendler-Scharr, A., Koss, A. R., de Gouw, J. A., Goldstein, A. H., Seco, R., Sjostedt, S. J., Park, J.-H., Guenther, A. B., Kim, S., Canonaco, F., Prévôt, A. S. H., Brune, W. H. and Jimenez, J. L.: Volatility and lifetime against OH heterogeneous reaction of ambient isoprene-epoxydiols-derived secondary organic aerosol (IEPOX-SOA), Atmos. Chem. Phys., 16(18), 11563–11580, doi:10.5194/acp-16-11563-2016, 2016.

Zhang, X.; Krechmer, J. E.; Groessl, M.; Xu, W.; Graf, S.; Cubison, M.; Jayne, J. T.; Jimenez, J. L.; Worsnop, D. R.; Canagaratna, M. R. A novel framework for molecular characterization of atmospherically relevant organic compounds based on collision cross section and mass-to-charge ratio. Atmos. Chem. Phys. **2016**, *16*, 12945–12959.

Marais, E. A., Jacob, D. J., Jimenez, J. L., Campuzano-Jost, P., Day, D. A., Hu, W., Krechmer, J., Zhu, L., Kim, P. S., Miller, C. C., Fisher, J. A., Travis, K., Yu, K., Hanisco, T. F., Wolfe, G. M., Arkinson, H. L., Pye, H. O. T., Froyd, K. D., Liao, J. and McNeill, V. F.: Aqueous-phase mechanism for secondary organic aerosol formation from isoprene: application to the southeast United States and co-benefit of SO_2 emission controls, Atmos. Chem. Phys., 16(3), 1603–1618, doi:10.5194/acp-16-1603-2016, 2016.

Hu, W. W., Campuzano-Jost, P., Palm, B. B., Day, D. A., Ortega, A. M., Hayes, P. L., Krechmer, J. E., Chen, Q., Kuwata, M., Liu, Y. J., de Sá, S. S., McKinney, K., Martin, S. T., Hu, M., Budisulistiorini, S. H., Riva, M., Surratt, J. D., St. Clair, J. M., Isaacman-Van Wertz, G., Yee, L. D., Goldstein, A. H., Carbone, S., Brito, J., Artaxo, P., de Gouw, J. A., Koss, A., Wisthaler, A., Mikoviny, T., Karl, T., Kaser, L., Jud, W., Hansel, A., Docherty, K. S., Alexander, M. L., Robinson, N. H., Coe, H., Allan, J. D., Canagaratna, M. R., Paulot, F. and Jimenez, J. L.: Characterization of a real-time tracer for isoprene epoxydiols-derived secondary organic aerosol (IEPOX-SOA) from aerosol mass spectrometer measurements, Atmos. Chem. Phys., 15(20), 11807–11833, doi:10.5194/acp-15-11807-2015, 2015.

Chapter 1: Introduction

1.1 Atmospheric organic aerosols

Atmospheric chemistry research endeavors to understand the complex interplay between gaseous, liquid, and solid chemical compounds and their various inputs and outputs in the indoor and outdoor environment. Aerosols, liquid or solid suspensions, are one of the least understood parts of the atmospheric system. Aerosols can affect the Earth's climate via direct or indirect radiative forcing,[1] cause disease in humans,[2] alter the Earth's hydrological cycle,[3] and reduce visibility.

Organic aerosol (OA) species constitute a major fraction of fine particulate matter, comprising 20–90% of fine particle mass in many regions.[4–6] Organic aerosols can be primary (POA), which are directly emitted (e.g. combustion-powered vehicles) into the atmosphere, or secondary (SOA), which are formed from the oxidation and condensation of emitted volatile organic compounds (VOC). SOA has been shown to make up a major fraction of fine particulate matter in both pristine and anthropogenically dominated areas.[7]

Understanding SOA sources and fates is necessary to build predictive capabilities in aerosol, climate, and geochemical models. Despite previous work in this area, large discrepancies between SOA measurements and model predictions persist.[8,9]

Studying SOA formation pathways often involves measurements of volatile SOA precursors and semivolatile gaseous intermediates. As there are thousands of different SOA-relevant gases in the troposphere,[10] new instrumentation and techniques are necessary to separate and measure the multitude of chemical compounds.

1.2 Chemical ionization mass spectrometry

Chemical ionization mass spectrometry (CIMS)[11] is an analysis technique in which one ionized chemical (a reagent ion) is used to impart charge to another analyte chemical. The analyte is then transported into a mass spectrometer, which produces a mass-to-charge ratio (*m/z)* for the analyte ion. By varying the type of reagent ion, one can selectively and sensitively analyze chemical compounds of many different types.

CIMS was originally developed for tropospheric and stratospheric chemistry measurements using quadrupole mass analyzers.[12,13] Since the 1970s, researchers have employed mass spectrometers configured for different CIMS reagent ions including Iodide, Acetate, NO^+, SF_6^-, CF_3O^-, and H_3O^+ (alternatively branded as Proton-Transfer Reaction MS, or PTR-MS).[14,15] Quadrupole instruments, however, suffer from poor time resolution when monitoring many ions due to a slow duty cycle. They are also limited to unit mass resolution.

Due to the large number of atmospheric chemical constituents, CIMS instruments that utilize a time-of-flight (ToF) mass analyzer have gained extensive use in atmospheric chemistry.[16–33] ToF-CIMS instruments allow for rapid (< 1 Hz) and continuous measurements of a large mass-to-charge (*m/z*) range, in contrast to quadrupoles. ToF instruments also allow for determination of accurate mass, from which elemental formulas can be extrapolated. They can also be configured with a multitude of reagent ions, or even to operate with alternating multiple reagent ions.[34]

1.3 Environmental ("smog") chambers

Environmental, or "smog," chambers have been indispensable tools of atmospheric chemistry research for at least six decades.[35] Commonly constructed of Teflon sheets, they can be situated outside, to use natural sunlight as a source of photochemical oxidants, or indoors, commonly surrounded by UV-emitting black lights. They vary in size from so-called "pillow bags" that hold tens of Liters of air, to massive installations that can be over 100 m^3.

Environmental chambers are frequently used to probe complex chemical reactions, study particle-phase chemical reactions, and determine secondary organic aerosol fractional mass yields. Fractional mass yields, which cannot be determined in flow tubes, are critical parameters in aerosol and climate models. SOA mass yield is a parameter that defines the mass of SOA formed per unit of SOA gaseous precursor.

A major drawback of environmental chambers is that the chamber walls provide a surface in which chemical compounds can be absorbed, in the case of Teflon-walled chambers, or onto which they can be adsorbed, in the case of steel-walled chambers. The loss of SOA-precursors to chamber walls can affect aerosol mass yields and reaction chemistry.

1.4 Thesis overview

This thesis describes three advances in the study of SOA formation in laboratory and field experiments.

Chapter 2 describes a new SOA formation pathway from isoprene. Chamber and field measurements are presented in which identified low volatility organic compounds condense directly into the particle phase. This pathway may help close the discrepancy between modeled and measured SOA in pristine areas and may prove to be an important aerosol source in pre-industrial conditions.

In Chapter 3 we describe a new experimental technique for measuring the extent of gas-phase wall losses in Teflon environmental chambers. Gas-phase wall losses are shown to be significant in SOA chamber experiments. We also provide a complete model and parameters for aerosol experimentalists and modelers attempting to quantitate SOA chamber experiments.

Chapter 4 details the application of an ion mobility mass spectrometer (IMS-MS) to atmospheric chemistry laboratory and field studies. We present results from the SOAS 2013, in which the instrument was deployed in a biogenic emission-dominated environment. The IMS-MS was able to separate isomers of isoprene and monoterpene oxidation products in the gas-phase and lend insight into the chemical oxidation processes of such products. BVOC oxidation products are generated in an oxidation flow reactor and analyzed with the IMS. We then compare the laboratory-generated products with field data to help identify potential sources of those products.

Chapter 5 describes the results of laboratory chamber experiments with varying liquid organic aerosol seed surface areas. We observe a temporal difference between time series with increasing amounts of seed aerosol, proving that it is possible to study gas-particle partitioning in environmental chambers. We then construct a kinetic box model that accurately reproduces the behavior of the gas-phase measurements with simple gas-particle partitioning theory. From that box model we measure the mass accommodation coefficient, α.

Chapter 2:
Formation of low volatility organic compounds and secondary organic aerosol from isoprene hydroxyhydroperoxide low-NO oxidation

Reprinted with permission from Krechmer, J. E., Coggon, M. M., Massoli, P., Nguyen, T. B., Crounse, J. D., Hu, W., Day, D. A., Tyndall, G. S., Henze, D. K., Rivera-Rios, J. C., Nowak, J. B., Kimmel, J. R., Mauldin, R. L., Stark, H., Jayne, J. T., Sipilä, M., Junninen, H., Clair, J. M. St., Zhang, X., Feiner, P. A., Zhang, L., Miller, D. O., Brune, W. H., Keutsch, F. N., Wennberg, P. O., Seinfeld, J. H., Worsnop, D. R., Jimenez, J. L. and Canagaratna, M. R.: Formation of low volatility organic compounds and secondary organic aerosol from isoprene hydroxyhydroperoxide low-NO oxidation, Environ. Sci. Technol., 49(17), 10330–10339, doi:10.1021/acs.est.5b02031, 2015. Copyright 2015 American Chemical Society.

2.1 Introduction

Atmospheric aerosols can have detrimental effects on human health[2] and are known to affect global climate both directly and indirectly.[36] Secondary Organic Aerosol (SOA) forms in the atmosphere by the oxidation of volatile organic compounds (VOCs), and typically is a major fraction of submicron aerosol mass.[6,7] VOCs can be emitted by human activity (anthropogenic) or vegetation (biogenic). While significant progress has been made in identifying VOC precursors and formation pathways of SOA, there is still significant uncertainty in these chemical processes and in the SOA global budget.[6,9,37]

Isoprene is a biogenic VOC and represents the largest emission of non-methane hydrocarbons to the Earth's atmosphere with global emissions of ~535 Tg C yr^{-1}.[38,39] In the atmosphere, isoprene reacts readily with hydroxyl radicals (OH) to produce organic peroxyl radicals (RO_2) that, under low-NO conditions, subsequently react with hydroperoxyl radicals (HO_2) and form isoprene hydroxyhydroperoxides (ISOPOOH, $C_5H_{10}O_3$).[40,41] Of the ISOPOOH isomers, two are atmospherically important: 4,3-ISOPOOH and 1,2-ISOPOOH.[42] The further oxidation of

ISOPOOH by OH produces key isoprene low-NO SOA precursor intermediates, isoprene epoxydiols (IEPOX, $C_5H_{10}O_3$), at yields greater than 75%.[41,43] Isoprene has been shown to form SOA under a variety of atmospheric conditions through various chemical pathways, including the heterogeneous uptake of IEPOX onto wet sulfate aerosol.[41,44–48] With reported SOA yields from isoprene that range 1-6% (although these may be lower limits)[49,50] biogenic emissions are thought to dominate the global sources of SOA with isoprene accounting for a substantial fraction.[8]

To date, most biogenic SOA formation and evolution mechanisms include equilibrium partitioning between semi-volatile gas-phase compounds (SVOC) and a liquid organic particle phase.[51,52] Recently Ehn et al. reported a new source of SOA from the irreversible condensation of extremely low-volatility organic compounds (ELVOC) produced from the ozonolysis of monoterpenes both in laboratory studies and ambient conditions.[20] In the laboratory, ELVOC were produced on rapid time scales from α-pinene, β-pinene, limonene, and cyclohexene and irreversibly condensed onto seed aerosol. High molar yields were observed: 7% for α-pinene and 17% for limonene. Detailed follow-up studies suggest that this process results from a peroxy radical (RO_2) autoxidation mechanism,[53] first proposed by Crounse et al.[54] Compared to SVOC, the extremely low volatility of ELVOC makes their relative contribution to SOA yields larger at low OA loadings, and makes them relevant to the growth of nanoparticles.

In this work, we directly investigate, using simultaneous gas-phase and particle composition measurements obtained during a chamber experiment, the link between low volatility organic compounds (LVOC) and SOA generated from the photo-oxidation of ISOPOOH and associated species under low NO conditions. We use a kinetic box model to investigate this production pathway, and present ambient measurements from the recent Southern Oxidant and Aerosol Study (SOAS; June-July 2013; http://soas2013.rutgers.edu/) to illustrate the impact of this pathway under ambient conditions. The properties of the identified condensing gas-phase species and the potential importance of this pathway for SOA formation from isoprene are discussed.

2.2 Experimental

2.2.1. Atmospheric Chamber Experiments.

Chamber experiments were performed as part of the Focused Isoprene eXperiment at the California Institute of Technology (FIXCIT) laboratory campaign during January 2014. FIXCIT was designed to be complementary to SOAS with the goal of elucidating the mechanisms behind key ambient observations of biogenic VOC chemistry in the southeast U.S. The laboratory effort involved an array of state-of-the-art instrumentation, with 18 gas- and aerosol-phase instruments operating throughout the study. Experiments were performed in two 24 m^3 FEP Teflon bags housed in an 8 × 5 × 3m insulated enclosure. A detailed description of the Caltech chamber facilities, the entire set of FIXCIT experiments, instrumentation and methods is provided in the campaign overview publication.[55]

This study focuses on FIXCIT experiment #17 (17 January 2014), which explored the OH-initiated oxidation of isoprene 4-hydroxy-3-hydroperoxy (4,3-ISOPOOH). 4,3-ISOPOOH is one of the two main atmospherically important ISOPOOH isomers (1,2-ISOPOOH is the other) [42]. ~56 ppb of synthesized 4,3-ISOPOOH was injected into the chamber and oxidized with a steady-state concentration of 1.2×10^6 molecules cm^{-3} of OH generated from the photolysis of 750 ppb hydrogen peroxide (H_2O_2) by UV black lights (peak at 350 nm).[55] After 2.5 hours, ~42 ppb of the ISOPOOH had reacted away. Aerosol growth was observed through increases in the AMS organic mass signals but no seed aerosol was added. The UV lights were then switched off and the chamber was sampled for an additional 4 hours. The reaction proceeded at 26°C and less than 5% relative humidity (RH). The experiment was performed under “low-NO” conditions with NO concentrations of less than 25 pptv during the experiment and a NO:HO_2 ratio of < 1:5.

2.2.2. Nitrate Chemical Ionization Mass Spectrometry (NO_3^--CIMS)

Measurements of highly oxidized gas-phase organic species were made with an Aerodyne high-resolution time-of-flight chemical ionization mass spectrometer (HRToF-CIMS), which has been described in previous publications.[56,57] In this work, the CIMS was equipped with an atmospheric-pressure nitrate-ion (NO_3^-) ionization source (Airmodus, Ltd.; hereafter NO_3^--CIMS). Originally developed and used for the detection of gas phase sulfuric acid and methanesulfonic acid,[58] the NO_3^- ions also cluster with highly oxidized organic species at high efficiency without fragmentation.[19,59]

Air from the chamber was drawn into the NO_3^- source at a rate of 3 SLPM through FEP tubing 2.0m long and with a 7.9mm inner diameter. The sample flow was then diluted with 8 SLPM of clean zero air (RH <8%) to provide ~ 11 SLPM of total sample flow into the NO_3^- source. A flow of 0.7 SLPM of the total 11 SLPM flow was drawn directly into the mass spectrometer from the source via a 300 µm pinhole.

Raw negative-ion spectra were acquired at a rate of 1 Hz and subsequently averaged to 1 minute. Data were analyzed using the Tofware (Tofwerk, AG and Aerodyne Research, Inc., version 2.4) toolkit developed for the IGOR Pro 6 analysis software package (Wavemetrics, Inc.). The NO_3^--CIMS was operated in “V-mode” and achieved a mass resolution of ~4100 at m/z 212 and above and a mass accuracy of < 5ppm, which enabled assignment of elemental composition to observed mass-to-charge values. A representative high-resolution fit is shown in Fig. 2.1.

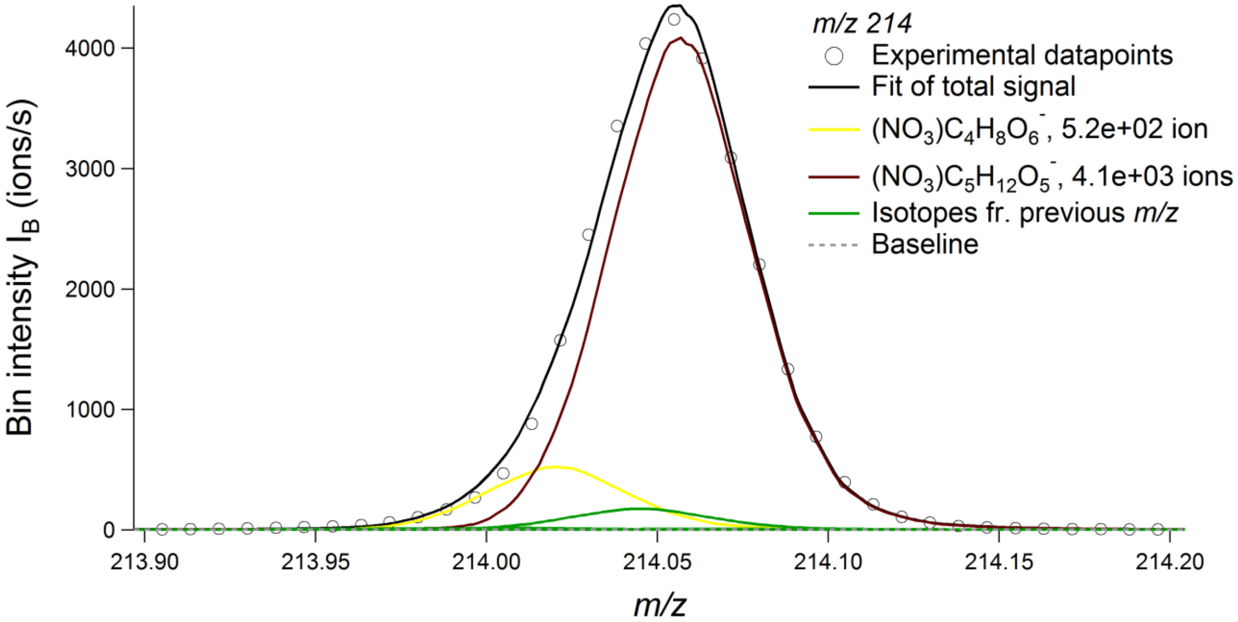

Figure 2.1. The high resolution mass spectrum peak fit for m/z 214, which is dominated by the $C_5H_{12}O_5$ LVOC.

The instrument was zeroed periodically by shutting off the flow from the chamber and drawing only clean house air for several minutes. Mass-to-charge calibrations were performed before and after every experiment and were further corrected point-by-point in data analysis using a combination of both nitrate reagent ions and previously identified Teflon-related ions coming from the inlet lines that bracket the m/z region of interest.

NO_3^--CIMS Quantification.

The concentration of gas-phase species X measured by the NO_3^--CIMS is quantified as [20]:

$$[X]_{chamber} = \frac{S_{X\cdot NO_3^-}}{S_{NO_3^-}+S_{HNO_3NO_3^-}+S_{(HNO_3)_2NO_3^-}} \times C_x \qquad (2.1)$$

where C_x is a compound-dependent calibration coefficient for a given temperature and pressure with units of molecules cm^{-3}, $S_{X\cdot NO_3^-}$ is the signal of the $X\cdot NO_3^-$ cluster, and the denominator is the sum of all reagent ions.

The calibration coefficient also includes signal loss due to diffusion-limited wall loss in the inlet tubing. This loss is included in the value of C as a multiplicative factor:[20]

$$C_{LVOC} = \frac{1}{f_{inlet}\, k_{ion}\, RT} \tag{2.2}$$

where f_{inlet} is the fraction of analyte that reaches the ionization source, and (1-f_{inlet}) is the fraction lost to the inlet walls via gaseous diffusion [60]. In this case, RT is the 200ms residence time of the analyte molecules in the ion/molecule reaction region, and represents the effect on the calibration coefficient from the amount of ion collisions in the charger. k_{ion} is the rate coefficient for ion formation from the analyte.

The value of f_{inlet} for the FIXCIT inlet was calculated to be ~7% using standard equations to calculate the loss of a species in a tube assuming laminar flow [60]. Inputs for this calculation include temperature (26C), pressure (98 kPa for a 252 m altitude in Pasadena, CA, USA), species diffusion coefficient for a model LVOC in air (~5 x10^{-6} m^2 s^{-1}) estimated using the SPARC calculator [61,62], sample tube inner diameter (0.00476 m), tube length (2m), and air flow rate of 5x10^{-5} m^3 s^{-1} corresponding to the sample gas flow of 3 SLPM. This process assumes that these species are of sufficiently low volatility that they are irreversibly lost to the walls (uptake coefficient of 1) and that there is no re-partitioning back to the gas-phase,[20] which is consistent with their behavior in the chamber as discussed elsewhere in this work. There is some uncertainty from this assumption, which is probably comparable with the uncertainty arising from the ion-molecule reaction rates. We also note that non-condensing species may also not be lost to the walls of the tubing. Thus we may overestimate the concentration of non-condensing species, but this is of no consequence to our analyses since these species do not contribute to the novel aerosol formation pathway discussed here.

The value of k_{ion} was estimated experimentally from laboratory calibrations. Low-volatility oxidized species were introduced into the NO_3^--CIMS via a heated diffusion cell and quantified via conversion to CO_2 by a heated platinum catalyst. The CO_2 was then measured using a LI-840A CO_2 analyzer (LI-COR).[63] The FIXCIT inlet was used in the calibrations to maintain the same f_{inlet} values. Malonic acid ($C_3H_4O_4$) was the most sensitive organic compound tested and was used as the primary LVOC calibrant since it is thought to cluster at rates close to the collision limit [59]. The calibration factor calculated from Equation 2.2 using the malonic acid k_{ion} measurements and FIXCIT f_{inlet} of 7% is $C = 7.9 \times 10^{10}$ molec. cm^{-3}. We apply the experimentally obtained value of $C = 7.9\times10^{10}$ molec. cm^{-3} for malonic acid to all of the measured LVOC because it has the highest sensitivity and therefore provides a lower bound on the LVOC concentrations. For comparison, the calibration factor calculated for sulfuric acid, which charges at a collision limited rate in the nitrate source,[64] is within 11 % (C_{LVOC} of 7.0×10^{10} molec. cm^{-3}, using k_{ion} value of 5×10^{9} molec. cm^{-3} from previous work[65] and our calculated value of $f_{inlet} = 0.07$) of the calibration factor calculated for malonic acid in this work. The assumption that all the detected LVOC species cluster with the reagent ion at or close to the collision limit is dependent on the LVOC having highly oxidized functional group contributions (e.g., hydroxyl and hydroperoxy) resulting in large dipole moments and polarizabilities, which is consistent with their measured elemental compositions and condensing behavior (discussed below).[66]

To track system stability and repeatability, a signal calibration was performed periodically, before or after experiments, by flowing a steady concentration of diethylene glycol (DEG) for several minutes, which was quantified using a catalytic converter and CO_2 analyzer following the method of Veres et al.[63] The instrument showed excellent stability and repeatability.

Fragmentation and clustering are not thought to play a significant role in the detection of LVOC. First, previous work has shown that formation of water clusters is not a preferred pathway in the ionization process.[67] Second, the NO_3^--CIMS efficiently measures oxidized dimers and trimers.[19] No dimers or trimers were detected and thus it is very unlikely that the LVOC are fragments of larger molecules.

CIMS bulk elemental analysis and uncertainty. The following equation was used to estimate the bulk elemental oxygen to carbon ratio (O:C) contribution to the aerosol phase from the 14 LVOC detected by the NO_3^--CIMS:

$$\frac{\mathrm{O}}{\mathrm{C}} = \frac{\sum_{\mathrm{n}=1}^{14}[\mathrm{LVOC}]_{\mathrm{n}}\mathrm{O}_{\mathrm{n}}}{\sum_{\mathrm{m}=1}^{14}[\mathrm{LVOC}]_{\mathrm{m}}\mathrm{C}_{\mathrm{m}}} \tag{2.3}$$

where O_n and C_m are the number of oxygen or carbon atoms, respectively, for a selected LVOC and $[LVOC]_n$ is the fractional contribution of each LVOC to the total condensed LVOC signal. The $[LVOC]_n$ were assigned based on the percent mixing ratios observed lost to the aerosol-phase. A similar equation was used for the elemental hydrogen to elemental carbon ratio, H:C:

$$\frac{H}{C} = \frac{\sum_{n=1}^{14}[LVOC]_n H_n}{\sum_{m=1}^{14}[LVOC]_m C_m} \tag{2.4}$$

where H_n and C_m are the number of hydrogen and carbon atoms, respectively for a selected LVOC.

A Monte Carlo simulation was performed to estimate the uncertainty of the O:C and H:C bulk elemental ratios for gas-phase organics measured by the NO_3^--CIMS. We assumed a relative uncertainty in the calibration factors between different LVOCs of 100%. In each run of the Monte Carlo method, the concentration of each LVOC was scaled with a random sensitivity consistent with the estimated uncertainty, and then used to calculate the weighted average O:C and H:C ratios.

The simulation was run 100,000 times (Figure 2.2) and the value of the 2σ deviation for each bulk elemental ratio was used as the uncertainty.

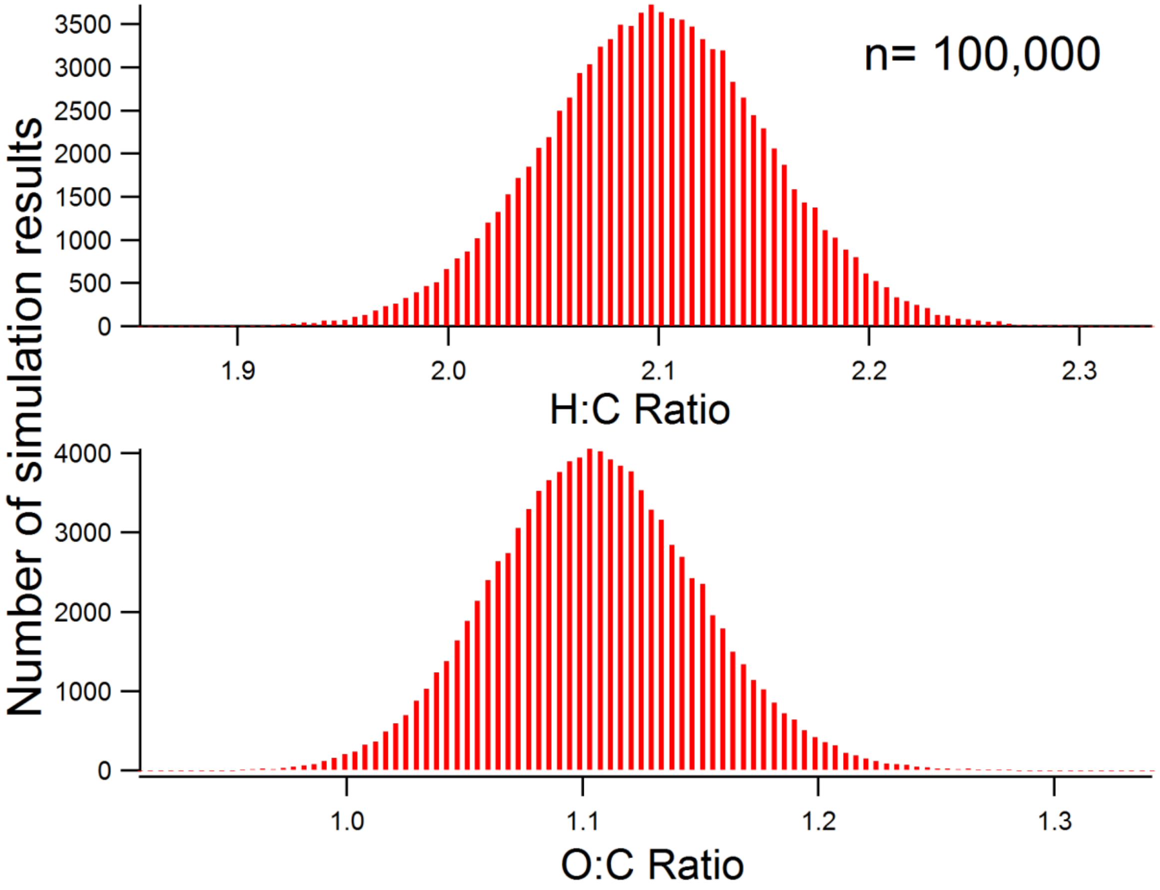

Figure 2.2. Histograms showing the results of the Monte Carlo simulation to determine the uncertainty of the CIMS elemental bulk ratios. The Monte Carlo simulation was run 100,000 times.

2.2.3. Aerosol Mass Spectrometer

Aerosol mass was measured by an Aerodyne High Resolution Time-of-Flight Aerosol Mass Spectrometer (hereafter AMS).[68] The instrument was calibrated with 350 nm NH_4NO_3 particles, and bulk composition was analyzed using the high resolution data analysis software package PIKA.[68] Elemental analysis (EA) was performed using the recently updated parameterization by Canagaratna et al.[69]

Aerosol liquid water was removed using a Nafion membrane diffusion drier prior to the AMS measurement. Aerosol losses due to particle bounce upon the AMS vaporizer were corrected using a collection efficiency (CE) of 0.75. The same CE factor was used by Nguyen et al.[45] during a study of IEPOX uptake onto ammonium sulfate seed. Line losses were observed to account for 20% of aerosol mass; accordingly, a correction factor of 1.2 was applied to all AMS data.

PMF analysis of ambient AMS data during SOAS. We obtained a time series of ambient ISOPOOH-SOA in the SOAS dataset by using the constrained positive matrix factorization (PMF) method as implemented in the multilinear engine (ME-2) software. In this analysis one of the factors extracted from the ambient organic data was constrained to have a mass spectrum that is similar to the FIXCIT ISOPOOH-SOA AMS spectrum. The theoretical principles of PMF ME-2 are described by Paatero.[70] ME-2 was run via the SoFi interface, v.4.6.[71] For the ME-2 setup, a range of a-values between 0 – 0.3 (fully constrained to partially constrained) were tested. We found clear and consistent time series of ISOPOOH-SOA in these different cases. We could not extract an ISOPOOH-SOA component in the free-PMF source apportionment, likely due to the low abundance of this factor (~2%) in the total OA being below the estimated detection limit of PMF (~5%).[72] Other sources of OA, including isoprene epoxydiols-derived SOA (IEPOX-SOA), monoterpene-derived SOA, and biomass burning OA (BBOA), are also resolved out concurrent with ISOPOOH-SOA, consistent with published PMF results for this study and site from another group.[44]

2.2.4. CF_3O^--CIMS

IEPOX, ISOPOOH, and other OVOC (oxygenated volatile organic compounds) measurements were obtained using CF_3O^--CIMS methods.[41,73,74]

2.2.5. Compounds associated with ISOPOOH

Other compounds (~7% by mole) present in the synthesized 4,3-ISOPOOH standard were introduced into the chamber with ISOPOOH. Two of the larger associated species initially present in the reaction chamber with potential importance to observed LVOC signals are thought to be 4,3-dihydroxy-C5-alkene (~1% of ISOPOOH) and 4-hydroxy-3-keto-C5 alkene (~0.1% of ISOPOOH) (Fig. 2.3). These compounds will react with OH at rates similar to ISOPOOH, and could have higher LVOC yields than ISOPOOH. While these species likely originated from the ISOPOOH synthesis or degradation, they will also be produced in the atmospheric oxidation of isoprene at levels not unlike those observed in this experiment (RO_2 + RO_2 reactions being the most obvious production pathway). Here, we consider the sum of LVOC formed from all reactants present in the chamber, as there is currently insufficient information to distinguish their origin.

For several reasons, we believe that it is improbable that the majority of LVOC and resulting SOA produced in this experiment arose from the impurities rather than the 4,3-ISOPOOH itself. First, the yield of SOA from all species in this experiment is ~4.2%. The LVOC that condense are not the contaminants themselves, since they are only observed when the UV lights are turned on and photochemical oxidation is active. Therefore, the contaminants would have to have SOA yields of ~60% in order to explain all the SOA formation. There are no known 4 or 5 carbon organic species that have an SOA yield of ~60%, and it is extremely unlikely that most of the diverse molecules comprising the impurities could have such high SOA yields. With a more typical SOA yield comparable to that of ISOPOOH, the contribution of the impurities to be observed SOA would be minor.

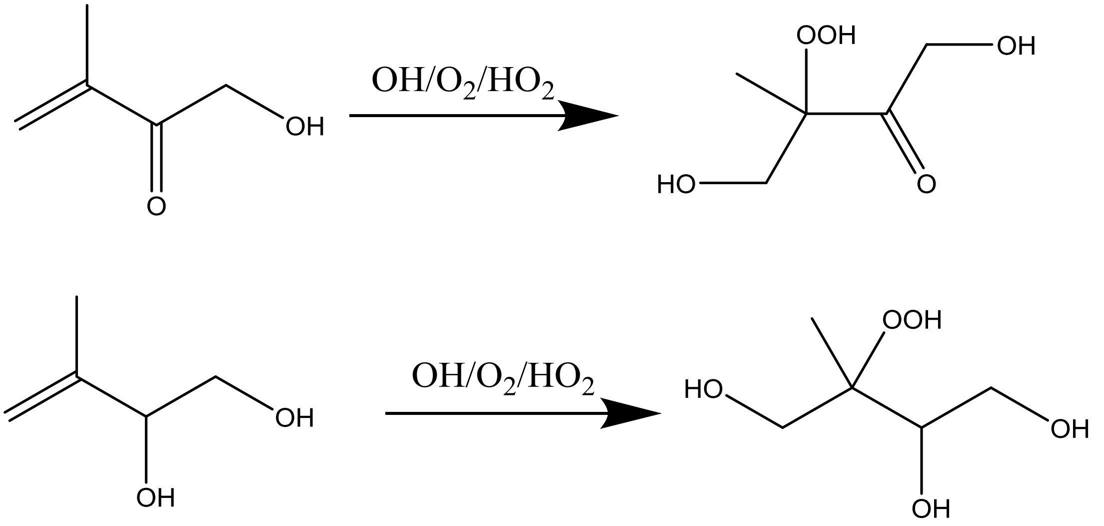

Figure 2.3. A mechanism showing the tentatively identified impurities of the 4,3-ISOPOOH standard (on the left) and their possible low-NO OH·-initiated reaction products on the right. Only products of addition to the double bond are shown, although it is estimated that 30% of the reaction proceeds via hydrogen abstraction for the lower structure.

The likely major oxidation product of the tentatively-identified 2-carbonyl-3-methyl-3-butane-1-ol impurity (Fig. 2.3) has an estimated vapor pressure (Table 2.1) 100 times too large to be condensing quickly at an OA level of 0.2 µg m^{-3}, as observed during this experiment. Even taking into account the uncertainty of the vapor pressure estimation method of a factor of 10 [75], this discrepancy is still too large by x10. Also, its amount is 25 times too small to explain the amount of $C_5H_{10}O_5$ observed in this experiment. Therefore we do not expect a significant contribution from this impurity to the observed condensing $C_5H_{10}O_5$ species.

The $C_5H_{12}O_5$ LVOC signal also is a possible product of from the tentatively-identified 3-methyl-3-butane-1,2-diol impurity (Fig. 2.3). The molar yield of a $C_5H_{12}O_5$ product could be ~60% from the impurity, based on structure-reactivity relationships.[76] Since this impurity is present at a level of ~1% of ISOPOOH and is estimated to react with OH at a similar rate, we can derive an upper limit yield of 0.6% as the molar ratio of the $C_5H_{12}O_5$ arising from the contaminant. Thus the SOA yield may be lower by that amount, assuming the identification, mechanisms, and estimated volatility of the products of this impurity are correct. We note that if that is the case, this 4,3-alkene-diol would represent a unique case of a C5 species with a phenomenal 60% SOA yield via condensation at OA levels below 1 μg m^{-3}, which is at least an order-of-magnitude larger than has been determined from any C5 species including isoprene and ISOPOOH, to our knowledge. In any case the reduction of the SOA yield arising from this potential correction is small compared to other uncertainties in the experimental and modeling system.

2.2.6. Kinetic Box Model

A chemical kinetic box model (KinSim v2 for IGOR Pro; http://www.igorexchange.com/node/1333) was used to simulate key experimental observations. KinSim uses the Backwards Differentiation Formula method to solve a system of chemical reactions treated as ordinary differential equations. The initial conditions were based on measured quantities and kinetic rate coefficients obtained from recent references (Table 2.2).

Hydroxyl radical (OH) concentrations in the chamber were estimated using the observed decay rate of ISOPOOH and its published reaction rate with OH.[41,77]

The aerosol uptake rate was modeled using the following equation:

$$k_{uptake}=\frac{1}{4}\bar{c}A\gamma \tag{2.5}$$

where $\bar{c}$ is the mean speed of LVOC molecules in the gas-phase, γ is the uptake coefficient, and A is the aerosol surface area.[78] Because the particles are small (< 50 nm), the correction for the transition regime is small and can be neglected.[78] Aerosol surface area was not measured for this experiment, so this quantity was estimated from measurements of a non-seeded, low-NO isoprene+OH oxidation experiment carried out on a different date with similar conditions in the same chamber. The total aerosol surface area time series in the model was reduced using the surface-area-to-mass ratio ($\frac{2}{3}$ power relationship) to account for the lower amount OA observed in this FIXCIT experiment. A loss rate for gas-phase species to the walls (k_{wall}) is also included in the model. As a first guess we utilize a value of 0.002 s^{-1}, which was taken from previous modeling of the Caltech chamber,[79] and this value is optimized with the model. It is important to note that it is not possible to experimentally determine wall uptake coefficients larger than ~6×10^{-6} from chamber experiments.[80] Wall loss rates for gas-phase species determined by the model were used to correct all SOA formation yields presented in this work.

The loss rate for organic aerosol to the chamber walls (2.5×10^{-4} s^{-1}) was constrained from the observed AMS SOA signal decay after the end of the photochemistry, which agrees with typical values for the particle sizes expected in this experiment for the Caltech chamber.[81] While the particle loss rate has a dependency on particle size, we estimate the range of particles observed in the AMS to be of a narrow size range from 50 to 150 nm. Particles smaller than 50 nm are not detected by the AMS and the particles are likely not larger than 150 nm because there is so little mass in this experiment. This would result in a variation of the particle wall loss rate of the order of a factor of 1.5 at most, for any realistic size distribution.[82] This is similar or smaller than the uncertainty in other parameters.

NO_3^--CIMS observations were used to constrain the values of k_{wall}, γ_{SOA}, and the yield of LVOC from their formation reactions.

Because the structures of LVOC are relatively similar to IEPOX (and do not contain double bonded carbon atoms), the loss rate for LVOC via reaction with OH is assumed to be similar to those of IEPOX with OH (0.8 -1.5 $\times10^{-11}$ cm^3 $molec^{-1}$ s^{-1}, isomer-dependent).[43] The integrated reaction rates are a few percent of the LVOC loss rates via aerosol formation or deposition to the chamber walls and are therefore not included in the model.

Some of the LVOC may contain hydroperoxide groups that are susceptible to photolysis. We can estimate their photolysis lifetime as 4.1 days using the chamber light intensity and spectrum, and the absorption cross section of hydroxymethylhydroperoxide (HHMP, $HOCH_2OOH$) as a surrogate species of similar functionality.[83] This results in a decay of 2% over the course of our experiment. Since the functional group composition of each LVOC is not precisely known and the photolyzed fraction of hydroperoxides is very small, photolysis is neglected in our model.

Uncertainty estimation for the model parameters, k_{wall}, γ_{SOA}, and the reaction yield (Y).

Estimation of the model parameters (k_{wall}, γ_{SOA}, and Y) that provide the best fit to experimental data was treated as a nonlinear regression problem. The optimization was based on minimizing the sum of the squares of the residuals (χ^2) between the model and observations. The optimization was performed in two ways: automatically, using the FuncFit function in Igor Pro 6, and manually. In the manual mode the model was run 10,000 times, stepping through different values of k_{wall}, γ_{SOA}, and Y. For each model result, the χ^2 of the model and measured traces were evaluated.

The uncertainties in the fitted model parameters ($\mathbf{m}_{L2} = [k_{wall}, \gamma_{SOA}, Y]^T$) were evaluated using the statistics of nonlinear regression.[84] We obtain 95% confidence limits on the model parameters by:[84]

$$\sigma = 1.96\ \mathrm{diag}(\mathrm{Cov}(\mathbf{m}_{L2}))^{1/2} \qquad (2.6)$$

We estimate the covariance matrix (inverse Hessian) for the fitted model parameters as:[84]

$$\mathrm{Cov}(\mathbf{m}_{L2}) \approx s^2\,(\mathbf{J}(\mathbf{m}_{L2})^T\,\mathbf{J}(\mathbf{m}_{L2}))^{-1} \qquad (2.7)$$

where Cov($\mathbf{m}_{L2}$) is the covariance matrix for the model results linearized about $\mathbf{m}_{L2}$, s is the measurement standard deviation, and $\mathbf{J}(\mathbf{m}_{L2})$ is the Jacobian matrix ($d\mathbf{r}/d\mathbf{m}$) of the residual vector $\mathbf{r}$, calculated about the least-squares solution $\mathbf{m}_{L2}$ using finite differences.

2.3 Results and Discussion

2.3.1 Dynamics of Gas-Phase LVOC and SOA

The time-dependent behavior of key species throughout the experiment is detailed in Fig. 2.4. After the reactant concentrations stabilized following injection (Fig. 2.4a), the UV lights were switched on at 20:30 UTC. From that point, ISOPOOH decreased due to reaction with OH and the IEPOX and LVOC concentrations increased rapidly; 45 minutes later, SOA was detected by the AMS and kept increasing while the LVOC concentration leveled and then decreased together with the SOA. This contrasts with the behavior of IEPOX, which continued to rise until the UV lights were turned off, at which point its concentration leveled out.

We can extrapolate the slope of the initial LVOC increase to follow the time trend of IEPOX past the point where SOA appears. The difference between the extrapolated concentration and the actual LVOC trace is used as an estimate of the amount of LVOC lost to aerosol up to that point in time (ΔLVOC in Fig. 1b). At 21:45 UTC, ΔLVOC was 62 pptv (0.39 μg m^{-3}) and SOA was 0.45 μg m^{-3}. The two concentrations are in good agreement within the uncertainties (± 100% for CIMS, ± 35% for AMS)[85,86]. Therefore the condensation of gas-phase LVOC from oxidation of 4,3-ISOPOOH and associated OVOC likely accounts for all or most of the SOA observed here.

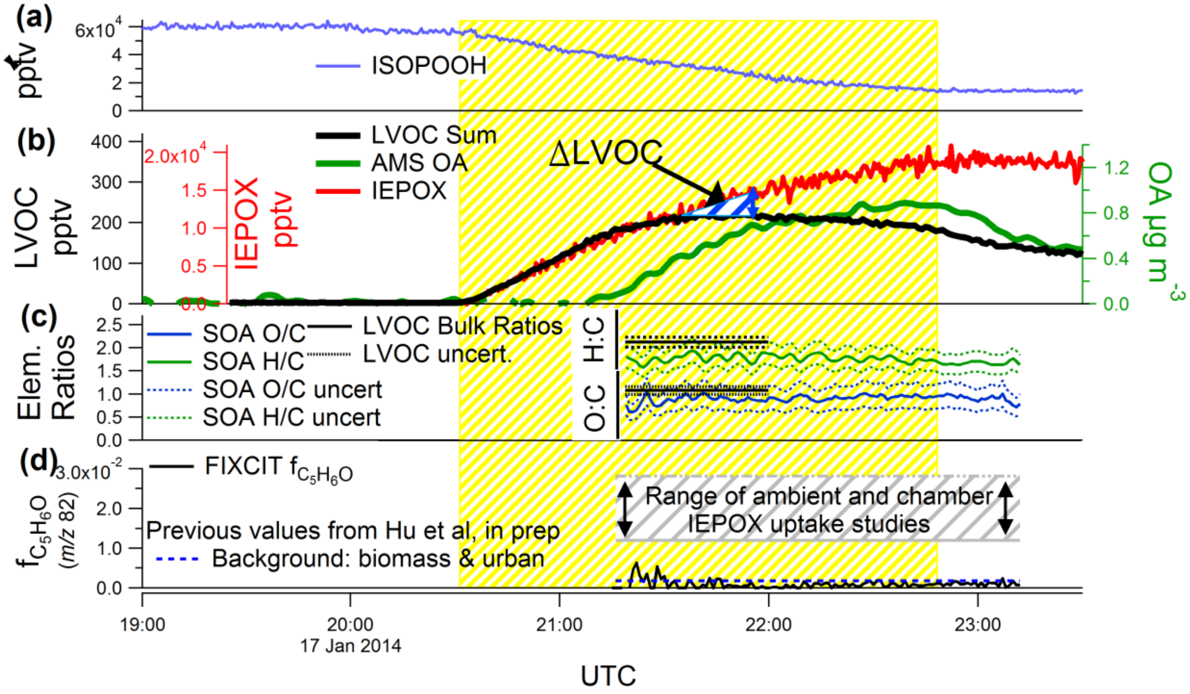

Figure 2.4. Time evolution of key species in the chamber during 4,3-ISOPOOH + OH oxidation: (a) ISOPOOH, (b) total observed LVOC, AMS SOA (with no adjustment to account for particles outside the size cutoff), and IEPOX**,** (c) AMS and LVOC atomic O:C and H:C, and (d) fraction of AMS signal at $C_5H_6O^+$ (f_{C5H6O}). Shaded yellow indicates UV lights on and active photochemistry.

FIXCIT included two other experiments (No. 2 & 21) in which isoprene OH-initiated oxidation was investigated under low-NO conditions. Many of the same LVOC were also observed; but SOA was not detected by the AMS in those experiments. It is unlikely that the LVOC alone would be able to homogenously nucleate, as their estimated vapor pressures (discussed below) are not low enough for that process. Therefore, we hypothesize that the ISOPOOH experiment led to SOA growth and the isoprene ones did not due to differences in the concentrations of pre-existing background nanoparticles between the experiments. Unfortunately, nanoparticle measurements were not performed due to space and flow constraints. Particles were detected and characterized after they grew to exceed the AMS size cutoff of ~50 nm diameter. It is also possible that some SOA was formed in the isoprene experiments, but that it was present in particle sizes below the AMS lower particle size transmission limit. Additionally, the upper limit concentration of 4,3-

ISOPOOH consumed in experiments 2 and 21 can be estimated at ⅓ and 1/7 of the 42 ppb of 4,3-ISOPOOH that reacted away in this experiment. SOA formation, limited by a high loss rate of LVOC to the walls, will be dependent on the ISOPOOH oxidation rate (ppbv/min), which was much higher in the ISOPOOH experiment. The much smaller LVOC production combined with the strong sink to the walls may explain why the AMS did not detect aerosol mass above 50 nm in the other isoprene experiments.

2.3.2 SOA Composition

The AMS spectrum of the SOA is characterized by electron impact mass fragment ions with a high fraction of m/z 43, typical of fresh SOA (Fig. 2.5) and m/z 29 (CHO^+), typical of species with alcohol functional groups.[69] $C_2H_3O^+$ dominates m/z 43 and is thought to be associated with non-acid oxygenated functional groups.[87] The SOA measured by the AMS and the gas-phase condensing species measured by the NO_3^--CIMS had consistent elemental composition: O:C of 0.90 ± 0.2 (AMS) vs. 1.1 ± 0.1 (CIMS), and H:C of 1.75 ± 0.25 (AMS) vs. 2.1 ± 0.1 (CIMS) (Figs. 2.4). No detectable organic N was present in either the gas or the particle phase, supporting the lack of prevalence of high-NO pathways in these experiments.

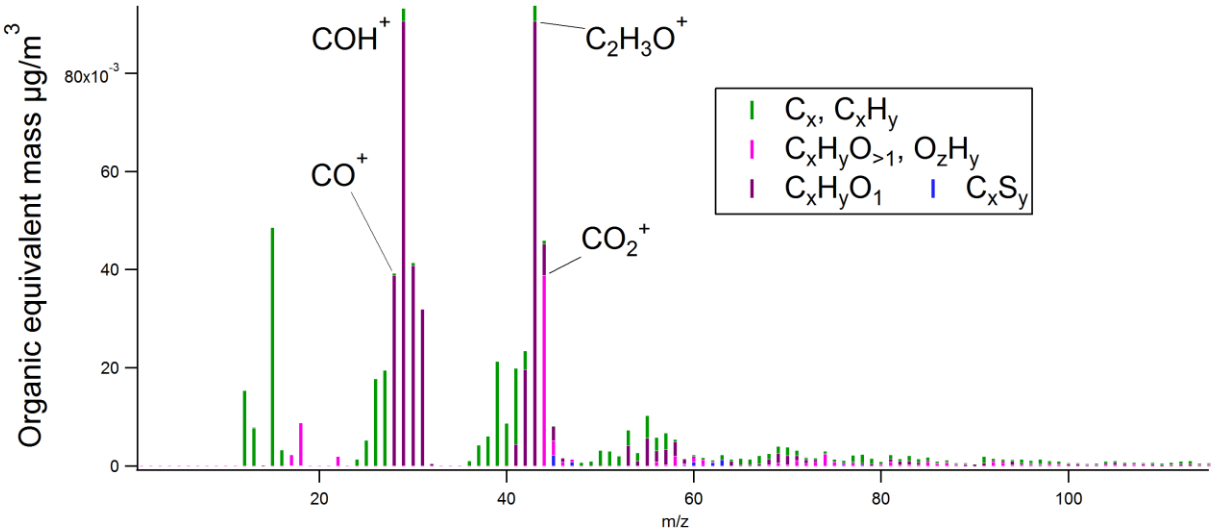

Figure 2.5. AMS spectrum at the point of peak gas-phase LVOC condensation (SOA concentration 0.61 µg m^{-3}). The signals at m/z 29 and 43 are similar by coincidence.

Previous studies have shown that a key pathway for the formation of SOA in the low-NO isoprene system is the uptake of IEPOX followed by aerosol phase reactions. However, such uptake is thought to require particle liquid water and is accelerated by wet acidic sulfate particles,[45,88] which makes it unlikely to be active in our experiment. The lack of such uptake is also consistent with the fact that IEPOX concentrations in the chamber do not decrease when the photochemistry stops. The fraction of signal at m/z 82, $C_5H_6O^+$ ($f_{C_5H_6O}f_{C_5H_6O}$) in the HR-AMS spectra is a good tracer of IEPOX-SOA[89] in well-characterized isoprene photochemical systems. $f_{C_5H_6O}$ observed for IEPOX-SOA (~22×10^{-3}) in laboratory and field studies is far higher than observed here. In this experiment, $f_{C_5H_6O}$ averages 0.9×10^{-3} (Fig. 2.4d). This value is 25 times lower than expected for pure IEPOX-SOA, and below typical background values from locations not influenced by IEPOX-SOA (urban, biomass-burning plumes, non-biogenic chamber SOA) and non-IEPOX forming isoprene studies (1.7-3.5×10^{-3}). Therefore SOA formation from IEPOX uptake plays at most a minor role in this experiment.

2.3.3. LVOC Composition

A representative NO_3^--CIMS mass spectrum (averaged over 30 minutes of peak LVOC production) and a list of the identified ions are given in Fig. 2.6 and Table 2.1. All of the LVOC are observed as clusters with the nitrate reagent ion ($[X{\cdot}NO_3]^-$). None of the LVOC was detected in appreciable quantity as deprotonated molecules, indicating that the cluster chemical ionization mechanism is efficient for these particular species. To our knowledge, this is the first published nitrate-ion spectrum of these isoprene/ISOPOOH oxidation products, although some of them have been identified in previous iodide-ion CIMS ambient data.[90]

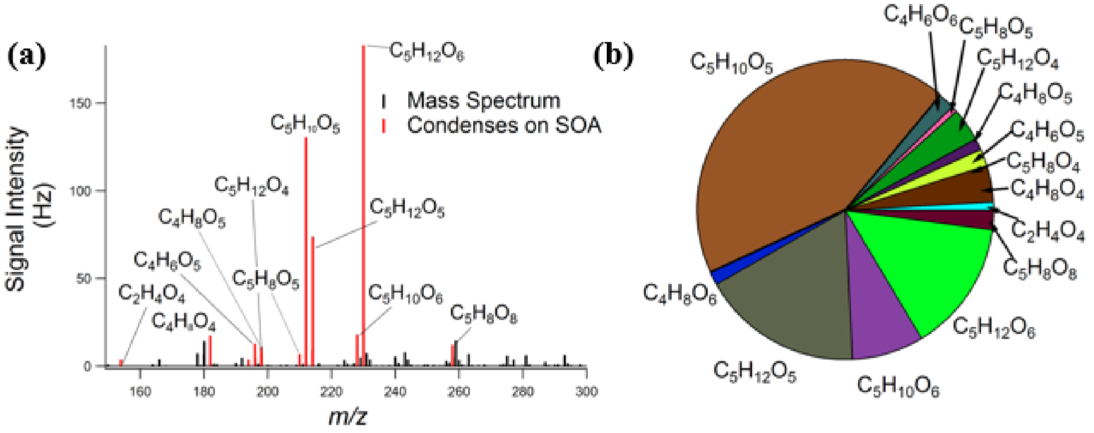

Figure 2.6. (a) NO_3^--CIMS gas-phase mass spectrum at the point of peak LVOC concentration (22:00 UTC). Species whose time evolution indicates condensation into the aerosol phase are highlighted in red. All species are detected as clusters with NO_3^- (*m/z* 62), which has been omitted for clarity, as have reagent ions, known contaminants, and isotopic peaks. **(b)** Estimated relative contributions of LVOC to the observed SOA.

Elemental Formula	**Ion Exact Mass**	**Species Mass [Da]**	**H:C**	**O:C**	**OS_C**
$C_2H_4O_4$	153.9993	92.0110	2.00	2.00	2.00
$C_4H_8O_4$	182.0306	120.0423	2.00	1.00	0.00
$C_5H_8O_4$	194.0306	132.0423	1.60	0.80	0.00
$C_4H_6O_5$	196.0099	134.0215	1.50	1.25	1.00
$C_4H_8O_5$	198.0255	136.0372	2.00	1.25	0.50
$C_5H_{12}O_4$	198.0619	136.0736	2.40	0.80	-0.80
$C_5H_8O_5$	210.0250	148.0372	1.60	1.00	0.40
$C_4H_6O_6$	212.0048	150.0164	1.50	1.50	1.50

$C_5H_{10}O_5$	212.0412	150.0528	2.00	1.00	0.00
$C_4H_8O_6$	214.0205	152.0321	2.00	1.50	1.00
$C_5H_{12}O_5$	214.0568	152.0685	2.40	1.00	-0.40
$C_5H_{10}O_6$	228.0356	166.0477	2.00	1.20	0.40
$C_5H_{12}O_6$	230.0518	168.0634	2.4	1.2	0
$C_5H_8O_8$	258.00979	196.02196	1.6	1.6	1.6

Table 2.1. Elemental formulas, exact masses, and elemental properties of the 14 ions observed condensing into the aerosol-phase.

Fourteen LVOC signals whose time series are indicative of condensation are highlighted in the mass spectrum and displayed in a pie chart (Fig. 2.6b) representing the relative contributions of individual LVOC to the total amount of condensing LVOC. The total condensing gas-phase amount is dominated (~75% by mixing ratio) by four ions, $C_5H_{10}O_5$ being the largest. All condensing LVOC are highly oxidized with O:C $\geq$ 0.8 (0.8-1.2). Thirteen have a 4- or 5-carbon backbone, which is consistent for products arising from the oxidation of ISOPOOH and associated C_5 compounds, ruling out gas-phase oligomerization reactions in their formation pathways. $C_2H_4O_4$ has a time series consistent with SOA formation, but its short carbon chain (and thus high vapor pressure) is consistent with condensation onto the aerosol via reactive uptake. The extent of condensation by reactive uptake of the C_4 and C_5 LVOC species is not known, however, we note that the observations can be explained from a simple condensation mechanism (i.e., no reactive uptake, see following section).

2.3.4. LVOC Functional Groups and Vapor Pressures

The fact that the LVOC are observed to condense onto the particle phase at SOA concentrations below 1 $\mu g\ m^{-3}$ indicates that their saturation concentrations (C^*) must be similar to or lower than the SOA concentration.[52] Some information about the functional groups that are likely to be present on the LVOC can be obtained by estimating their C^* based on their elemental composition and different functional group assumptions. A list of possible functional group combinations for each of the assigned elemental formulas is shown in Table 2.2**.** The SIMPOL.1 structure-activity relationship[91] was used to estimate C^*.

Elemental Formula	C* (µg m^{-3})	Nc	-C=O	-OH	-C(O)OH	-OOH	-C(O)OOH	-C=C	Fraction Lost
$C_2H_4O_4$	5.79E+05	2		1			1		0.42
$C_2H_4O_4$	2.05E+04	2			1	1			
$C_4H_8O_4$	4.88E+01	4		2	1				0.32
$C_4H_8O_4$	1.25E+02	4	1	3					
$C_4H_8O_4$	3.53E+03	4			1	1			
$C_4H_8O_4$	9.08E+03	4	1	1		1			
$C_4H_8O_4$	2.68E+04	4				2		1	
$C_4H_8O_4$	9.96E+04	4		1			1		
$C_5H_8O_4$	1.55E+01	5		2	1			1	0.01
$C_5H_8O_4$	3.98E+01	5	1	3				1	
$C_5H_8O_4$	1.48E+02	5			2				
$C_5H_8O_4$	3.80E+02	5	1	1	1				

$C_5H_8O_4$	9.76E+02	5	2	2					
$C_5H_8O_4$	1.12E+03	5			1	1		1	
$C_5H_8O_4$	2.88E+03	5	1	1		1		1	
$C_5H_8O_4$	3.16E+04	5		1			1	1	
$C_5H_8O_4$	7.07E+04	5	2			1			
$C_5H_8O_4$	7.75E+05	5	1				1		
$C_4H_6O_5$	2.43E+00	4		1	2				0.29
$C_4H_6O_5$	6.25E+00	4	1	2	1				
$C_4H_6O_5$	4.74E+01	4	1	2		1		1	
$C_4H_6O_5$	4.53E+02	4	1		1	1			
$C_4H_6O_5$	1.16E+03	4	2	1		1			
$C_4H_6O_5$	3.44E+03	4	1			2		1	
$C_4H_6O_5$	4.97E+03	4			1		1		
$C_4H_6O_5$	1.28E+04	4	1	1			1		
$C_4H_6O_5$	3.77E+04	4				1	1	1	
$C_4H_8O_5$	3.25E-01	4		3	1				0.21
$C_4H_8O_5$	2.36E+01	4		1	1	1			
$C_4H_8O_5$	6.06E+01	4	1	2		1			
$C_4H_8O_5$	6.64E+02	4		2			1		

$C_4H_8O_5$	4.39E+03	4	1			2			
$C_4H_8O_5$	4.81E+04	4				1	1		
$C_5H_{12}O_4$	2.65E+00	5		4					0.86
$C_5H_{12}O_4$	1.92E+02	5		2		1			
$C_5H_{12}O_4$	1.39E+04	5				2			
$C_5H_8O_5$	1.29E-01	5		3	1				0.17
$C_5H_8O_5$	3.30E-01	5	1	4					
$C_5H_8O_5$	9.75E-01	5		1	2				
$C_5H_8O_5$	2.51E+00	5	1	2	1				
$C_5H_8O_5$	6.44E+00	5	2	3					
$C_5H_8O_5$	7.40E+00	5		1	1	1		1	
$C_5H_8O_5$	2.39E+01	5	1	2		1			
$C_5H_8O_5$	1.82E+02	5	1		1	1			
$C_5H_8O_5$	2.09E+02	5		2			1	1	
$C_5H_8O_5$	4.67E+02	5	2	1		1			
$C_5H_8O_5$	1.73E+03	5	1			2			
$C_5H_8O_5$	4.07E+03	5	1	1		1			
$C_5H_8O_5$	5.12E+03	5	1	1			1		
$C_5H_8O_5$	1.51E+04	5				1	1	1	

$C_4H_6O_6$	1.60E-02	4		2	2				0.4
$C_4H_6O_6$	6.68E-01	4					2		
$C_4H_6O_6$	1.16E+00	4			2	1			
$C_4H_6O_6$	2.98E+00	4	1	1	1	1			
$C_4H_6O_6$	2.26E+01	4	1	1		2		1	
$C_4H_6O_6$	3.27E+01	4		1	1		1		
$C_4H_6O_6$	8.41E+01	4	1	2			1		
$C_4H_6O_6$	5.56E+02	4	2			2			
$C_4H_6O_6$	6.09E+03	4	1			1	1		
$C_4H_6O_6$	2.21E+05	4	2			1			
$C_5H_{10}O_5$	1.30E-01	5		3	1				0.69
$C_5H_{10}O_5$	2.43E+01	5	1	2		1			
$C_5H_{10}O_5$	7.16E+01	5		1		2		1	
$C_5H_{10}O_5$	1.76E+03	5	1			2			
$C_5H_{10}O_5$	3.35E-01	5	1	4					
$C_4H_8O_6$	3.99E-01	4	1	3		1			0.3
$C_4H_8O_6$	2.89E+01	4	1	1		2			
$C_4H_8O_6$	3.17E+02	4		1		1	1		

$C_5H_{12}O_5$	1.26E+00	5		3		1			0.48
$C_5H_{12}O_5$	9.15E+01	5		1		2			
$C_5H_{12}O_5$	9.15E+01	5		1		2			
$C_5H_{10}O_6$	6.15E-02	5		2	1	1			0.9
$C_5H_{10}O_6$	1.44E-01	5		3	1				
$C_5H_{10}O_6$	1.58E-01	5	1	3		1			
$C_5H_{10}O_6$	4.67E-01	5		2		2		1	
$C_5H_{10}O_6$	3.38E+01	5				3		1	
$C_5H_{10}O_6$	1.26E+02	5		1		1	1		
$C_5H_{12}O_6$	5.95E-01	5		2		2			0.14
$C_5H_{12}O_6$	4.31E+01	5				3			
$C_5H_8O_8$	1.10E-05	5		2			2		0.27
$C_5H_8O_8$	1.91E-05	5		2	2	1			
$C_5H_8O_8$	1.45E-04	5		2	1	2		1	
$C_5H_8O_8$	7.96E-04	5				1	2		
$C_5H_8O_8$	1.38E-03	5			2	2			
$C_5H_8O_8$	3.56E-03	5	1	1	1	2			

$C_5H_8O_8$	4.08E-03	5		3		1	1	1	
$C_5H_8O_8$	1.05E-02	5			1	3		1	
$C_5H_8O_8$	1.00E-01	5	1	2		1	1		
$C_5H_8O_8$	2.96E-01	5		1		2	1	1	
$C_5H_8O_8$	6.62E-01	5	2			3			
$C_5H_8O_8$	6.94E-01	5		2		1	1	1	
$C_5H_8O_8$	1.63E+00	5		3			1	1	
$C_5H_8O_8$	7.26E+00	5	1			2	1		

Table 2.2. List of possible functional group compositions for all elemental formulas of observed LVOC, along with their estimated saturation concentrations (*C^**) estimated with the SIMPOL model.[91] Contributions are listed from: “N_c”, the number of carbon atoms; “C=O”, ketones and aldehydes; “OH,” hydroxyl groups; “COOH,” carboxylic acids; “OOH,” hydroperoxyl groups; “CO(O)OH,” peroxy acids; and “C=C,” carbon-carbon double bonds. The impact of *C^** of aldehydes and ketones are only slightly different, so they were grouped together here for simplicity.

The base vapor pressure for a 4- or 5-carbon structure (without oxygenated functional groups) is high (e.g. 0.72 Atm. for isoprene), but decreases substantially with the addition of functional groups. Unlike e.g. terpene oxidation products, which have larger carbon numbers, isoprene oxidation products will only have low enough C^* to condense if their oxygen is present in functional groups that efficiently reduce C^*. We consider only O and H atoms because nitrogen-containing functional groups are not consistent with the observed signals. Isoprene low-NO chemistry tends to produce neighboring hydroperoxyl and hydroxyl functional groups.[92] For example, $C_5H_{10}O_5$ has a double bond equivalency (DBE, the number of double bonds or rings) of one. It is unlikely that the C=C bond in ISOPOOH and associated OVOC survived oxidation, and thus we could assign one O to one epoxide, carboxyl, or carbonyl group. The four remaining O could be present as either two hydroperoxyl groups ($C^* = 1.8 \times 10^3$ µg m^{-3}), one hydroperoxyl and two hydroxyl groups ($C^* = 24$ µg m^{-3}) or four hydroxyl groups ($C^* = 0.34$ µg m^{-3}). Thus the presence of different functional groups can result in a difference of 4 orders-of-magnitude in C^*. Although the addition of a hydroperoxyl group results in a larger decrease of C^* than the addition of a hydroxyl group, the latter is more efficient at reducing C^* per O atom. The most likely identity of the condensing $C_5H_{10}O_5$ species is thus a C_5 epoxyl- or carbonyl-tetrol, although a C_5 epoxyl- (or carbonyl-) hydroperoxydiol, and C_5 carboxyl triol are also plausible given the fact that C^* estimation methods have uncertainties of about one order of magnitude.[75] On the other hand, a carbonyl dihydroperoxide is not expected to partition through simple condensation based on vapor pressure, although it could still contribute to the particle phase via heterogeneous reactive uptake reactions. The large number of possible structures and variability of associated C^* values demonstrate the difficulty of parameterizing these species' wall and aerosol loss rates based on bulk properties such as the number of oxygen and carbon atoms.[79]

Fig. 2.7 illustrates the results of this method for all condensing LVOC. Structures containing the maximum number of –OOH groups consistent with the measured composition tend to be too volatile to result in the observed condensing behavior. On the other hand, structures containing the maximum number of –OH groups are consistent with condensation at SOA ~ 1 µg m^{-3} in most cases. As for the case of $C_5H_{10}O_5$, some structures containing a mixture of –OH and –OOH may also condense under the conditions of our experiment. Thus we do not need to invoke oligomerization reactions to explain the observed SOA growth. Note that two or more isomers of differing volatility may comprise some of the detected signals. Unfortunately, a more precise determination of the molecular structures of the condensing LVOC is not possible with the available data.

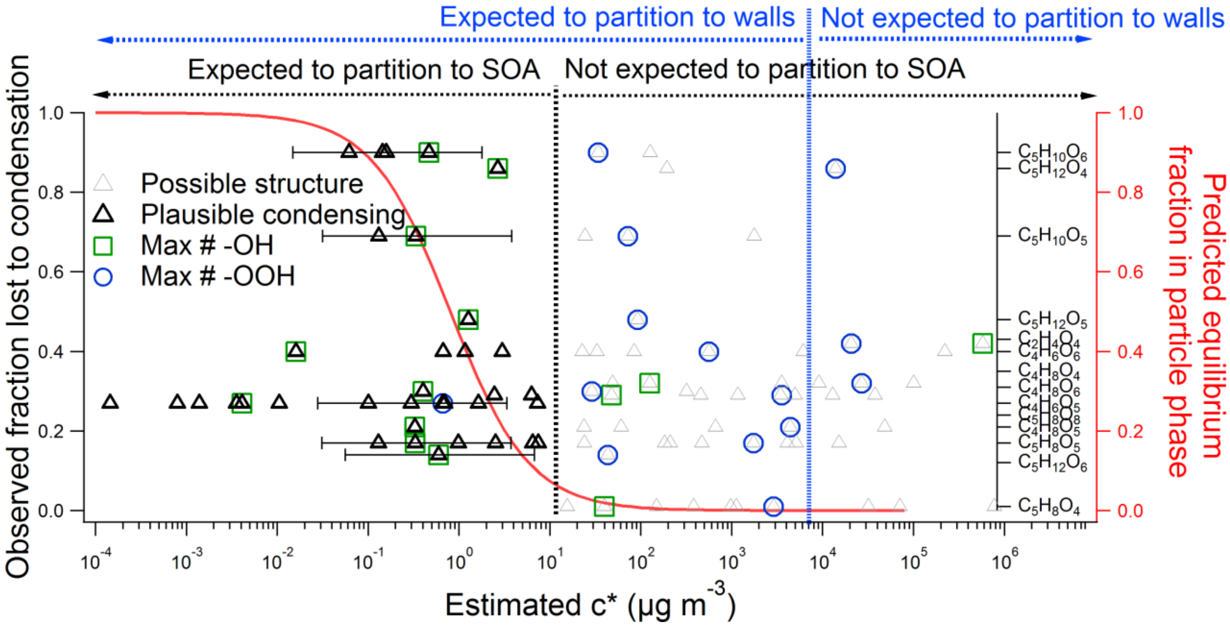

Figure 2.7. Left axis: fraction of gas-phase LVOC lost to aerosol uptake (estimated as described in main text) vs. their estimated saturation concentrations (*C**) from SIMPOL. Right axis: equilibrium particle-phase fraction for the peak aerosol concentration (0.85 µg m^{-3}) vs *C**. For each detected ion, a range of *C** was estimated for different possible functional group contents. Error bars are the estimated uncertainty (1σ) of SIMPOL [75].

2.3.5. Model Results

To better understand the observed LVOC temporal behavior, we implemented a kinetic box model. Model results for $C_5H_{10}O_5$ are compared to experimental data in Fig. 2.8a and its structure and key parameters are shown in Fig. 2.8b and Table 2.3**.** The model was constrained to match all observed variables, while keeping its structure as simple as possible and the number of fitted parameters as low as possible. It was possible to reproduce the behavior of the largest-concentration and SOA-condensing LVOC assuming that LVOC were formed from ISOPOOH + OH and were lost to the chamber walls and to the aerosol.

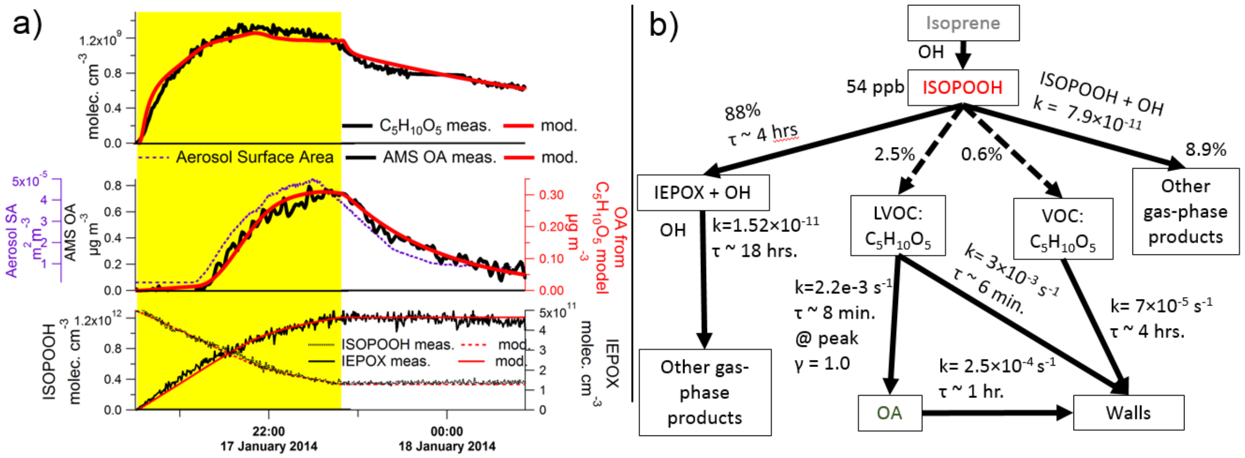

Figure 2.8. a) Time series of modeled (red) and measured (black) gas and aerosol concentrations for the largest LVOC by contribution to SOA mass, $C_5H_{10}O_5$. The model SOA (middle, right axis) gives the fractional contribution of $C_5H_{10}O_5$ to the aerosol and the surface area has been binomially smoothed across 10 points. The LVOC was fit with two modeled isomers: one with γ_{SOA}=1.0, $k_{wall} = 3.0 \times 10^{-3}$ s^{-1} and a branching ratio of 2.5%; and another with γ_{SOA}=0, $k_{wall} = 7.0 \times 10^{-5}$, and a branching ratio of 0.6%. b) Schematic of the kinetic box model used to simulate the production of LVOC $C_5H_{10}O_5$ and its losses to organic aerosol (OA) and chamber walls. The dashed lined represents the proposed LVOC formation pathways. Isoprene is shown for reference, but was not present in the main experiment discussed in this work. Rate coefficients are in units of molec. cm^{-3} s^{-1} unless otherwise specified.

Species or condition	**Initial value**
ISOPOOH	1.29 x 10^{12} molecules cm^{-3}
Temperature	25 °C
RH	< 5%

Reaction	**Rate Coefficient at 25 °C (cm^3 $molecule^{-1}$ s^{-1} unless noted otherwise)**	**Reference**
ISOPOOH + OH→	7.9 × 10^{-11}	Paulot et al. 2009, 2012 [41,77], Xie et al. 2013 [93]
→ IEPOX + OH	88%	
→ $C_5H_{10}O_5^{c}$	2.5%	This work
→$C_5H_{10}O_5^{nc}$	0.6%	This work
→Other Products	8.9%	
IEPOX + OH→Other Products	1.5 × 10^{-11}	Bates et al. 2014 [43]
OA→Wall	2.5 × 10^{-4} s^{-1}	Cocker et al. 2001 [81]
$C_5H_{10}O_5^{c}$ →Wall	3.0 × 10^{-3} s^{-1}	This work
$C_5H_{10}O_5^{c}$ → SOA	2.2 × 10^{-3} at peak 1.4 × 10^{-5} mean (γ = 1.0)	Seinfeld & Pandis [78] This work
$C_5H_{10}O_5^{nc}$ → Wall	7 × 10^{-5} s^{-1}	This work
$C_5H_{10}O_5^{nc}$ → SOA	0 s^{-1}	

Table 2. 3. Kinetic box model initial conditions, reactions, and rate coefficients to reproduce the observed time-dependent behavior of $C_5H_{10}O_5$. The non-condensing isomer of $C_5H_{10}O_5$ is denoted with a “nc” superscript, the condensing isomer with a “c” superscript.

The initial rise of the LVOC concentrations allows constraining the extent to which these species are predominantly formed from ISOPOOH + OH, or from the oxidation of IEPOX (or other 1st generation products) by OH. Fig. 2.9a-b show the relative rise in concentration from the LVOC and IEPOX before the appearance of SOA, as well as the expected time dependences for 1st, 2nd, and later generation products of ISOPOOH. The rate coefficient used for OH oxidation of IEPOX and subsequent IEPOX products is 1.52×10^{-11} cm^3 $molec.^{-1}$ s^{-1}, as recently reported for cis-β IEPOX (the isomer with the largest rate coefficient, providing an upper bound for the reaction rate)[43]. The time when LVOC and IEPOX rise represents a period when only one source and one sink (chamber walls; shown in Fig. 2.10) are dominant. When LVOC are modeled as 1st generation products of ISOPOOH + OH, the model curve lies in the middle of the measured traces and follows almost the same path as the IEPOX measurement (as expected since IEPOX is a 1st generation product of ISOPOOH+OH). The later generation product assumptions produce traces that are significantly delayed, then exhibit a sharper relative increase later in this period. Thus we conclude that most LVOC are formed as minor products of the ISOPOOH+OH reaction. Two LVOC lie in between the 1st and 2nd generation curves in Fig. 2.10b. This may just be due to experimental variability and instrument noise, as several LVOC lay just as far to the other side of the 1st generation curve. Potentially a few LVOC may have a contribution of later generation reactions.

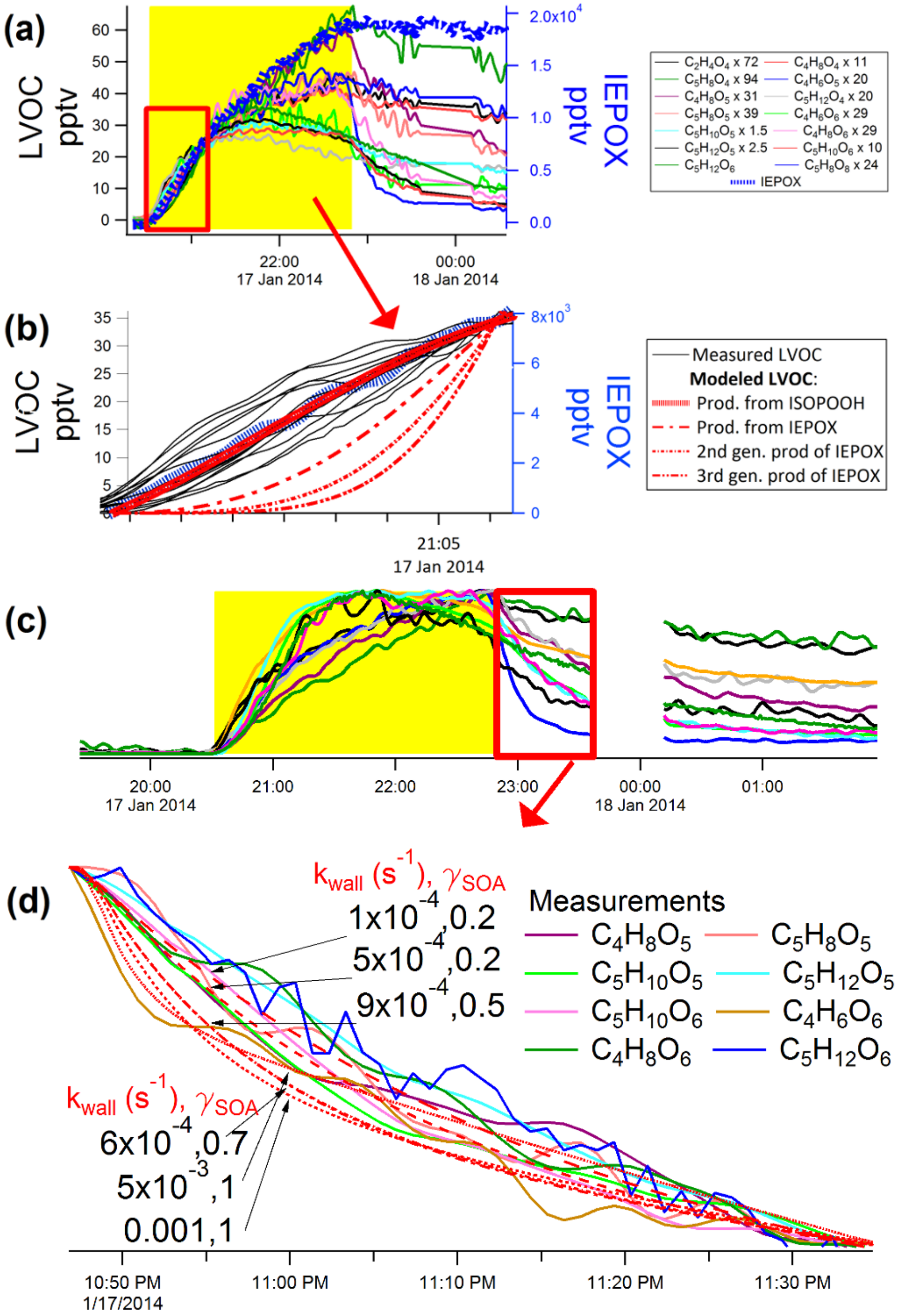

Figure 2. 9. Time series of the measured LVOC and gas-phase IEPOX. Traces in panels **(a)** and **(b)** are scaled to overlap at the time in the experiment in which SOA was first detected, and the point when UV lights are turned off in panels **(c)** and **(d)**. Panel **b** is a close-up of a. Panel **d** depicts the highlighted region in panel **c**, with the starting concentration scaled to one arbitrary point and the concentration observed at 23:35 scaled to zero. Model results for a range of wall loss rates and aerosol uptake coefficients are also shown. This has been modeled with the

parameters also used in Fig. 4. For clarity, not all LVOC are shown in panel **d**. In panels **a** and **b** IEPOX has been binomially smoothed (5 points) and in panel **d** the LVOC have been binomially smoothed (5 points).

Next, we turn our attention to constraining the uptake coefficient for LVOC uptake to SOA (γ_{SOA}) and the wall loss rate (k_{wall}) (Fig. 2.9d). The time evolution of this experiment contains information to potentially constrain these values separately due to drastic changes in their relative importance within different time periods. First, there is an initial period (20:30-21:10 UTC) before SOA appears when wall loss dominates as a sink, then a second period (21:30-end) when SOA is present in variable concentrations.

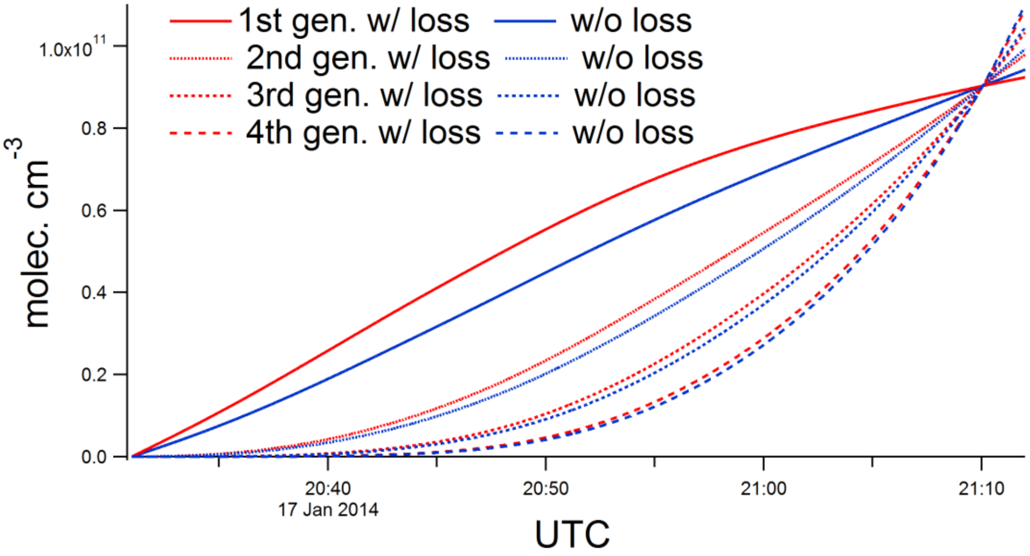

Figure 2.10. Time evolution of the products from different generations of oxidation calculated with the kinetic model with and without wall losses. The contribution of wall losses during the initial period shown is small. The traces are all scaled to the value of the largest trace at 21:10 UTC.

An aerosol uptake coefficient γ_{SOA}=1.0 ± 0.1, a wall loss rate of $k_{wall} = 3.0 \times 10^{-3}\ s^{-1} \pm 7.5 \times 10^{-4}\ s^{-1}$, and an ISOPOOH + OH branching ratio for $C_5H_{10}O_5$ of 2.5% ± 0.6% best reproduces the observed time series for the SOA-condensing $C_5H_{10}O_5$ isomer. These values correspond to a first-order uptake rate (lifetime) of $k_{SOA} \sim 2.2 \times 10^{-3}\ s^{-1}$ (τ ~8 min) at the peak of OA surface area and a wall-loss time scale of ~6 min. A detailed explanation of the parameter estimation method and related uncertainty is provided above in the methods section.

The time-dependent LVOC behavior after the lights are turned off shows substantial variations in the LVOC relative loss rates to wall plus aerosol (Fig. 2.9c and d, respectively). The measured LVOC traces are compared with the results of several model runs for multiple values of γ_{SOA} and k_{wall} (Fig. 2.10d). The majority of traces lie within a relatively narrow range of uptake coefficients ($k_{wall} =$ 1.0 × 10^{-4} to ~5.0 × 10^{-3} and γ_{SOA}~0.5-1).

We note that most detected LVOC reach a plateau ~ 2 h. after the lights are turned off. This could be due to two different reasons: (a) equilibrium is being reached and a substantial gas-phase fraction remains for all LVOC; or (b) the presence of (at least) one condensing and one non-condensing isomer for each compound detected. Gas-wall partitioning for oxidized species can be approximately modeled with an equivalent OA mass of ~ 5 mg m^{-3}.[94,95] Since these LVOC are observed to condense on OA concentrations 10^4 times lower, their C^* must be of the order of 1 µg m^{-3}, and a substantial gas-phase fraction cannot remain in equilibrium with the high equivalent wall concentrations. Thus we conclude that the presence of at least one non-condensing isomer is the most likely explanation, which is consistent with the range of possible C^* shown in Fig. 2.7. For example, the observed time series of $C_5H_{10}O_5$ (Fig. 2.8b) could only be matched by simulating the formation of two isomers, one of which is lost to the aerosol and one of which was not (Fig. 2.11). The non-condensing isomer was fit with a k_{wall} = 7.0 × 10^{-5} (τ_{wall} ~ 4 hr). Branching ratios of 2.5% and 0.6% (Table 2.3) for the condensing and non-condensing isomers, respectively, provided a quantitative match with the observations.

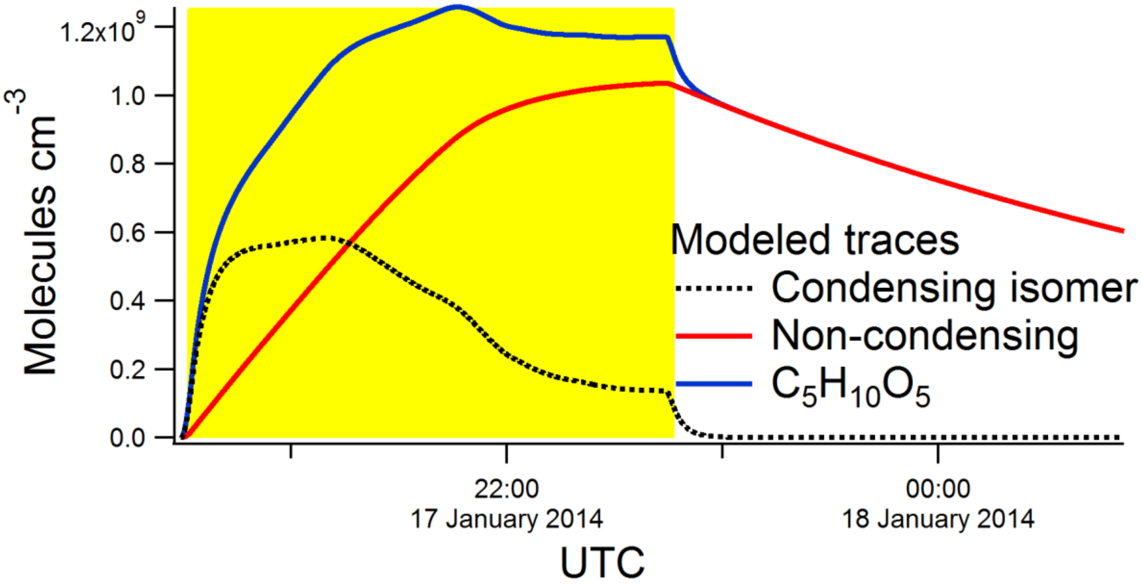

Figure 2.11. Time series for the two modeled isomers that comprise the $C_5H_{10}O_5$ modeled trace. The isomer that condenses is of low-volatility and is rapidly lost to the walls and aerosol as soon as the lights are turned off. The non-condensing isomer is slowly lost to the walls and accounts for the large amount of sum $C_5H_{10}O_5$ remaining at the end of the experiment. Note that the non-condensing isomer may be lost to the inlet less efficiently than the condensing isomer, and thus may have an overestimated concentration, but this is of no consequence for the SOA modeling.

The second and third highest aerosol-contributing LVOC, $C_5H_{12}O_5$ and $C_5H_{12}O_6$ were also modeled and are shown in Figs. 2.12, 2.13 along with their uptake coefficients. These wall loss rates are consistent and are in the expected range for low volatility species based on previous modeling studies of experiments in the Caltech chamber and other facilities (Fig. 2.14).[79]

$C_5H_{12}O_6$ is the largest observed signal in the gas phase spectrum, contributing the third-largest amount of mass to SOA. Previous works[41,49,96] have proposed that this species could possibly form from the gas-phase oxidation of ISOPOOH by OH with a subsequent reaction with O_2 and HO_2, resulting in a C_5 dihydroxy dihydroperoxide (Fig. 2.15), although this species was not observed in that study. However, the time dependence of the $C_5H_{12}O_6$ increase (Fig. 2.13) appears intermediate between a first-generation and second-generation mechanism, suggesting multiple potential formation pathways.

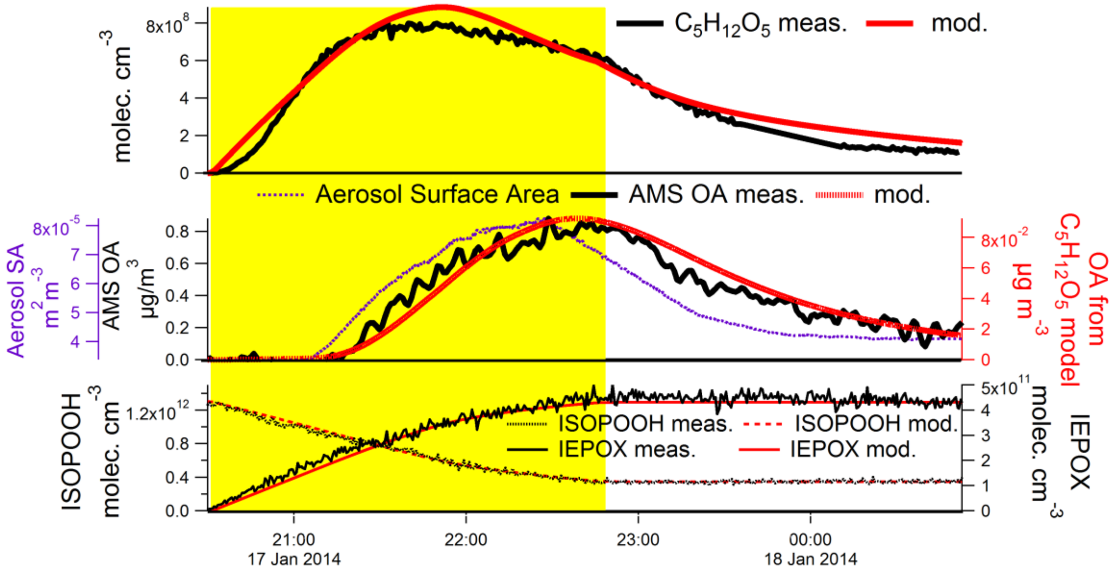

Figure 2.12. Time series of measured (red) and modeled (black) gas and aerosol concentrations for $C_5H_{12}O_5$. The LVOC was fit with one modeled species with optimized values of $\gamma_{SOA} = 0.2$, $k_{wall} = 1 \times 10^{-4}$, and an ISOPOOH + OH reaction rate branching ratio of 0.4%. The model SOA (middle, right axis) gives the approximate fractional contribution of $C_5H_{12}O_5$ and the surface area has been binomially smoothed across 10 points.

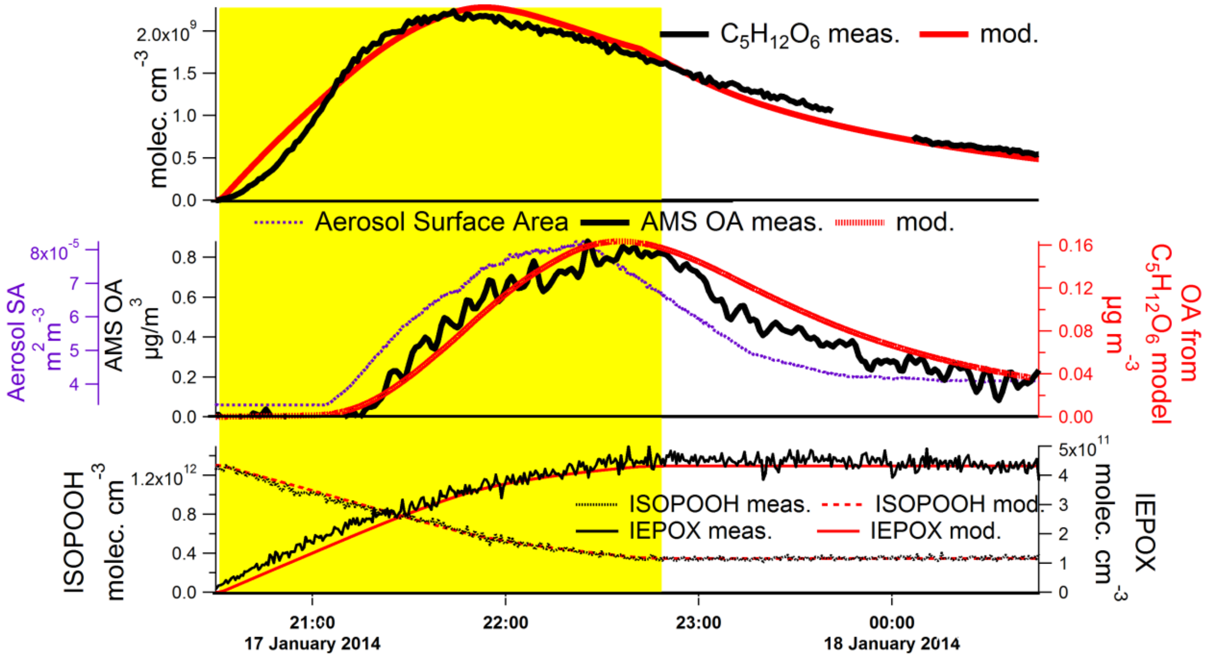

Figure 2.13. Model time series for C5H12O6. The model was run with $C_5H_{12}O_6$ as a first-generation product of ISOPOOH oxidation. This LVOC was fit with one modeled species using values of $\gamma_{SOA} = 0.1$ and $k_{wall} = 1.5\times10^{-4}$ s^{-1} and an ISOPOOH + OH reaction rate branching ratio of 1.0%. The model SOA (middle, right axis) gives the approximate fractional contribution of $C_5H_{12}O_6$ and the surface area has been binomially smoothed across 10 points.

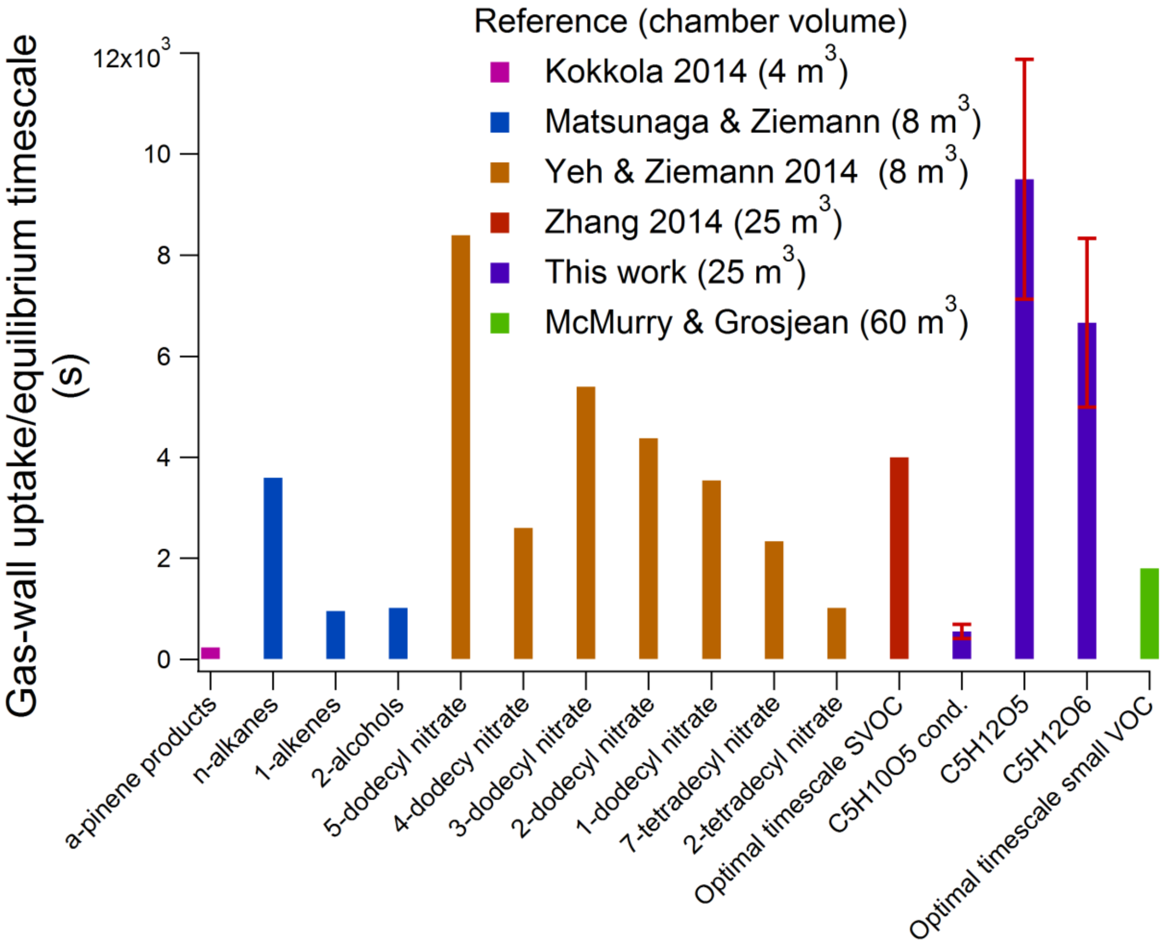

Figure 2.14. Gas-wall equilibrium time scales from gas-phase species in this work compared to values presented in previous works. Previous values are taken from Zhang et al., Yeh and Ziemann [95], McMurry and Grosjean[80], Matsunaga and Ziemann [94], and Kokkola et al. [97].

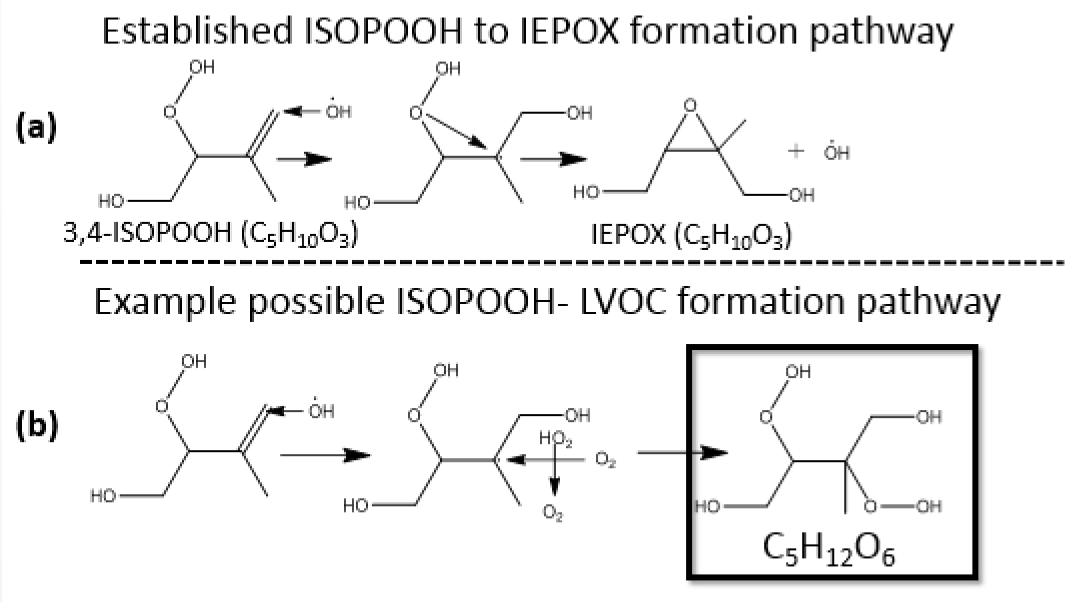

Figure 2.15. Possible formation mechanism for one of the observed LVOC: $C_5H_{12}O_6$, as originally proposed in Paulot et al.[41] A species consistent with the elemental composition of the species in the square was detected in this study by the NO_3^--CIMS. Reaction **b** proceeds via addition of the hydroxyl radical one side of the double bond in ISOPOOH, producing the same intermediate as for IEPOX. However, then addition of O_2 occurs at the adjacent tertiary carbon followed by reaction with HO_2 that transfers a hydrogen atom, forming a hydroperoxy group. The established IEPOX formation mechanism **(a)** is shown above for comparison.

2.3.6. Ambient Observations

The fourteen condensing species detected during the ISOPOOH chamber experiment were also observed in the ambient environment by the same NO_3^--CIMS (with a shorter (0.7m) inlet) at the Centreville, AL supersite during the SOAS campaign in summer 2013. The site was a rural, mixed-forest site where a substantial fraction of isoprene oxidation proceeds through the low-NO isoprene pathway. The diurnal cycles for the four most abundant LVOC are shown in Fig. 2.16a. ISOPOOH concentrations show a broad maximum, peaking at 16:00 (CDT) as shown in Fig. 2.16b. These LVOC show temporal behavior consistent with isoprene + OH oxidation products, and not of other biogenic hydrocarbons, such as monoterpenes, or of NO_3 chemistry products, which peaked at night. The diurnal cycle of modeled LVOC production rates is also presented in Fig. 2.16a. The production is estimated as:

$$P[LVOC] = Y_{LVOC}\, k_{ISOPOOH-OH}[ISOPOOH][OH]$$

where Y_{LVOC} is the total LVOC yield determined from the chamber experiments, and the [ISOPOOH] and [OH] concentrations are from the actual SOAS measurements (Fig. 2.16b). The estimated production rate is consistent with the LVOC diurnal profiles observed in the atmosphere. The main loss of the LVOC is expected to be condensation onto the aerosol. Scaling the time scales observed in the chamber by the ratio of the surface areas provides a time constant for this process of the order of 30 min., which is consistent with the rapid decrease in LVOC concentrations in the afternoon.

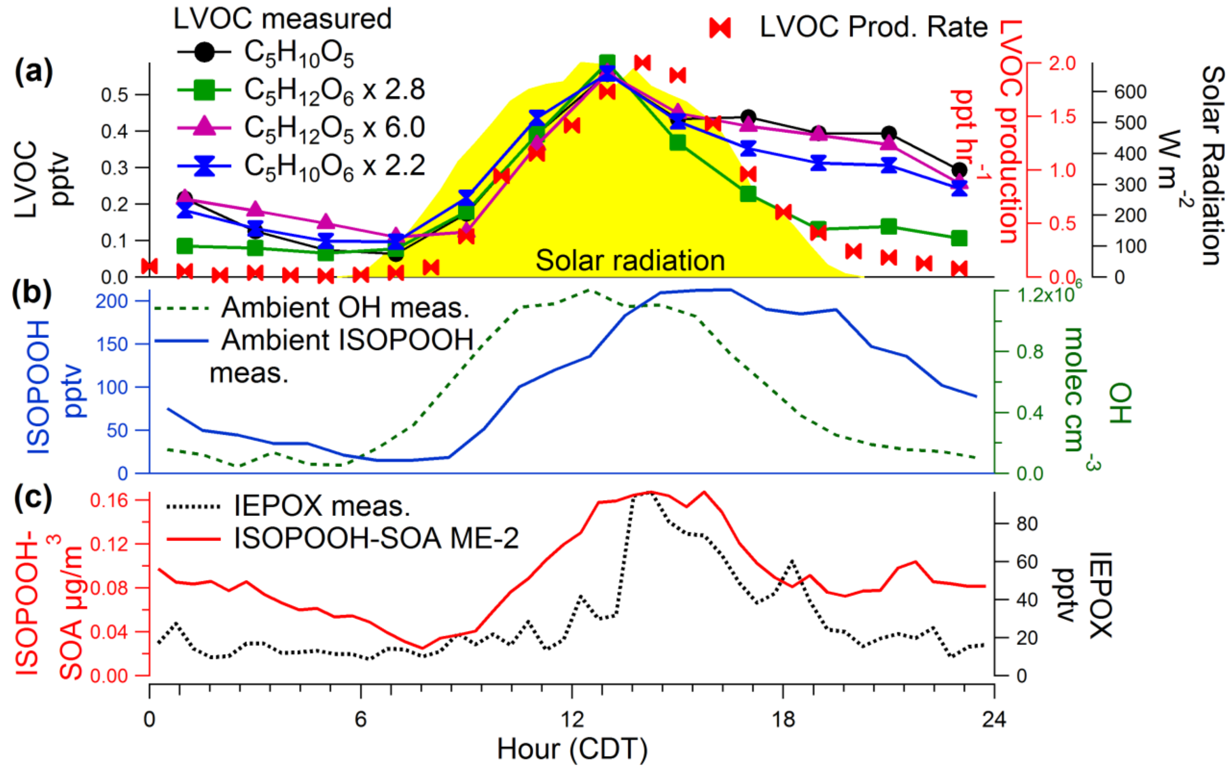

Figure 2.16. Diurnal cycles of ambient measurements during the SOAS field study from a 10-day period beginning 22 June 2013: (a) key LVOC identified in the laboratory; and **(b)** OH and ISOPOOH. Also shown in panel **(a)** is the LVOC production rate (k[ISOPOOH][OH]) multiplied by a yield of ~1%. All of the diurnal cycles peak around 13:00 CDT when solar radiation and OH are at peak levels. **(c)** ISOPOOH SOA estimated with factor analysis of ambient AMS data and ambient IEPOX. ISOPOOH and OH were binomially smoothed using over 5 or 2 data points, respectively, before diurnal averaging. The time scale of aerosol uptake is estimated at ~4 min.

We also performed a Positive Matrix Factorization analysis of the ambient AMS SOAS data in which we constrained the spectrum from FIXCIT ISOPOOH-SOA. The details and results of this analysis are provided above in the methods section of this chapter and Fig. 2.16c, respectively. We obtained an average ISOPOOH-SOA SOAS ambient concentration of ~95 ng m^{-3}, which accounts for ~2% of the observed ambient OA. This is consistent with our estimated peak concentration of 85 ng m^{-3} by integrating the area under the production rate curve in Fig. 2.16a and assuming a comparatively slow loss (~12 h) via dry deposition.[98]

A full model for the observed ambient traces would also need to consider surface deposition as well as growth of the boundary layer and entrainment at its top,[99] which is beyond the scope of this work. The fact that some LVOC signals persist into the night when production should be much slower suggests that some fraction of the signal is composed of more volatile non-condensing isomers.

2.3.7 Atmospheric Implications

Assuming that all of the maximum chamber SOA peak concentration of 0.85µg m^{-3} was due to LVOC condensation from oxidation of 42 ppbv of ISOPOOH, we obtain a wall-loss corrected SOA mass yield of 4.2% from 4,3-ISOPOOH. The relatively large gas-phase loss to the walls (Fig. 2.17) results from the large ratio of wall surface area to aerosol surface area. At the peak of the aerosol surface area, this ratio is $1:2 \times 10^{-5}$. The total estimated uncertainty of the SOA yield has contributions from the instruments, aerosol surface area, standard impurities, and wall loss correction uncertainties. We estimate the overall uncertainty on the SOA yield from 4,3-ISOPOOH via the LVOC pathway as a factor of 2.5. Compared to values in a previous study of the effect of seed-to-chamber surface area ratio on aerosol mass yields (Table 1 in ref. [79]), the surface area ratio in this study is in a range in which vapor wall deposition has been shown to reduce SOA yields.

These small SOA concentrations (< 1 µg m^{-3}) are unusual for most SOA-focused experiments at Caltech or other chambers. Our results suggest that SOA yields determined at low "atmospherically relevant" SOA loadings may have significant low biases if vapor losses to walls are not accounted for (Fig. 2.18).[100,101]

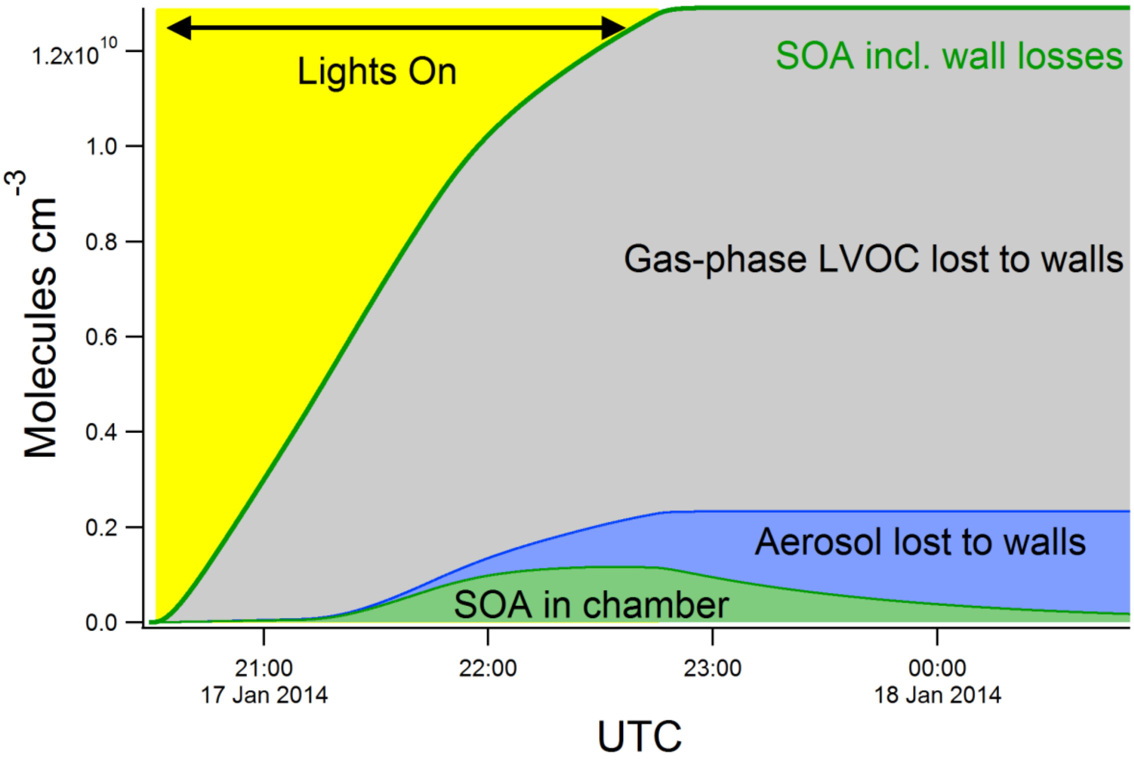

Figure 2.17. Model results for runs with and without sinks to the chamber walls for $C_5H_{10}O_5$. The difference between the two models is used to calculate the increase in SOA yield as it incorporates the amount of gas-phase material that could have formed SOA, if losses to the walls had not been active. The traces are stacked on top of one another.

Under the assumption that all SOA in the chamber experiment was formed from the oxidation of 4,3-ISOPOOH (see above text for possible role of other OVOC present in chamber), we estimate the implied global SOA production rates via this mechanism. First, we estimate the 4,3-ISOPOOH yield from isoprene. The total ISOPOOH yield from isoprene + OH + O_2 + HO_2 reactions is estimated to be > 75% (molar) yield.[41]. Here, we assume the 4,3-ISOPOOH isomer to compose~40% (±10%) of ambient ISOPOOH production.[42,102] We do not know the LVOC yield from 1,2-ISOPOOH. Thus, the non-IEPOX SOA yield from isoprene via 4,3-ISOPOOH is estimated at 2.3%. If 1,2-ISOPOOH has the same yield of condensing SOA as observed in this experiment, the calculated non-IEPOX SOA yield from isoprene would be 5.8%. To estimate the global SOA production we use the estimated fraction of isoprene peroxy radicals reacting with HO_2 (43%),[103] giving a final global production of 5 Tg yr^{-1} (via 4,3-ISOPOOH only) of SOA, or ~ 3.3% of the estimated annual SOA production from all sources of ~150 Tg yr^{-1}. [8,37] This non-IEPOX SOA source is comparable in magnitude to the maximum potential SOA formation of the ELVOC pathway (6.5 Tg yr^{-1})[20] though not in nucleation potential, meaning the new SOA formation pathway is likely to be atmospherically significant. Furthermore, because this SOA was observed to grow nanoparticles and to condense on OA below 1 μg m^{-3} at room temperature, this pathway would be operative in clean ambient environments with low OA concentrations and especially contribute to the growth of nanoparticles, which traditional SVOCs cannot do.[104]

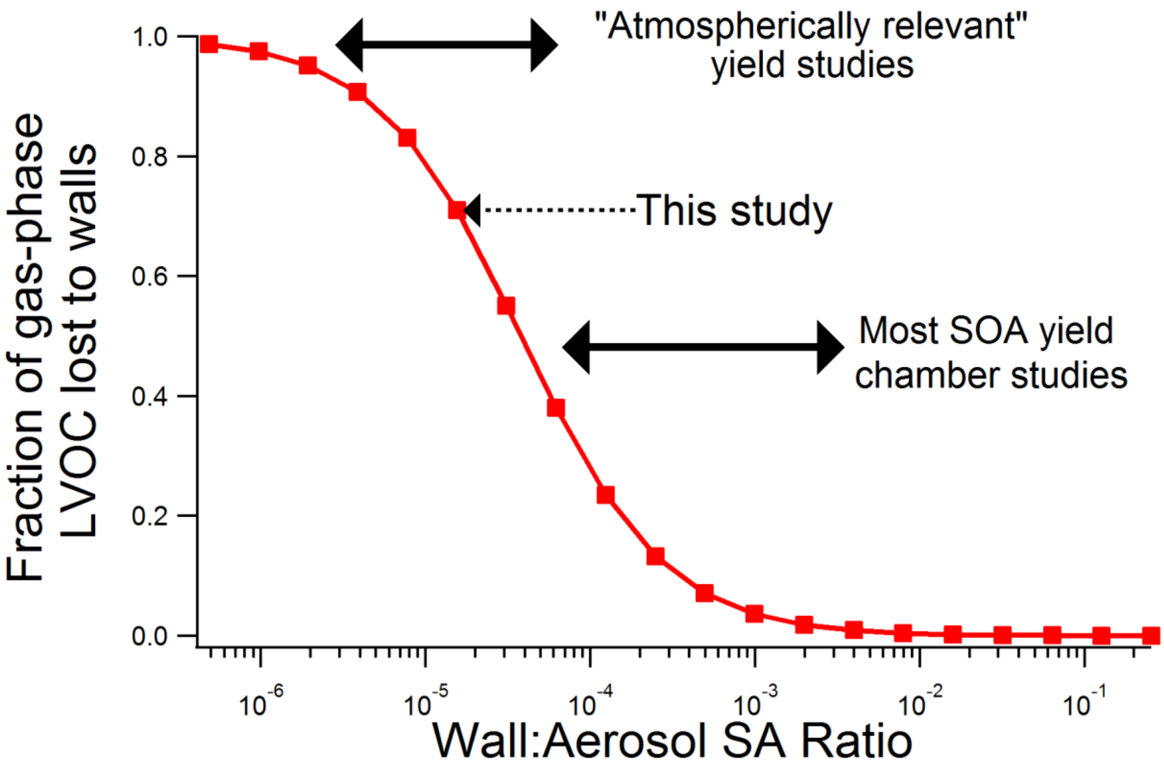

Figure 2.18. The fraction of gas-phase LVOC lost to the chamber walls versus the Wall:Aerosol surface area ratio, calculated using the kinetic box model and assuming a constant aerosol surface area for each case, for simplicity. Note that this figure assumes irreversible condensation with the SOA uptake coefficient γ_{SOA} = 1.0 determined for $C_5H_{10}O_5$ in this study.

Although IEPOX forms from isoprene at high yields, its uptake into atmospheric aerosol is often at a slow rate,[88] leading to large losses to dry deposition and OH reaction.[98] The non-IEPOX SOA source proposed in this work forms from small amounts of gas-phase LVOC with high yields, as the LVOCs rapidly condense onto existing particulate matter. It has recently been proposed[46] that IEPOX uptake may only explain half of aerosol formed from low-NO isoprene oxidation; the SOA pathway in this work may account for a fraction of that missing SOA source.

Future laboratory studies should investigate the molecular identities and formation mechanisms of these LVOC, the effect of conditions such as temperature and aerosol water, and the potential formation of LVOC from other isoprene reaction pathways. Of special interest is the yield of LVOC and SOA from 1,2-ISOPOOH. In addition, the lifetime of the SOA produced via this chemistry should be investigated.[105,106]

Chapter 3*:*
Quantification of Gas-Wall Partitioning in Teflon Environmental Chambers Using Rapid Bursts of Low-Volatility Oxidized Species Generated in Situ

Reprinted with permission from Krechmer, J. E., Pagonis, D., Ziemann, P. J. and Jimenez, J. L.: Quantification of Gas-Wall Partitioning in Teflon Environmental Chambers Using Rapid Bursts of Low-Volatility Oxidized Species Generated in Situ, Environ. Sci. Technol., 50(11), 5757–5765, doi:10.1021/acs.est.6b00606, 2016. Copyright 2015 American Chemical Society

3.1 Introduction

Environmental or "smog" chambers have played an integral role in atmospheric aerosol research for decades.[35] Commonly constructed from sheets of fluorinated ethylene propylene (FEP) Teflon, these chambers are often employed as reaction vessels in which volatile organic compounds (VOC) are reacted with atmospheric oxidants to form secondary organic aerosols (SOA). SOA comprises a substantial fraction of fine particular matter,[7] which is the subject of intense study because of large but uncertain effects on radiative forcing[36] and negative impacts on human health.[2] Quantification of the SOA yield, defined as the mass of SOA formed per unit mass of volatile organic compound (VOC) precursor reacted, is often the primary objective of SOA chamber experiments. Yields from chamber experiments are typically parameterized and used in three-dimensional computer models, which are used to study the effects of aerosols on air quality and climate.

Gas-wall partitioning (GWP) of organic compounds is a recently reported phenomenon that can lead to substantial underestimation of SOA yields. Loss of gas-phase organic compounds to Teflon chamber films was first investigated systematically in 1985 by McMurry and Grosjean,[80] although those authors focused on very volatile compounds and reported undetectable partitioning to Teflon walls over a 5 h period.[107] In contrast to these results, Ziemann and co-workers[94,108] have recently observed that substantial fractions of semivolatile hydrocarbons and oxidized organic compounds partitioned reversibly to the walls of Teflon chambers with equilibration time scales of tens of minutes, and that the absorptive partitioning capacity of the walls was equivalent to an organic aerosol mass concentration of ~10 mg m^{-3}. Since then, several studies have attempted to account for the effects of gas-wall partitioning in chamber experiments by using model parameters similar to those measured by Ziemann and co-workers, and report that it can lead to underestimates of SOA yields by factors ranging from 1.1 to 6 [109] and loss of ~35% of primary organic aerosol emitted from biomass burning.[110]

Despite these recent studies, the time scales for reaching GWP equilibrium, τ_{GWE}, and the equivalent organic mass concentration of the walls, C_w, and consequently the effect of GWP on SOA yields, remain controversial. Studies conducted by adding known concentrations of standard compounds to the chamber and then measuring GWP using gas chromatography have reported τ_{GWE} ~10–100 min and C_w ~2–40 mg m^{-3}, [94,108] whereas other studies that have employed CIMS or Laser-Induced Phosphorescence (LIP) to measure GWP of compounds generated *in situ* from reactions ranging in length from 10 min to 7 h have reported volatility-dependent values of these parameters with much different ranges of τ_{GWE} ~8–300 h and C_w ~0.0004–300 mg m^{-3}.[111–113]

In this work we demonstrate a new technique to study GWP that removes some of the uncertainties inherent in previous experimental studies. We generated semi- and low-volatility organic compounds *in situ* in an environmental chamber and used real-time “inlet-less” mass spectrometry to monitor the formation and wall loss of several classes of gaseous compounds simultaneously, whose volatilities span six orders of magnitude. We present values of τ_{GWE} and C_w from these experiments, compare to the literature, and present recommended parameters for modeling GWP. We also demonstrate potential biases when using CIMS with inlets and ion sources that allow for significant contact of compounds with the walls.

3.2 Experimental Methods

3.2.1 Chemicals

The following chemicals, with purities and supplier, were used: 1-hexanol, 1-heptanol, 1-octanol, 1-nonanol, 1-decanol, 1-undecanol, and 1-dodecanol (>99.9%; PolyScience); NO (99%, Matheson Tri-gas); and methyl nitrite was synthesized according to Taylor et al.[114] and stored in liquid nitrogen under vacuum until used.

3.2.2 Environmental chamber

Experiments were conducted in an 8 m^3 Dupont Teflon FEP environmental chamber filled with clean, dry air from an AADCO (Cleves, OH, USA) Model 737-14A clean air generator. The bag is suspended inside a curtained frame with UV blacklights on two sides. The bag temperature (when lights are off) is the same as the laboratory temperature, typically about 22^{o}C due to the laboratory ventilation system. Other chamber details have been described previously.[108] The chamber can be actively mixed by turning on a small Teflon-coated fan.

Using CO_2 as a tracer it was determined that the chamber contents could be completely mixed by turning the fan on for 20 s (Figures 3.1), so that mixing time was used in the experiments reported here. We used an LI-840A (LI-COR, Lincoln, Nebraska, USA) non-dispersive infrared CO_2 analyzer to measure sudden changes in the concentration of CO_2 in the chamber following rapid injections of a CO_2 standard gas. CO_2 data were acquired at a rate of 1 Hz, which was necessary to visibly observe the rapidly changing concentrations involved in measuring the active mixed time scale.

To measure the active mixing time scale, a set quantity of CO_2 was injected from a cylinder via a glass bulb. The exact quantity of CO_2 is unimportant; it is only necessary that the injected quantity be significantly higher than the concentration in the chamber and that it is injected quickly through a single chamber port. A small Teflon-coated fan was then turned on inside the bag. The fan creates eddies in the bag, which are visible as variances in the measured CO_2 concentration observed by the analyzer. This behavior is shown for four such injections in Figure 3.1, with the final concentrations subtracted so that the traces lay on top of one another at the end of the experiment. Every trace shows oscillating concentrations for ~ 15 seconds, but all four settle down to a stable value after 20 s. This point of stability defines the actively mixed time scale. Note that this should be understood as a ~95% time scale, as opposed to the 1/e (63%) time scales derived for τ_{GWE} via fitting, as described in the rest of this text.

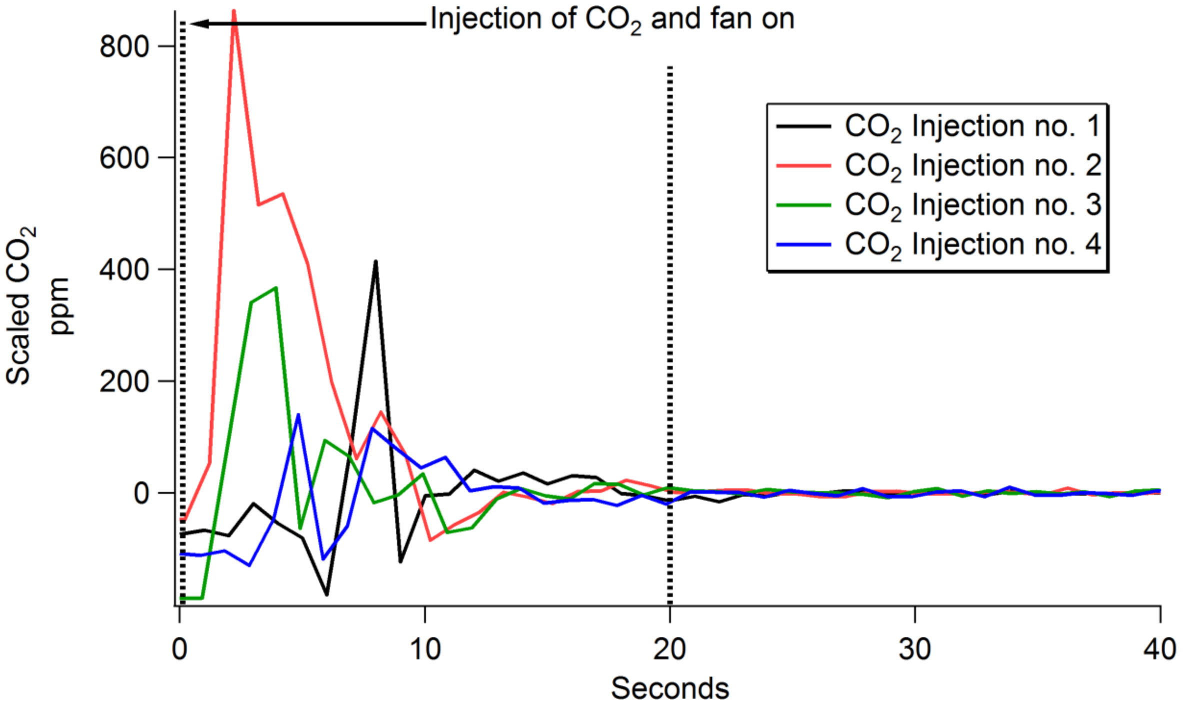

Figure 3.1. Results of an experiment to determine the active mixing time scale (when using a fan) for our environmental chamber. CO_2 time series traces are scaled so that their ending values are the same. The oscillations in the beginning are due to incomplete mixing of CO_2 in the bag. The dotted vertical line on the left denotes when

the fan was turned on and the one on the right denotes the point at which the chamber is well-mixed (20 s). Note that this should be understood as a ~95% time scale, as opposed to the 1/e (63%) time scales derived for τ_{GWE} via fitting, as described on the main text.

The same procedure was followed to measure the passive mixing time scale, when no fan was used. As expected, the passive mixing time scale was much longer (~700 s) than the actively mixed time scale (~20 s). The passive time scale mixing traces are shown in Figure 3.2 in the same format as Figure 3.1.

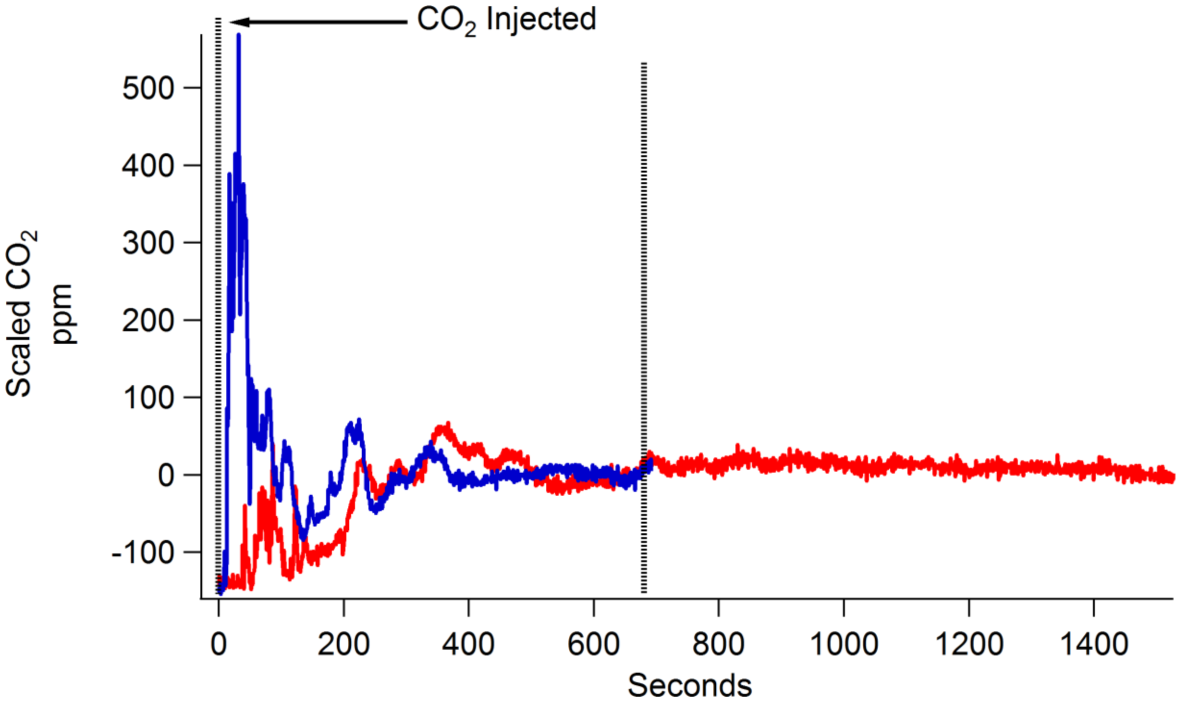

Figure 3.2. Results of an experiment to determine the passive mixing time scale for our environmental chamber. CO_2 time series traces are scaled so that their ending values are the same. The irregular oscillations in the beginning are due to incomplete mixing of CO_2 in the bag. The dotted vertical line denotes the point at which the chamber is considered to be well-mixed (~ 700 s). Note that this should be understood as a ~95% time scale, as opposed to the 1/e (63%) time scales derived for t_{GWE} via fitting, as described on the main text.

3.2.3 Chemical ionization mass spectrometry (CIMS) measurements.

Gas-phase reaction products were monitored using an Aerodyne high-resolution time-of-flight mass spectrometer employing chemical ionization sources (HR-ToF-CIMS; hereafter CIMS).[22] The CIMS acquires the entire high-resolution mass-to-charge (*m/z*) spectrum at a time resolution of 1 s. This enabled us to simultaneously monitor dozens of compounds, including isobaric species (e.g. $C_7H_{13}NO_6$ and $C_8H_{17}NO_5$, both *m/z* 207), in real time.

A key feature of these experiments was the use of a nitrate ion source (hereafter: NO_3-CIMS; AirModus Oy and Aerodyne Research, Inc.) for measurements of semi- and low-volatility oxidized organic compounds in the gas-phase. This instrument has been described in previous publications.[22,24,58] Critical to this work, it is considered to be an "inlet-less" source design. That is, the source is constructed with concentric sample and sheath flows and a short residence time in order to minimize diffusive losses of sample to the source walls prior to ionization.[115] This enables the NO_3-CIMS to measure "sticky" compounds like sulfuric acid (H_2SO_4),[58] which would otherwise be irreversibly lost to the source walls on first contact. 10 standard L min^{-1} (SLPM) of sample air was drawn from the chamber to the NO_3^- source through an electropolished stainless steel tube 0.7 m in length and 0.015 m inner diameter. Using standard equations and assuming laminar flow and irreversible uptake ($\gamma_{wall} = 1$),[60] we estimate that 35% of the analyte is lost via gaseous diffusion to the NO_3-CIMS inlet walls. Figure 3.3 shows how the time response of the NO_3-CIMS to a finite period of zero air is nearly instantaneous, supporting the lack of inlet memory effects for this instrument. An explanation of how to calculate diffusive losses can be found below.

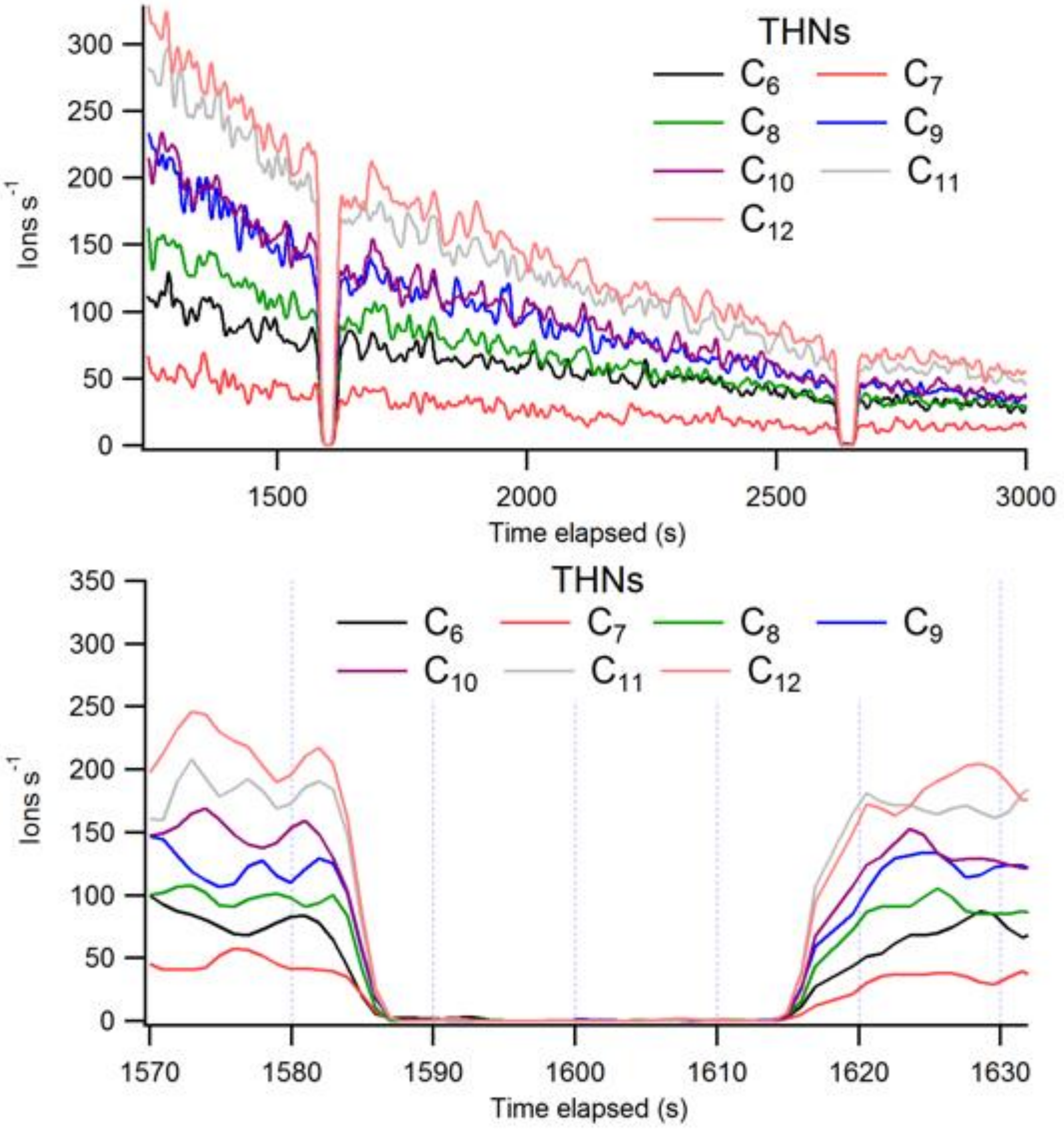

Figure 3.3. Time series of trihydroxynitrates (THNs) in which the NO3-CIMS inlet was removed from the chamber and flooded with air from a clean air generator. Two such "zeroing" periods are depicted in the figure. The bottom panel is a zoomed in version of the first "zeroing." The time response of the instrument was < 5 s, which corresponds to the residence time of the inlet and source.

In addition, an iodide ion source (I-CIMS) was used for comparison purposes.[90,116] I^- reagent ions were generated by running 2 SLPM of ultra-high purity (UHP) nitrogen gas (N_2) through a polonium-210 ionizer and into an ion molecule reaction region (IMR; Aerodyne Research, Inc.). 2 SLPM of sample air was simultaneously drawn from the chamber to the IMR through a 0.7 m long PTFE Teflon line with a 0.0048 m inner diameter. The I-CIMS inlet is estimated to have larger diffusive losses to the inlet walls than the NO_3-CIMS at ~77%. The IMR is a stainless steel chamber with a volume of 47 cm^3 and residence time of 100 ms [16] under typical operating conditions. Flow in the IMR is complex due to mixing of two equal perpendicular flows and can enhance contact of analyte with IMR chamber walls.

Data from both CIMS configurations were saved and analyzed at a time resolution of 1 s. Longer experiments (>10 hr) were averaged to 1 min resolution before analysis to reduce processing time. Analysis was performed using the Tofware (Tofwerk, AG and Aerodyne, version 2.5) toolkit within the IGOR Pro 6 software package (Wavemetrics, Inc.). Because this study was only concerned with relative changes in gas-phase concentrations of individual compounds in time, for which the CIMS response is linear,[57,90] we did not calibrate compound sensitivities and so report results in units of ions s^{-1}.

Wall losses of gas-phase species to CIMS' inlet walls due to gaseous diffusion were estimated using equations provided in[60].

The fraction of species penetrating a tube can be expressed by η [Ref: 60]:

$$\eta_{tube} = \exp[-\xi Sh] \tag{3.1}$$

where *Sh* is the Sherwood number and is calculated for laminar flow as[60]:

$$Sh = 3.66 + \frac{0.2672}{\xi + 0.10079\,\xi^{1/3}} \tag{3.2}$$

in which ξ is a dimensionless diffusion parameter[60]:

$$\xi = \frac{\pi D L}{Q} \tag{3.3}$$

and *D* is a species diffusion coefficient, *L* is the tube length, and *Q* is the volumetric rate of flow through the tube. In this work, we used the online SPARC calculator[61,62] to calculate a diffusion coefficient for an example molecule. We refer the reader to the literature reference for more detailed information on these calculations.[60]

3.2.4 Experimental design.

Chamber experiments were conducted over a several-month period (Table 3.1). In a typical experiment, 4 to 7 1-alcohols with carbon numbers ranging from C_6 to C_{12} were added simultaneously to the chamber and the fan was turned on for 20 s. Initial concentrations were 0.63, 0.42, 0.37, 0.22, 0.14, 0.10, and 0.09 ppmv for C_6–C_{12}, respectively, with a total concentration ≤ 2 ppmv. Using compound vapor pressures calculated using SIMPOL.1[91], these concentrations correspond to saturation ratios for each compound of $<10^{-3}$. After adding the alcohols, 5 ppmv each of methyl nitrite and NO were added and the fan was again turned on for 20 s to ensure that all precursors were well mixed. Concentrations NO and NO_2 were measured using a Model 42 Thermo Gas Analyzer. 3 to 5 minutes later, the UV blacklights were turned on at 100% intensity (corresponding to $J_{NO2} \sim 0.61$ min^{-1}) for precisely 10 s to initiate production of OH radicals and subsequent VOC reactions,[117] and the gas-phase products were monitored using the CIMS. Although the amount of alcohol that reacted was too small to be measured, based on GC-FID measurements made in a previous study when 2-decanol was reacted under similar conditions for 60 s, it is estimated that the fraction of each alcohol reacted here was ~2–3%, corresponding to a total of ~50 ppbv.

No.	HC Precursor (s)	[HC]	[NO] (ppm)	[MeNO2] (ppm)	Reagent Ion	Line Length	Light Burst Duration	Other
1	1-Alkanols: C_6, C_8, C_{10}, C_{12}	2.1	2.9	2.8	NO_3^-	0.7 m	10 s	
2	1-Alkanols: C_6, C_8, C_{10}, C_{12}	0.9	3.3	2.7	NO_3^-	0.7 m	10 s	
3	1-Alkanols: C_6-C_{12}	2.0	2.9	2.7	NO_3^-	0.7 m	10 s	
4	1-Alkanols: C_6-C_{12}	1.9	3.0	2.8	NO_3^-	Variable	10 s	
5	1-Alkanols: C_6-C_{12}	2.0	3.3	2.9	I^-	Variable	10 s	
6	1-Alkanols: C_6-C_{12}	2.0	3.2	2.6	I^-	0.7 m	10 s	> 10 hr
7	1-Alkanols: C_6-C_{12}	2.0	3.1	2.7	I^-	0.7 m	10 s	Long experiment; open holes in bag to test leak hypothesis
8	1-Alcohols: C_6, C_8, C_{10}, C_{12}	0.05	3.1	0.35	I^-	0.7 m	1 hr	> 20 hr Long oxidation time

Table 3.1. Summary of relevant conditions under which some experiments were performed. Multiple wall loss measurements were obtained for many of the experiments.

It important to note that the experiments were designed to isolate the effects of GWP on the measured concentrations of gas-phase products by minimizing or eliminating competing partitioning processes.

First, to avoid partitioning of gaseous compounds to particles, all experiments were performed with no detectable condensation sink to particles present in the chamber (corresponding to an infinite (or very long compared to the experiments) condensation sink time scale. The condensation time scale (τ, in units of s) can be calculated using the following formulas[78]:

$$k_{uptake}=\frac{1}{4}\bar{c}A\gamma \tag{3.4}$$

$$\tau_{cond}=\frac{1}{k_{uptake}} \tag{3.5}$$

where $\bar{c}$ is the mean speed of LVOC molecules in the gas-phase, γ is the uptake coefficient, and A is the aerosol surface area. $\bar{c}$ was calculated for a representative molecular weight of 250 amu. Because any particles present would be <50 nm, the Fuchs-Sutugin correction for the transition regime is small[118] and can be neglected. Particle number concentrations and surface area were continuously monitored using an ultrafine condensation particle counter (UCPC, TSI 3776) with a particle size cutoff of 2.5 nm and a counting efficiency of 100% at 3 nm and 60% at 2.5 nm. Prior to each experiment the chamber was thoroughly flushed for at least 24 hr and irradiated with full-strength UV lights for several hours. Initial particle concentrations were 0 cm^{-3}, corresponding to a condensation sink of 0 s^{-1}. The UCPC size cutoff of 2.5 nm means that there could have been particles smaller than 2.5 nm in the chamber, but the condensation sink would still be negligible.

Experiments were aborted if they rose above 200 cm^{-3} during an experiment. In select experiments the particle mass concentration was also monitored using a TSI 3081 scanning mobility particle sizer (SMPS) with a TSI 3772 condensation particle counter, with a particle size cutoff of 10 nm and a counting efficiency of 100% at 30 nm and 60% at 12 nm. No measurable particle mass was observed when particle number concentrations were less than 200 cm^{-3}.

Second, initial total concentrations of added VOCs were low enough and the irradiation time short enough to prevent VOC precursors from partitioning into the aerosol phase and to limit the amount of oxygenated low-volatility products formed in a short photochemical reaction period. Only a very small fraction (~2–3%) of the VOCs was consumed in an experiment. This very short "burst" of photochemical oxidation was deliberate: longer irradiation by UV lights would have resulted in a less precisely defined start time for the GWP process, and may have also resulted in SOA formation, thus providing a competing sink for vapors. Since only a very small fraction of the VOCs reacted during one burst, the lights could be turned on for three or four of these 10 s bursts (while allowing time between for products formed in the previous burst to equilibrate with the walls) before particle concentrations exceeded 200 cm^{-3} and forced termination of the experiment, thus providing multiple opportunities per experiment to monitor dynamic gas-wall partitioning. No dependence of τ_{GWE} on the burst number within a given experiment was observed (Figure 3.4).

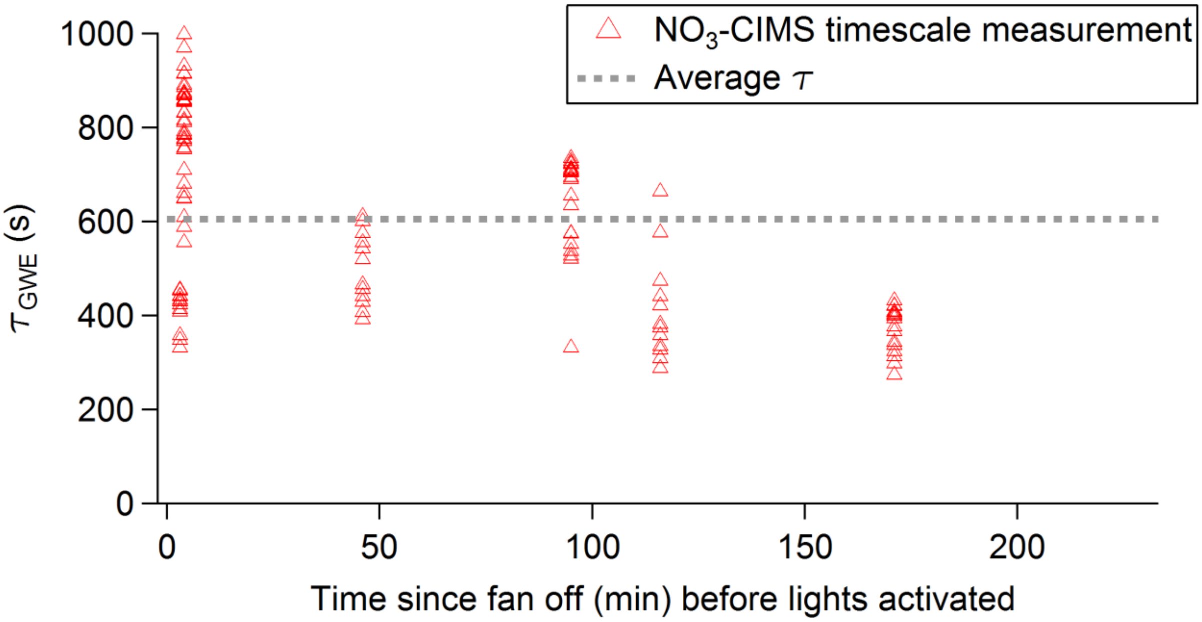

Figure 3.4. τ_{GWE} measurements from the NO_3-CIMS as a function of the time elapsed since the fan was turned off in the chamber.

3.3 Results and Discussion

3.3.1 Determination of gas-wall partitioning time scales

The CIMS detected small quantities (estimated to be in the ppt range) of first and second generation trifunctional and tetrafunctional products formed from the OH radical-initiated oxidation of the 1-alcohols under high-NO conditions. The same products, consisting of dihydroxynitrates (DHN), trihydroxynitrates (THN), and dihydroxycarbonylnitrates (DHCN), were formed from each of the C_6-C_{12} 1-alcohol precursors, consistent with previous studies of alkane and alkene oxidation.[119,120] The I-CIMS also detected first generation hydroxynitrates that were not detected by the NO_3-CIMS. All detected products and some of their molecular properties are listed in Table 3.2, and a mechanism for their formation is shown in Figure 3.5.

Compound Class	**Formula**	**MW**	**NO_3^- MW**	**I^- MW**	**Precursor**	**SIMPOL c^* ($\mu g\ m^{-3}$)**
DHCN	$C_6H_{11}NO_6$	193	255	320	Hexanol	3.34E+01
DHCN	$C_7H_{13}NO_6$	207	269	334	Heptanol	1.30E+01
DHCN	$C_8H_{15}NO_6$	221	283	348	Octanol	5.05E+00
DHCN	$C_9H_{17}NO_6$	235	297	362	Nonanol	1.95E+00
DHCN	$C_{10}H_{19}NO_6$	249	311	376	Decanol	7.50E-01
DHCN	$C_{11}H_{21}NO_6$	263	325	390	Undecanol	2.88E-01
DHCN	$C_{12}H_{23}NO_6$	277	339	404	Dodecanol	1.10E-01
DHN	$C_6H_{13}NO_5$	179	241	306	Hexanol	2.46E+02
DHN	$C_7H_{15}NO_5$	193	255	320	Heptanol	9.65E+01
DHN	$C_8H_{17}NO_5$	207	269	334	Octanol	3.76E+01
DHN	$C_9H_{19}NO_5$	221	283	348	Nonanol	1.46E+01
DHN	$C_{10}H_{21}NO_5$	235	297	362	Decanol	5.57E+00
DHN	$C_{11}H_{23}NO_5$	249	311	376	Undecanol	2.16E+00
DHN	$C_{12}H_{25}NO_5$	263	325	390	Dodecanol	8.29E-01
THN	$C_6H_{13}NO_6$	195	257	322	Hexanol	1.69E+00
THN	$C_7H_{15}NO_6$	209	271	336	Heptanol	6.59E-01
THN	$C_8H_{17}NO_6$	223	285	350	Octanol	2.55E-01
THN	$C_9H_{19}NO_6$	237	299	364	Nonanol	9.85E-02
THN	$C_{10}H_{21}NO_6$	251	313	378	Decanol	3.79E-02
THN	$C_{11}H_{23}NO_6$	265	327	392	Undecanol	1.45E-02
THN	$C_{12}H_{25}NO_6$	279	341	406	Dodecanol	5.55E-03
HN	$C_6H_{13}NO_4$	163	225	290	Hexanol	3.56E+04
HN	$C_7H_{15}NO_4$	177	239	304	Heptanol	1.40E+04
HN	$C_8H_{17}NO_4$	191	253	318	Octanol	5.49E+03
HN	$C_9H_{19}NO_4$	205	267	332	Nonanol	2.14E+03
HN	$C_{10}H_{21}NO_4$	219	281	346	Decanol	8.30E+02
HN	$C_{11}H_{23}NO_4$	233	295	360	Undecanol	3.21E+02
HN	$C_{12}H_{25}NO_4$	247	309	374	Dodecanol	1.23E+02

Table 3.2. Formulas, molecular weights, detected ion masses for both the I^- and NO_3^- ionization techniques, alkanol precursor, and estimated saturation concentration for all detected oxidation products. The functional group composition of each molecule is given in the first column, where DHCN=dihydroxycarbonylnitrate, DHN=dihydroxynitrate, THN=trihydroxynitrate, and HN=hydroxynitrate.

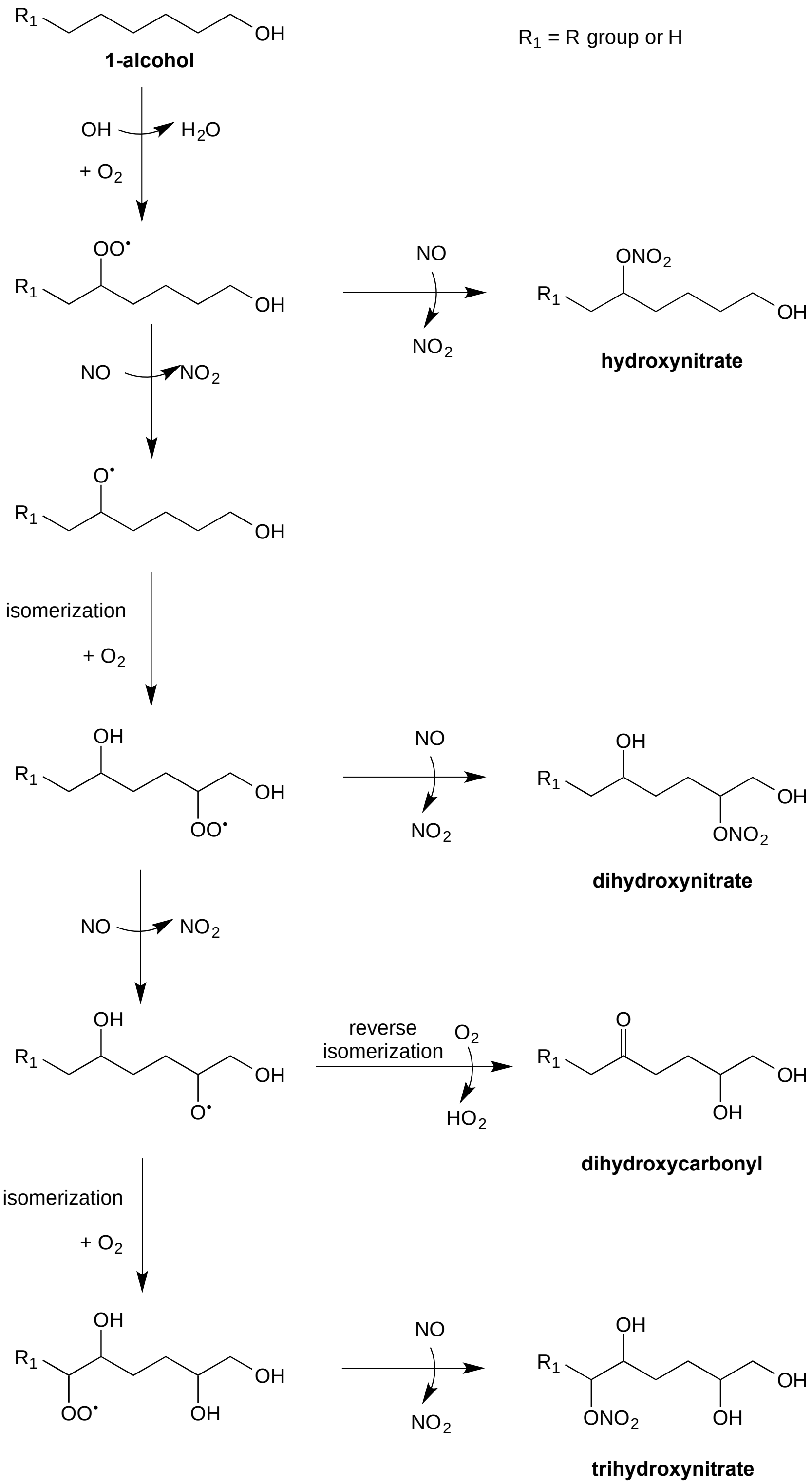

Figure 3. 5. Chemical mechanism for the formation of the oxidized gas-phase products detected in this work.

As an example, the time profiles of the C_6-C_{12} THN formed during one experiment in which the UV lights were turned on for 10 s are shown in Figure 3.6. The ion signals increased almost immediately after the lights were turned on and then reached a peak at 16 s. We attribute the slight delay in the peak time to the residence time of the sample air in the inlet and ion source (estimated to be 1 and 3 s, respectively), as well as a short initial warm-up period for the UV lights (1-2 s), and believe that the observed peak signals correspond to the maximum concentrations of products in the chamber. In previous studies[94,108] in which VOCs were added to the chamber (rather than being formed *in situ*) and concentrations were measured over time using gas chromatography, the peak concentration was not observable because the sampling line was allowed to equilibrate for 20 min prior to sample collection. Instead, the initial concentration was determined from the amount of VOC injected.

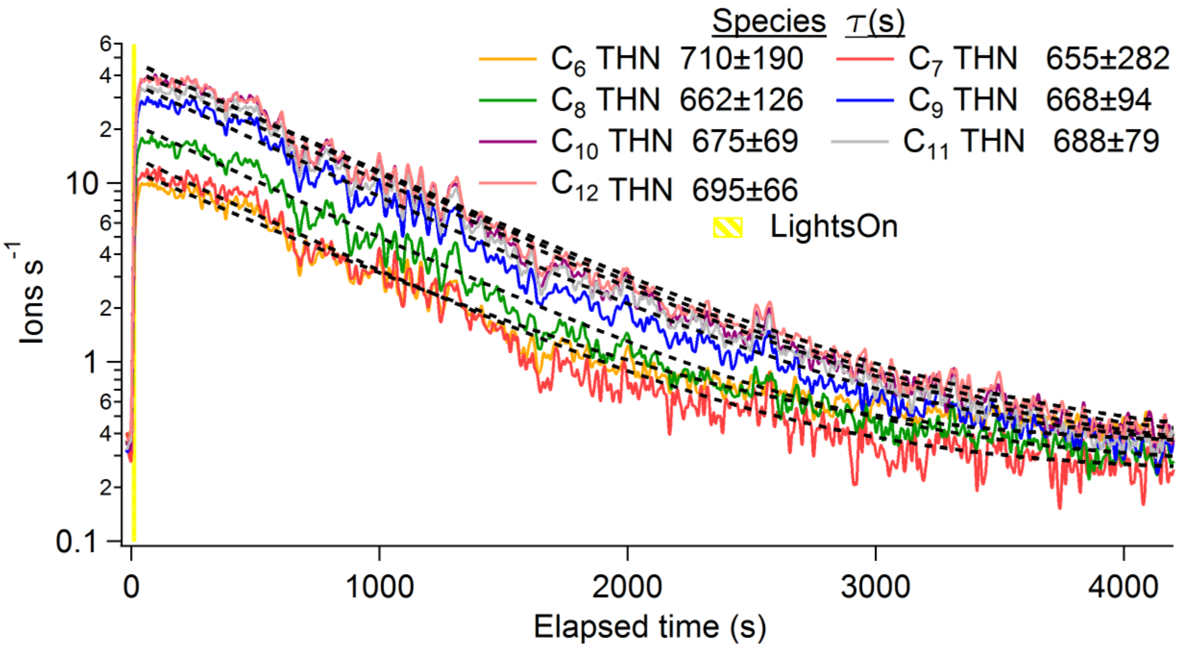

Figure 3.6. Time series for gas-phase C_6-C_{12} trihydroxynitrates (THN) as observed by the NO_3-CIMS during one typical gas-wall partitioning experiment. The UV lights were turned on for 10 s, leading to a rapid increase in the concentrations of reaction products for ~16 s, and then a rapid decline for ~20 min before gas-wall equilibrium was reached after ~45 min. The dotted black lines show single exponential fits used to extract gas-wall partitioning timescales, which are listed for each compound in the legend along with an uncertainty (standard deviation). Data

were acquired at 1 Hz, but the traces shown here have been smoothed over 30 seconds using a binomial algorithm to reduce random noise and improve visual clarity.

After reaching their peak, the gas-phase concentrations of the observed reaction products decreased monotonically. This decay was not due to further reactions, since there were no OH radicals in the chamber after the UV lights were turned off (the lifetime of OH radicals estimated from the total 1-alcohol concentration of ~2ppmv and an OH radical rate constant[121] of 1.4×10^{-11} cm^3 $molecule^{-1}$ s^{-1} was ~1 ms), and the added NO prevented formation of O_3 and NO_3 radicals. There were also no particles in the chamber into which the gas-phase products could partition and thus not be observable with the CIMS. The only sink available was therefore gas-wall partitioning. The time scale for reaching gas-wall partitioning equilibrium was determined from least-squares fits of the observed product decays to the following exponential equation:

$$y(t) = y_E + (y_0 - y_E)\ exp(-\frac{t-t_0}{\tau_{GWE}}) \qquad (3.6)$$

where t_0 is the time of the peak in the compound concentration, y_0 is peak value of y, y_E is an offset that is held at the final or equilibrium concentration, and τ_{GWE} is the time scale of the decay to equilibrium. The value of τ_{GWE} depends on the time scales of both condensation and evaporation.[94] However, under the conditions of most of our experiments ($c^* << C_w$) theoretical analysis (Figure 3.7) shows that τ_{GWE} is also the time scale for condensation to the walls.

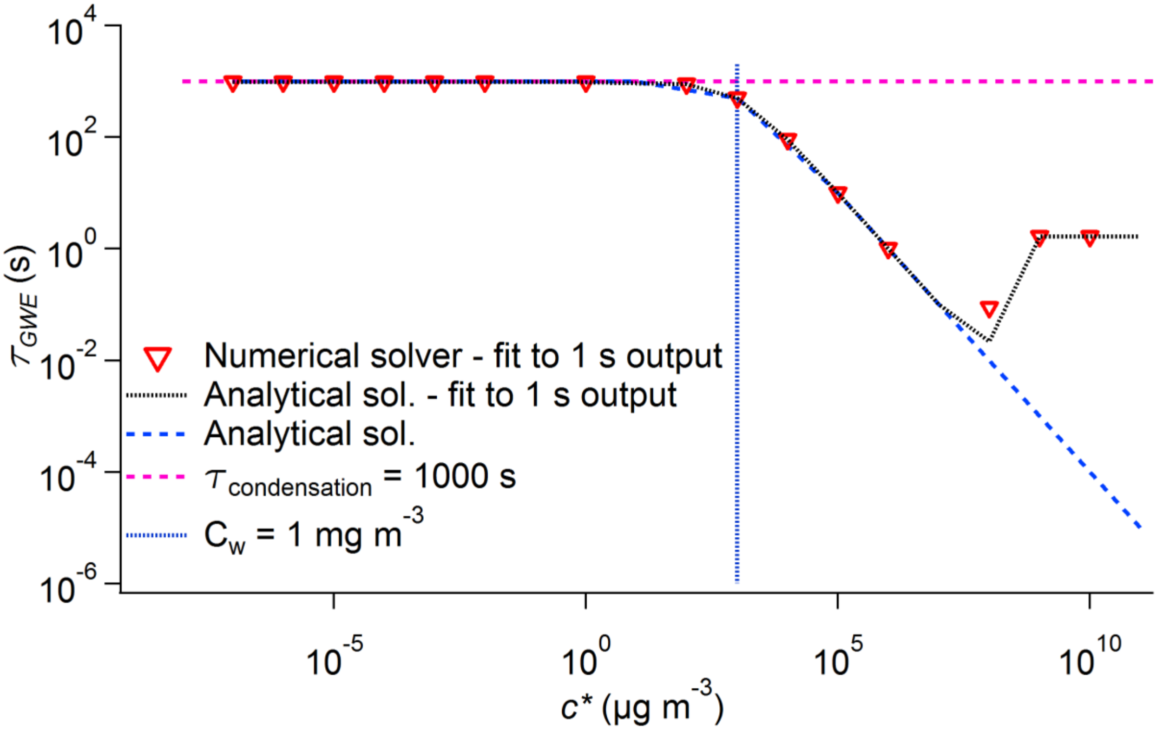

Figure 3.7. Results of a simple chamber model, in which a single gas-phase species condenses into the wall and evaporates off of it (assuming C_w = 1 mg m^{-3}). The model was solved analytically and also implemented numerically in the KinSim software within Igor Pro,[24] which produced consistent results (as shown). The gas-wall equilibrium time scale (τ) was determined by fitting the model results in a similar way as the experimental data. It is observed that the equilibrium time scale is equal to the condensation time scale (i.e., the inverse of the condensation rate, specified here as 0.001 s^{-1}) until the species c^* value approaches and exceeds the equivalent wall concentration (C_w). For higher c^*, most of the species remains in the gas-phase, and thus there is only a very small change due to wall partitioning, and the time scale reaches very low values. When the model output is used with 1 s time resolution to match the measurements in this work, time scales much shorter than 1 s cannot be reliably determined with this procedure. This leads to the observed departure between the analytical and fitted results. Note that there is an apparent disagreement between the trend of decreasing τ_{GWE} predicted in Fig. 3.7 at $C^* > C_w$ and the lack of observation of that trend for the most volatile species (from the Ziemann group) in Figure 3.9. One plausible explanation for this difference is that the wall accommodation coefficient is $\alpha \ll 5 \times 10^{-6}$ for the most volatile molecules studied ($C^* \sim 1 \times 10^5$ -1×10^6 μg m^{-3}) but not for less volatile molecules. This could lead to longer τ_{GWE} than predicted in Fig. 3.7 for those molecules. We note, however, that other explanations may also be possible.

3.3.2 Potential artifacts in I-CIMS measurements

We performed the same experiments in the I-CIMS configuration and observed differences in time series between the two CIMS techniques, as shown in Figure 3.8. The NO_3-CIMS trace rose immediately when the lights were turned on and reached a peak 16 s into the experiment. The I-CIMS (2 SLPM through a 0.7 m Teflon FEP 4.8 mm ID sampling line; residence time of 0.5 s), however, reached a peak 100 to 500 s into the experiment, depending on the volatility of the measured compound. As stated above, the NO_3-CIMS is considered to be an “inlet-less” source and is designed to minimize sample contact with source surfaces. The I-CIMS, however, employs an aluminum IMR in which the reagent-ion molecules mix turbulently with sample air to enhance mixing and allow efficient clustering of reagent ions and sample molecules. The residence time and flow pattern of sample in the IMR appears to be long enough for gas-wall adsorptive partitioning to the IMR surfaces. Therefore, we attribute this delay to the time required for the surfaces in the IMR to reach gas-wall adsorptive partitioning equilibrium. This delay causes the I-CIMS to falsely observe a later and lower-value peak than it otherwise would. Because of the observed delay, we separately report the gas-wall partitioning time scales and partitioning fractions measured using the I-CIMS and NO_3-CIMS.

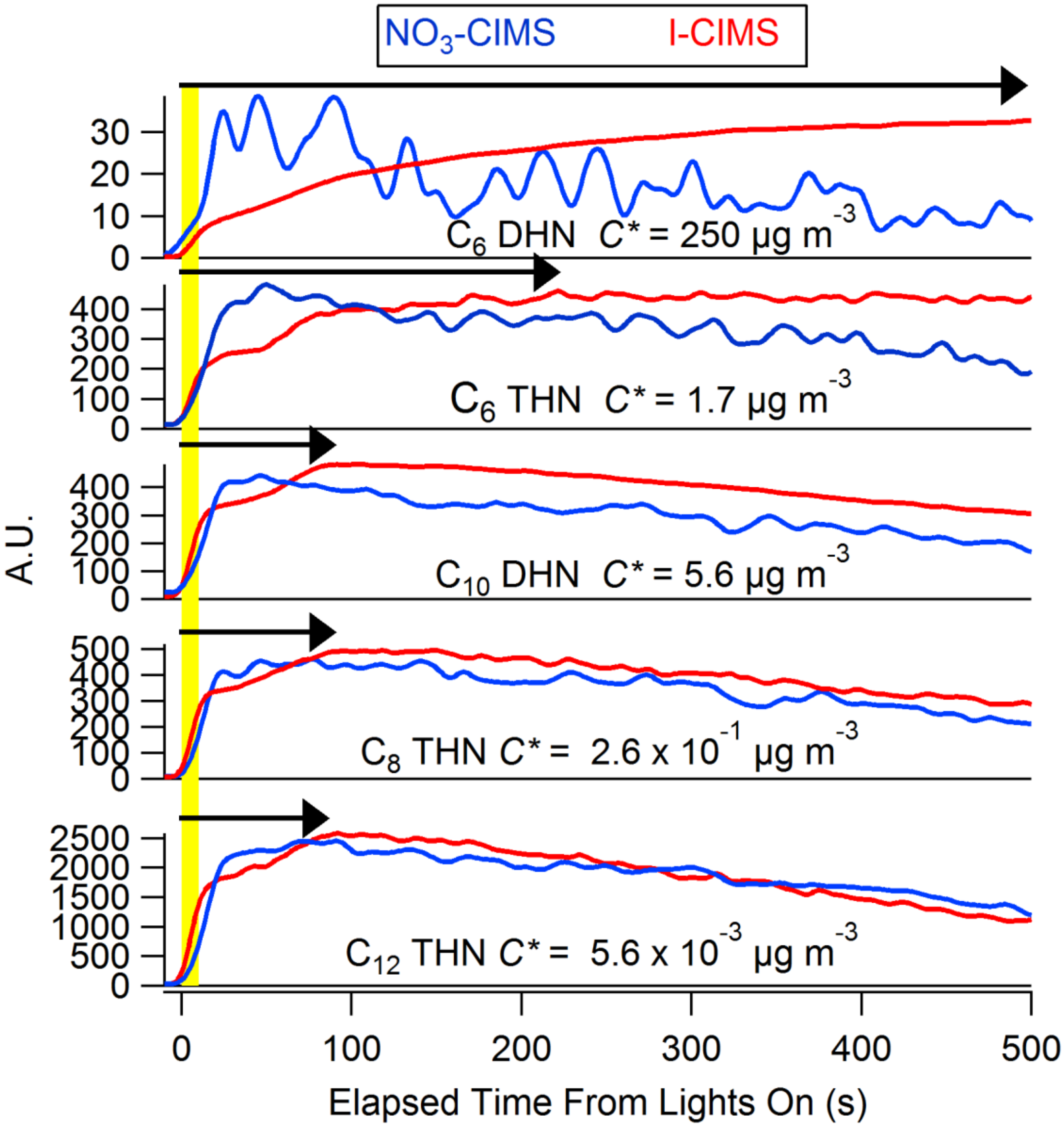

Figure 3.8. Time profiles of product formation and wall loss measured with the NO_3-CIMS and I-CIMS for selected dihydroxynitrates (DHN) and trihydroxynitrates (THN). All traces have been smoothed over 30 points (= 30 s) using a binomial algorithm to improve signal-to-noise ratio and scaled to achieve similar peak concentrations. The arrows denote the approximate time at which the I-CIMS time profile reaches a peak.

3.3.3. Range of time scales for reaching gas-wall partitioning equilibrium

Average time scales for reaching gas-wall partitioning equilibrium for all compounds investigated in this study are presented as a function of estimated saturation concentration (c^*) in Figure 3.9. c^* for each species was estimated using the SIMPOL vapor pressure estimation method,[91] which has an uncertainty of approximately one order of magnitude in each direction.[75]

We observed time scales that range from 7 to 13 min across all species, with an average value of 10 min. Also in Figure 3.9, the data from this experiment are compared with data from previously published gas-wall partitioning measurements.[94,108,111–113,122] The time scales determined by Ziemann and co-workers[94,108,122] fall within the range of 8–140 minutes. In combination, these results suggest that gas-wall partitioning operates quickly enough to affect most SOA chamber experiments, which typically range from several minutes to hours. The relative impact of wall losses on a given experiment will depend on the time scale and volatility distribution of the products formed, the size of the chamber, and the competing time scales of partitioning to aerosols.

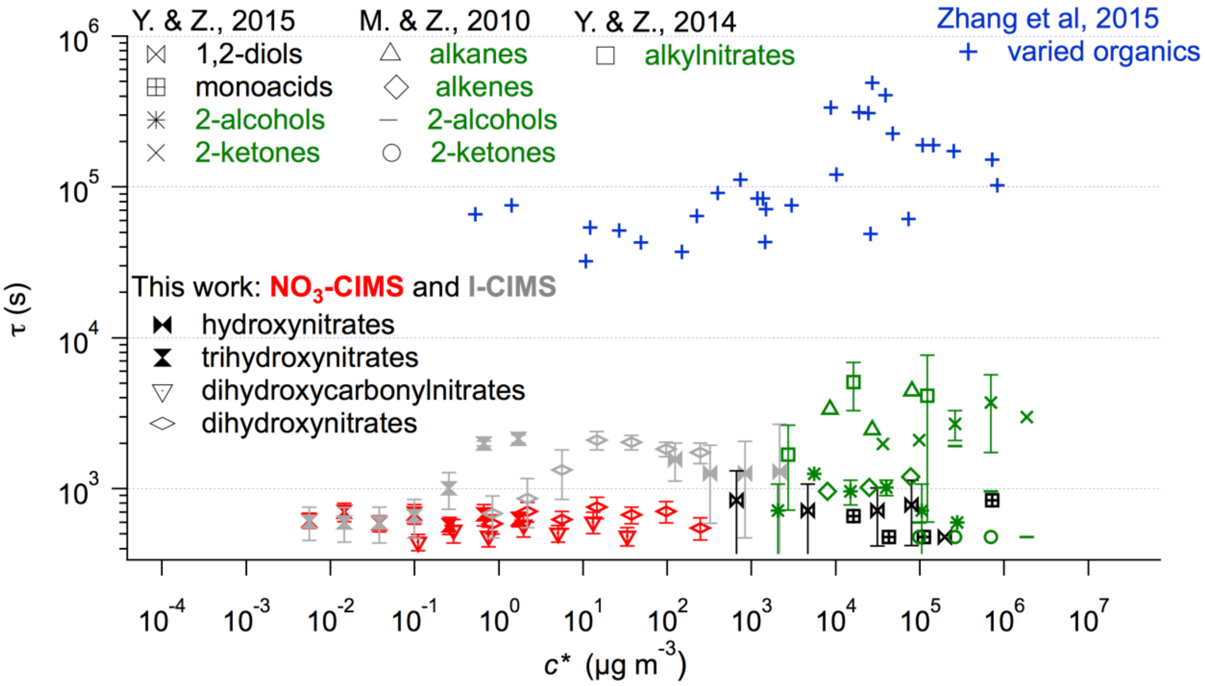

Figure 3.9. Relationship between gas-wall partitioning timescales and compound saturation concentration. Values determined in this study and those from M&Z 2010, Y&Z 2014, 2015 are timescales for reaching gas-wall partitioning equilibrium, while those from Zhang et al. 2015 are timescales for first-order loss without equilibration.[94,108,111,122] Values from this study are averages for replicate experiments, and error bars denote the standard error of the mean. Some error bars are smaller than their symbol and thus not visible. Saturation concentrations were estimated using SIMPOL.[91] I-CIMS measurements are overlaid as gray points for comparison with NO$_3$-CIMS values. Because hydroxynitrates were not detected by the NO$_3$-CIMS, timescales for these compounds are only reported for the I-CIMS, and no values are included for the two most volatile hydroxynitrates due to lack of sufficient replicates. Values from Ziemann and co-workers are only included for compounds that

underwent sufficient partitioning for timescale measurements, and monofunctional compounds are highlighted in green.

The values of τ_{GWE} measured with the NO_3-CIMS displayed no dependence on compound chemical-physical properties, such as functional groups, oxidation state (OSc)[123], elemental oxygen to elemental carbon ratio (O/C), or volatility, unlike results from Ziemann and co-workers,[94,108,122] who reported some higher values for alkanes and monofunctional ketones and nitrates. Nonetheless, the majority of the values they measured lie in the same range measured here, as shown in Figure 3.9. Differences in either the turbulent mixing coefficient or wall accommodation coefficients could account for the range of values,[80] but the evidence presented here or previously does not clearly point to one or the other. Therefore, when modeling SOA chamber experiments, we recommend using two values: a faster time scale of 600 s for multifunctional compounds, and a slower time scale of 1800 s for monofunctional compounds and hydrocarbons (Figure 3.10; 7).

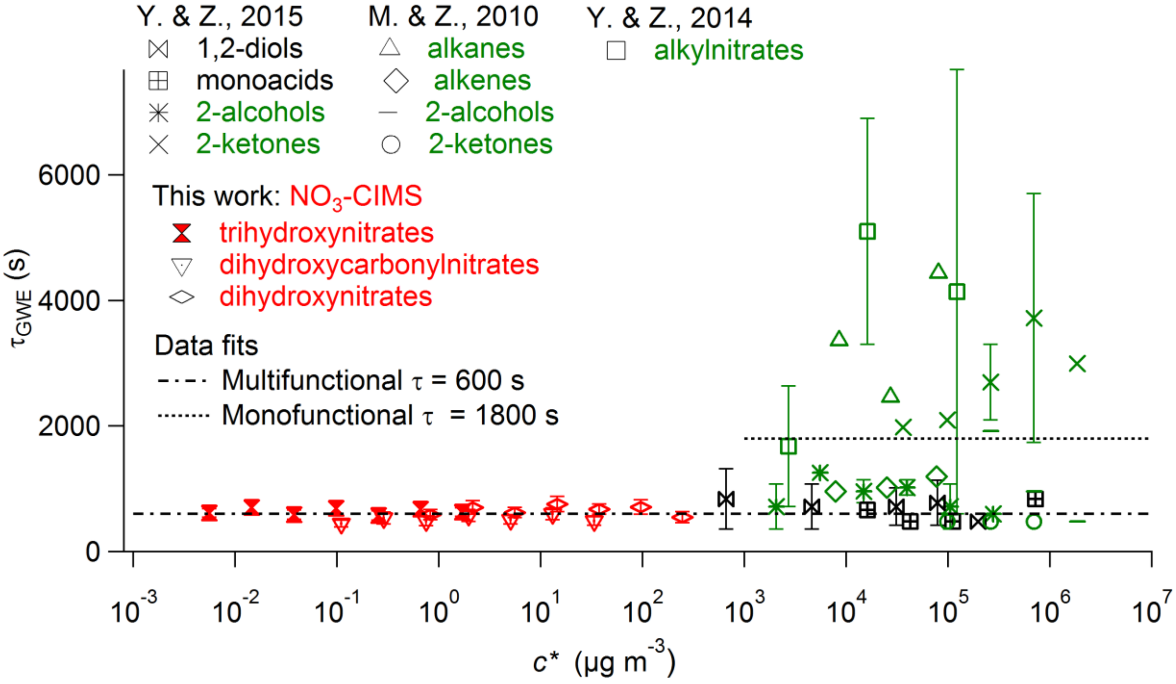

Figure 3.10. Proposed parameterizations of τ_{GWE} for use in simulations of chamber experiments. The value of each constant fit is provided in Table 3.3. All of these values were obtained in 8 m^3 chambers. A correction for chamber size is also shown in Table 3.3 and Figure 3.12.

Recommendations for Quantification of Gas-Wall Partitioning Measurements

1. No particles should be present in the chamber
2. Check and repair all leaks in the chamber
3. Use species formed in-situ
4. Use very short oxidation times
5. Minimize contact between sample and surfaces (short inlet lines, laminar flow, high flow rates, IMR with low wall interactions, etc.)
6. If possible, monitor several species of different $c*$ simultaneously

---

Recommended Parameters for Modeling Gas-Wall Partitioning

1. C_w as a function of c^{*} [a]
   - $C_w = 10 - 30 \times 10^3$ μg m^{-3} for $c^{*} > 10^4$
   - $C_w = 16(c*)^{0.6}$ μg m^{-3} for $c* < 10^4$
   - $C_w = 16$ μg m^{-3} for $c* < 1$
2. τ_{GWE} (Gas-wall equilibrium timescale)
   - For multifunctional compounds: $\tau_{GWE} = 600$ s
   - For monofunctional compounds: $\tau_{GWE} = 1800$ s
3. Chamber-size correction to τ_{GWE}[80]

$$\frac{1}{\tau_{cond}} = k_{cond} = \frac{A}{V}\frac{2}{\pi}\sqrt{k_e D}$$

$$k_e = 0.004 + (5.6 \times 10^{-3})(V)^{0.74}$$

(See the Supplement for more information on this correction)

[a] Using SIMPOL-derived saturation concentrations

Table 3.3. Recommendations for experimental measurements of GWP, and recommended parameters for modeling GWP in chamber experiments.

Across different NO_3-CIMS experiments, τ_{GWE} varied with an average relative standard deviation of 33%, as shown in Figure 3.11. The causes of experiment-to-experiment variation are not understood, but may be related to changes in the natural convection time scale in the chamber due to differences in the room ventilation operation, or to other unknown factors. Time scales measured with the I-CIMS were consistent with NO_3-CIMS measurements for low volatility compounds, but were approximately four times higher at high volatilities ($c^* > 0.1$ μg m^{-3}). We tentatively attribute this discrepancy to adsorptive processes in the I-CIMS inlet and IMR. The better agreement of τ_{GWE} at low c^* may stem from irreversible loss of low-volatility species to inlet and IMR walls, thus leading to detection of only molecules that have not interacted with walls with a similar time scale as the NO_3-CIMS. For species of larger c^*, adsorption to the wall is likely followed by slow re-evaporation, leading to the observed much longer I-CIMS time scales. In support of our claim that the 7–13 min time scales measured with the “inlet-less” NO_3–CIMS are essentially artifact-free values, and that the longer time scales measured with the I-CIMS are due to sampling effects, we note that the values measured with the NO_3-CIMS are essentially the same as the time scales of 6 and 10 min measured previously for irreversible loss of $ClONO_2$ and N_2O_5 to the walls of a humidified, passively mixed 6 m^3 Teflon-coated chamber by using *in situ* FTIR to monitor compound loss from the gas phase.[124]

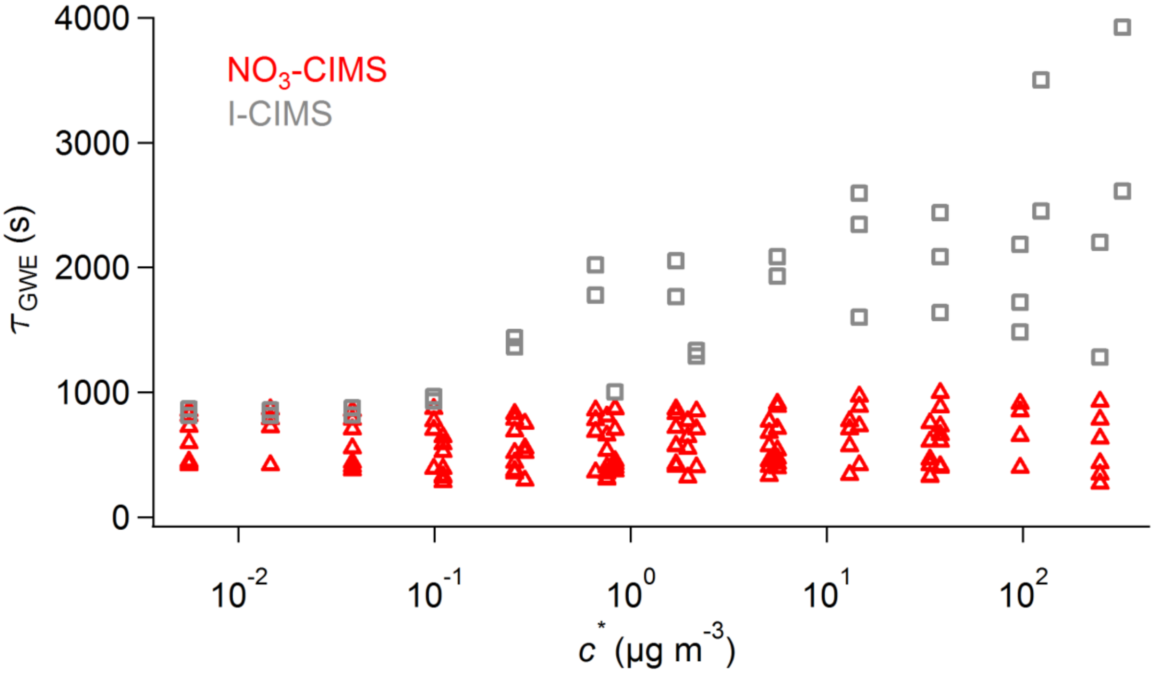

Figure 3.11. Equilibrium time scale (τ_{GWE}) vs. estimated c^* for all of the wall loss measurements in this study, colored by CIMS ionization source. This figure gives an indication of the experiment-to-experiment variability, as well as longer apparent time scales in I-CIMS measurements of higher volatility species ($c^* > 0.1$ µg m^{-3}), which are thought to be due to wall interactions (adsorption followed by slow re-evaporation) in the inlet line and ion source.

Finally, in order to use the recommended time scales for environmental chambers of other sizes, we suggest that for an approximately cubic chamber the recommended τ_{GWE} values of 10 and 30 min be adjusted with the equations shown in Table 3.3. The expected dependence of τ_{GWE} on surface-area-to-volume ratio (A/V) is weak, and the chambers used in this and Caltech's work are estimated to have the slowest τ_{GWE} for any chamber size. For typical chamber sizes used in the community, τ_{GWE} is estimated to vary by ~20 % due to chamber size (Figure 3.12).

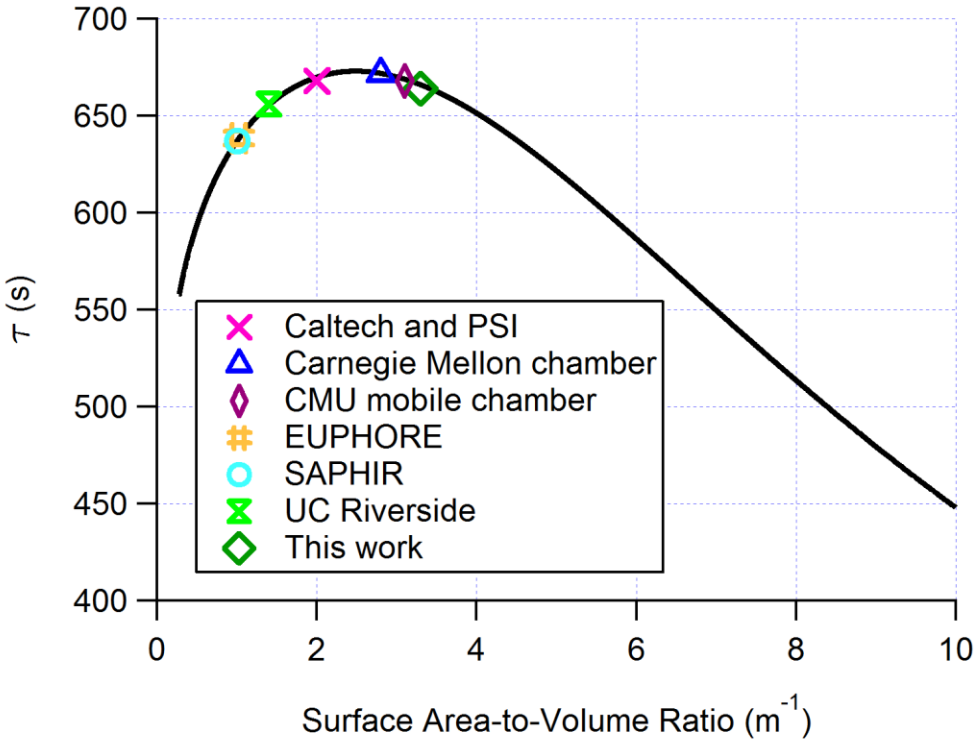

Figure 3.12. Estimated wall condensation time scale versus chamber surface-area-to-volume ratio (A/V) for a various chamber sizes using the equations in Table 3.3.

3.3.4 Equivalent wall mass concentrations

It has been observed in these and earlier experiments[94,108,122] that compounds do not undergo continuous loss to the chamber walls, but instead partition between the gas phase and Teflon film until an equilibrium is reached. This equilibrium state depends on compound volatility, and can be modeled analogously to gas-particle absorptive partitioning theory,[94] as originally developed by Pankow.[51] Briefly, gas-wall partitioning theory treats the chamber walls as having an "equivalent mass concentration," C_w, into which gas phase compounds can partition. The fraction of an organic compound that partitions into the walls at equilibrium approximately follows the equation

$$\frac{[OC]_w}{[OC]_g} = K_w C_w = \frac{RTC_w}{M_w \gamma_w P^0} \qquad (3.7)$$

where K_w is the gas-wall partitioning coefficient and is equal to $RT/M_w\gamma_w P^0$, where M_w is the mean molecular mass of the Teflon film (assumed to be 250 g mol^{-1})[94], R is the gas constant, T is the temperature (295 K in this case), and P^0 is the liquid vapor pressure of the compound at the experimental temperature.

γ_w is the activity coefficient for the compound absorbed into the Teflon film. γ_w is assumed here to be 1, following Matsunaga and Ziemann,[94] who selected this value for simplicity since no information is available to constrain it and in order to enable a quick comparison between aerosol and wall partitioning. Real values of $\gamma_w >> 1$ are possible, and there is some limited evidence for different γ_w for hydrocarbons and oxygenates.[108]

The actual value has important implications for the physical model of wall partitioning. The physical thickness of the Teflon film needed to account for C_w is 1.5 nm or smaller (see Supp. Info.) This is similar to a monolayer, which appears to conflict with the absorptive partitioning assumption. However, this estimate assumes both γ_w=1 and a mean molecular weight (MW) of the absorbing phase of 250.[94] It is likely that a much deeper layer of Teflon is interacting with the absorbed organic molecules. That can be explained by a higher MW for the Teflon films, as is clearly the case. Complementary to that, it is possible that γ_w>>1, which would also favor the participation of a thicker teflon layer in the partitioning. These considerations remain speculative, and future studies to clarify the wall-organic interaction at the molecular level would be useful.

Substituting the saturation concentration[52]

$$c^* = \frac{M_w \gamma_w P^0}{RT} \tag{3.8}$$

then gives the equation

$$\frac{[OC]_w}{[OC]_g} = K_w C_w = \frac{C_w}{C^*} \tag{3.9}$$

In this work, we use $F_g = [\mathrm{OC}]_g/[\mathrm{OC}]_T$, the ratio of the concentration of an organic compound in the gas phase at equilibrium relative to its total (initial) concentration, to represent the fraction of compound remaining in the gas phase at equilibrium. Using equations (3.8) and (3.9), the extent of gas-wall partitioning, represented by F_g, can be calculated for a range of equivalent mass concentrations, C_w, as a function of compound saturation concentration as

$$F_g = \left(1 - \frac{1}{1+\frac{C_w}{C^*}}\right) \tag{3.10}$$

Five such gas-wall partitioning curves are shown in Figure 3.13 for values of C_w ranging from 0.3 to 30 mg m^{-3}.

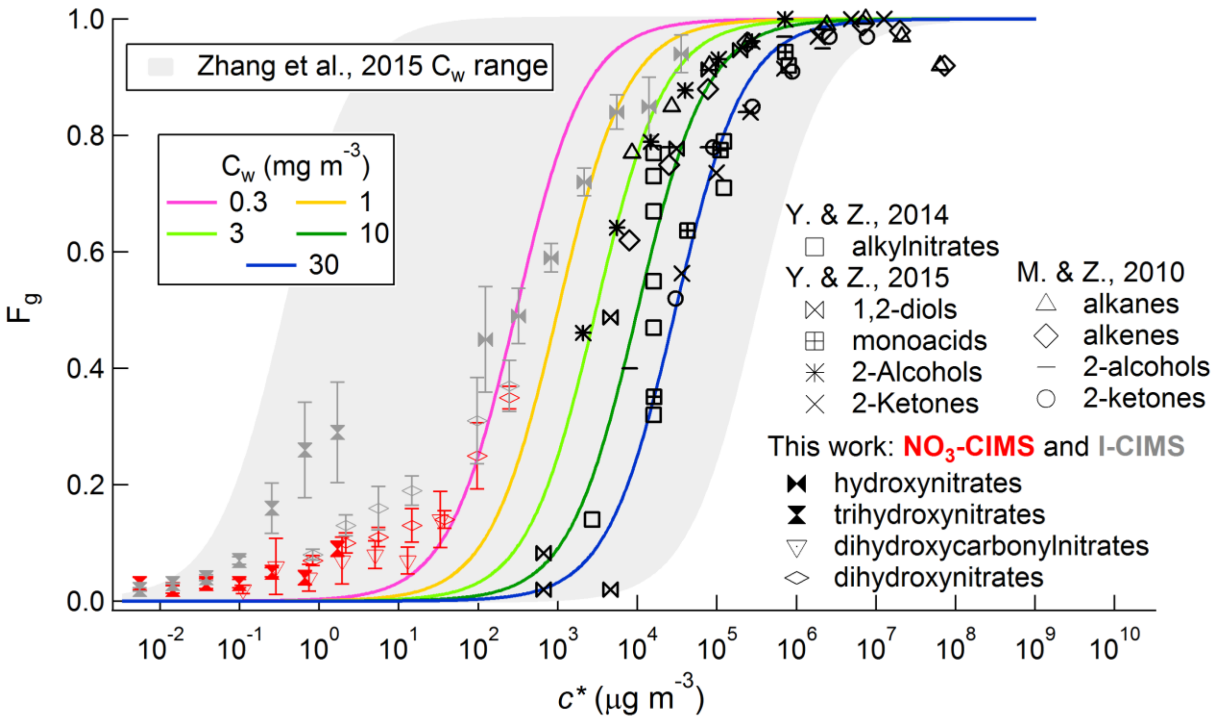

Figure 3.13. Relationship between extent of gas-wall partitioning (represented as the fraction of gas-phase species remaining in the chamber after equilibrium is achieved, F_g) and compound saturation concentration. Measurements obtained in this work are shown with literature values from the Ziemann group.[94,108,122] For the data from Zhang et al.[111], in which no partitioning values (F_g vs. c^*) were provided, C_w is shown as a range. Values of F_g from this work are mean values from all the experiment replicates, and the error bars denote the standard error of the

mean. Saturation concentration for all included species was estimated using SIMPOL.[91] Hydroxynitrates were only observed by the I-CIMS.

Figure 3.13 also shows measured values of F_g as a function of c^* for all organic compounds investigated in this study, together with literature data. Results from Ziemann and co-workers [94,108,122] are consistent with C_w ~ 3-30 mg m^{-3}, whereas Zhang et al.[111] reported a much wider range of C_w values from ~0.0004–300 mg m^{-3}. It is difficult to determine the values of C_w for most of the trifunctional and tetrafunctional compounds formed in the present study, because they lie in a c^* range (10^{-2} to 10^1) in which all of the model partitioning curves converge to $F_g = 0$, and thus are more susceptible to small errors due to background subtractions or other reasons. The hydroxynitrates and some of the lower carbon number (C_6-C_8) dihydroxynitrates lie along model partitioning curves with C_w ~ 0.3-3 mg m^{-3}.

There are several possible explanations for the somewhat lower values of C_w determined in this work compared to those reported previously. First, the SIMPOL method for estimating vapor pressures and c^* is potentially a large source of error. SIMPOL calculations have an estimated uncertainty of one order of magnitude for the monofunctional and difunctional compounds used to develop the method,[75] but uncertainties will grow with increasing functionalization. SIMPOL also does not account for intramolecular interactions between functional groups, which are certain to be important for the multiple hydroxyl groups present in the compounds studied here. Second, the values of C_w calculated from experimental results are actually values of $\gamma_w C_w$, and for simplicity it is assumed that the compounds form an ideal solution in the FEP Teflon film, so that $\gamma_w = 1$. Because the compounds and the $–[CF_2CF_2]_n–$ and $–[CF_2CF(CF_3)]_n–$ subunits that make up the polymer film have very different composition, however, and the actual amount of Teflon material available for partitioning (i.e., the “true” C_w) is likely to be similar for all compounds, it is likely that differences in reported values of C_w also reflect differences in γ_w. Third, there is an apparent trend of decreasing C_w with increasing compound functionalization, which is in contrast with the more nearly constant values reported by Ziemann and co-workers.[94,108] Many of the compounds measured here are trifunctional or tetrafunctional, whereas most of those measured by Ziemann and co-workers were monofunctional or difunctional,[94,108,122] and thus the impact of errors in SIMPOL and activity coefficients may be different.

Our data indicate a dependence of C_w on c^* (Figure 3.14), and for the purposes of modeling chamber studies we recommend a volatility-dependent parameterization of C_w in Table 3.3, which is shown graphically in Figure 3.14. We performed additional vapor pressure calculations with the SPARC[61,62] calculator, but the data did not collapse into clearer trends when doing so. Therefore, we caution that these parameters depend on the SIMPOL estimated vapor pressures, and that the dependence may reflect systematic errors in the vapor pressure estimations for the investigated compounds, as discussed above. Thus, we recommend that SIMPOL be used when employing our parameterization for modeling for purposes, even if a different vapor pressure estimation method is used elsewhere in the model.

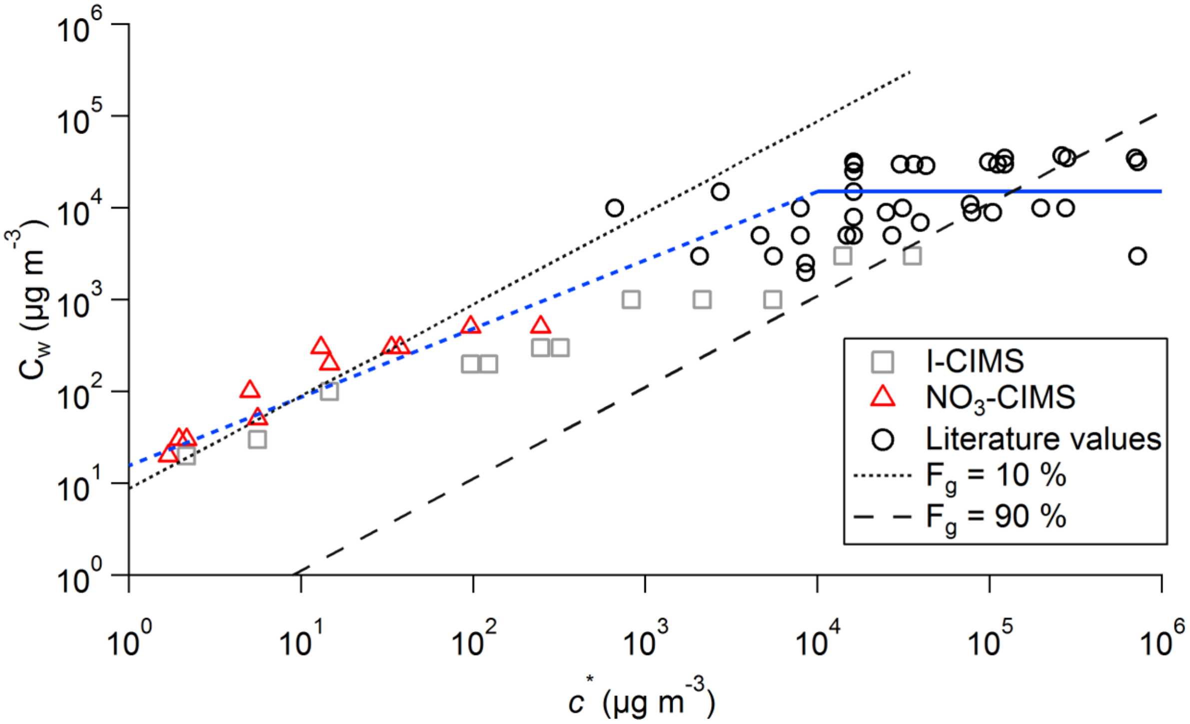

Figure 3.14. Average equivalent wall mass concentration (C_w) values for measured species in this work, as determined by both CIMS techniques, and previously reported values from the Ziemann Group[94,108,122] as a function of c^*. C_w values could not be reliably determined in this work for species with $c^* < 1$, as F_g values in Figure 3.13 are close to zero. A piecewise function is provided to parameterize this dependence on the simulation of chamber experiments (equations shown in Table 3.3). c^* values are estimated from SIMPOL[91], and we recommend that SIMPOL is used as well before applying our parameterization to any species. Note that the I-CIMS values are thought to be biased low (see main text) and are shown by reference, but not used to determine the fits.

For the first time, gas-wall partitioning measurements for the entire range of c^* values relevant to SOA formation are now available (Figure 3.13), and can be used to estimate the wall-loss of compounds formed in chamber reactions and determine the degree to which SOA yield corrections may be required. Compounds with $c^* > 10^6$ µg m^{-3} will remain almost entirely in the gas phase and will not partition significantly to the walls, whereas those with $c^* < 10^2$ µg m^{-3} will eventually (after the chamber-dependent equilibrium time scale and depending on the amount of organic aerosol present) reside almost entirely in the walls. Compounds with $10^2 > c^* > 10^6$ µg m^{-3} will partition to very different extents, ranging from ~10-90%, depending on their volatility and functional group composition. Since SOA formation in most chemical systems is likely to involve reaction products in that c^* range, corrections for gas-wall partitioning should be incorporated into the analysis of all SOA chamber experiments. We also note that when the parent compound in a chamber reaction is an intermediate- or semi-volatile compound (IVOC and SVOC) in the $c^* = 10^2\text{-}10^6$ μg m^{-3} range, the effects of gas-wall partitioning of the parent compound on the yields of SOA and specific products must also be considered. However, as long as the parent compound is in gas-wall partitioning equilibrium when its concentration in the gas phase is measured before and after reaction, partitioning corrections are simple.[122]

3.3.5 Sensitivity studies

We also conducted several experiments in which we selectively changed one variable at a time to explore the impact of key experimental variables on the quantification of gas-wall partitioning.

Effect of experiment duration: In addition to the ~1 h experiments discussed above, we also recorded data for ~10-h duration to evaluate whether a much slower decrease in compound concentrations could be observed after the initial rapid decay and equilibration observed following a typical 10 s reaction. Compound concentrations were extremely stable, however, changing by <5% during the ~10 h measurement period following gas-wall partitioning equilibrium.

Effect of chamber leaks**:** Next, we performed an experiment in which four small (6.4 mm diameter) holes were opened in the Teflon bag to mimic the effects of substantial leaks prior to turning on the lights for 10 s. As in previous experiments, we observed a rapid exponential decrease in compound concentrations due to gas-wall partitioning after the lights were turned off, which in this case was followed by a slow, prolonged decay as ambient air slowly leaked into the chamber (which was under slight negative pressure due to the sampling instruments) and diluted the compound concentrations. Most of the decay in the compound concentrations again occurred within the first hour, but the gas-wall partitioning time scale increased by a factor of ~3 due to the leaks. This indicates that leaks of the size created here, which are not uncommon in environmental chambers that are not carefully maintained, can distort the interpretation gas-wall partitioning measurements.

***Effect of active mixing*:** In a few experiments we also investigated the effects of active mixing on time scales of gas-wall partitioning. The results of these experiments are shown in Figure 3.15. When the fan was turned on for an entire burst, the average value was τ_{GWE}=100 s. The fan-on time scale is a factor of 6 less than the average value of 600 s reported in Fig. 3.15. In other experiments, we turned the fan on for 60 s at different points during the decay. The results in Fig. 3.15b show that the wall loss decay is accelerated by the fan, but returns to its original trajectory as soon as the fan is turned off. The timing of active mixing thus appears to influence the effect on gas-wall partitioning.

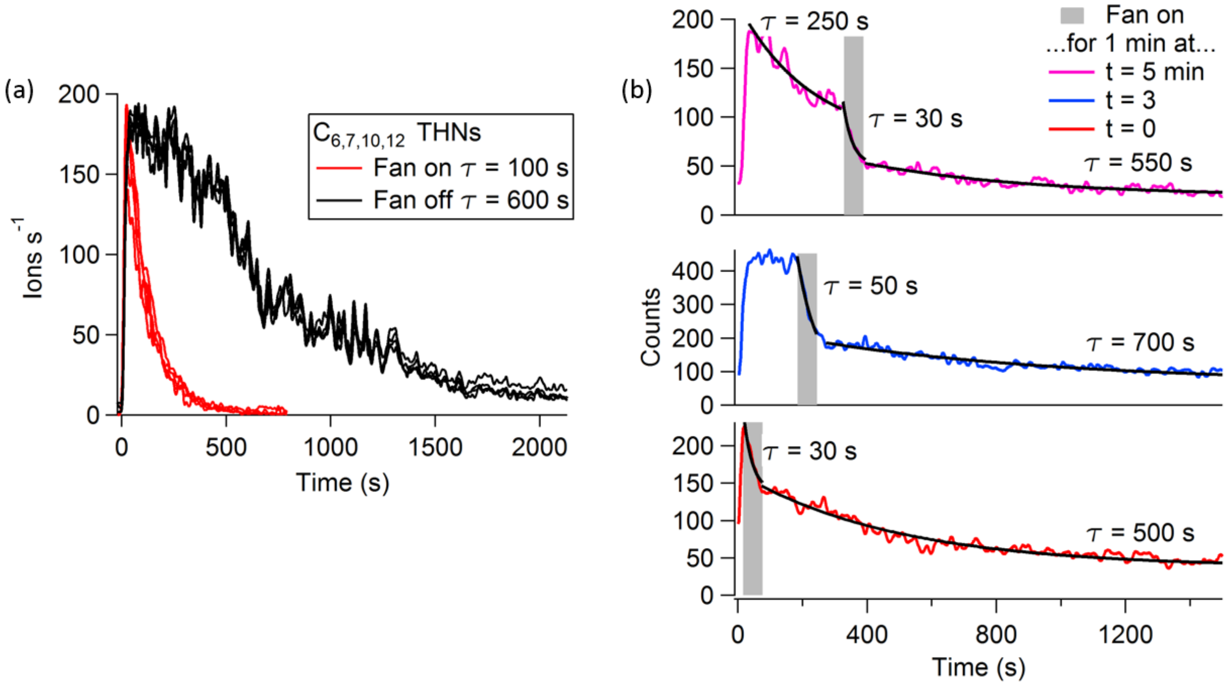

Figure 3.15. (a) Time series for select THNs in two separate wall loss bursts: one in which the fan was left on for the experiment duration and one in which it was off for the duration. **(b)** Averaged time series for several DHNs in three different bursts in which the fan was turned on for 1 minute either 0, 3, or 5 minutes into the experiment.

Exponential fits were applied to each of the three time periods in the burst: when before the fan, during the fan, and after the fan.

It is important to note in this regard that in the experiments conducted by Ziemann and coworkers[7,8,29] the same type of fan was turned on for 1 min to mix compounds that had been added to the chamber over a period of ~5 min. Although the above results indicate that the time scales measured in those experiments were influenced by the use of the fan, its effect was not always sufficient to achieve time scales <8 min, the minimum value that could be measured by their methods. Instead, time scales ranged from <8 min to ~100 min, with an average of ~25 min. The fan may have had a smaller effect in those experiments because most of the compounds investigated were hydrocarbons or monofunctional that partitioned more slowly to the walls, and also because the compounds first had to be mixed in the chamber before significant partitioning could occur, a process that takes ~20 s.

***Effect of longer oxidation period*:** We also conducted an experiment with a longer oxidation period (10% UV lights for 1 hr) and longer total duration (22 hours). During this experiment, we observed a rapid initial increase in compound concentrations, followed by a long slow decay. In this case, values of τ_{GWE} obtained by fitting the exponential decay curves using the procedure described above were much larger than those measured in our previous experiments, ranging from about 2 to 8 h. A possible reason is that when the oxidation period is of similar or longer duration than the gas-wall partitioning time scale the system may not be far from equilibrium when the UV lights are turned off and oxidation ends. Subsequent decays will then be smaller, making it more difficult to determine the time scale. However that was not observed in a previous experiment with a 2 hr oxidation time using the NO3-CIMS.[24] Unlike in other experiments, in this experiment a small amount of aerosol (1 μg m^{-3} maximum) was produced, which could have introduced a weakly competing gas-particle partitioning process that contributed to the increase in gas-wall partitioning time scale. Further investigation of this topic is recommended.

3.3.6 Calculation of additional chamber parameters

Correction of τ_{GWE} for chamber size. This formulation was originally proposed by McMurry and Grosjean[80] and parameterized by Palm et al.,[125] as follows:

$$\frac{1}{\tau_{cond}} = \frac{k_{cond}}{0.59} = \frac{A}{V}\frac{2}{\pi}\sqrt{k_e D} \tag{3.10}$$

where A (V) is the chamber surface area (volume), D is the coefficient of molecular diffusion (here: 7×10^{-6} m^2 s^{-1}), and k_e is the coefficient of eddy diffusion, represented as a chamber volume-dependent function:[125]

$$k_e = 0.004 + (5.6 \times 10^{-3})(V)^{0.74} \tag{3.11}$$

where V is the chamber volume in m^3. We add a scaling factor of 0.59 to the value of τ_{cond} determined in Equation 1 to match the observed average time scale from this work (600 s). Equation 3.11 is plotted in Figure 3.12 as a function of A:V for a cubic chamber, with the Caltech chamber and the chamber used in this work highlighted.

Note that the chamber size correction supplied in Equation (3.11) depends on the wall mass accommodation coefficient of organic vapors, α, being larger than ~6 x 10^{-6}. In the case where α is much smaller, then the following equation applies[80]:

$$\left(\frac{A}{V}\right)\left(\frac{\alpha_{w,i}\bar{C}_i}{4}\right) = -k_{cond} \tag{3.12}$$

In cases of intermediate α, the full equation should be used[80]:

$$\frac{dC_{v,i}}{dt} = \left(\frac{A}{V}\right)\left(\frac{\alpha_{w,i}\bar{C}_i/4}{\frac{\pi\alpha_{w,i}\bar{c_i}}{(D_iK_e)^{\frac{1}{2}}}+1}\right)\bar{C}_{v,i} = -k_{cond}\bar{C}_{v,i} \tag{3.13}$$

The evaporation rate can be calculated from the following expression[94]:

$$k_{evap} = k_{cond}\frac{C^*}{C_w} \tag{3.14}$$

while noting that the following expression also applies[94]:

$$\tau_{gwe} = \frac{1}{k_{cond}+k_{evap}} \tag{3.15}$$

Estimate of physical thickness of wall mass concentration (*C_w*). Here, we provide an estimate of the thickness of FEP chamber surface necessary to account for an equivalent wall mass concentration (C_w) similar to the values determined in this study. The surface area of the bag used in these experiments is 24 m^3 and its volume is 8 m^3. The density of FEP is reported to be 2.2 g cm^{-3}.[126] Using a C_w of 10 mg m^{-3} in the following equation:

$$T = \frac{C_wV}{A\rho_w} \tag{3.16}$$

where V is the volume of the bag, A is the surface area of the chamber walls and ρ is the density of Teflon, we obtain an equivalent thickness value (T) of 1.5 nm.

This estimate is only provided for reference, as the physical details of the roughness and depth of Teflon film that may be interacting with the gas-phase are not well understood.

Estimate of physical thickness due to particle deposition to chamber walls. Here, we provide an estimate of the thickness of material buildup on chamber walls due to particle deposition during SOA experiments. We assume 2 years before FEP bag replacement and an average of 3 experiments per week. We use 1.3 g m^{-3} as a typical material density for chamber SOA.[127] We use this equation:

$$T = f_w\frac{C_{SOA}V}{A\rho_{SOA}} \tag{3.17}$$

which is analogous to the previous one. We assume a chamber in which the average experiment produces 300 μg m^{-3} of particles, of which 50 % deposits on the walls (f_w = 0.5), with the rest of the particles being either sampled by the instrumentation or exhausted at the end of the experiment. Under those assumptions, the mass of deposited particles accumulated would be equivalent to a 12 nm thick after 2 years of experiments. For an experimental regime at lower concentrations in which the average experiment produces 3 μg m^{-3} (with all other parameters kept constant), the layer of particles would be 0.12 nm thick after 2 years of experiments. We note that much of the particle material can be removed during chamber cleaning procedures (e.g. continuous flushing with zero air, UV light irradiation, ozone injection, added humidity, and heating), and thus these values represent upper limits.

3.3.7 Recommendations and implications

Recommended experimental guidelines for quantifying gas-wall partitioning and recommended parameters for modeling and analyzing chamber experiments are shown in Table 3.3. Additional research is needed to increase the accuracy and precision of the parameters and to ascertain their true variability and its causes. The effect of parameters such as temperature and humidity on gas-wall partitioning should also be characterized. Differences in activity coefficients or possibly accommodation coefficients for interactions of different types of organic compounds with Teflon films may explain some of the differences in reported values of C_w and τ_{GWE}. Turbulent mixing in chambers is weakly forced by small temperature gradients and the resulting buoyancy, as well as intermittent deformation of the bag from ventilation systems. Thus it seems likely that some variability in τ_{GWE} values measured in different chambers and in replicate experiments in one chamber may be due to variations in turbulent mixing time scales. However, the reasons for the large differences between the results presented here and those of Zhang et al.[111] remain unclear.

While differences in turbulent mixing can likely explain differences of a factor of 2 to 3, it seems unlikely that they could result in differences of several orders of magnitude. On the basis of the results presented here, the use of long chamber reaction times and/or the effects of compound sorption in the inlet and IMR of the CIMS used in the Caltech study might be at least part of the reason for the differences.

The values of τ_{GWE} measured without and with active mixing in our study are of the order of the mixing time scales for a passive tracer (Fig. 3.1 and 3.2), consistent with transport to the walls being the limiting process for achieving gas-wall partitioning equilibrium.[80] Thus, we recommend similar use of passive tracers to characterize turbulent mixing in chambers, which will be useful for modeling gas-wall partitioning and will allow comparison with the mixing observed in our chamber and others. We also recommend that the experimental protocol used in this study be tested in other chambers, if possible with instrumentation that reduces any inlet and tubing effects

The implications of our results for correcting chamber SOA yields reported in past studies are complex and require detailed investigations that take into account the volatility distributions of precursors, intermediates, and SOA species, as well as the amount and properties of the seed aerosol and SOA formed.

Chapter 4:
Ion Mobility Spectrometry-Mass Spectrometry (IMS-MS) for on- and off-line analysis of atmospheric gas and aerosol species

Adapted from: Krechmer et al. Atmos. Meas. Tech. 2016, 9(7), 3245–3262

4.1 Introduction

Organic aerosol (OA) species constitute a major fraction of airborne particles globally, comprising 20–90% of fine particle mass in many regions[4–6] and is either directly emitted into the atmosphere in the particle phase ("primary" OA, POA) or formed from gas-to-particle conversion processes ("secondary" OA, SOA). Estimates of global SOA budgets from current atmospheric chemistry models are uncertain.[8,9] OA and its gas-phase precursors comprise thousands of unique molecules.[10,128] Obtaining comprehensive and speciated measurements of all of these organic molecules strains the limits of conventional instrumentation.[6,129]

Ultra-high-resolution mass spectrometry (UHRMS; mass resolution > 50,000) techniques, such as FTICR-MS or Orbitrap-type instruments,[128] can be combined with direct infusion techniques to characterize thousands of organic compounds simultaneously. Direct infusion comprises a number of soft ionization sources, such as electrospray ionization (ESI), that introduce the sample into an ionization source without prior separation. Despite the increase in mass resolution, UHRMS cannot, however, resolve structural isomers without a prior separation step and accurate quantification of observed species is complicated by ion suppression/matrix effects. [129] Instruments with MS/MS fragmentation capability (as in a triple-quadrupole mass analyzer), can also be used to identify organic molecules, including isomers. Since MS/MS is usually performed by scanning over a narrow range of mass-to-charge ratios (*m/z*), these measurements typically have a limited range of species that can be monitored during time-resolved measurements. An authentic standard is also necessary to verify a compound's unique fragmentation pattern.

Thus, molecular-level identification of individual organic species is often achieved by coupling mass spectrometry with a separation technique such as liquid chromatography (LC) or gas chromatography (GC). Reverse-phase (RP) LC followed by mass spectrometry using ESI, a very "soft" ionization technique due to the almost exclusive formation of molecular ions,[96,130–132] is often used to separate and identify OA constituents. LC/MS methods (and GC/MS) require authentic standards, however, and solvent matrix effects and solvent-analyte reactions can potentially have detrimental effects on the sample.[129] GC methods are also inefficient for characterizing aerosol constituents like WSOC because prior derivatization steps are needed to convert these species into volatile derivatives that can be resolved by GC columns. Derivatization methods have been found to degrade species such as oligomers and organosulfates, resulting in misidentification.[6] GC techniques also require heating, which has been shown to decompose some organic species to CO_2 or other small molecules.[133] Recent analytical advances such as the Volatility and Polarity Separator (VAPS) have increased the fraction of WSOC that is amenable to GC/MS analysis without derivatization, but a large portion remains uncharacterized[134]

Ion mobility spectrometry (IMS) is a well-established separation technique, the principles of which were first laid out in 1903.[135] Previously known as plasma chromatography or gaseous electrophoresis,[136] IMS has gained prominence and utility over the last 15 years with rapidly increasing numbers of commercially available instruments.[137] IMS separates gas phase ions based on a property known as ion mobility, K, which is sensitive to molecular structure (i.e., ion size and shape/conformation) and ion-molecule interactions with a buffer gas such as nitrogen, helium, or air. Since IMS separations are based on gas-phase mobility rather than polarity, they are not limited by solvent or stationary phase constraints. Thus, IMS can be used to separate species with different structures that are not easily separated by LC and GC techniques. Such species include isomers, which are species with the same atomic composition arranged in different structures, and isobars, which are compounds of different atomic composition but overlapping mass numbers.[138] In fact, IMS-MS (IMS separation coupled with mass spectrometric detection of ions) has been demonstrated as a powerful replacement for LC/MS in complex fields of analysis such as lipids, metabolites, water quality, and pharmaceuticals.[139–142]

In this work we demonstrate the first application of IMS-MS for molecular-level analysis of both aerosol- and gas-phase atmospheric constituents. All measurements are carried out on a TOFWERK IMS-TOF (Thun, Switzerland). We present offline filter analyses of aerosol constituents using an ESI source coupled to an IMS-TOF instrument. Separation of WSOC species and aerosol-phase organosulfate isomers are demonstrated. Collisionally induced dissociation (CID) is used to distinguish chemically bound oligomers from weakly bound clusters and for identification of molecules. We also present measurements of gas phase species using a custom NO_3^- chemical ionization (CI) source coupled to the IMS-TOF. This ion source was used to enable detection of highly oxidized species in the gas phase that are likely to directly condense onto particles.[58,115] Time-resolved on-line IMS-MS measurements (time resolution of 5 minutes) with this source from a field campaign (SOAS 2013 in Centreville (CTR), Alabama) and from laboratory flow reactor studies are discussed. The use of trend lines in the 2-dimensional IMS-MS plots to identify species with related molecular structures, even within complex high-resolution mass spectra, is highlighted.

4.2 Experimental

4.2.1 IMS-MS

A schematic of the IMS-TOF instrument is provided in Fig. 4.1a. The IMS cell of the instrument is both pressure and temperature-controlled and contains two resistive coated glass tubes[143] separated by a Bradbury-Nielsen (BN) ion gate[144] along which a uniform electric field is applied (reduced electric field strength approx. 2 Townsend (1 Td = 10^{-21} V m^2)). The IMS cell is maintained at or above atmospheric pressure to increase IM resolving power and can be operated between room temperature and 150°C. Nitrogen (N_2) is usually used as the buffer gas and IMS pressure can be set between 800 and 1400 mbar.

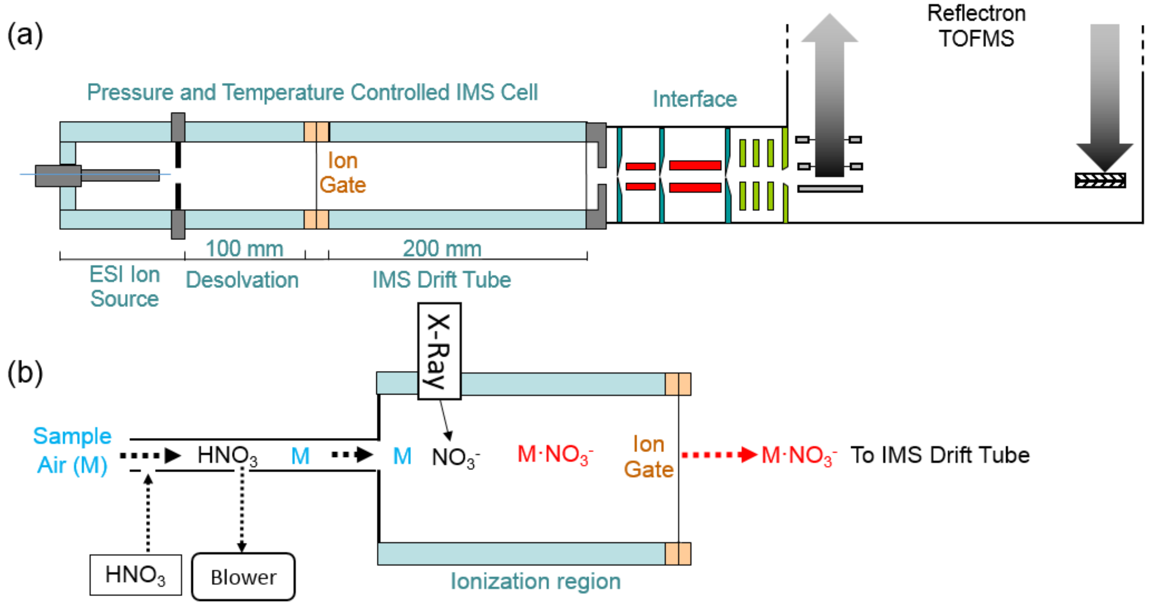

Figure 4.1. A schematic diagram of the IMS-TOF (panel a). The instrument can be used with different ionization sources, including the ESI source shown in panel (a) and the custom-built nitrate-ion chemical ionization source (NO3--CI) attached to the front.

Ions from an ionization source are pulsed through the BN gate and separated in the 20.5 cm-long drift tube. A clean, dry N_2 gas counter current flow of 1.2 standard L min^{-1} (SLPM at 21 °C and 101.3 kPa) is introduced from a liquid N_2 dewar into the drift tube to induce ion-neutral collisions. After exiting the drift tube, ions are transferred to the pressure reduction interface (containing two quadrupole ion guides) and through a 0.3 mm pinhole before being detected with a TOFWERK HTOF time-of-flight mass spectrometer (TOF MS). IMS separation occurs on the millisecond time scale and thus couples well with TOF MS, which operates on a microsecond time scale. IMS-TOF instruments can therefore acquire many mass spectra for each ion mobility spectrum.[140] The mass spectral resolution m/dm_{50} of the instrument is typically 3500 - 4000 FWHM at *m/z* 250.

As described in the following sections, ions from condensed-phase samples are generated by ESI and from gas-phase samples by a custom online CI that utilizes NO_3^- as a reagent ion. To improve signal intensity, sensitivity, signal-to-noise, and duty cycle, ions are pulsed into the drift region using a multiplexed gating scheme.[145,146] With multiplexing, the IMS-TOF achieves a 50% IMS duty cycle (i.e., 50% of the ions generated could be analyzed), as opposed to < 1% in standard pulsed mode, leading to an increase in ion transmission of approximately 100 fold. With post-processing, the IMS resolution (t/dt_{50}) routinely exceeds 200. Data analysis is performed using the data analysis package “Tofware” (version 2.5.3, www.tofwerk.com/tofware) running in the Igor Pro (WaveMetrics, OR, USA) environment. All IMS drift time plots and IMS-MS spectra shown in the chapter have been post-processed in the multiplexed domain for reduction of systematic and random noise during the multiplexing process and enhancement of the modulation.[147]

The IMS-TOF used in this work can also provide CID analyses in which ions are fragmented immediately after the IMS drift cell and before they are transmitted into the TOF.[143] The information obtained from CID is similar to that obtained from traditional MS/MS measurements, but since CID occurs immediately after ion mobility separation (IMS-CID-MS), it has two key advantages: 1) fragment and precursor ions appear at the same IMS drift time, allowing for easy correlation between fragments and precursor; and 2) CID spectra can be simultaneously obtained over the entire m/z range without need for pre-selection or limited scanning of mass regions as in traditional MS/MS measurements. For the examples reported in this work, we utilized typical CID potential differences between the exit of the first quadrupole and the entrance of the second quadrupole ranging from 1 to 30 V.

Drift times measured during any given IMS-MS experiment are dependent on the pressure and temperature of the drift tube. These dependencies as well as the instrument electric field can be accounted for to obtain a related parameter known as reduced mobility, K_0:

$$K_0 = \frac{L^2}{V t_d} \frac{P}{P_0} \frac{T_0}{T} \tag{4.1}$$

where L is the length of the drift tube, V is the applied electric field potential, t_d is the drift time of the analyte, P and P_0 are the actual and reference pressures, respectively, and T and T_0 are the actual and reference temperatures, respectively.[137] If the instrument is calibrated and conditions are well-controlled, molecular collision cross sections (Ω) can be extracted from the measured reduced mobilities by using the Mason-Schamp equation.[148–150]

$$\Omega = \frac{1}{K_0}\frac{3qz}{16N}(\frac{2\pi}{\mu kT_{eff}})^{\frac{1}{2}} \tag{4.2}$$

in which K_0 is mobility, q is the elementary charge, z is the charge number, N is the neutral gas number density, μ is the reduced mass of the analyte-buffer gas pair, k is the Boltzmann constant, and T_{eff} is the effective temperature.

Collision cross sections can more accurately be calculated using a momentum transfer scan law that includes field-dependent corrections for both collisional momentum transfer and collision frequency (α and β terms, respectively).[151]

$$\Omega = \frac{1}{K_0}\frac{3qz}{16N}\left(\frac{2\pi}{\mu kT}\right)^{\frac{1}{2}}\left[1+\left(\frac{\beta_{MT}}{\alpha_{MT}}\right)^2\left(\frac{v_d}{v_T}\right)^2\right]^{-\frac{1}{2}} \tag{4.3}$$

in which K_0 is mobility, q is the elementary charge, z is the charge number, N is the neutral gas number density, μ is the reduced mass of the analyte-buffer gas pair, k is the Boltzmann constant, T is the standard temperature, v_d is the drift velocity, and v_T is the thermal velocity.[151] α_{MT} and β_{MT} are calculated as follows:

$$\alpha_{MT} = \frac{2}{3}\left[1+\hat{m}\hat{c}+\widehat{M}\hat{h}\right] \tag{4.4}$$

$$\beta_{MT} = \left[\frac{2}{\hat{m}(1+\hat{m})}\right]^{\frac{1}{2}} \tag{4.5}$$

where m and M are the ion and neutral masses, respectively; $\hat{m}$ and $\widehat{M}$ are the mass fractions of the colliding pair; $\hat{c}$ is the fraction of collisions that cool the ion; and $\hat{h}$ is the fraction of collisions that heat the ion.[151]

IMS drift times and mobilities obtained under the same buffer gas conditions are reproducible and transferable. The measured Ω can be compared with literature or previous experiment values to identify molecular structures without the use of an analytical standard.

4.2.2 ESI-IMS-TOF and filter samples

Ambient filters were collected during the 2013 Southern Oxidant and Aerosol Study (SOAS; https://soas2013.rutgers.edu/) at the Look Rock, TN, USA site (LRK; Budisulistiorini et al., 2015). Detailed description of aerosol filter collection, storage, and extractions during SOAS at the LRK site was previously reported.[152] In the current study, an aerosol extract from June 16, 2013 (intensive sample 3, which was collected from 4-7 PM local time) was used to demonstrate the abilities of ESI-IMS-MS in the chemical characterization of ambient SOA at the molecular level. In addition, laboratory-generated SOA produced from the reactive uptake of authentic *trans*-β-IEPOX, *cis*-β-IEPOX, and δ-IEPOX onto acidified sulfate aerosol under dark conditions were collected onto Teflon filters (1.0-µm pore size, Tisch Environmental, EPA $PM_{2.5}$ membrane) for analysis by the ESI-IMS-MS technique. Details of chamber experiments, including filter extraction procedures for Teflon filters and operating conditions, have been previously described by Lin et al.[153,154] Certain isoprene SOA constituents, including the organosulfate derivatives of 2-methylglyceric acid and of the 2-methyltetrols, were synthesized in-house as recently described by Rattanavaraha et al.[136] and Budisulistiorini et al.[152] respectively. Synthesis details for authentic *trans*-β-IEPOX, *cis*-β-IEPOX, and δ-IEPOX (as a racemic mixture of the diastereomers) were described by Lin et al.[153,154] and Zhang et al.[156] It is noted here that since the multiphase chemistry of IEPOX isomers contributed greatly to the SOA mass at the LRK site,[152] these chamber experiments were used to complement the ESI-IMS-MS results from LRK.

Aerosol filter samples were analyzed offline using an ESI source coupled to the IMS-MS instrument. 5 µL of the sample were injected for analysis at a flow rate of 1 µL min^{-1}. The IMS was operated at 50°C and 1000 mbar, mass spectra were recorded from *m/z* 10 to 1200 in both positive and negative ion mode. ESI potential was at 1600 V.

4.2.3 NO_3^- CI-IMS-MS

In this work gas-phase ions were generated and coupled to the IMS-TOF with a custom built nitrate ion chemical ionization source (hereafter CI-IMS-TOF). The design constraints on the CI source for this IMS-TOF are: 1) ions must be formed at a pressure ~1 atmosphere (atm) so that they can be directly coupled to the drift tube of the IMS-TOF which is operated at a pressures of about 1 atm; and 2) the ions formed from the CI source must be formed at, or be efficiently transferred into, the high voltage (~10 kV) of the inlet of the IMS-TOF. The main components and operating principles of the source are shown in Fig. 4.1b. An X-ray ionizer (Hamamatsu, Inc., Japan) was aimed into the reaction/desolvation region to initiate ionization. To provide the precursor for the reagent ion, 5 standard cm^3 min^{-1} (sccm) of clean, dry N_2 gas from the boil-off of a liquid N_2 dewar flowed across a glass vial of fuming nitric acid (HNO_3) into the reaction region.

The nitrate CI mechanism comprised a series of reactions. First, an X-ray emitter initiated an ionization process that resulted in the formation of nitrate ions (NO_3^-) from the gas-phase nitric acid (HNO_3). The nitrate ions then clustered with sample molecules to form an ion-molecule cluster:

$$(\mathrm{n}+1)\mathrm{HNO_3} \rightarrow (\mathrm{HNO_3})_\mathrm{n}\mathrm{NO_3^-} + \mathrm{H^+} \tag{4.6}$$

The nitric acid-nitrate clusters then collided with analyte molecules in the sample air, initiating ion-molecule reactions that either deprotonated (Eq. (4.7)) or clustered (Eq. (4.8)) with the target analytes:

$$(\mathrm{HNO_3})_n\mathrm{NO_3^-} + \mathrm{HX} \rightarrow (\mathrm{HNO_3})_n + \mathrm{HNO_3} + \mathrm{X^-} \tag{4.7}$$

$$(\mathrm{HNO_3})_n\mathrm{NO_3^-} + \mathrm{HZ} \rightarrow (\mathrm{HNO_3})_n + (\mathrm{NO_3^-})\mathrm{HZ} \tag{4.8}$$

where HX in (4.7) must be a highly acidic compound such as sulfuric acid (H_2SO_4) or methanesulfonic acid (MSA) and HZ in (4.8) is a highly functionalized and oxidized species [22,58,115] . All of these reactions take place inside a reaction region floated at a voltage above that of the BN gate. Thus, ions were formed at maximum electrical potential and moved at a steady speed through the drift tube.

The single-chamber design of our NO_3^- source differs from the source design of Eisele and Tanner[58] in its lack of concentric sample and sheath flows. As a result, the X-rays directly interact with sample air molecules without time for conversion of all ions to NO_3^-. While clustering with NO_3^- is the dominant ionization mechanism, we also observe additional minor ionization pathways. The most significant of the additional mechanisms is deprotonation via O_2^-, which primarily produced $[M\text{-}H]^-$ ions from carboxylic acids and has been studied extensively in atmospheric pressure chemical ionization sources (APCI).[157–159]

The CI-IMS-TOF was deployed for a 7-week period during the SOAS field campaign at the Centreville, AL, USA supersite (CTR). Data were acquired at 5-minute time resolution for the duration of the campaign. This 5-minute time resolution was chosen due to low ambient signals. Time resolutions as low as a data point every 5 seconds were utilized in laboratory experiments in which generated analyte concentrations were higher. The drift and desolvation tubes were maintained at 60° C for the first half of SOAS and 150° C for the second half. Higher temperatures reduced clustering between analyte and water molecules (due to high ambient humidity levels) in the drift tube but decreased ion mobility resolution. Dry N_2 gas counterflow can also be used to limit such clustering in the drift tube, but it was not employed during the campaign. The pressure in the drift tube typically fluctuated from 5-20 mbar above atmospheric pressure. Variations in pressure and temperature are corrected for during post-processing using Eq. (4.1).

Laboratory experiments were also conducted to investigate the gas-phase chemistry of biogenic VOC oxidation with the CI-IMS-TOF. In these experiments, a counterflow of N_2 was utilized with the drift tube maintained at a temperature of 100° C. Oxidation products of isoprene, α-pinene, and limonene were generated by reaction with ozone (O_3) and/or hydroxyl (OH) radicals inside a Potential Aerosol Mass (PAM) oxidation flow reactor [160,161] via the reaction $O_3 + h\nu \rightarrow O_2 + O(^1D)$ followed by the reaction $O(^1D) + H_2O \rightarrow 2OH$. O_3 was generated by irradiating O_2 with a mercury lamp (λ = 185 nm) outside the PAM reactor.

4.3 Offline IMS-MS Measurements of ambient SOA

4.3.1 ESI-IMS-MS of Ambient Aerosol filter

Figure 4.2 shows an example of a 2D ESI-IMS-MS spectrum measured from a SOAS (LRK site, June 16, 2013) aerosol filter sample. In the two-dimensional (2D) image, IMS drift time is shown on the vertical axis and *m/z* is displayed on the horizontal axis. Because we have not corrected the data for transit times outside of the IMS drift cell, we report drift times as “apparent drift times.” The panel above the 2D plot shows the mass spectrum that results from summing across all displayed IMS drift times. The ion mobility spectrum on the right of Fig. 4.2 is the sum ion mobility spectrum for all displayed high-resolution *m/z* values (*m/z* 50 – 600).

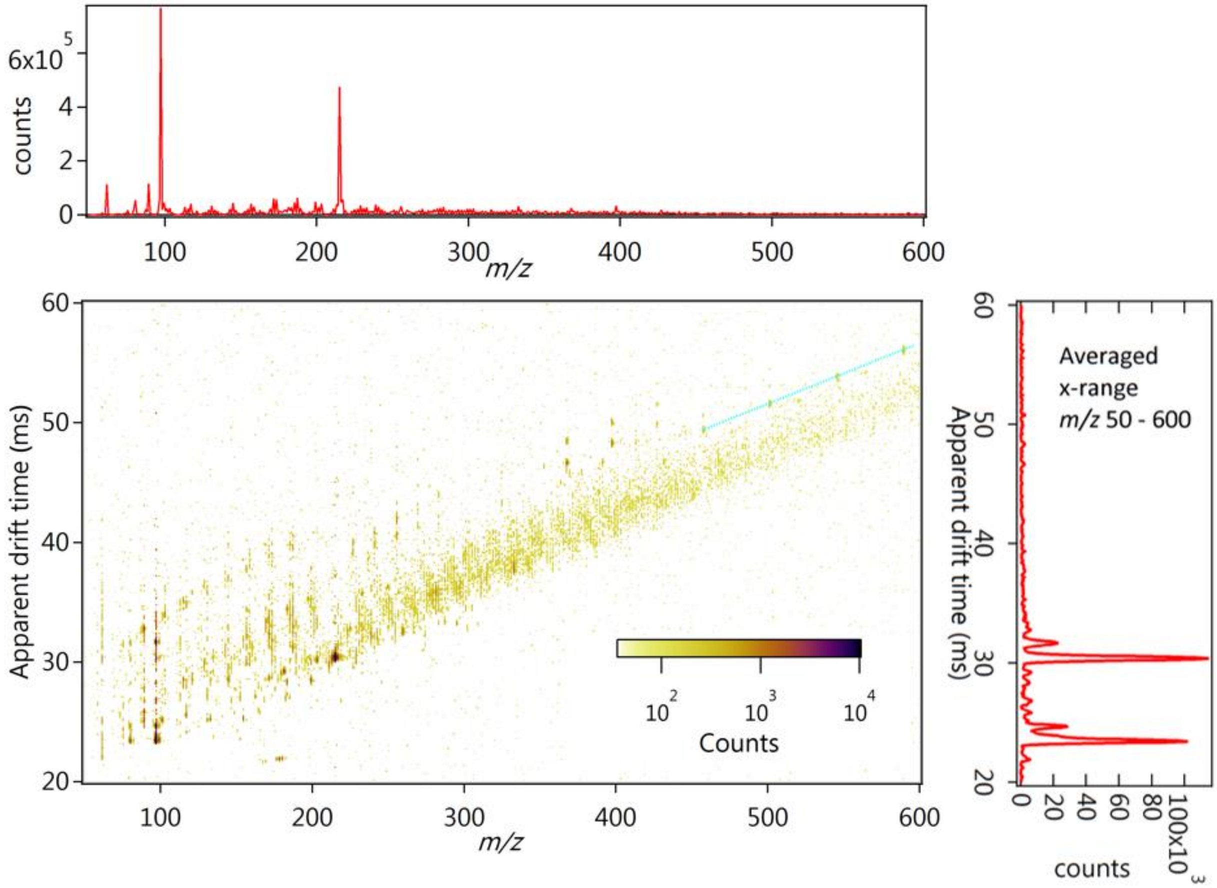

Figure 4.2 A typical representation of IMS-MS data in two-dimensional (2D) format for a SOAS filter sample (LRK site, June 16, 2013) analyzed via ESI-IMS-MS. The 2D graph plots drift time vs. mass-to-charge (m/z) ratio. The top mass spectrum is the total mass spectrum for all displayed drift times (20-60 ms). The plot on the right is a total ion mobility spectrum for the entire displayed m/z rage (50 - 600). The light blue line points out an example mass mobility correlation, or “trend line.”

Hundreds of individual features are visible as dark-colored points in the 2D plot. Each feature corresponds to an individual molecule that was ionized, separated, and detected with ESI-IMS-MS; the horizontal position of each feature corresponds to a high-resolution *m/z* from which the elemental composition is derived. The vertical position of each feature is the IMS drift time, which is used to obtain its reduced mobility and thus information about its molecular structure. Since compounds with different structures will generally have different drift times, the mobility separation helps deconvolve complex mass spectral features (including isomers and isobars) that are otherwise unresolvable by TOF-MS alone. Stark et al.[162] have shown that a high resolution TOF with a MS resolution m/dm$_{50}$ of 4000 cannot unambiguously resolve peaks beyond *m/z* 100 due to the multitude of species present. The addition of an extra drift time dimension increases effective resolving power of the spectrometer while also providing valuable structural information about the analyte. In addition to individual features, mass-mobility correlations, or "trend lines" in the 2D spectrum can be used to elucidate bulk chemical composition in complex samples.[140] For example, a distinct series of high-intensity peaks in the top right of the Fig. 4.2 2D plot that begins at *m/z* 458 and DT ~46 ms and ends at *m/z* 590 and DT ~55 ms. Trend lines of relevance to atmospheric chemistry will be discussed in detail in section 4.4.2.

4.3.2 Separation of unresolved WSOC and Isomeric Species

Previous LC/MS analyses of the filter material collected from the LRK site shown in Fig. 4.2 indicated the presence of WSOC species that could not be chromatographically resolved using LC due to solvent and column constraints.[152] For example, Figure 4.3a shows that during LC analysis, *m/z* 215 (trihydroxymethylbutylsulfate)[163] co-elutes with *m/z* 199 (sulfate ester of 2-methylglyeric acid)[48] and other WSOC species at *m/z* 183 (sulfate ester of 3,4-dihydroxybutan-2-one),[164] 155 (glycolic acid sulfate), [165,166] and 133 (malic acid). On the other hand, as shown in Figure 4.3b, some of these WSOC ions can be distinguished from each other by their ion mobility drift times: *m/z* 215 has a drift time that is clearly larger than the others, *m/z* 199 and 183 have intermediate drift times, and *m/z* 155 and 133 have the lowest drift times. The drift times of *m/z* 155 and *m/z*

133 differ from each other slightly. Further ion mobility separation of *m/z* 199 and *m/z* 183, however, appears to be limited by similarity in their CCS.

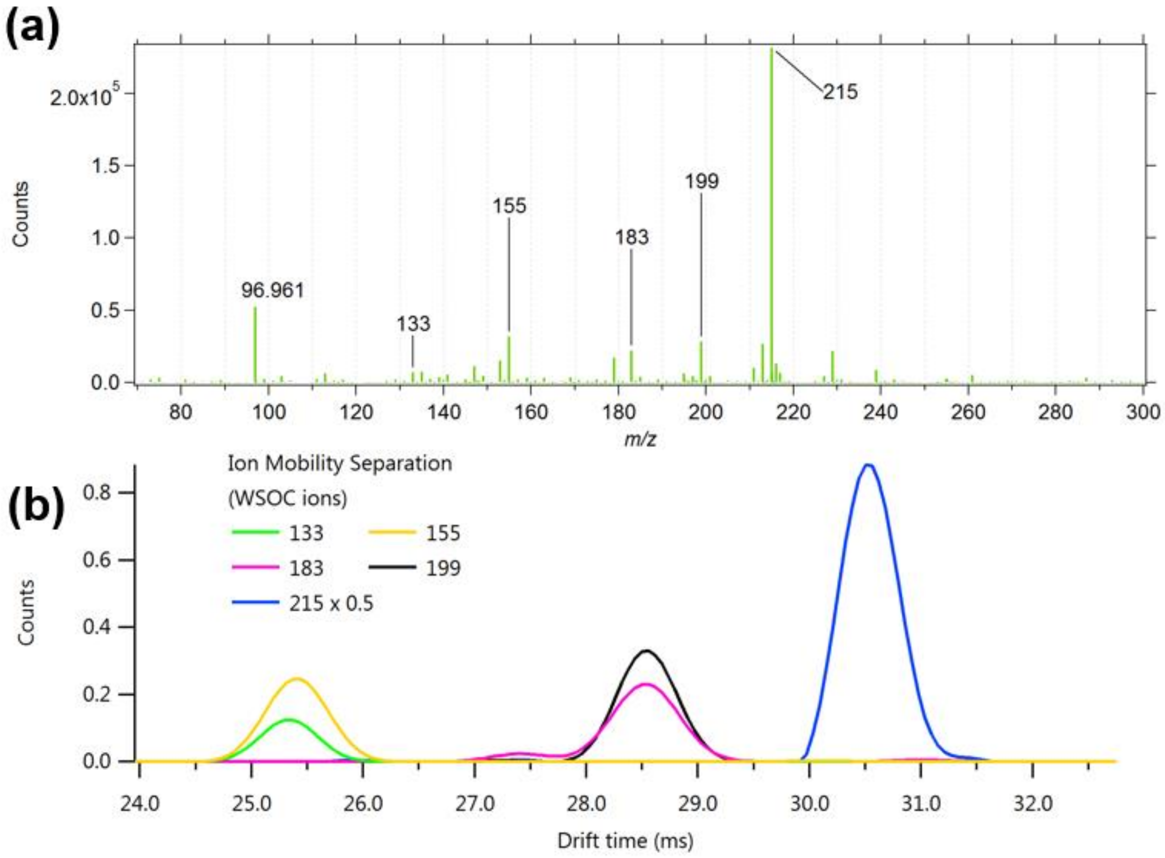

Figure 4.3 (a) An ESI-LC-MS filter mass spectrum (MS) extracted from the liquid chromatogram peak corresponding to the water-soluble organosulfate signal at m/z 215. The filter was taken during the SOAS campaign at the LRK site on June 12, 2013. LC is unable to resolve all of the compounds shown in the chromatogram. The ion mobility spectra for the MS peaks highlighted in (a) are shown in (b). The IM spectra were extracted from separate mass spectra and then placed together in the graph above for clarity. The water-soluble organic compounds are resolved by the IMS-TOF. The intensity for the ion mobility peak at m/z 215 has been scaled by a factor of 0.5 for visibility, as indicated in the legend.

In Fig. 4.3a, the dominant signal is due to *m/z* 215, a particle-phase organosulfate formed from isoprene oxidation under low-NO conditions.[154,167] Figure 4.4 provides a mechanism for this process. Isoprene (C_5H_8), the largest non-methane hydrocarbon emission[39] can form organosulfate aerosol in the presence of acidified sulfate aerosol under low-NO conditions.[49,167–170] Isoprene forms several epoxydiol isomers (collectively IEPOX) via OH radical-initiated oxidation of hydroxyhydroperoxide (ISOPOOH) intermediates.[40,41] IEPOX can be taken up by acidic aerosol at relatively short time scales[88,171] and reacts in the particle phase to form organosulfates. Several previous publications[163,167–169,172,173] specifically identified a hydroxy sulfate ester (HSE; $C_5H_{11}O_7S^-$, 215.02 Da) as a large component of ambient and laboratory filter samples. Its molecular structure, however, has up to eight possible isomers,[163] three of which are thought to be the major ones (Fig. 4.5) that depend on the IEPOX isomer from which it is derived. It is not well established which isomers predominate in atmospheric aerosol.

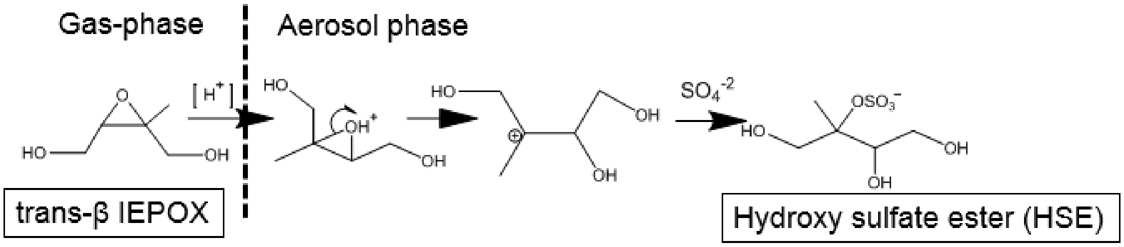

Figure 4.4 A formation reaction series for the hydroxy sulfate ester (HSE) under acidic aerosol uptake of IEPOX, as originally outlined in [167]. Gas-phase IEPOX is taken up into acidic aerosol. Then, in the presence of sulfate, it can undergo esterification to form the hydroxy sulfate ester, an isomer of which is shown on the far right.

To investigate whether IMS-MS can be utilized to distinguish between the different HSE isomers, we analyzed laboratory samples of organosulfate aerosol generated from the reactive uptake of different IEPOX isomers along with one ambient filter from the LRK site (June 16, 2013). A reference standard, sodium dodecyl sulfate (SDS; $NaC_{12}H_{25}SO_4$; 288.372 g mol^{-1}) was added to each filter analysis to correct any changes in drift times between experiments. Structures of the different HSE products and their IEPOX precursors can be found in Fig. 4.5.

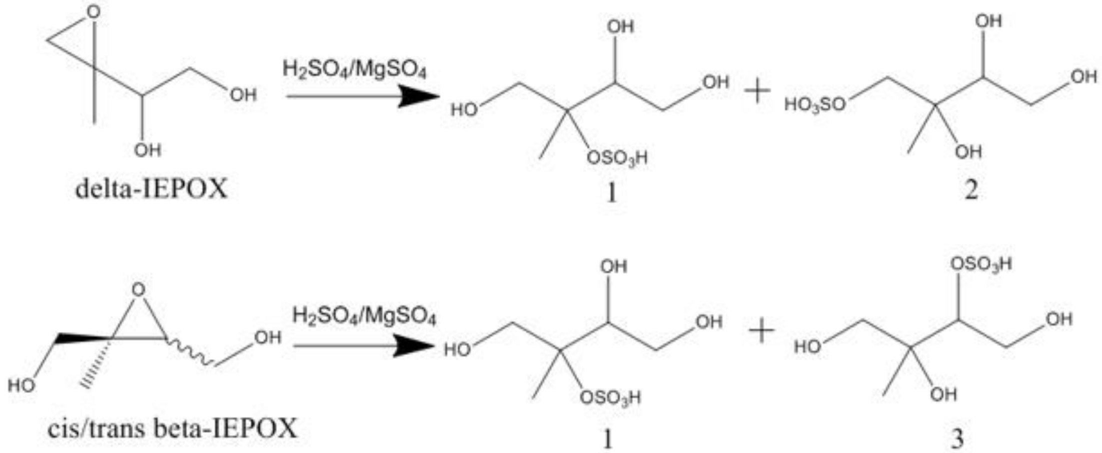

Figure 4.5 A scheme depicting the different HSE structural isomers from IEPOX reactive uptake under acidic particle-phase conditions.

The IMS spectra obtained from the laboratory HSE species are shown in Fig. 4.6, along with assigned structures. Three main isomers characterized by distinct drift times are observed as expected based on the mechanism shown in Fig. 4.4. The laboratory standard HSE derived from cis-β IEPOX and trans-β IEPOX both show isomers at drift times 41.75 and 41.95 ms, but the relative ratios of the isomers at these drift times are different for the two precursors. The third peak in the cis-β IEPOX IMS spectrum at 41.6 ms does not appear to be related to HSE. It is linked, instead, to another ion that is isobaric with HSE and is observed as a shoulder on the HSE peak in the high resolution mass spectrum. The reactive uptake of δ-IEPOX also yields two trihydroxybutylsufate (also hydroxy sulfate ester, or HSE) isomers as expected. One isomer that is observed at 41.75 ms is identical to that produced from cis-β IEPOX while the other is observed at a drift time of 42.03 ms.

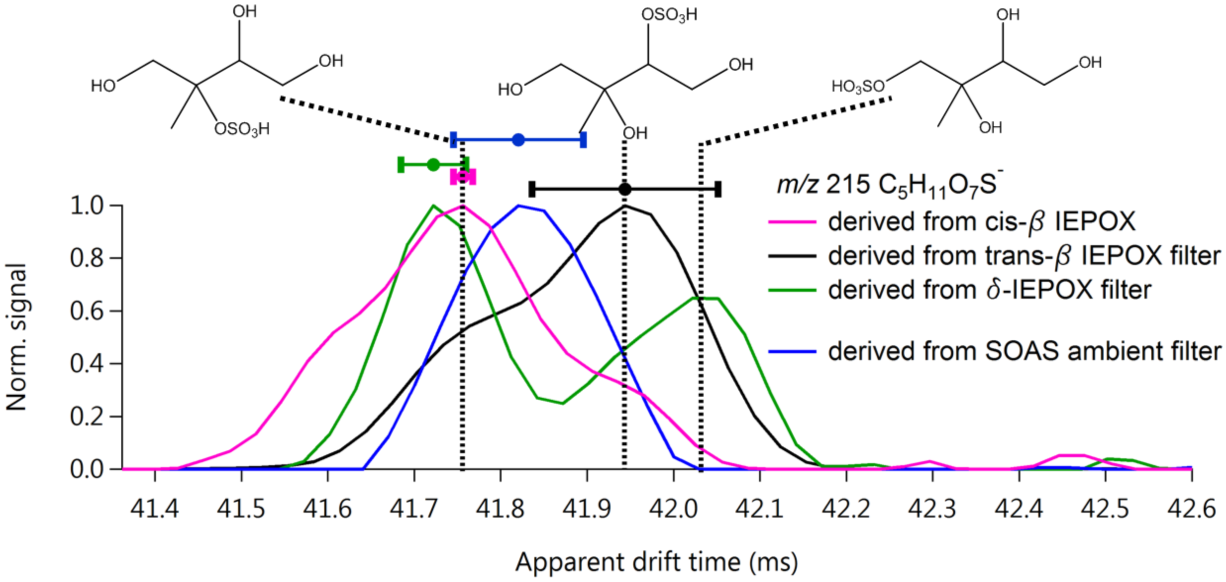

Figure 4.6. Ion mobility spectra of HSE ($C_5H_{11}O_7S^-$) in four different aerosol filter samples. Dashed vertical lines indicate the three different IMS peaks/isomers observed in different combinations in each sample. All spectra have been normalized to facilitate qualitative comparison. The bars on the top denote the uncertainty in the drift time dimension for each peak and were determined from the standard error of the mean of a mobility calibration compound from its average drift time.

The HSE species in the LRK ambient sample produces one broad ion mobility peak at a drift time of 41.82 ms. This 41.82 ms peak lies between the drift times observed for HSE isomers 1 and 3. The HSE isomer 1 can be produced from both β-IEPOX and δ-IEPOX, but the absence of the HSE isomer 2, which is also a product of δ-IEPOX, suggests that δ-IEPOX does not contribute significantly to the observed ambient HSE. These observations are consistent with recent results which found that δ-IEPOX is only produced with a 3% yield.[43] The measured IMS drift time of ambient HSE lies between the two different IMS drift times measured for HSE produced from chamber experiments with cis-β and trans-β IEPOX products. This suggests that both cis-β and trans-β IEPOX contribute to the observed ambient HSE at LRK. This is consistent with recent *ab initio* calculations in the literature[174] that have also concluded that 1,2-ISOPOOH (the atmospherically dominant isomer[42]) has a 58% reaction pathway preference for cis-β IEPOX and an 42% preference for trans-β IEPOX, although the same work showed an experimental preference for trans-β IEPOX.

The ambient and laboratory filter results shown in Fig. 4.6 were analyzed without any pre-separation of the inorganic sulfate seeds from the organic aerosol species. Although the capability to separate the HSE isomers was demonstrated, resolution was likely reduced due to clustering in the drift tube between HSE ions and neutral sulfuric acid molecules formed from the acidic seed. The data in Fig. 4.6 were obtained at a drift tube pressure that was slightly higher than ambient (1400 mbar) to improve the ion mobility resolution.

4.3.3 Molecular Information from IMS-CID-MS

In section 4.3.2, isomer identification is achieved by direct measurements of the ion mobilities of laboratory standards. Molecular-level information can also be achieved by utilizing the IMS-MS technique with CID. Figures 4.7a and 4.7b show CID analysis of a synthesized standard of the 2-methylglyeric acid organosulfate derivative ($C_4H_7O_7S^-$; exact calculated mass: 198.99 g mol^{-1}). This compound produces a CID pattern that contains two distinct peaks that appear at the same drift time as the precursor ion; identical drift times for precursor and fragment ions are expected as the fragmentation takes place after IMS separation (IMS-CID-MS). Taken together, the ions at *m/z* 199 (which corresponds to the 2-methylglyeric acid organosulfate derivate), m/z 119 (neutral loss of SO_3) and at *m/z* 97 (which corresponds to HSO_4^-) confirm the chemical structure of the standard and the fact that it contains sulfate. The peaks mentioned above in IMS-CID-MS spectrum corresponding to the precursor drift time (Fig. 4.7b) match the MS/MS spectrum published in Gómez-González et al.,[169] demonstrating that IMS-CID-MS fragmentation patterns are consistent with traditional tandem mass spectrometry measurements.

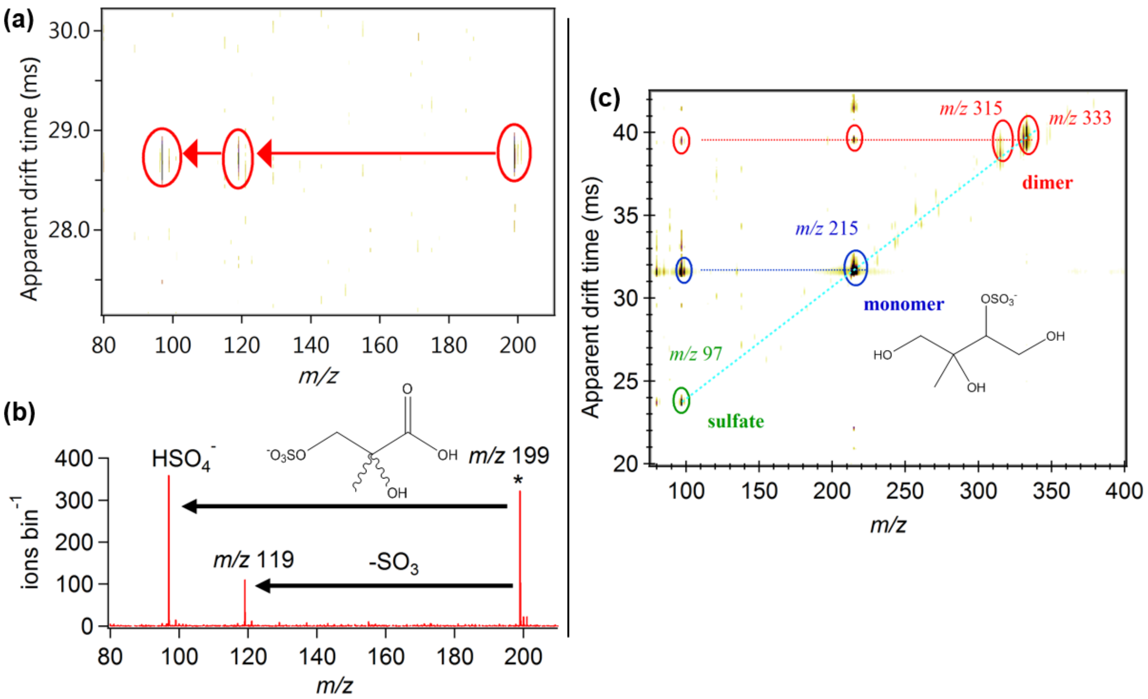

Figure 4.7. (a) 2D IMS-CID-MS plot for a synthesized chemical standard of 2-methylglyeric acid organosulfate derivative and (b) its characteristic fragment ion mass spectrum. The CID mass spectra match previously published MS/MS measurements.[169] (c) 2D IMS-CID-MS plot of a chamber-generated aerosol filter sample. Organic aerosol was generated in the UNC smog chamber from the reactive uptake of authentic IEPOX onto acidic sulfate aerosol under dark conditions.[153,154] Deprotonated and dehydrated organosulfate dimers and monomers are observed. The organosulfate dimer (*m/z* 333) is observed decaying into the organosulfate monomer (*m/z* 215) and both are observed further decomposing into HSO_4^-, which also matches previous literature results.[168]

Figure 4.7c shows the 2D plot for an aerosol filter sample derived from the reactive uptake of authentic IEPOX onto acidified sulfate aerosol under dark chamber conditions and analyzed using ESI-IMS-CID-MS. The plot shows a series of signals that correspond to elemental formulas of deprotonated ($[M-H]^-$) and dehydrated ($[M-H_2O]^-$) hydroxyl sulfate ester dimers and trimers from condensed-phase accretion reactions. These oligomers are readily identified in the 2D IMS-MS spectrum because they lie along the same diagonal trend line (See section 4.4.2 below for more discussion of trend lines). Figure 4.7c was achieved with a CID potential of 28 volts (fragmentation occurs in the region of the second quadrupole). The fragmentation of the dimer at *m/z* 333 results in the loss of neutral C_5 dihydroxycarbonyl, which leaves the original trihydroxybutylsulfate at *m/z* 215 as an observable fragment ion. This pathway was previously established in the literature [168]. The CID fragmentation pattern of *m/z* 215 is also consistent with previous MS/MS analysis [169] which shows that HSE fragments into HSO_4^-, detected at *m/z* 97, and an undetectable neutral molecule. As in the case of Figs. 4.7a and 4.7b, the presence of the HSO_4^- fragment in the CID spectra of both the dimer and the monomer is a clear indication that they both contain sulfate moieties.

4.4 Online IMS-MS of Biogenic VOC (BVOC) Oxidation Products in Gas Phase

One goal of the SOAS 2013 campaign was to understand the reactions that lead to oxidation of BVOC. During SOAS the NO_3^- IMS-TOF was deployed at the Centreville, Alabama field site, which is influenced by isoprene and terpene BVOCs. Previous studies have shown that NO_3^- CI can be used to efficiently and selectively detect highly oxidized molecules with multiple oxygenated functional groups that are photochemically produced from isoprene and terpenes in the gas phase.[19,22,175] In ambient environments these highly oxidized gas-phase species are present at low ambient concentrations (ppt levels), but they can condense onto particles and be a significant contribution to particle growth and particle composition.[20] The IMS-MS measurements described here provide the opportunity to detect the isomeric and isobaric variants of these species that cannot be resolved with the NO_3^- CIMS techniques measurements alone. This information is important for developing a better understanding of the reaction pathways that form these highly oxidized species and for characterizing their partitioning behavior between the gas and particle phases. To our knowledge, this is the first deployment of an IMS-MS instrument for field measurements of gas phase species.

During SOAS 2013 the NO_3^- IMS-MS data was collected at high-time resolution with a 2D IMS-MS spectrum every 5 min. Figure 4.8a shows a 2D NO_3-IMS-MS plot obtained by averaging over one 8-hour period of SOAS CTR field data. The grey crosses in the background of the plot are peaks observed in the ambient measurements. On top of the ambient data are markers corresponding to BVOC oxidation products generated from ozonolysis and low-NO photooxidation of specific BVOC precursors (isoprene, limonene, and α-pinene) in the laboratory PAM oxidation flow reactor. High-resolution peak fitting of the IMS-TOF mass spectra[176] is used to assign molecular formulas to the ion signals obtained for the data in Fig. 4.8a. The reduced mobility of each ion in the lab and field measurements shown in Fig. 4.8a was calculated from the measured drift times and pressure using Eq. (4.1).

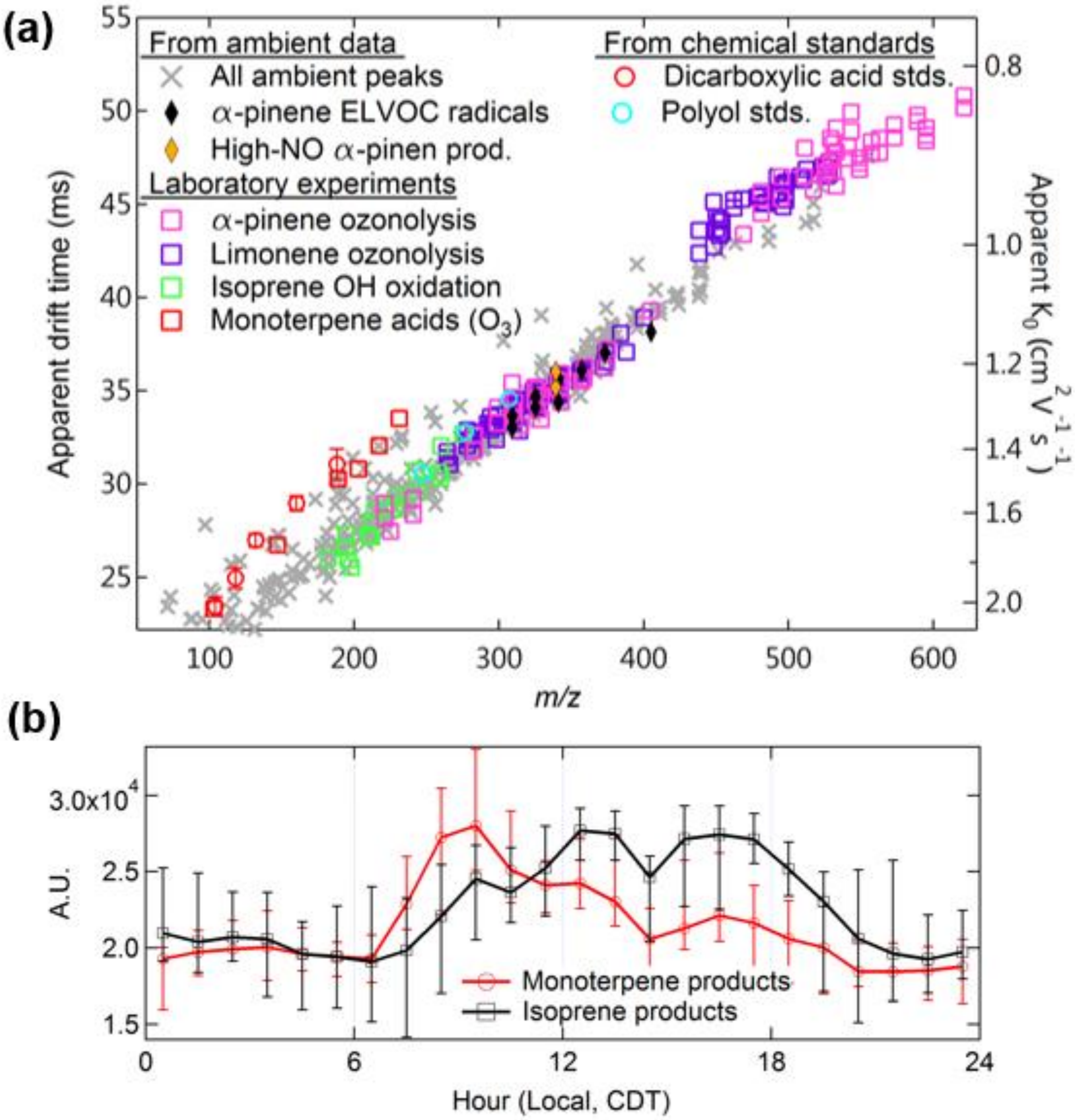

Figure 4.8. 2D plot showing an 8-hour average of SOAS NO_3-IMS-MS spectra acquired at the CTR supersite. Data from laboratory measurements of chemical standards and BVOC oxidation studies are plotted on top of the ambient data. Monoterpene and isoprene products were generated in a PAM oxidation flow reactor by oxidation with O_3 and OH and analytical standards were sublimated before ionization. **(b)** Diurnal cycles for the sum of the monoterpene and isoprene peaks highlighted in **(a)** over a 2-week period during the SOAS campaign. Dicarboxylic acid standards comprised C_3, C_4, C_5, C_7, and C_9 dicarboxylic acids and polyol standards included threitol, xylitol, and mannitol.

The molecular formulas obtained from the field and laboratory data are consistent with previously published NO_3-CIMS gas phase BVOC product spectra.[19,23,24] Many of the elemental compositions detected in the mass spectral range of *m/z* 180 - 250 correspond to previously identified products of isoprene oxidation[23,24] and the majority of the ion signals detected between *m/z* 300 - 425 match the formulas of α-pinene and limonene monomeric products that were previously identified as highly oxidized multifunctional organic compounds (HOMs).[20,23] Also highlighted are the α-pinene HOMs peroxy radicals,[177] which will be discussed in the next section. Ion signals detected between *m/z* 425- 600 in Fig. 4.8a correspond to α-pinene and limonene HOMs dimers that are observed in the laboratory experiments.[19,23] Although some HOMs dimer signals were observed, most of the HOMs dimer signals did not have sufficient S/N during the ambient measurements, likely due to inlet losses and poor ion transmission. Two isomers of a key high-NO α-pinene ozonolysis product ($C_{10}H_{15}NO_8$ clustered with NO_3^-, *m/z* 339) are included in Fig. 4.8a. This product was previously identified as a high-NO nitrate-containing oxidation product of α-pinene in ambient NO_3^-[178] and I^--CIMS measurements.[26] Other organic nitrate gas-phase compounds were not observed with sufficient S/N in the CI-IMS-TOF ambient data.

Ambient diurnal cycles of the summed mass spectral signals of the isoprene and monoterpene oxidation products are shown in Fig. 4.8b. The diurnal averages are derived over a two-week period in the middle of the SOAS campaign. The isoprene-attributed signal peaks in the late afternoon and declines rapidly at night. On the other hand, the monoterpene signal, which is obtained by summing over all ions identified as α-pinene and limonene oxidation products in Fig. 6a, peaks in the early morning and decline throughout the day. Both are consistent with other published SOAS results.[24]

The new information provided from the IMS-TOF is the reduced mobility of each ion, which as shown in Fig. 4.8a can be calculated from the measured drift times and pressure using Eq. (4.1). The reduced mobilities measured for ambient ions lie in the same regions of the 2D IMS-MS space as the laboratory products of the isoprene and terpene products. Comparisons between IMS measurements of laboratory and field IMS measurements for the same ion could provide a valuable means of identifying the precursors of the isobaric/isomeric species that are separated with the IMS. However, such detailed intercomparisons are precluded in this case by the fact that the two datasets were obtained under different operating conditions that cannot be accounted for with Eq. (4.1). In particular, the ambient data was collected without a nitrogen counterflow in the IMS drift tube and under conditions of high ambient humidity (mean temperature and relative humidity (RH) of ambient air were 25 °C and 83%)[179] while the laboratory data was collected with a nitrogen counterflow and negligible humidity (~15%). It is also important to note that the absolute values of the reported reduced mobilities for this study should be taken with caution since they were not explicitly calibrated with an IMS standard. Most accepted ion mobility standards,[180] and many of the molecules studied in this work strongly cluster with the NO_3^- reagent ion from the CI source or water, which were both present in large quantities in the drift tube, particularly during SOAS. As a result, the typical conditions used for mobility calibrations (ESI-IMS-MS) do not reproduce the drift tube conditions under which the ambient and/or PAM IMS-TOF measurements were made. Future studies should address the issue of validating ion mobility calibration compounds that work well with different CIMS ionization schemes.

Figure 4.8a depicts many examples of isomeric and isobaric compounds in the ambient and laboratory data that are separated in the ion mobility drift space and that would not have been separated in *m/z* space with a medium resolution (~ 4000 resolving power) TOF-MS. A list of the BVOC HOM ions observed following BVOC oxidation in the PAM reactor is given in Table 4.1, along with the number of isomers observed for each HOM. Examples of the types of separations observed in the laboratory and ambient data are illustrated in Fig. 4.9 with three MS peaks. All three MS peaks (two from laboratory experiments and *m/z* 339 from ambient data) in Fig. 4.9 have been analyzed with multi-peak high-resolution analysis.[162] The peaks at *m/z* 240 and 310 ($C_5H_6O_7$, $C_9H_{12}O_8$, $C_{10}H_{16}O_7$ clustered with NO_3^-) were previously identified as low-NO α-pinene ozonolysis products[19] and the peak at *m/z* 339 ($C_{10}H_{15}NO_8$ clustered with NO_3^-) was previously identified as a high-NO nitrate-containing oxidation product of α-pinene with I^--CIMS measurements.[26] For *m/z* 240 ($C_5H_6O_7$ clustered with NO_3^-), the fact that the IMS drift time profile shows a single peak confirms the existence of only a single compound at this mass. The MS peak at *m/z* 310 is fit using two isobaric peaks corresponding to NO_3^- clusters of $C_9H_{12}O_8$ and $C_{10}H_{16}O_7$. Two IMS peaks are observed for the unit mass MS peak, confirming the two-constituent fit, but a key advantage of the IMS in this case is that it clearly helps identify the presence of two distinct species without the need for any multi-peak fitting. Given systematic uncertainties in mass spectral peak fitting,[176] the ratio of the IMS peaks could give a more accurate intensity ratio. Finally, the MS peak at *m/z* 339 is fit entirely with one elemental formula (NO_3^- cluster of $C_{10}H_{15}NO_8$) but two IM peaks are observed. In this case, the IMS provides new information not available from MS alone, indicating that it is likely comprised of at least two structural isomers. Taken together, the examples in Fig. 4.9 illustrate the fact that separation along the IMS dimension can significantly increase the number of organic species that are measured and identified compared to MS alone.

Formula	Ion *m/z* clustered with NO_3^-	Number of isomers	Precursor	Ref.	Formula	Ion *m/z* clustered with NO_3^-	Number of isomers	Precursor	Ref.
$C_7H_{10}O_4$	220.05	1	α-pinene	1	$C_9H_{14}O_5$	264.07	1	limonene	3
$C_5H_6O_6$	224.00	1	α-pinene	1	$C_9H_{16}O_5$	266.09	1	limonene	3
$C_5H_6O_7$	240.00	1	α-pinene	1	$C_{10}H_{16}O_5$	278.09	1	limonene	3
$C_7H_8O_8$	282.01	1	α-pinene	1	$C_9H_{14}O_6$	280.07	1	limonene	3
$C_8H_{12}O_7$	282.05	1	α-pinene	1	$C_9H_{15}O_6$	281.08	1	limonene	3
$C_8H_{12}O_8$	298.04	1	α-pinene	1	$C_9H_{16}O_6$	282.08	1	limonene	3
$C_{10}H_{14}O_7$	308.06	1	α-pinene	1	$C_{10}H_{14}O_6$	292.07	1	limonene	3
$C_9H_{12}O_8$	310.04	1	α-pinene	1	$C_{10}H_{16}O_6$	294.08	1	limonene	3
$C_{10}H_{16}O_7$	310.08	1	α-pinene	1	$C_9H_{14}O_7$	296.06	1	limonene	3
$C_8H_{12}O_9$	314.04	1	α-pinene	1	$C_9H_{15}O_7$	297.07	1	limonene	3
$C_{10}H_{14}O_8$	324.06	1	α-pinene	1	$C_9H_{16}O_7$	298.08	1	limonene	3
$C_{10}H_{16}O_8$	326.04	1	α-pinene	1	$C_{10}H_{14}O_7$	308.06	2	limonene	3
$C_9H_{12}O_9$	326.07	1	α-pinene	1	$C_{10}H_{16}O_7$	310.08	2	limonene	3
$C_9H_{14}O_9$	328.05	1	α-pinene	1	$C_{10}H_{17}O_7$	311.09	1	limonene	3
$C_{10}H_{14}O_9$	340.05	2	α-pinene	1	$C_9H_{15}O_4(HNO_3)$	312.08	1	limonene	3
$C_9H_{12}O_{10}$	342.03	2	α-pinene	1	$C_9H_{15}O_8$	313.07	1	limonene	3
$C_{10}H_{16}O_9$	342.07	1	α-pinene	1	$C_9H_{16}O_8$	314.07	1	limonene	3
$C_{10}H_{14}O_{10}$	356.05	2	α-pinene	1	$C_{10}H_{14}O_8$	324.06	2	limonene	3
$C_{10}H_{16}O_{10}$	358.03	2	α-pinene	1	$C_{10}H_{15}O_8$	325.07	1	limonene	3
$C_9H_{12}O_{11}$	358.06	1	α-pinene	1	$C_{10}H_{16}O_8$	326.07	1	limonene	3
$C_{10}H_{14}O_{11}$	372.04	1	α-pinene	1	$C_9H_{14}O_5(HNO_3)$	327.07	1	limonene	3
$C_{10}H_{16}O_{11}$	374.02	1	α-pinene	1	$C_{10}H_{14}O_9$	340.05	3	limonene	3
$C_{10}H_{14}O_{13}$	404.03	1	α-pinene	1	$C_{10}H_{15}O_9$	341.06	2	limonene	3
$C_{17}H_{26}O_{11}$	468.14	1	α-pinene	1	$C_{10}H_{16}O_9$	342.07	2	limonene	3
$C_{18}H_{26}O_{11}$	480.14	3	α-pinene	1	$C_{10}H_{14}O_{10}$	356.05	1	limonene	3
$C_{19}H_{28}O_{11}$	494.15	2	α-pinene	1	$C_{10}H_{15}O_{10}$	357.05	1	limonene	3
$C_{20}H_{32}O_{11}$	510.18	2	α-pinene	1	$C_{10}H_{16}O_{10}$	358.06	1	limonene	3
$C_{17}H_{26}O_{14}$	516.12	1	α-pinene	1	$C_{10}H_{14}O_{11}$	372.04	1	limonene	3
$C_{20}H_{30}O_{12}$	524.16	2	α-pinene	1	$C_{10}H_{15}O_{11}$	373.05	1	limonene	3
$C_{19}H_{28}O_{13}$	526.14	2	α-pinene	1	$C_{10}H_{16}O_{11}$	374.06	1	limonene	3

$C_{18}H_{26}O_{14}$	528.12	2	α-pinene	1
$C_{18}H_{28}O_{14}$	530.14	2	α-pinene	1
$C_{17}H_{26}O_{15}$	532.12	2	α-pinene	1
$C_{20}H_{30}O_{13}$	540.16	2	α-pinene	1
$C_{20}H_{32}O_{13}$	542.17	2	α-pinene	1
$C_{17}H_{26}O_{16}$	548.11	2	α-pinene	1
$C_{20}H_{30}O_{14}$	556.15	2	α-pinene	1
$C_{18}H_{28}O_{16}$	562.13	2	α-pinene	1
$C_{20}H_{30}O_{15}$	572.15	2	α-pinene	1
$C_{20}H_{32}O_{15}$	574.00	1	α-pinene	1
$C_{20}H_{30}O_{16}$	588.14	2	α-pinene	1
$C_{18}H_{28}O_{18}$	594.12	3	α-pinene	1
$C_{20}H_{30}O_{18}$	620.13	2	α-pinene	1
$C_2H_4O_4$	154.00	0	isoprene	2
$C_4H_8O_4$	182.03	1	isoprene	2
$C_5H_8O_4$	194.03	2	isoprene	2
$C_4H_6O_5$	196.01	1	isoprene	2
$C_4H_8O_5$	198.03	1	isoprene	2
$C_5H_{12}O_4$	198.06	1	isoprene	2
$C_5H_8O_5$	210.03	1	isoprene	2
$C_4H_6O_6$	212.00	1	isoprene	2
$C_5H_{10}O_5$	212.04	1	isoprene	2
$C_4H_8O_6$	214.02	0	isoprene	2
$C_5H_{12}O_5$	214.06	1	isoprene	2
$C_5H_{10}O_6$	228.04	2	isoprene	2
$C_5H_{12}O_6$	230.04	1	isoprene	2
$C_5H_9O_7$	243.02	1	isoprene	3
$C_5H_{10}O_7$	244.03	1	isoprene	3
$C_5H_8O_8$	258.01	1	isoprene	3
$C_5H_9O_8$	259.02	0	isoprene	3
$C_5H_{10}O_8$	260.03	2	isoprene	3
$C_5H_9O_9$	275.01	1	isoprene	3
$C_9H_{22}O_{12}$	384.10	1	limonene	3
$C_{10}H_{15}O_8(HNO_3)$	388.06	1	limonene	3
$C_9H_{22}O_{13}$	400.09	1	limonene	3
$C_{20}H_{24}O_7$	438.14	1	limonene	3
$C_{21}H_{28}O_6$	438.18	1	limonene	3
$C_{22}H_{26}O_6$	448.16	1	limonene	3
$C_{19}H_{30}O_8$	448.18	1	limonene	3
$C_{18}H_{28}O_9$	450.16	1	limonene	3
$C_{22}H_{28}O_6$	450.18	1	limonene	3
$C_{21}H_{26}O_7$	452.16	2	limonene	3
$C_{20}H_{24}O_8$	454.14	2	limonene	3
$C_{19}H_{28}O_9$	462.16	1	limonene	3
$C_{21}H_{26}O_8$	468.15	1	limonene	3
$C_{19}H_{28}O_{10}$	478.16	1	limonene	3
$C_{22}H_{26}O_8$	480.15	1	limonene	3
$C_{18}H_{28}O_{11}$	482.15	1	limonene	3
$C_{20}H_{22}O_{10}$	484.11	1	limonene	3
$C_{21}H_{26}O_9$	484.15	1	limonene	3
$C_{22}H_{30}O_8$	484.18	1	limonene	3
$C_{20}H_{30}O_{10}$	492.17	2	limonene	3
$C_{19}H_{28}O_{11}$	494.15	2	limonene	3
$C_{18}H_{26}O_{12}$	496.13	2	limonene	3
$C_{19}H_{30}O_{11}$	496.17	1	limonene	3
$C_{18}H_{28}O_{12}$	498.15	1	limonene	3
$C_{22}H_{28}O_9$	498.16	1	limonene	3
$C_{20}H_{36}O_{10}$	498.22	2	limonene	3
$C_{20}H_{30}O_{11}$	508.17	2	limonene	3
$C_{20}H_{32}O_{11}$	510.18	1	limonene	3
$C_{19}H_{30}O_1$	512.16	2	limonene	3
$C_{20}H_{30}O_{12}$	524.16	3	limonene	3
$C_{19}H_{28}O_{13}$	526.14	2	limonene	3
$C_{22}H_{26}O_{11}$	528.14	2	limonene	3
$C_{19}H_{30}O_{13}$	528.16	2	limonene	3

Table 4.1. Elemental formulas, *m/z* values, and the number of isomers measured with IMS-TOF. Data were extracted from O_3 and/or OH oxidation of the BVOCs (isoprene, limonene, and α-pinene) in the PAM reactor.

Elemental formulas were previously identified in the literature: 1. [19], 2. [24], 3. [23]. All compounds were detected as clusters with the nitrate ion (NO_3^-). Some compounds previously identified in the abovementioned literature were not observed in these laboratory experiments and are listed as having 0 isomers.

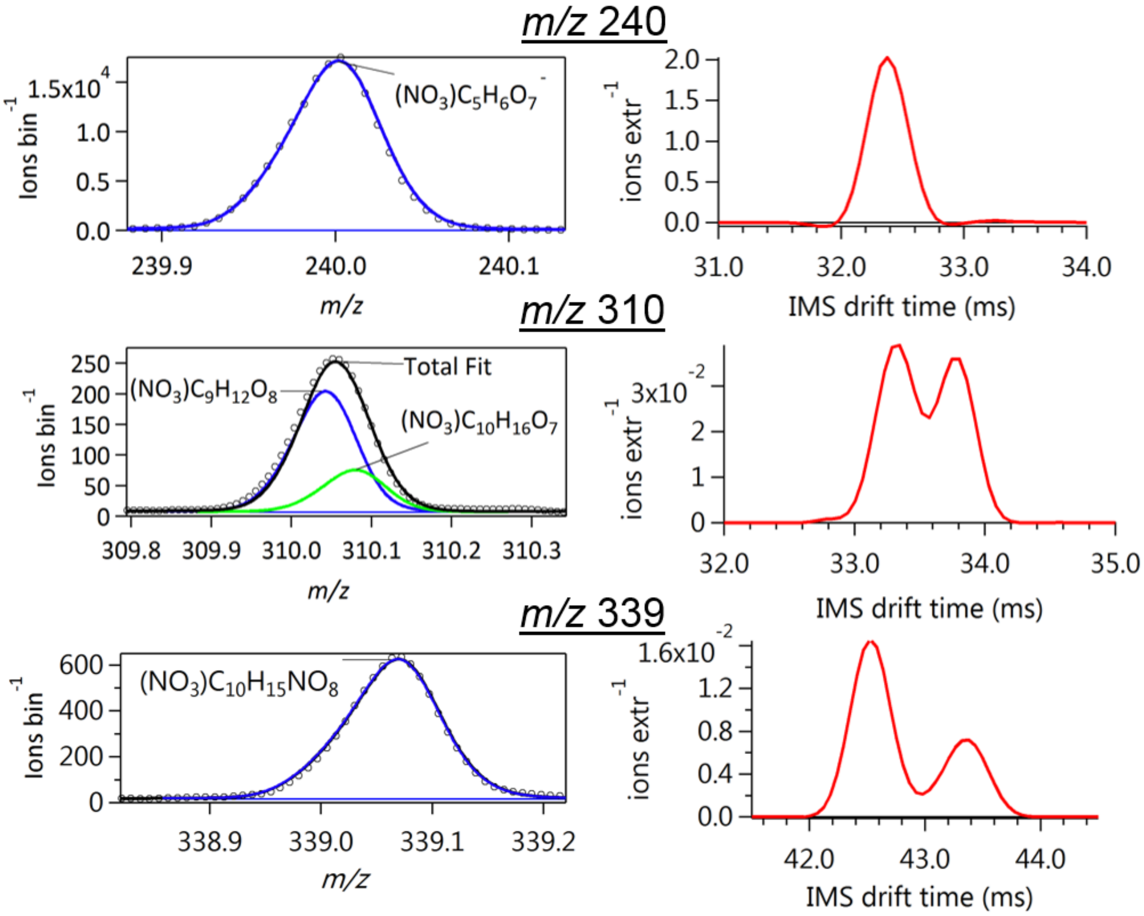

Figure 4.9. High-resolution peak fits for three gas-phase compounds along with the corresponding IM spectrum for each of the displayed mass-to-charge regions. The compounds selected include a single isomer (*m/z* 240), isobaric compounds (*m/z* 310), and isomeric compounds (*m/z* 339). The elemental formulas at *m/z* 240 ($C_5H_6O_7$ clustered with NO_3^-) and *m/z* 310 ($C_9H_{12}O_8$ and $C_{10}H_{16}O_7$ clustered with NO_3^-) were previously identified as α-pinene ozonolysis products.[19] In this work they were extracted from spectra obtained during PAM flow reactor experiments of α-pinene oxidation with O_3 and OH. $C_{10}H_{15}NO_8$ (*m/z* 339 clustered with NO_3^-) was previously identified as a high-NO α-pinene oxidation product.[26] The HR peak fits and IMS data shown for *m/z* 339 are extracted from ambient SOAS data.

As discussed earlier, the custom NO_3^- CI source used in this study has a minor contribution from O_2^- ion chemistry that primarily deprotonates acids, in addition to the dominant NO_3^- ionization scheme. IMS-TOF measurements of commercially available dicarboxylic acids in the laboratory show a distinctly different trend line with a higher drift times per *m/z* than the isoprene/monoterpene trend lines. The BVOC oxidation products show signals that lie along this acid trend line and match the elemental formulas corresponding to many deprotonated acidic, monoterpene oxidation products that were identified in the aerosol phase in previous literature.[181] The acids were detected at uncharacteristically high drift times, but with *m/z* values that corresponded to the $[M\text{-}H]^-$. The higher drift time measured for these small acid anions indicates that they traveled through the drift tube as a weakly bound cluster, likely with the neutral HNO_3 molecules present in the drift tube, and were subsequently declustered in the instrument quadrupoles and detected in the TOF as the $[M\text{-}H]^-$ ion. In fact, weak $[M+NO_3]^-$ cluster signals are observed at the same high drift time for all of the acids in Fig. 4.8. This capability of using the ion mobility drift time correlations to distinguish between clustered and deprotonated molecules can be particularly valuable for analyzing complex CIMS spectra obtained with reagents such as the acetate ion which are known to participate in multiple ionization pathways (i.e. deprotonation and clustering).[182]

4.4.1 Time-resolved measurement of gas-phase isomers

As an additional example of high-resolution MS peak fitting, we provide the mass spectral peak at *m/z* 220 observed during SOAS (see Fig. 4.6). The high-resolution mass spectral peak was completely fit (Fig. 4.10b) with one elemental formula: $C_7H_{10}O_4$ (*m/z* 220.046), clustered with NO_3^-. This elemental formula was identified in previous NO_3^--CIMS literature as a HOM produced from α-pinene ozonolysis.[19] In Figure 4.10c, we provide extracted IM spectra from the identified MS peak at three different points in the time series. The SOAS IMS data for this ion indicates the presence of two isomers. Two IMS peaks were detected with the same drift times on all four dates and times, but with different relative concentrations. The signals of these two isomers is plotted as a function of time for an 8-day period during the SOAS campaign in Fig. 4.10a. The fact that the time series of both compounds are similar suggests that they are both monoterpene oxidation products with sources and sinks that are similar in composition and magnitude. This is consistent with the laboratory measurements of α-pinene oxidation products that also indicate the presence of isomeric constituents at *m/z* 220.

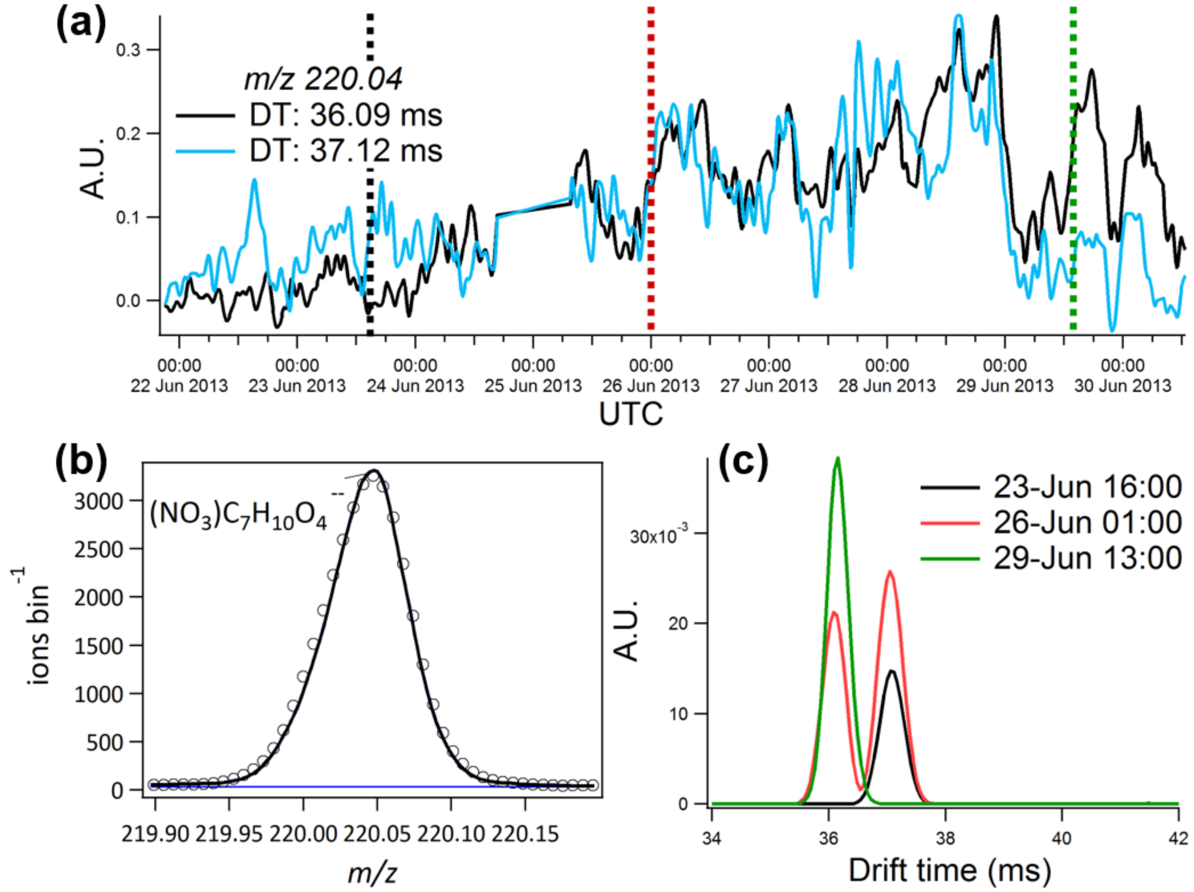

Figure 4.10. (a) is a time series of two isomers observed in ion mobility space in the high resolution (HR) mass spectral fit for the identified HOM [19], $C_7H_{10}O_4$ (detected as a cluster of NO_3^-), produced from α-pinene ozonolysis. The HR peak (b) for this mass is fit by a single $(NO_3)C_7H_{10}O_4^-$ species. (c) shows the ion mobility spectrum for $C_7H_{10}O_4$ at three different points in the time series. IM spectra shown are obtained after post-processing of the raw multiplexed ion mobility data.

Organic molecules with the same elemental formula can have vastly different vapor pressures depending on the chemical functional groups they contain.[24] Thompson et al.,[183] recently utilized the time-resolved IMS-TOF data from SOAS to confirm that the gas-particle partitioning of pinic acid that was measured during SOAS with the Filter Inlet for Gases and AEROsols High-Resolution Chemical Ionization Mass Spectrometer (FIGAERO-CIMS; Lopez-Hilfiker et al., 2014) technique was affected by interference from isomeric species. The IMS-TOF detected two different mobility peaks at the ion corresponding to pinic acid ($C_9H_{10}O_4^-$) with very different relative time trends and concentrations during day and night. The IMS-TOF observations were in agreement with other evidence, such as thermograms, that also suggested the presence of additional isomeric or isobaric compounds with different vapor pressures from pinic acid.

4.4.2 IMS-MS Trend Lines of α-pinene HOMs

Consistent correlations between mass and mobility are visible in 2D plots of complex samples such as Fig. 4.8a. These correlations, also known as "trend lines", describe the increase in collision cross section or decrease in mobility resulting from increasing functionalization of the molecule. As a result, they can be used to resolve structurally similar (similar size/shape) compounds that are otherwise unresolved in a standard the mass spectrum. Previously, trend lines have been used to separate classes of structures as diverse as large biomolecules,[184] metabolites,[141,143,185] lipids,[139] and petroleum constituents.[186]

Figure 4.11 shows an example of trend lines observed in the ambient SOAS 2D NO_3^-IMS-MS spectra of α-pinene HOMs radicals and neutral molecules. Mentel and coworkers (2015) have proposed that stable α-pinene HOMs molecules are formed from α-pinene peroxy radicals by three possible termination steps: formation of a carbonyl group; formation of a hydroxy group; and formation of a hydroperoxy group. Peroxy radicals are key intermediates in the rapid chemical formation of monoterpene HOM.[20,53,177,187] The peroxy radicals identified in this work have elemental formulas $C_{10}H_{15}O_x$, where x = 7 - 10. Some higher-oxygen radicals (O_{11}-O_{15}) were detected in the high-resolution mass spectrum, but had too little signal to extract statistically significant IMS peaks. While only the most intense isomers are shown in Fig. 4.11, multiple isomers are observed for the radicals and the neutral products. The trend lines are drawn for reference between the most intense isomers of each class of species. Termination products for each of the identified peroxy radicals are shown in Fig. 4.11 with arrows denoting their peroxy radical precursors. The hydroxy and hydroperoxy termination products were not separated in the IM spectra, however. We suspect this may be due to less-than-ideal operating ambient operating conditions, or because the two products have such similar CCS that they cannot be separated by this instrument. The most intense carbonyl termination products lie along a line with drift times that are consistently much lower than the radicals. The carbonyl products also lie along a different line than the -OOH/-OH termination products. The elemental formulas for the hydroperoxy and hydroxy termination products overlap for neighboring radicals. For example, the $C_{10}H_{15}O_9$ radical produces a hydroxy termination product with the same elemental formula ($C_{10}H_{16}O_8$) as the hydroperoxy termination product of $C_{10}H_{15}O_8$ peroxy radical. This example illustrates the utility of the IMS-MS 2-D space for readily identifying groups of ions with similar functionalities and/or formation pathways within a complex mass spectrum.

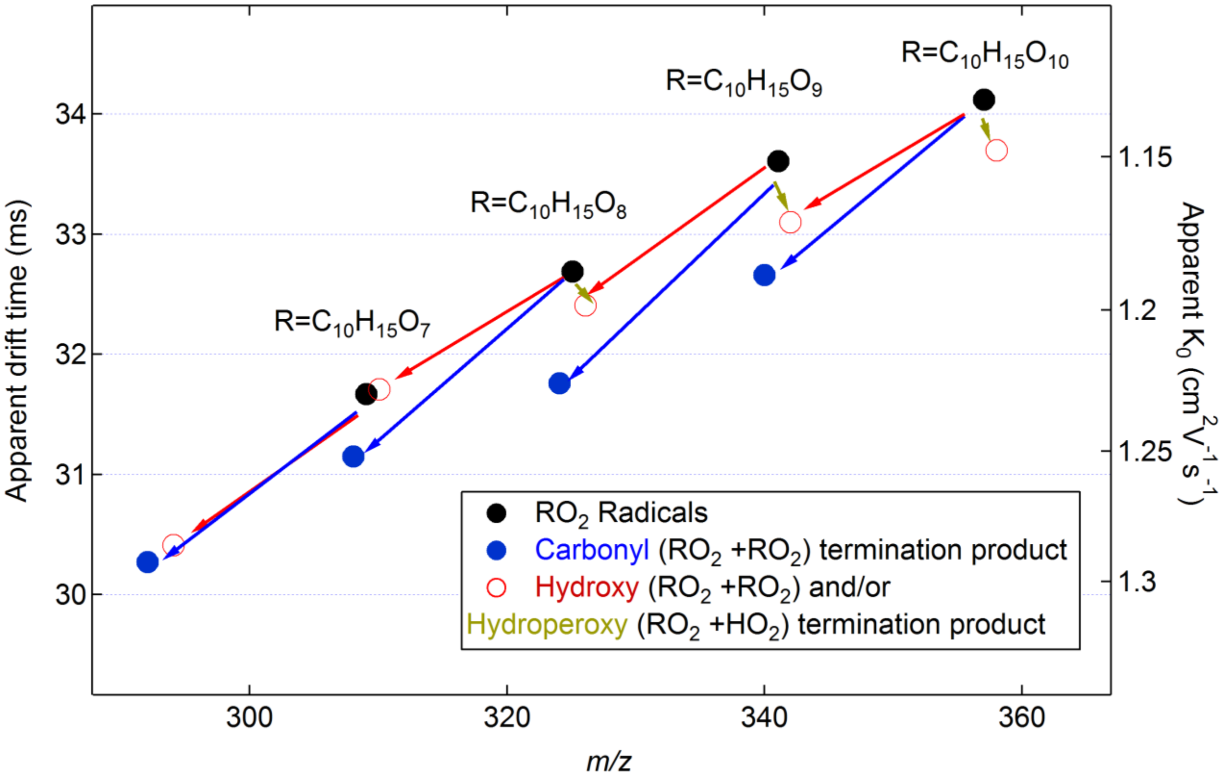

Figure 4.11. 2D IMS-MS plot of select extracted masses from ambient SOAS NO_3-IMS-MS data. Peroxy radicals ($C_{10}H_{15}O_x$, where x = 7 - 10) are presented in 2D space, along with their hydroperoxy (-OOH; $C_{10}H_{16}O_x$), hydroxy (-OH; $C_{10}H_{16}O_{x-1}$), and carbonyl (=O; $C_{10}H_{14}O_{x-1}$) termination products, as identified in [177].

In Fig. 4.11 the relative difference between the reduced mobility trend lines of the peroxy radicals and their hydroxyl/hydroperoxy and carbonyl products changes with degree of oxidation of the peroxy radical. This indicates changes in molecular structure of the peroxy radical and/or product structures with the degree of oxidation. In the α-pinene system, several large changes in structure are expected to take place during oxidation due to the opening of the 4-membered ring as well as potential ring-closure reactions of peroxy radicals.[177,187] A detailed investigation of the structural information that can be extracted from these reduced mobility trends is beyond the scope of this chapter. A forthcoming publication will focus on modeling molecular structures and collisional cross sections of these species.

4.4.3 Investigation of bonding in α-pinene HOM dimers

Previous isotopic substitution (H/D) experiments with NO_3^--CIMS[187] suggest that terpene HOM dimers are formed from covalent peroxy bonds between corresponding monomer units rather than weak intermolecular interactions. Here, we utilize the CID capability of the IMS to investigate the intermolecular bond strength in α-pinene HOM dimers. IMS-CID-MS data was measured for CID voltages ranging from 0 to 20 V. Since the HOM dimers are detected as NO_3^- clusters, this CID experiment allowed for investigating the strength of the monomer-monomer bond relative to the weakly bound dimer-NO_3^- bond. Figure 4.12 shows the average 1-D MS obtained for 20V CID of the HOM dimer. The mass spectrum is averaged only over the drift time region that corresponds to the dimer signals in the 2D IMS-CID-MS. A key result from Fig. 4.12 is that this CID MS only contains nitrate ion (NO_3^-) as the primary ionic fragmentation product. These ions result from fragmentation of the weakly bound cluster between the nitrate ion and the HOMs dimer. The absence of monomer signals in the CID-MS (they would have been found in the blue highlighted region) suggests that the monomer units in the dimer are not weakly bound clusters (i.e. they are bound more strongly, likely with a covalent bond). In the future, this technique can be calibrated for standard molecules and be used in a similar manner to characterize relative chemical bond strengths within gas phase molecules and clusters.

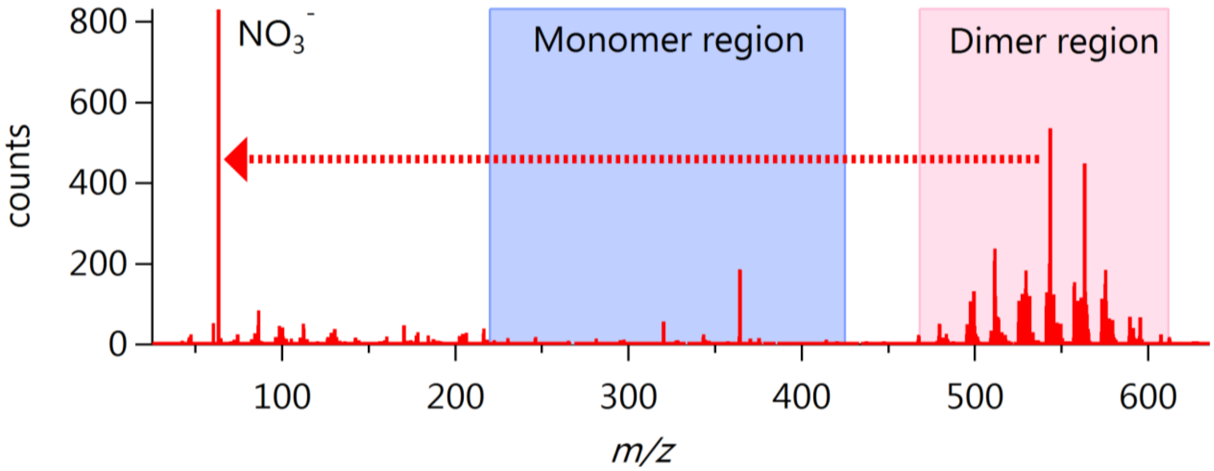

Figure 4.12. A 20V CID-MS of laboratory α-pinene ozonolysis products averaged over the drift time region of the HOMs dimers (52-55 ms) in the 2D IMS-MS plot. Note that these data were acquired under different operating conditions than those in Figure 4.8, leading to slightly different IMS drift times. The appearance of NO_3^--signal in the CID-MS results from fragmentation of the weak bond between NO_3^--and the α-pinene HOMs dimer. The absence of monomer fragments in the CID-MS at this same voltage suggests that the monomer units within the dimers are bonded to each other more strongly (likely via covalent bonding). The large peak in the monomer region is a perfluoroheptanoic acid calibrant (*m/z* 363).

4.5 Conclusions

We apply ion mobility spectrometry-mass spectrometry as a new technique for the analysis of atmospheric gas- and aerosol-phase species. Aerosol-phase data were taken from the offline ESI-IMS-MS analysis of filter samples. Using the filter samples, we demonstrated the capability of this technique to separate water soluble species and structural isomers of species such as trihydroxybutylsulfate that are not readily separated by other techniques such as LC/MS and GC/MS. The use of IMS-CID-MS to obtain spectra that are analogous to conventional MS/MS spectra is demonstrated. The fact that precursor and fragment ions are aligned in 2D IMS-MS plots is used to obtain molecular structure information and to elucidate the monomer building blocks that make up higher molecular weight oligomers observed from experiments involving the reactive uptake of IEPOX onto wet acidic sulfate aerosol.

Online gas-phase IMS-MS data was acquired for laboratory ozonolysis and photooxidation experiments (using isoprene, α-pinene, and limonene precursors) and from ambient measurements during the SOAS 2013 field campaign. The NO_3^- CI source used for these measurements allowed for detection of highly oxidized molecules in the gas phase. The HOMS produced from oxidation of α-pinene, in particular, are investigated in more detail and time-resolved separation of isomeric and isobaric species produced from this system is demonstrated. The 2D IMS-MS space (*m/z* vs. IMS drift time) measured for α-pinene HOMs is used to identify trend lines that separate out reactants and products from different chemical reaction pathways. Moreover, IMS-CID-MS spectra of the HOMS dimers are used to confirm that the monomer units within these molecules are not weakly bound. Taken together, the gas and aerosol IMS-TOF datasets provide valuable chemical information that cannot be obtained from high-resolution mass spectrometry alone. More characterization of compound trend lines in 2D space and theoretical collisional cross section (CCS) calculations is necessary to realize the IMS-TOF's potential as a tool for bulk analysis.

Chapter 5:
Direct measurements of gas-particle partitioning and mass accommodation coefficients in an environmental chamber

5.1 Introduction

Gas/particle partitioning (GPP) is a fundamental physical process describing the interaction between atmospheric organic gases and particles. Originally treated as an adsorptive process,[188,189] most atmospheric models currently treat GPP of organic compounds as an absorptive process.[51,52,190] In this model, semivolatile organic gases condense into and evaporate from particles until quickly reaching a volatility- and available organic aerosol mass-dependent equilibrium.[51,190] Semivolatile equilibrium partitioning is often parameterized using a volatility basis set, which lumps the amount of condensable material in the air in multiple bins spaced typically by a decade of the saturation mass concentration of the compound.[52] GPP has been incorporated into numerous box, regional, and global model[191–195] as a default treatment of organic aerosol formation and evolution.

Still, modeling of GPP by rapid absorptive equilibrium remains controversial. There are now several real-time analysis techniques capable of measuring GPP of trace organic compounds at relatively high time resolution in the field.[28,134,196,197] Many of these measurements have shown substantial disagreements with theory and one another, however.[198,199] Some recent works have even suggested that GPP is not valid under certain conditions due to strong kinetic limitations, and more detailed treatments are required to match atmospheric observations.[200–204]

GPP is expected to have a large influence on secondary organic aerosol (SOA) mass concentrations predicted by atmospheric models. Most models use parameterizations of the SOA yield, i.e. the mass of SOA formed per unit mass of volatile organic compound (VOC) precursor reacted.[205] Almost all experiments quantifying SOA mass yields that have been used in models were performed in Teflon-walled environmental chambers.[49,205–208] However, it has recently been reported that Teflon chambers suffer from losses of semivolatile gaseous compounds to chamber walls.[79,94,209,210] Wall losses can have strong effects on aerosol mass yields,[79] and could also affect conclusions about chemical composition and processes gleaned from chamber experiments. The question even arises: if wall losses are substantial for a certain range of compounds, and fast enough to be on similar time scales as the approach to equilibrium GPP, is it possible to observe and accurately characterize GPP in environmental chambers?

In mathematical representations of the kinetics of GPP, the mass accommodation coefficient (α; also known as the sticking coefficient; and equal to the evaporation coefficient at equilibrium) is a critical parameter that defines the fraction of gas/particle collisions that result in a colliding species being taken up by a particle. α for organic species was historically assumed to be 1, mostly from liquid evaporation measurements.[211–213] More recent measurements of mass accommodation coefficients for aerosol-phase compounds[214–216] range across two orders of magnitude and do not resolve this question. A very wide range of values (as low as 0.001) has been used in models and data fitting, sometimes as a tuning parameter which might obscure other model structural limitations.[79,217–220]

Given the discrepancies that persist between ambient SOA measurements and models,[8,9] the substantial fraction of organic material in the atmosphere which is thought to be semivolatile,[25] and the difficulty of quantifying GPP in field studies,[199] it is important to closely examine the validity of GPP theory under as simple experimental conditions as possible. It is also important to further evaluate the impact that losses of vapors to Teflon chamber walls may have in SOA yield measurements. Herein, we conduct fundamental gas/particle partitioning experiments in an environmental chamber. A well-characterized simple chemical system is used to produce low-volatility organic compounds very rapidly, which are taken up by liquid organic seed particles and/or the Teflon chamber walls. Both gas-phase products and total aerosol volume and surface area concentrations are continuously monitored. A simple but comprehensive box model is used to quantify $c^*$and α. We discuss the implications for quantifying gas/particle partitioning under more complex conditions.

5.2 Materials and Methods

5.2.1 Environmental chamber experiments

A schematic outlining the chamber and instruments used in this work is shown in Figure 5.1. We conducted all of our experiments in the one of the two chambers in the CU Environmental Chamber (CUEC) Facility. The CUEC bag was constructed of FEP Teflon with a maximum volume of 20 m^3. The enclosure temperature was maintained at 26 ± 1° C for all experiments. The chambers were filled with clean, dry (< 1% RH) air from two AADCO Model 737-15 clean air generators (Cleaves, OH, USA). The chambers were equipped with an automated flushing system that alternately evacuated and refilled the bag when it was not in use (~5% of full volume every 5 minutes), while maintaining the bag volume at ~95% of maximum volume using differential pressure between the bag and climate-controlled enclosure. Running the automated flushing sequence overnight before each experiment ensured that each experiment started with aerosol concentrations of 0 particles cm^{-3} as measured with an ultrafine condensation particle counter

(UCPC, TSI model 3776 with a diameter cutoff of 2.5 nm).

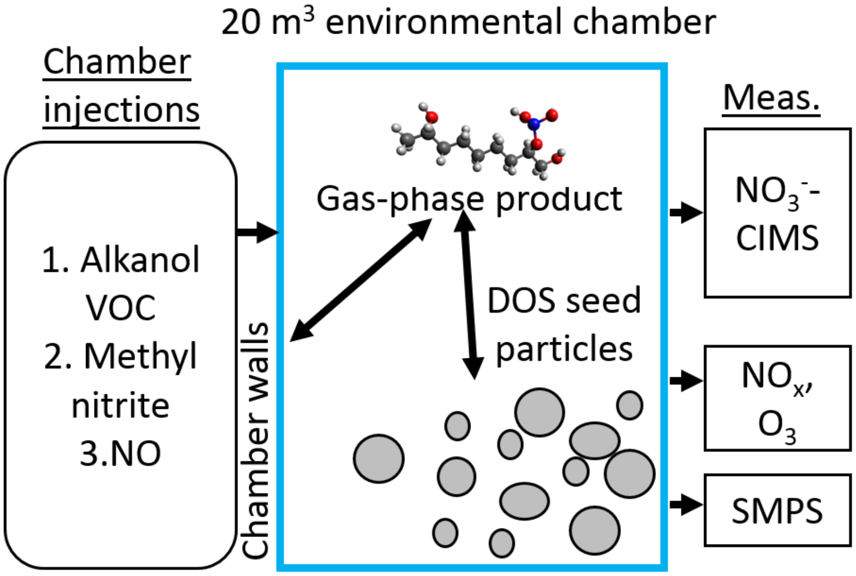

Figure 5.1 A schematic of the chamber experiment setup used in this study.

The experimental procedure is similar to the one detailed in Krechmer et al.[209] to measure vapor wall losses to Teflon walls, but with the addition of seed aerosol. First, we injected dioctyl sebacate (DOS; >97%; Sigma-Aldrich; $c^* < 0.1$ μg m^{-3} [91]) liquid seed aerosol into the chamber using a custom-built evaporation-condensation generator.[221] We then diluted the chamber with clean air until the DOS seed surface area reached a desired level. The evaporation-condensation generator was tuned to produce aerosol with a lognormal surface area distribution centered at 200 nm. A scanning mobility particle sizer (SMPS) comprised of a TSI model 3080 electrostatic classifier and model 3775 condensation particle counter monitored aerosol volume, surface area, and number concentration. We provide a summary of different experiments and seed concentrations in Table 5.1.

Exp. Number	**Seed**	**CS s^{-1}**	**~ Start Conc. $\mu g\ m^{-3}$**	**S.A. $\mu m^2\ cm^{-3}$**
1	DOS	0.0042	2.9	130
2	DOS	0.0060	4.5	180
3	DOS	0.0087	5.8	210
4	DOS	0.013	11	400
5	DOS	0.016	13	500
6	DOS	0.031	23	900
7	DOS	0.11	80	3100
8	DOS	0.16	120	4600
9	DOS	0.15	140	4800

Table 5.1. A list of the experiments with initial DOS seed surface area, concentration, and calculated condensation sink rates (assuming α=1).

After the seed aerosol concentration stabilized, we injected 50 µL of 1-hexanol, 40 µL of 1-octanol, 25 µL of 1-nonanol, 18 µL of 1-decanol, and 12 µL of 1-dodecanol (all >99% purity; Sigma-Aldrich) into the chamber by gently heating the liquids into a clean nitrogen stream (UHP liquid nitrogen evaporate) flowing into the chamber. This resulted in a total VOC concentration in the chamber of 1.4 ppm. We then turned on a Teflon-coated fan inside the bag for 1 min to mix the contents. Finally, we injected 4 ppm of NO (99%, Matheson Tri-gas) and 4 ppm of methyl nitrite ($MeNO_2$, synthesized via[114]) into the chamber as pure gases using a small glass bulb and mixed the contents again for 1 min.

To initiate chemical production, we turned on the chamber UV black lights (~300-400 nm) at 100% intensity ($J_{NO2} = 7.7 \times 10^{-3}\ s^{-1}$) for precisely 10 s via computer-control. $MeNO_2$ formed OH radicals, which then oxidized the alkanols forming several oxidized products,[209] including hydroxynitrates (HN), dihydroxynitrates (DHN), trihydroxynitrates (THN), and carbonyl dihydroxynitrates (CDHN). A list of the compounds, along with their exact masses and estimated saturation concentrations (c^*) is provided in Table 5.2. We were able to continuously monitor the latter three types of products with a chemical ionization mass spectrometer (CIMS). This "rapid burst" method, developed previously,[209] is critical to these experiments because it produces compounds over a wide range of volatiles over the entire volume of the chamber much faster than the vapors can equilibrate with the particles and walls. After each burst, the system was left to come to equilibrium for either 1 or 1.5 hr.

Compound Class	**Formula**	**MW**	**NO_3^- MW**	**Precursor**	**SIMPOL c^* ($\mu g\ m^{-3}$)**
CDHN	$C_6H_{11}NO_6$	193	255	Hexanol	3.34E+01
CDHN	$C_8H_{15}NO_6$	221	283	Octanol	5.05E+00
CDHN	$C_9H_{17}NO_6$	235	297	Nonanol	1.95E+00
CDHN	$C_{10}H_{19}NO_6$	249	311	Decanol	7.50E-01
CDHN	$C_{12}H_{23}NO_6$	277	339	Dodecanol	1.10E-01
DHN	$C_6H_{13}NO_5$	179	241	Hexanol	2.46E+02
DHN	$C_8H_{17}NO_5$	207	269	Octanol	3.76E+01
DHN	$C_9H_{19}NO_5$	221	283	Nonanol	1.46E+01
DHN	$C_{10}H_{21}NO_5$	235	297	Decanol	5.57E+00
DHN	$C_{12}H_{25}NO_5$	263	325	Dodecanol	8.29E-01
THN	$C_8H_{17}NO_6$	223	285	Octanol	2.55E-01
THN	$C_9H_{19}NO_6$	237	299	Nonanol	9.85E-02
THN	$C_{10}H_{21}NO_6$	251	313	Decanol	3.79E-02
THN	$C_{12}H_{25}NO_6$	279	341	Dodecanol	5.55E-03

Table 5. 2. The gas-phase alkanol oxidation products measured in this study. Products are grouped by compound and classified as the following: CDHN=dihydroxycarbonylnitrate, DHN=dihydroxynitrate, THN=trihydroxynitrate, and HN=hydroxynitrate.

The amount of aerosol produced by each photooxidation burst comprised an average of 7% of the total aerosol volume in the chamber (Figure 5.2). Therefore, the system can be modeled assuming that the gas-phase compounds are partitioning into pure DOS particles and not into a product compound mixture. The specific molecules studied here are estimated to form ~ 20 ppt and account for < ~5% of the SOA. The majority of the aerosol formed is likely to be semivolatile hydroxynitrates, which are not detectable by the nitrate CIMS.[209]

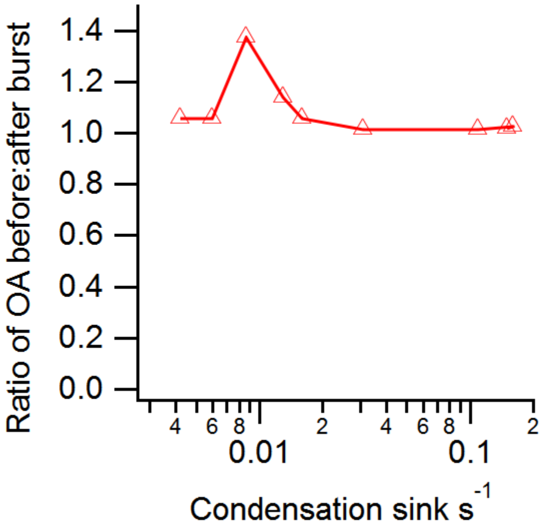

Figure 5. 2. The ratio of the amount of OA before and after each burst, showing that only a small amount of aerosol is produced relative to the amount of seed. A line is provided at 1 for guidance. Removing the outlier does not alter results for α or model-derived c^*.

5.2.2 NO_3-CIMS

A chemical ionization time-of-flight mass spectrometer equipped with a nitrate ion ionization source (NO_3-CIMS) monitored gas-phase product concentrations. The instrument[16,22] and nitrate source[58] have been described extensively in previous works. We used the instrument in a configuration similar to the one in Krechmer et al.[209] Notably here, we placed the instrument inside the CUEC enclosure directly adjacent to the reactor bag. This allowed us to use a 0.6 m long electropolished stainless steel inlet to isothermally bring 10 standard L min^{-1} (defined as 25° C, 1 Atm) of sample air directly from the bag to the instrument without dilution. The short inlet with a sub-sampled center flow minimizes wall losses and results in a residence time of sampled air in the instrument inlet and source of < 4 s. The NO_3-CIMS acquired spectra at 1 Hz. We then processed instrument data using Tofware (Tofwerk, AG and Aerodyne, version 2.5.8) toolkit within IGOR Pro 6 (Wavemetrics, Inc.) at the same time resolution. The NO_3-CIMS detected gaseous product molecules as clusters with the nitrate ion, but the NO_3^- prefix has been removed from reported formulas throughout this paper for clarity. An example mass spectrum of some of the product compounds is provided in Figure 5.3.

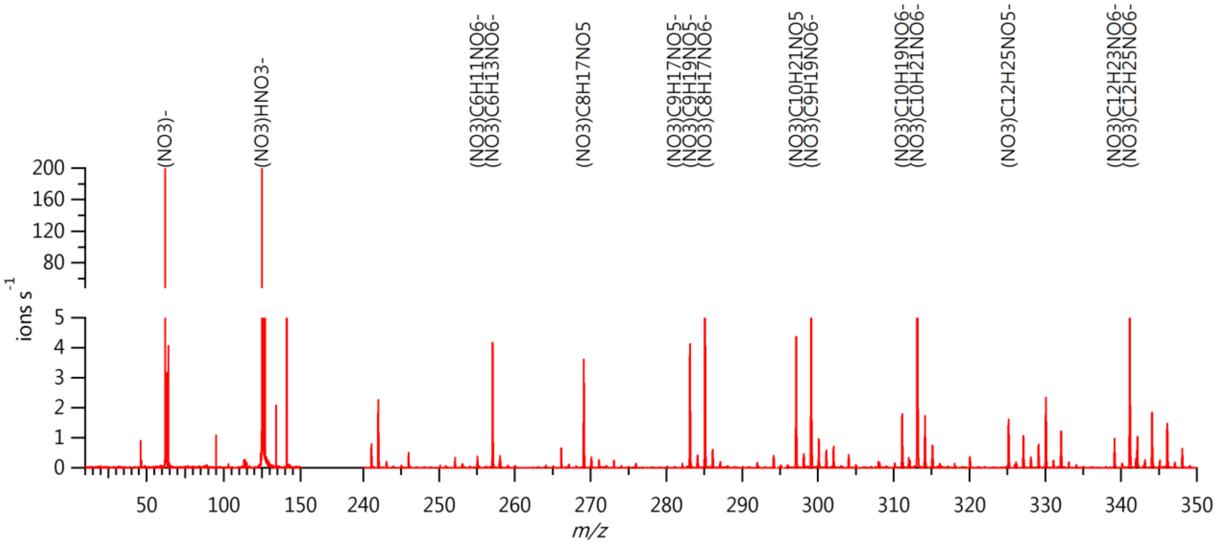

Figure 5.3 A NO3-CIMS mass spectrum averaged over a 5-minute period at the peak of one of the bursts. The axes have been split to show both the reagent ions and the smaller-signal oxidized products

5.2.3 Box model

A chemical kinetic box model was used to simulate the behavior of gas- and aerosol-phase compounds, accounting for partitioning and evaporation of each oxidized products to walls and particles. A schematic of the model is shown in Figure 5.4. The model was solved using KinSim v3.24 within IGOR Pro[222].

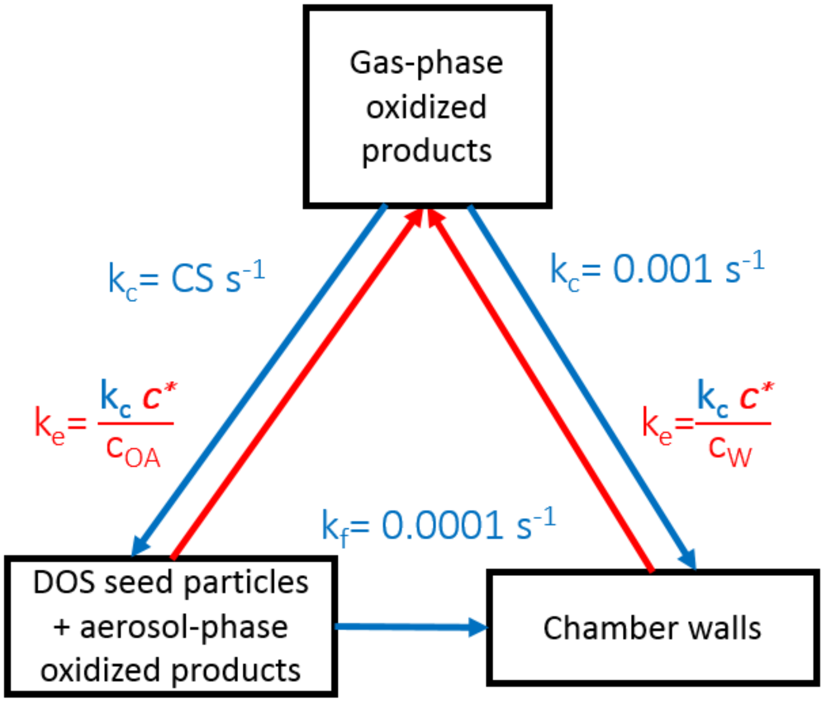

Figure 5.4. A schematic diagram of the kinetic box model used in this work. All rate constants are first order and in units of s-1.

The vapor wall loss rate, or condensation rate k_c was determined using the procedure of Krechmer et al.,[209]\ the results of which are shown in Figure 5.5. Repeated measurements resulted in an average rate of 9.5 × 10^{-4} ± 1 × 10^{-4} s^{-1} ($\tau_{GW\,\mathrm{E}}$= 1060 ± 60 s) for the 20 m^3 CUEC bag at 27° C. The evaporation rate of gases from the walls (k_e) was determined using partitioning theory, since the forward rate and the equilibrium constant are known. k_e depends on the measured condensation rate, the saturation concentration of the gaseous compound (c^*), and the equivalent wall mass concentration:[94]

$$k_e = \frac{k_c C^*}{C_w} \qquad [5.1]$$

The value of the equivalent wall concentration was taken from the parameterization in Krechmer et al.[209]

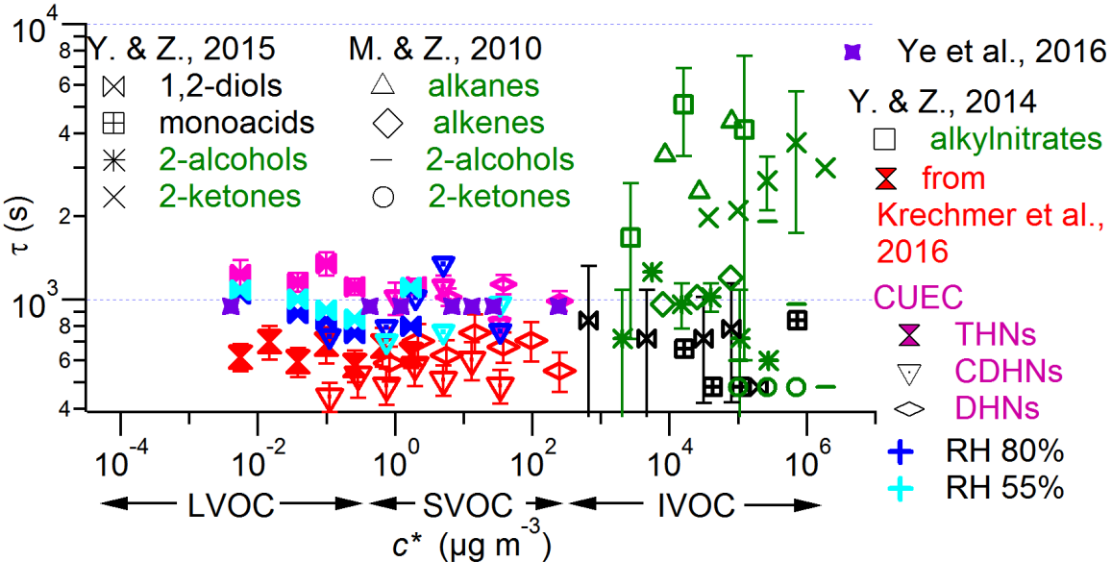

Figure 5.5. Wall loss rates for the 20 m3 chamber, shown with previously reported measurements from Matsunaga and Ziemann,[94] Yeh and Ziemann,[108] Krechmer et al.,[209] and Ye et al.[210] The CUEC values are the ones determined for this work. Select experiments were conducted to evaluate the effect of humidity on vapor-phase wall loss rates. No systematic effect of humidity was detected.

The aerosol onto which gases can condense is represented by the suspended particle condensation sink (CS). The CS can be calculated using the following formula:[78,213]

$$CS = \int_0^{\infty} r \cdot F_{FS}(r) \cdot N(r) \cdot dr \qquad [5.2]$$

in which r is the particle radius, $N(r)$ is the particle number size distribution, and $F_{FS}(r)$ is the Fuchs-Sutugin correction for gas-phase diffusion in the transition regime:[78,213]

$$F_{FS} = \frac{K_n+1}{0.377K_n+1+\frac{4}{3}\alpha^{-1}{K_n}^2+\frac{4}{3}\alpha^{-1}K_n} \qquad [5.3]$$

where Kn is the Knudsen number and α is the mass accommodation coefficient. Using the CS, we can calculate the lifetime for gaseous condensation:[78,118,213]

$$\tau_{cond} = \frac{1}{4\pi \cdot D \cdot CS} \qquad [5.4]$$

where D, the molecular diffusion coefficient, was estimated to be 7×10^{-6} m^2 s^{-2} [223]. The rate (k_c) of gases condensing on particles is the inverse of the time scale, τ_{cond}.

Mass accommodation coefficients exist for uptake of gaseous compounds to both the chamber walls and particles. This work will deal exclusively with α to particles, however, as values of α_{wall} cannot be quantified by our procedures above values of 6×10^{-6},[80,209] which is the case here.

We calculated the evaporation rate of gas-phase products from the aerosol in the same manner as for the walls, but with the SMPS-measured aerosol organic mass concentration (C_{OA}) in the denominator in place of the equivalent wall concentration (C_W).

We estimated the mass accommodation coefficient (α) and the compound saturation concentration (c^*) from a model fit to experimental data by treating the system as a nonlinear regression problem. The optimization was based on minimizing the sum of the squares of the residuals (χ^2) between the gas-phase model and observation time series. This optimization was performed using the FuncFit built-in function in Igor Pro 7, which uses the Levenberg-Marquardt method. The uncertainties in the fitted model parameters were evaluated using the statistics of nonlinear regression[224] and expressed as 2σ confidence intervals.

5.3 Results and Discussion

5.3.1 Dependence on seed surface-area

Figure 5.6 shows examples of the time evolution of gas-phase products for a range of initial DOS seed aerosol concentrations. When there was no seed aerosol in the chamber, the gas-phase compounds were lost to the walls of the chamber with an e-folding lifetime of ~1000 s. Low-volatility compounds such as $C_{12}H_{25}NO_6$ and $C_{10}H_{21}NO_6$ (both trihydroxynitrates) decreased at an increasingly rapid rate with increasing DOS surface areas. Even a relatively small aerosol surface area increased the CS enough relative to the wall loss rate ($0.001\ s^{-1}$) to strongly increase the vapor loss rate. A surface area of 180 $\mu m^2\ cm^{-3}$ corresponded to a CS of $0.006\ s^{-1}$, or a factor of 6 larger than the wall loss rate. At larger seed surface areas, such as the experiment conducted at an aerosol surface area of 900 µm^2 cm^{-3}, the CS (0.03 s^{-1}) was thirty times larger than the wall loss rate and dominated the vapor sink.

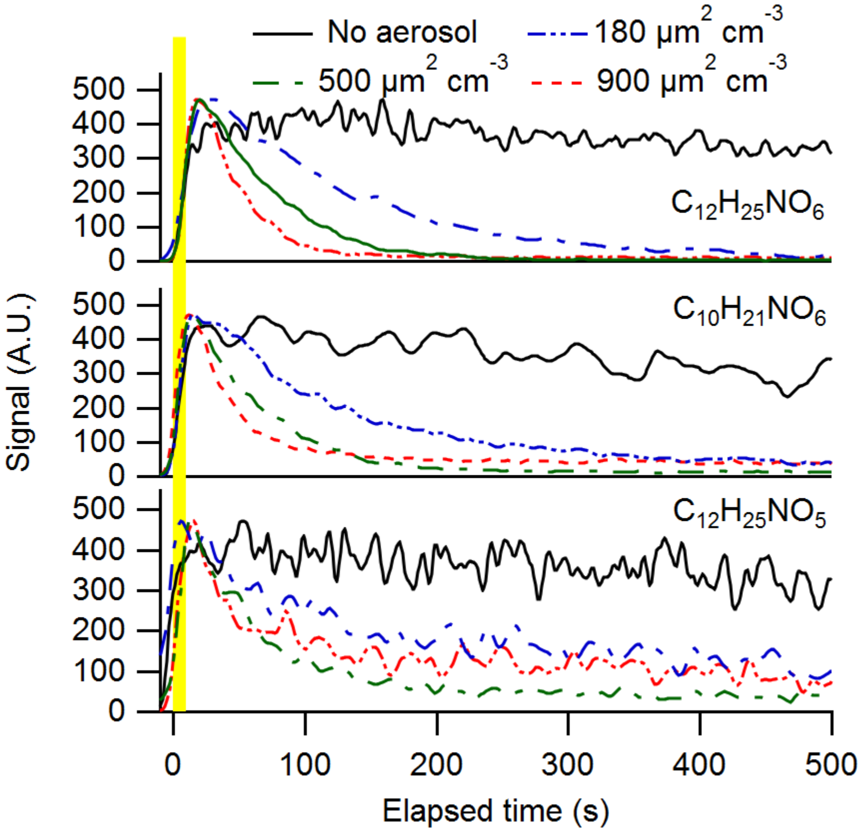

Figure 5.6. NO_3-CIMS time series depicting gas-phase loss kinetics. Low-volatility compounds (middle and top) such as the $C_{12}H_{25}NO_6$ and $C_{10}H_{21}NO_6$ trihydroxynitrates (THN) condense at increasingly rapid rates with higher aerosol surface areas. Compounds were detected as clusters with the NO3- ion, which has been removed for clarity here. All traces have been binomially smoothed across 10 (1s) points for visual clarity and scaled to the maximum for comparison.

The seed surface area dependence observed here is qualitatively consistent with that reported by Zhang et al.,[79] who measured the SOA formed from toluene oxidation at different seed surface areas. The strong dependence of the compound decay rate on aerosol surface area indicates that it should be possible to separate vapor uptake to the walls vs. particles.

To that end, Figure 5.6 provides clear evidence that SOA experiments conducted with large amounts of absorbing seed aerosol should not suffer from low biases in yields due to vapor-phase wall losses to the same extent as experiments conducted under lower concentrations. In experiments with large seed concentrations, a major fraction of the low and semi-volatile vapor mass will be rapidly taken up by the particle-phase, rather than the walls. At longer experimental times, however, the walls will continue to take up semivolatile compounds that are approximately in equilibrium with the particles due to the large equivalent wall mass concentrations, C_w,[94]. Eventually the continuous vapor-phase uptake by the walls will denude the particles.[210]

5.3.2 Kinetic box model results

In experiments with seed aerosol, two sinks acted on the vapors in parallel: loss to the walls and loss to the aerosol. In addition, the vapors also had two additional sources from volatility-dependent evaporation from the walls and particles.

First, we quantified the e-folding equilibrium timescale of the combined loss processes by fitting the measured compound time series to an exponential decay equation:

$$C(t) = y_E + (y_0 - y_E)\, exp(-\frac{t-t_0}{\tau_{GE}}) \qquad [5.5]$$

in which t_0 is the time of the peak in the compound concentration (immediately after the 10 s formation burst), y_0 is peak value of $C(t)$, where $C(t)$ is the concentration as a function of time, y_E is an offset concentration that is established at the final or equilibrium concentration, and τ_{GE} is the timescale of the gas' approach to total equilibrium.

We then used a box model (see methods) to reproduce the behavior of the decaying time series. Generally, two degrees of freedom can be constrained by this method as there are two unique pieces of information in the experimental trace: the initial rate of decay, and the ending equilibrium concentration. Kinetics (i.e. accommodation coefficient, α) are especially constrained by the initial rate of decay, while the system thermodynamics (c^*) are constrained by the equilibrium concentration.

The values of c^* produced by the model may not represent the actual vapor pressure of the molecule, however. First, an activity coefficient for each compound in a DOS-dominated matrix may apply. Second, there could be a systematic error in the derived $c*$ because the fitting model uses the C_w parameterization in Krechmer et al.,[209] which was derived based on c^* estimates from SIMPOL.[91] In Figure 5.7 we have plotted the model-derived c^* against SIMPOL-derived c^* for the compounds used in this study. Figure 5.7 shows that c^* determined by both methods evolve similar with carbon number, and are within the estimated uncertainty of SIMPOL[75] for species with 2 hydroxyl groups. However, $c*$ from our model are systematically higher than SIMPOL estimates for compounds with 3 hydroxyl groups. This could be due to intramolecular hydrogen bonding of those compounds leading to higher $c*$ than expected from the simple group contribution method in SIMPOL.[225] It is also possible that those more polar species have a higher activity coefficient in the relatively nonpolar DOS matrix, although a difference of 1.5 orders-of-magnitude on the activity coefficient upon addition of a functional group would be unexpected. In addition, the c^* values reported in this work have an implicit dependence on the C_w parameterization in Krechmer et al.[209] from which they cannot be separated. In the rest of this work we make it clear in the text if we are referring to a SIMPOL-derived c^* value or a model-derived c^* value. Future studies should target the direct quantification c^* values for low volatility compounds, which would enable more accurate quantification of $c*$ and C_w for multifunctional compounds, and thus smaller uncertainties in applying our results to atmospheric systems.

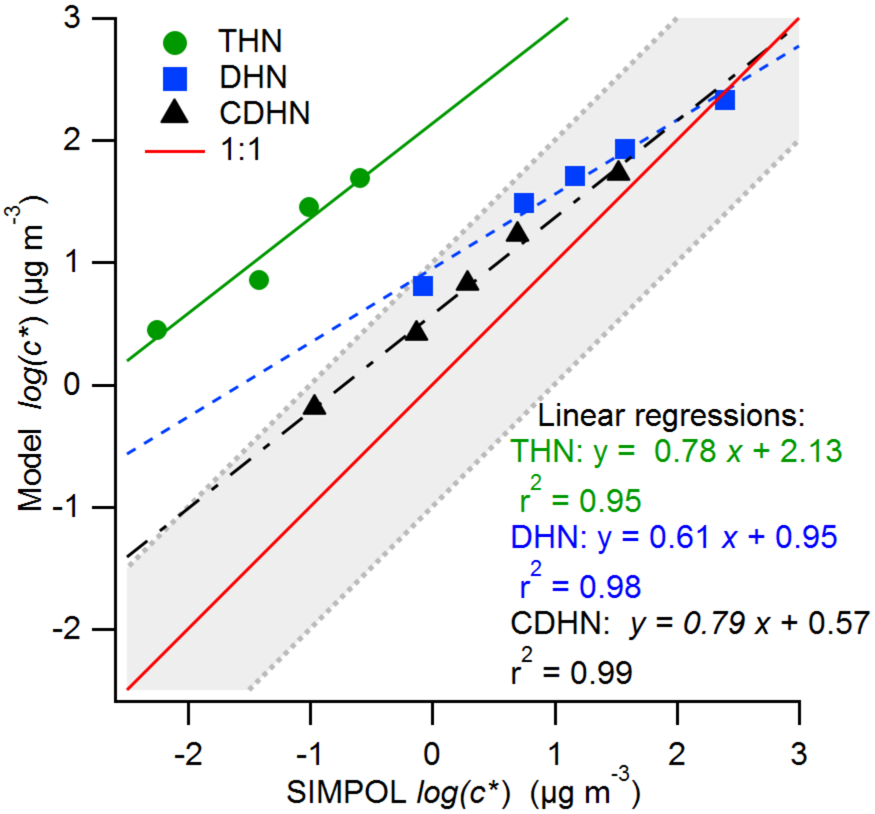

Figure 5. 7. Model-fitting determined saturation concentrations (c^*) as a function of SIMPOL-estimated c^* values for the compounds in this study. The gray area represents the estimated uncertainty of SIMPOL of +/- 1 order of magnitude.[75] c^* values derived from both methods decrease linearly as carbon number increases, but with different lines for different functionality types (THN: trihydroxynitrate; DHN: dihydroxynitrate: CDHN: carbonyldihydroxynitrate). Model-determined c^* values are systematically higher than SIMPOL-determined ones. The discrepancy increases at lower volatilities.

Figure 5.8 provides an example of how the model was used to quantify α and c^* for an example compounds. The equilibrium concentration is dependent on the value of c^*, while the initial loss rate is dependent on α. The C_{12} CDHN declined rapidly in the first few minutes of the experiment. Two model runs, in which α = 1, matched the decrease very closely, despite having very different c^*values. The model runs with α = 0.1 and 0.01 declined far too slowly, supporting that the value of α is well constrained close to ~1. Model traces with c^*= 0.26 would eventually arrive at the same equilibrium value at the end of the experiment, but do not in the time displayed due to the lower α values of 0.1 and 0.01.

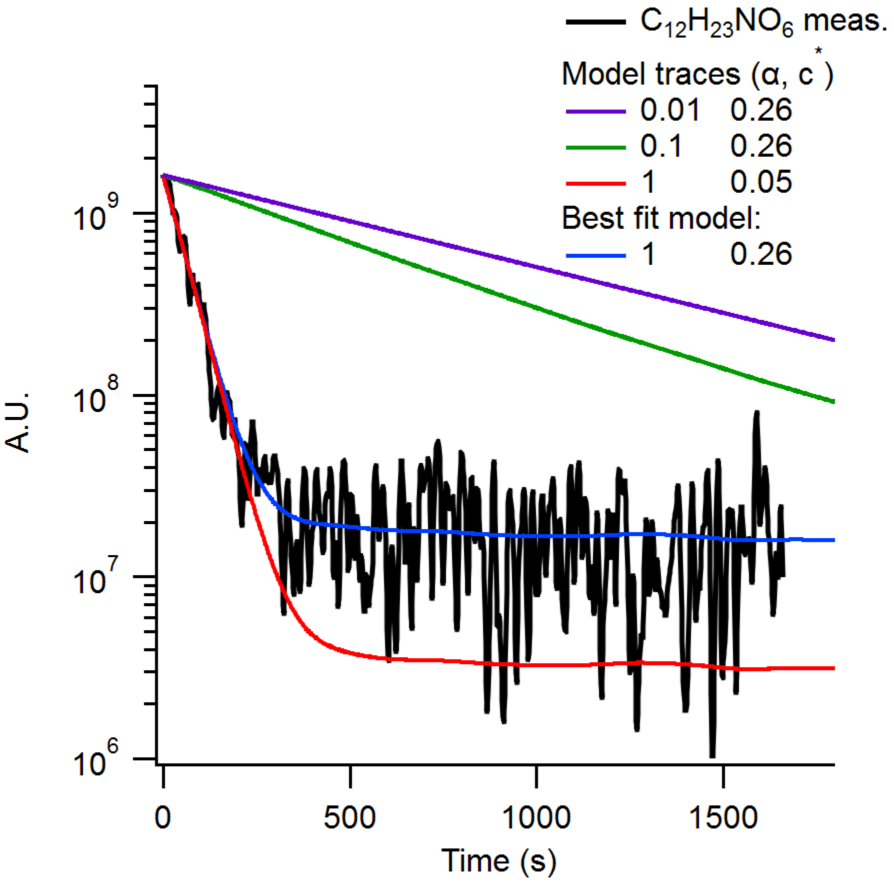

Figure 5.8. Example measurement trace for one compound, together with the best fit from the model and several model traces with alternative α and c* parameters. The latter are shown to qualitatively illustrate the ability of the model to constrain these parameters. Measurement traces were binomially smoothed across 10 points.

5.3.3 Inferring the value of α

Figure 5.9 shows all the decay timescales extracted from fits to measurements for experiments with different CS values. Each point represents the decay timescale of one compound during one experiment and is colored according to *c** from SIMPOL.[91] Also shown are predicted timescale values, generated by running the kinetic box model for different values for α and the CS, and fitting the model output gas-phase time series with an exponential fit.

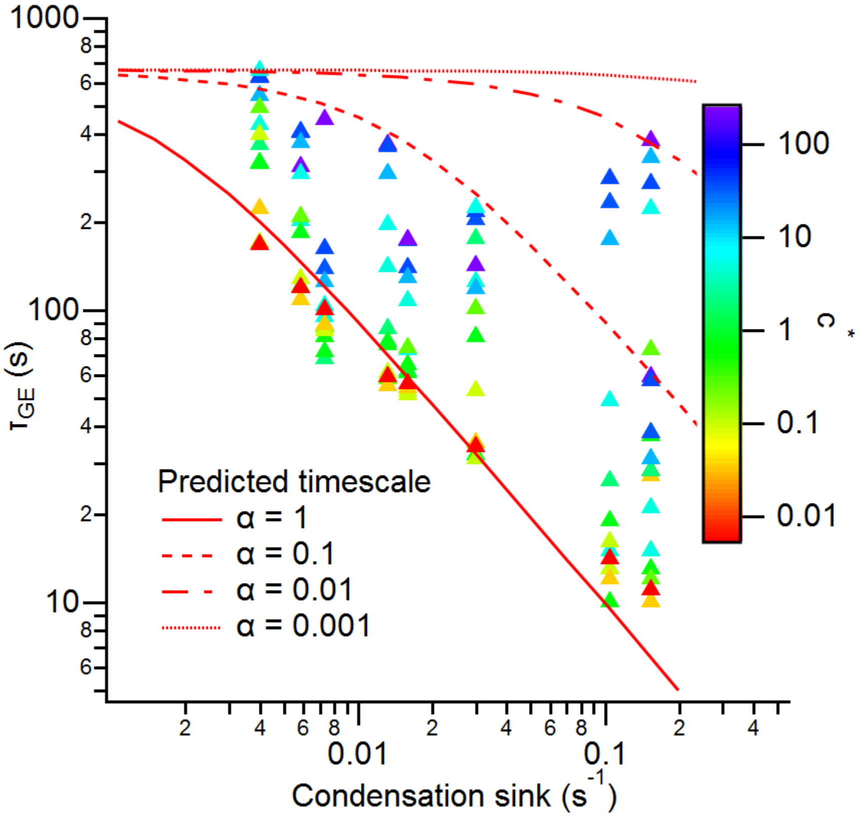

Figure 5.9. Measurement-derived equilibrium time scales (τGE, datapoints) for each gas phase compound at different seed aerosol CS values. The predicted time scales were determined by running the box model for different values of α and with varying amounts of organic seed aerosol. Compounds are colored according to SIMPOL-estimated c*.

The lowest volatility compounds (generally THNs and CDHNs) lie along the modeled line corresponding to α = 1, while no measured decays have substantially faster timescales than the model prediction. This agreement suggests that the model captures the key processes controlling the timescales for these compounds. The compounds that lie above the α = 1 line are consistent with the model if values of α < 1 are used (dashed lines).

We then run the model using the fitting algorithm to determine the values of α and c^* that best fit the measured trace. In Figure 5.10, α values from this work are presented as averages for each compound across all different seed experiments along with previously reported literature values for liquid organic particles. The literature values included are split into two categories:

older measurements of bulk organic liquid compounds,[211,226,227] and more recent studies that attempt to quantify α for aerosol particles.[214–216,223] The values from this work for liquid particles average 0.7. The error bars shown describe the standard error of the mean of the set of measurements from different seeded experiments. The literature aerosol data, if averaged, are similar to our results over the range of overlap. Values of α for the lowest volatility compounds are better constrained than for the semivolatile compounds. α as a function of carbon number is also shown as an alternate parameterization in Figure 5.11.

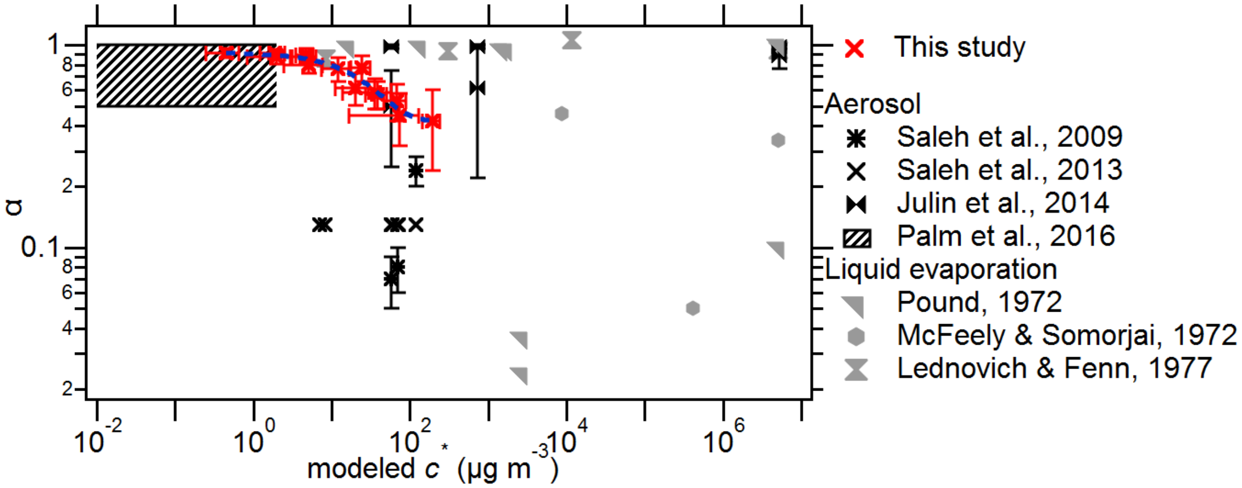

Figure 5.10. Mass accommodation coefficients determined by this study along with literature values for liquid organics as a function of model-determined c^*. The points from this study are the average for each compound across multiple experiments. Error bars from this work represent the standard error of the mean for all experiments for each compound. Error bars in historical works are as reported. Literature values are from [211,214–216,223,226,227]. The data have been fit with an exponential of the form: $\alpha = 0.42 + 0.49e^{-0.03c^*}$

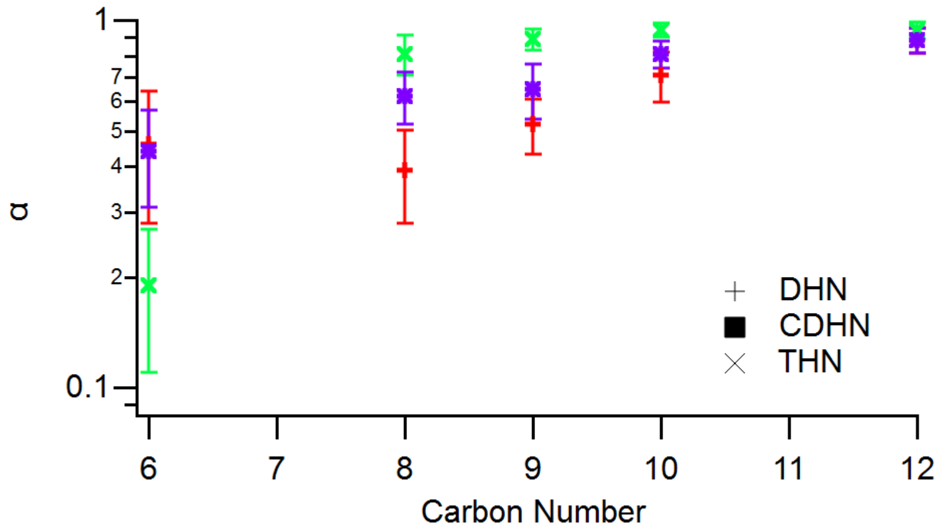

Figure 5. 11. Average values of α as a function of the number or elemental carbon atoms per molecule. This provides an alternative, carbon number-based view of the α results.

A dependence of α on volatility is observed, with α decreasing at higher volatility. This relationship was not previously apparent in any one study, nor the ensemble of available literature reports. No very low values (e.g. 0.001), that have been invoked in literature fitting exercises,[79,217,218,220] are observed for any of the compounds in this study. Due to the reasons discussed above regarding the linkage between c^* and C_w, the parameterization provided in the caption should be calculated in models using SIMPOL-derived c^* values, even if other estimation methods are used for other purposes within the model.

We focus next on the uncertainties on these results. Experiments with different initial CS show little variation in α, but some variation in c^* of about x10 (Fig. 5.12-13). Experiments with very low CS have more uncertainty due to potential variations of the wall loss timescale (due to random variations on chamber turbulence and mixing[209]), while experiments with very high CS have higher uncertainty because condensation is so fast that it already proceeds to a significant extent while the UV lights are on, and when there could be some inhomogeneity in the chamber due to spatial variation in the UV light field. However, no significant difference on the averaged results is observed if we exclude experiments with the highest and lowest CS (Figure 5.14). We performed several sensitivity studies to investigate the impact of the assumed C_w on the retrieved parameters (Figure 5.15-5.19), which show little impact for low-volatility species. Higher volatility compounds have a noticeable effect for large changes in C_w, but without impacting our conclusions.

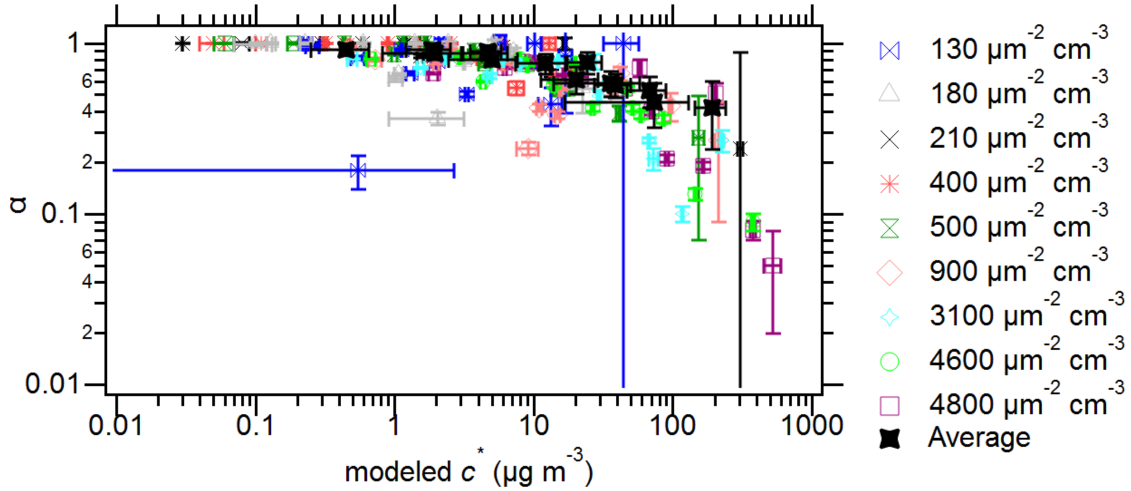

Figure 5. 12. Values of α determined for each compound for each individual DOS seed surface area experiment. Also shown are arithmetic means for each compound across the entire set of different seeded experiments. Error bars shown represent are fitting uncertainties as two standard deviations (2σ).

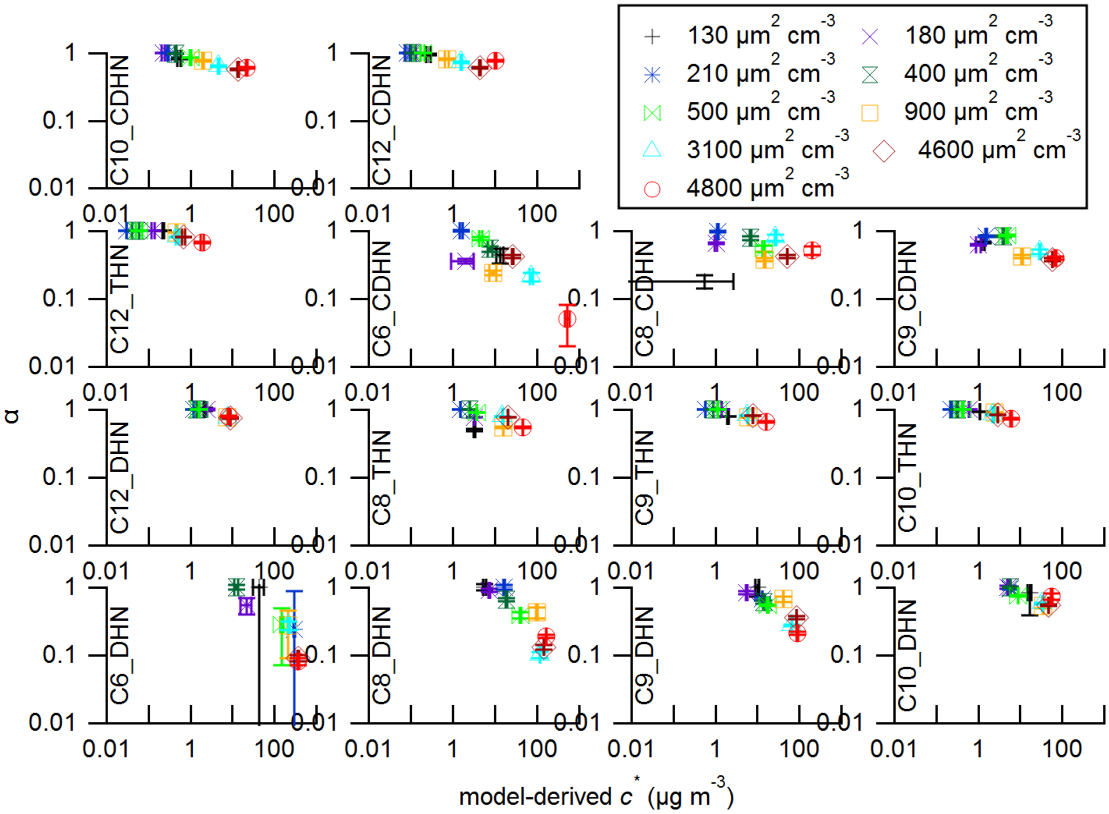

Figure 5.13. α and c* values derived from model fits for each compound and the first burst of each seeded experiment. Error bars shown represent the fitting uncertainties as two standard deviations (2σ).

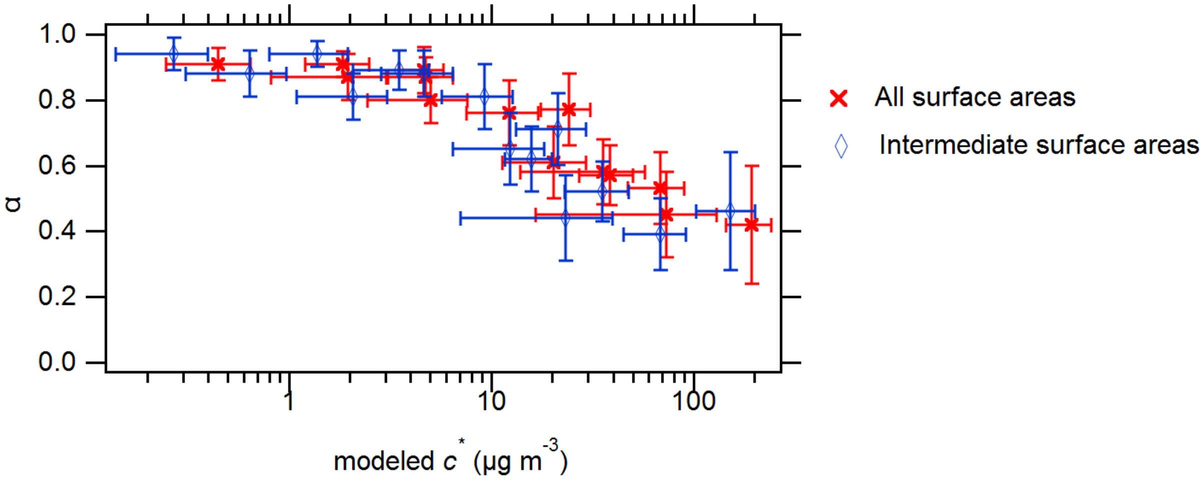

Figure 5.14. Average (arithmetic mean) values of α and modeled c^* values. One set is averaged across all experiments. The other is only averaged over intermediate aerosol seed surface areas (400 - 3000 µm^2 cm^{-3}).

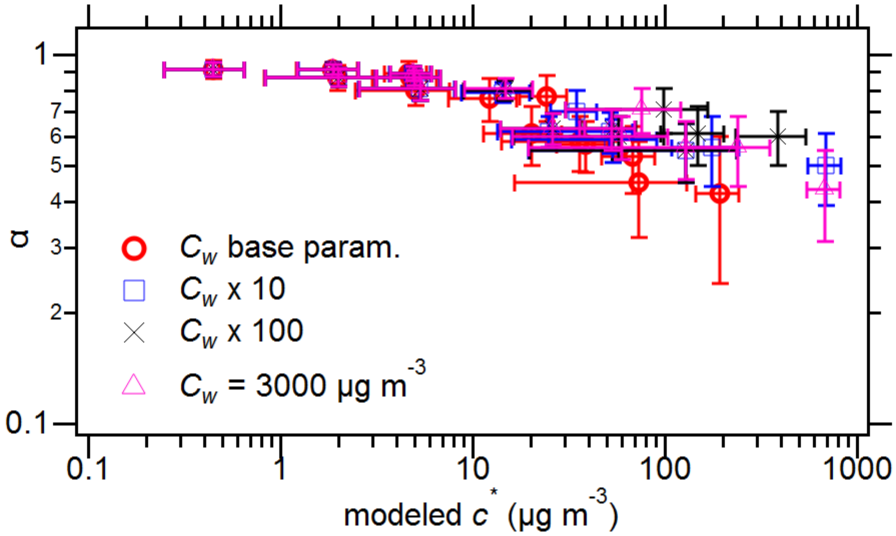

Figure 5.15. Average (arithmetic mean) values of α and c^* when the model is run for every compound and every experiment with different values of C_w.

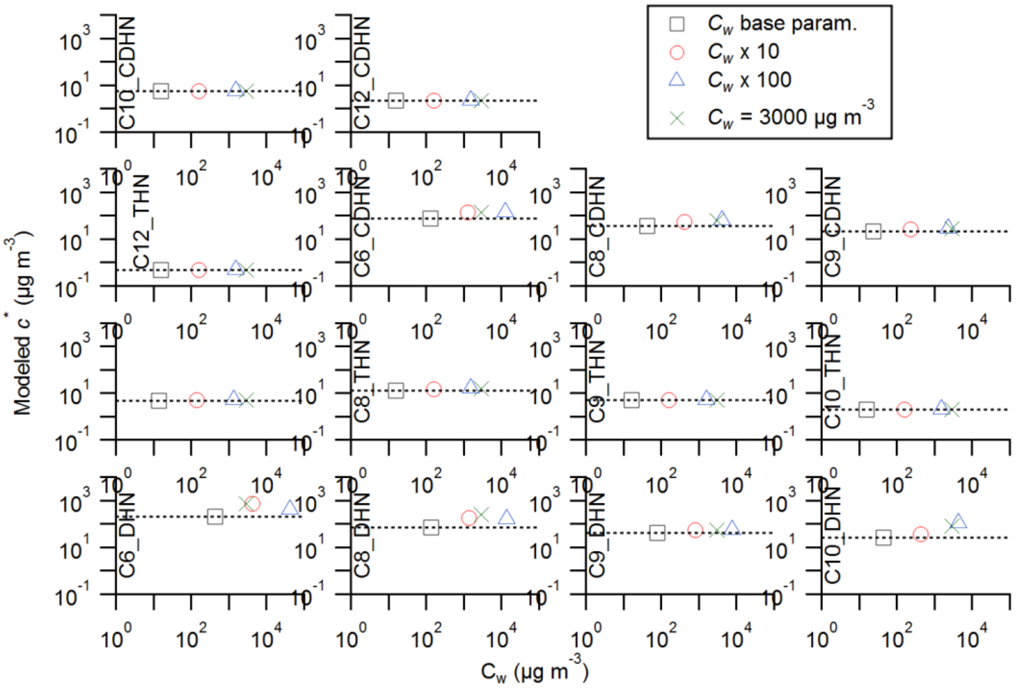

Figure 5.16. Plots for each compound showing the sensitivity of model-derived values of c^* as a function of Cw. The dashed black line indicates the value of c^* for the base case Cw parameterization using the values in Krechmer et al.[209]

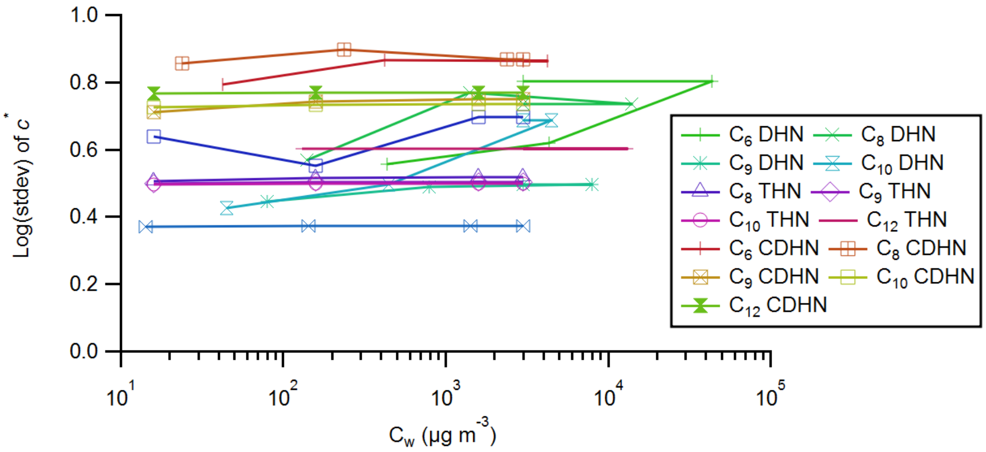

Figure 5.17. The logarithm of the standard deviation of the set of c^* measurements derived for all the experiments of each compound (for the different DOS CS) vs. the C_w used in the model fit. A value of 1 indicates a standard deviation of one order of magnitude. No obviously better C_w value emerges that would greatly reduce the differences in c^* values derived for experiments with different seed CS.

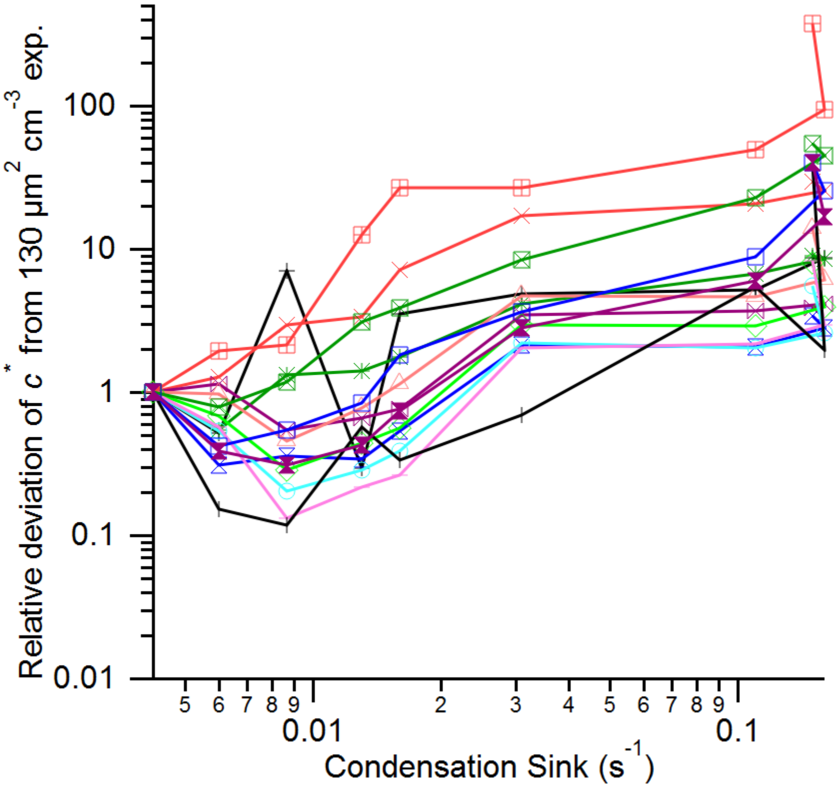

Figure 5.18. Model-determined values of *c**, for each compound, normalized to the value determined from the lowest aerosol seed experiment. The plot suggests a trend of increasing *c** as a function of condensation sink.

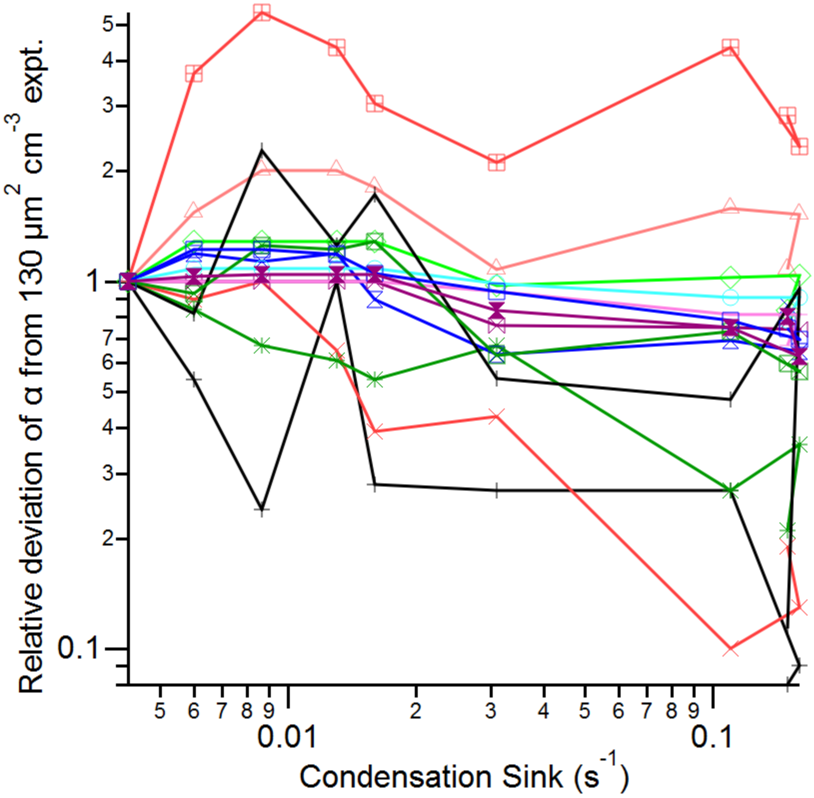

Figure 5.19. Model-determined values of α, for each compound, normalized to the value determined from the lowest aerosol seed experiment. No systematic trend is evident.

5.3.4 Implications for aerosol mass yield measurements

In this work we have established that GPP theory can accurately capture gas/particle partitioning during chamber experiments, provided that vapor wall losses are taken into account and the accommodation coefficient is estimated from the measurements. This allows us to explore quantitatively how vapor losses to Teflon walls may impact aerosol mass yields for experiments with a liquid absorbing seed. Since uptake onto highly viscous particles might be slower, the impacts on yields determined here represent a lower limit.

To obtain estimates of the yield underestimation (i.e. correction) factor, hereafter Φ, we ran the box model with an aerosol-forming compound twice, with gas-phase wall losses turned on or off. We performed model runs for a wide range of CS and c^*/C_w values, and determined the modeled aerosol mass yield for that single compound with and without wall losses. Finally, the amount of aerosol produced without wall losses was divided by the amount produced with wall losses to derive a yield correction factor, hereafter Φ. Results are shown in Figure 5.20. Φ ranges from 1 to ~4, which is a similar to the range of ~1.1-4.2 reported in Zhang et al.[79] based on experimental yield measurements with varying amounts of initial solid ammonium sulfate seed. Φ is highest for semivolatile compounds (c^* ~5-25 μg m^{-3}) in experiments with low aerosol concentrations. Φ is lowest for low volatility species if CS is larger than the wall loss rate, or when a large CS overwhelms the walls as a possible vapor-phase sink, as previously suggested.[79,94,228,229] Figure 5.20 shows two markers denoting example compounds. If an experiment measured aerosol formation from pinic acid (c^* = 3.6 μg m^{-3}) at a seed concentration of 1.4 μg m^{-3}, much of the compound would be lost to the walls and Φ~ 2.5. An experiment that studied SOA formation from tricarballylic acid (c^* = 2 × 10^{-2} µg m^{-3}) using a large amount of seed aerosol (75 µg m^{-3}) would not need an SOA yield correction ($\Phi = 1$).

Figure 5.20 is intended as a guide to inform the design of future environmental chamber SOA yield quantification experiments while minimizing the impact of vapor wall losses. Our results have been derived for a specific experimental arrangement, however, and do not recommend that they be used to quantitatively correct previous SOA experiments conducted using very different experimental methods and sequences. In particular, the yield correction analysis in this work assumed that the oxidation period is relatively short, so that semivolatile species that condense first onto the particles are not completely denuded by the effect of the walls. The addition of gas-phase production over an extended period would change the time evolution of the approach to equilibrium with the particle and wall phases, as well as potentially result in substantial changes of CS vs. time. Furthermore, our model runs did not incorporate the simultaneous presence of a wide range of compounds with different c^*, which is expected to be the case for any realistic SOA system, nor include particle-phase chemistry such as oligomerization, which would change the equilibrium conditions. Finally, we have focused this study on liquid organic seeds. Future work should perform similar experiments and modeling using solid, inorganic, glassy, and other types of aerosol seed to determine the effects of aerosol phase on GPP experiments.

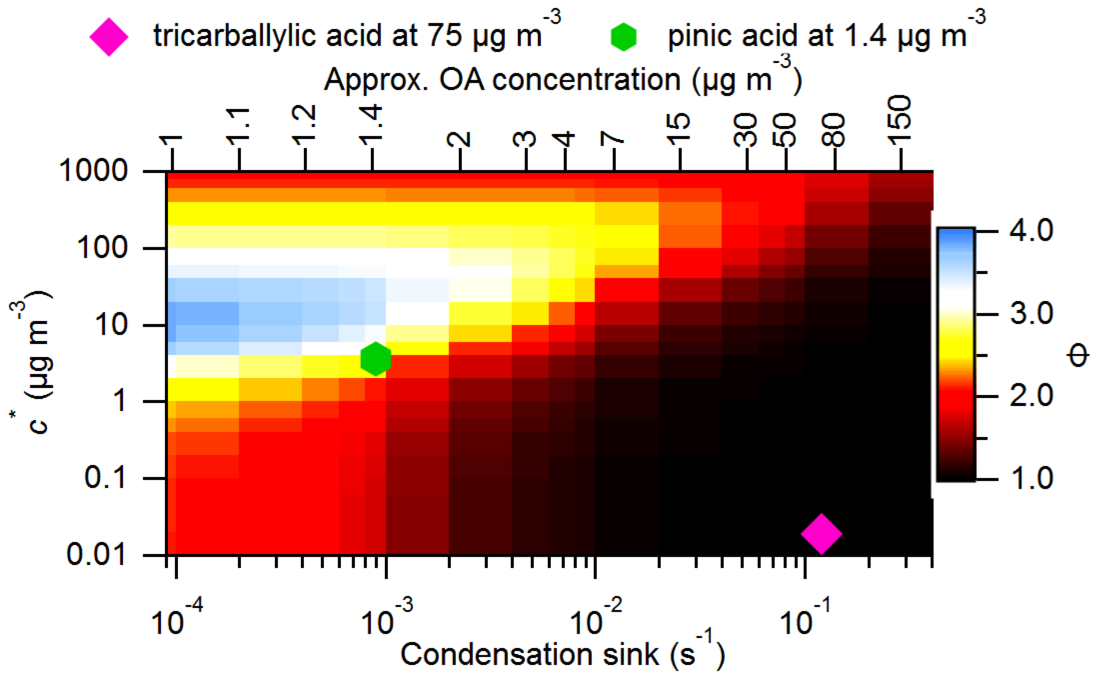

Figure 5.20. A matrix providing an aerosol mass yield correction factor (Φ) for an SOA experiment given the c^* of an aerosol forming product SVOC and the CS. This assumes that production of the SVOC ends quickly after the experiment start so that the system reaches equilibrium. It does not account for product mixes, oligomerization, or heterogeneous particle-phase chemistry.

Chapter 6: Thesis Conclusions

First, this thesis described a new SOA formation pathway from isoprene that provides a missing source of tropospheric organic aerosol. Gas-phase low volatility organic compounds (LVOC), produced from oxidation of isoprene 4-hydroxy-3-hydroperoxide (4,3-ISOPOOH) under low-NO conditions, were observed during the FIXCIT chamber study. Decreases in LVOC directly correspond to appearance and growth in secondary organic aerosol (SOA) of consistent elemental composition, indicating that LVOC condense (at OA below 1 μg m^{-3}). This represents the first simultaneous measurement of condensing low volatility species from isoprene oxidation in both the gas and particle phases. The SOA formation in this study is separate from previously described isoprene epoxydiol (IEPOX) uptake. Assigning all condensing LVOC signals to 4,3-ISOPOOH oxidation in the chamber study implies a wall-loss corrected non-IEPOX SOA mass yield of ∼4%. By contrast to monoterpene oxidation, in which extremely low volatility VOC (ELVOC) constitute the organic aerosol, in the isoprene system LVOC with saturation concentrations from 10^{-2} to 10 μg m^{-3} are the main constituents. These LVOC may be important for the growth of nanoparticles in environments with low OA concentrations. LVOC observed in the chamber were also observed in the atmosphere during SOAS-2013 in the Southeastern United States, with the expected diurnal cycle. This previously uncharacterized aerosol formation pathway could account for ∼5.0 Tg yr^{-1} of SOA production, or 3.3% of global SOA

A new technique for quantifying vapor-phase wall losses in environmental chambers is presented. Partitioning of gas-phase organic compounds to the walls of Teflon environmental chambers is a recently reported phenomenon than can affect the yields of reaction products and secondary organic aerosol (SOA) measured in laboratory experiments. Reported time scales for reaching gas- wall partitioning (GWP) equilibrium (τ_{GWE}) differ by up to 3 orders of magnitude, however, leading to predicted effects that vary from substantial to negligible. The technique involves photochemically generating semi- and low-volatility oxidized organic compounds (saturation concentration $c^* < 100$ μg m^{-3}) in rapid bursts in situ in an 8 m^3 environmental chamber, so that their decay in the absence of aerosol could be measured using a high-resolution chemical ionization mass spectrometer (CIMS) equipped with an "inlet-less" NO_3^- ion source. Measured τ_{GWE} were 7−13 min (rel. std. dev. 33%) for all compounds. The fraction of each compound that partitioned to the walls at equilibrium follows absorptive partitioning theory with an equivalent wall mass concentration in the range 0.3−10 mg m^{-3}. Measurements using a CIMS equipped with a standard ion−molecule reaction region showed large biases due to the contact of compounds with walls. On the basis of these results, a set of parameters is proposed for modeling GWP in chamber experiments.

A new instrumental analysis technique, ion mobility mass spectrometry, is applied to the analysis of gas- and aerosol-phase compounds for the first time. Molecular ions of gas-phase organic species are measured online with IMS–MS after ionization with a custom-built nitrate chemical ionization (CI) source. This CI–IMS–MS technique is used to obtain time- resolved measurements (5 min) of highly oxidized organic molecules during the 2013 Southern Oxidant and Aerosol Study (SOAS) ambient field campaign in the forested SE US. The ambient IMS–MS signals are consistent with laboratory IMS–MS spectra obtained from single-component carboxylic acids and multicomponent mixtures of isoprene and monoterpene oxidation products. Mass-mobility correlations in the 2-D IMS–MS space provide a means of identifying ions with similar molecular structures within complex mass spectra and are used to separate and identify monoterpene oxidation products in the ambient data that are produced from different chemical pathways. Water-soluble organic carbon (WSOC) constituents of fine aerosol particles that are not resolvable with standard analytical separation methods, such as liquid chromatography (LC), are shown to be separable with IMS–MS coupled to an electrospray ionization (ESI) source. The capability to use ion mobility to differentiate between isomers is demonstrated for organosulfates derived from the reactive uptake of isomers of isoprene epoxydiols (IEPOX) onto wet acidic sulfate aerosol. Controlled fragmentation of precursor ions by collisionally induced dissociation (CID) in the transfer region between the IMS and the MS is used to validate MS peak assignments, elucidate structures of oligomers, and confirm the presence of the organosulfate functional group.

The results of environmental chamber experiments with varying seed surface areas were presented. Experiments utilizing the burst method described above were performed with liquid organic DOS seed in the chamber. We observed quantifiable differences in the behavior of the gas-phase measurements that depended on the aerosol seed surface area. A kinetic box model was able to reproduce the behavior of the time series with simple gas-particle partitioning theory. From the model we inferred a measurement of the mass accommodation coefficient, α.

The advances described in this thesis have contributed to greater understanding of secondary organic aerosols in laboratory and chamber studies. Future work should focus on using knowledge of vapor-phase wall losses to reevaluate SOA mass yields in chamber studies. Additional work characterizing specific SOA precursors with the IMS-MS instrument will enable structural determination and identification.

Bibliography

(1) Stocker, T. F.; Qin, D.; Platner, G. K. Climate Change 2013: The Physical Science Basis. *Work. Gr. I Contrib. to Fifth Assess. Rep. Intergov. Panel Clim. Chang. Summ. Policymakers (IPCC, 2013)* **2013**.

(2) Pope III, C. A.; Dockery, D. W. Health effects of fine particulate air pollution: lines that connect. *J. Air Waste Manage. Assoc.* **2006**, *56*, 709–742.

(3) Ramanathan, V.; Crutzen, P. J.; Kiehl, J. T.; Rosenfeld, D. Aerosols, Climate, and the Hydrological Cycle. *Science (80-.).* **2001**, *294*, 2119–2124.

(4) Murphy, D. M.; Cziczo, D. J.; Froyd, K. D.; Hudson, P. K.; Matthew, B. M.; Middlebrook, A. M.; Peltier, R. E.; Sullivan, A.; Thomson, D. S.; Weber, R. J. Single-particle mass spectrometry of tropospheric aerosol particles. *J. Geophys. Res.* **2006**, *111*, D23S32.

(5) Zhang, Q.; Jimenez, J. L.; Canagaratna, M. R.; Allan, J. D.; Coe, H.; Ulbrich, I.; Alfarra, M. R.; Takami, A.; Middlebrook, a. M.; Sun, Y. L.; et al. Ubiquity and dominance of oxygenated species in organic aerosols in anthropogenically-influenced Northern Hemisphere midlatitudes. *Geophys. Res. Lett.* **2007**, *34*, L13801.

(6) Hallquist, M.; Wenger, J. C.; Baltensperger, U.; Rudich, Y.; Simpson, D.; Claeys, M.; Dommen, J.; Donahue, N. M.; George, C.; Goldstein, A. H.; et al. The formation, properties and impact of secondary organic aerosol: current and emerging issues. *Atmos. Chem. Phys.* **2009**, *9*, 5155–5236.

(7) Jimenez, J. L.; Canagaratna, M. R.; Donahue, N. M.; Prevot, A. S. H.; Zhang, Q.; Kroll, J. H.; DeCarlo, P. F.; Allan, J. D.; Coe, H.; Ng, N. L.; et al. Evolution of organic aerosols in the atmosphere. *Science* **2009**, *326*, 1525–1529.

(8) Spracklen, D. V.; Jimenez, J.; Carslaw, K.; Worsnop, D. R.; Evans, M. J.; Mann, G. W.; Zhang, Q.; Canagaratna, M. R.; Allan, J.; Coe, H.; et al. Aerosol mass spectrometer constraint on the global secondary organic aerosol budget. *Atmos. Chem. Phys.* **2011**, *11*, 12109–12136.

(9) Tsigaridis, K.; Daskalakis, N.; Kanakidou, M.; Adams, P. J.; Artaxo, P.; Bahadur, R.; Balkanski, Y.; Bauer, S. E.; Bellouin, N.; Benedetti, A.; et al. The AeroCom evaluation and intercomparison of organic aerosol in global models. *Atmos. Chem. Phys.* **2014**, *14*, 10845–10895.

(10) Goldstein, A. H.; Galbally, I. E. Known and Unexplored Organic Constituents in the Earth's Atmosphere. *Environ. Sci. Technol.* **2007**, *41*, 1514–1521.

(11) Munson, M. S. B.; Field, F. H. Chemical Ionization Mass Spectrometry. I. General

Introduction. *J. Am. Chem. Soc.* **1966**, *88*, 2621–2630.

(12) Eisele, F. L. Identification of tropospheric ions. *J. Geophys. Res. Atmos.* **1986**, *91*, 7897–7906.

(13) Arnold, F.; Henschen, G. First mass analysis of stratospheric negative ions. *Nature* **1978**, *275*, 521–522.

(14) Huey, L. G. Measurement of trace atmospheric species by chemical ionization mass spectrometry: Speciation of reactive nitrogen and future directions. *Mass Spectrom. Rev.* **2007**, *26*, 166–184.

(15) de Gouw, J.; Warneke, C. Measurements of volatile organic compounds in the earth's atmosphere using proton-transfer-reaction mass spectrometry. *Mass Spectrom. Rev.* **2007**, *26*, 223–257.

(16) Bertram, T. H.; Kimmel, J. R.; Crisp, T. A.; Ryder, O. S.; Yatavelli, R. L. N.; Thornton, J. A.; Cubison, M. J.; Gonin, M.; Worsnop, D. R. A field-deployable, chemical ionization time-of-flight mass spectrometer. *Atmos. Meas. Tech.* **2011**, *4*, 1471–1479.

(17) Chhabra, P. S.; Lambe, A. T.; Canagaratna, M. R.; Stark, H.; Jayne, J. T.; Onasch, T. B.; Davidovits, P.; Kimmel, J. R.; Worsnop, D. R. Application of high-resolution time-of-flight chemical ionization mass spectrometry measurements to estimate volatility distributions of α-pinene and naphthalene oxidation products. *Atmos. Meas. Tech.* **2015**, *8*, 1–18.

(18) Brophy, P.; Farmer, D. K. Clustering, methodology, and mechanistic insights into acetate chemical ionization using high-resolution time-of-flight mass spectrometry. *Atmos. Meas. Tech.* **2016**, *9*, 3969–3986.

(19) Ehn, M.; Kleist, E.; Junninen, H.; Petäjä, T.; Lönn, G.; Schobesberger, S.; Dal Maso, M.; Trimborn, a.; Kulmala, M.; Worsnop, D. R.; et al. Gas phase formation of extremely oxidized pinene reaction products in chamber and ambient air. *Atmos. Chem. Phys.* **2012**, *12*, 5113–5127.

(20) Ehn, M.; Thornton, J. A.; Kleist, E.; Sipilä, M.; Junninen, H.; Pullinen, I.; Springer, M.; Rubach, F.; Tillmann, R.; Lee, B.; et al. A large source of low-volatility secondary organic aerosol. *Nature* **2014**, *506*, 476–479.

(21) Friedman, B.; Brophy, P.; Brune, W. H.; Farmer, D. K. Anthropogenic Sulfur Perturbations on Biogenic Oxidation: SO 2 Additions Impact Gas-Phase OH Oxidation Products of α- and β-Pinene. *Environ. Sci. Technol.* **2016**, *50*, 1269–1279.

(22) Jokinen, T.; Sipilä, M.; Junninen, H.; Ehn, M.; Lönn, G.; Hakala, J.; Petäjä, T.; Mauldin, R. L.; Kulmala, M.; Worsnop, D. R. Atmospheric sulphuric acid and neutral cluster measurements using CI-APi-TOF. *Atmos. Chem. Phys.* **2012**, *12*, 4117–4125.

(23) Jokinen, T.; Berndt, T.; Makkonen, R.; Kerminen, V.; Junninen, H.; Paasonen, P.; Stratmann, F.; Herrmann, H.; Guenther, A. B.; Worsnop, D. R.; et al. Production of extremely low volatile organic compounds from biogenic emissions: Measured yields and atmospheric implications. *Proc. Natl. Acad. Sci. U.S.A.* **2015**, *112*, 7123–7128.

(24) Krechmer, J. E.; Coggon, M. M.; Massoli, P.; Nguyen, T. B.; Crounse, J. D.; Hu, W.; Day, D. A.; Tyndall, G. S.; Henze, D. K.; Rivera-Rios, J. C.; et al. Formation of low volatility organic compounds and secondary organic aerosol from isoprene hydroxyhydroperoxide low-NO oxidation. *Environ. Sci. Technol.* **2015**, *49*, 10330–10339.

(25) Lopez-Hilfiker, F. D.; Mohr, C.; D'Ambro, E. L.; Lutz, A.; Riedel, T. P.; Gaston, C. J.; Iyer, S.; Zhang, Z.; Gold, A.; Surratt, J. D.; et al. Molecular Composition and Volatility of Organic Aerosol in the Southeastern U.S.: Implications for IEPOX Derived SOA. *Environ. Sci. Technol.* **2016**, *50*, 2200–2209.

(26) Lee, B. H.; Mohr, C.; Lopez-Hilfiker, F. D.; Lutz, A.; Hallquist, M.; Lee, L.; Romer, P.; Cohen, R. C.; Iyer, S.; Kurtén, T.; et al. Highly functionalized organic nitrates in the southeast United States: Contribution to secondary organic aerosol and reactive nitrogen budgets. *Proc. Natl. Acad. Sci. U.S.A.* **2016**, *113*, 1516–1521.

(27) Mohr, C.; Lopez-hilfiker, F. D.; Zotter, P.; Prévôt, A. S. H.; Xu, L.; Ng, N. L.; Scott, C.; Williams, L. R.; Franklin, J. P.; Zahniser, M. S.; et al. Contribution of Nitrated Phenols to Wood Burning Brown Carbon Light Absorption in Detling, United Kingdom during Winter Time. *Environ. Sci. Technol.* **2013**, *47*, 6316–6324.

(28) Lopez-Hilfiker, F. D.; Mohr, C.; Ehn, M.; Rubach, F.; Kleist, E.; Wildt, J.; Mentel, T. F.; Lutz, A.; Hallquist, M.; Worsnop, D.; et al. A novel method for online analysis of gas and particle composition: description and evaluation of a Filter Inlet for Gases and AEROsols (FIGAERO). *Atmos. Meas. Tech.* **2014**, *7*, 983–1001.

(29) Lopez-Hilfiker, F. D.; Mohr, C.; Ehn, M.; Rubach, F.; Kleist, E.; Wildt, J.; Mentel, T. F.; Carrasquillo, A. J.; Daumit, K. E.; Hunter, J. F.; et al. Phase partitioning and volatility of secondary organic aerosol components formed from α-pinene ozonolysis and OH oxidation: the importance of accretion products and other low volatility compounds. *Atmos. Chem. Phys.* **2015**, *15*, 7765–7776.

(30) Yatavelli, R. L. N.; Stark, H.; Thompson, S. L.; Kimmel, J. R.; Cubison, M. J.; Day, D. a.; Campuzano-Jost, P.; Palm, B. B.; Hodzic, a.; Thornton, J. a.; et al. Semicontinuous measurements of gas–particle partitioning of organic acids in a ponderosa pine forest using a MOVI-HRToF-CIMS. *Atmos. Chem. Phys.* **2014**, *14*, 1527–1546.

(31) Yatavelli, R. L. N.; Mohr, C.; Stark, H.; Day, D. a.; Thompson, S. L.; Lopez-Hilfiker, F. D.; Campuzano-Jost, P.; Palm, B. B.; Vogel, A. L.; Hoffmann, T.; et al. Estimating the contribution of organic acids to northern hemispheric continental organic aerosol. *Geophys. Res. Lett.* **2015**, *42*, 6084–6090.

(32) Zhao, Y.; Huang, D.; Huang, L.; Chen, Z. Hydrogen peroxide enhances the oxidation of oxygenated volatile organic compounds on mineral dust particles: a case study of methacrolein. *Environ. Sci. Technol.* **2014**.

(33) Aljawhary, D.; Lee, A. K. Y.; Abbatt, J. P. D. High-resolution chemical ionization mass spectrometry (ToF-CIMS): Application to study SOA composition and processing. *Atmos. Meas. Tech.* **2013**, *6*, 3211–3224.

(34) Brophy, P.; Farmer, D. K. A switchable reagent ion high resolution time-of-flight chemical ionization mass spectrometer for real-time measurement of gas phase oxidized species: characterization from the 2013 southern oxidant and aerosol study. *Atmos. Meas. Tech.* **2015**, *8*, 2945–2959.

(35) Haagen-Smit, A. J. Chemistry and physiology of Los Angeles Smog. *Ind. Eng. Chem.* **1952**, *44*, 1342–1346.

(36) Myhre, G.; Shindell, D.; Bréon, F.-M.; Collins, W.; Fuglestvedt, J.; Huang, J.; Koch, D.; Lamarque, J.-F.; Lee, D.; Mendoza, B.; et al. Anthropogenic and Natural Radiative Forcing. In *Climate Change 2013: The Physical Science Basis. Contribution of Working Group I to the Fifth Assessment Report of the Intergovernmental Panel on Climate Change*; Stocker, T. F., Ed.; Cambridge University Press: Cambridge, United Kingdom and New York, NY, USA, 2013.

(37) Heald, C. L.; Coe, H.; Jimenez, J. L.; Weber, R. J.; Bahreini, R.; Middlebrook, a. M.; Russell, L. M.; Jolleys, M.; Fu, T.-M.; Allan, J. D.; et al. Exploring the vertical profile of atmospheric organic aerosol: comparing 17 aircraft field campaigns with a global model. *Atmos. Chem. Phys.* **2011**, *11*, 12673–12696.

(38) Guenther, A. B.; Jiang, X.; Heald, C. L.; Sakulyanontvittaya, T.; Duhl, T.; Emmons, L. K.; Wang, X. The Model of Emissions of Gases and Aerosols from Nature version 2.1 (MEGAN2.1): an extended and updated framework for modeling biogenic emissions. *Geosci. Model Dev.* **2012**, *5*, 1471–1492.

(39) Guenther, A.; Nicholas, C.; Erickson, D.; Fall, R.; Geron, C.; Gradel, T.; Harley, P.; Klinger, L.; Lerdau, M.; Mckay, W. A.; et al. A global model of natural volatile organic compound emissions. *J. Geophys. Res.* **1995**, *100*, 8873–8892.

(40) Crutzen, P. J.; Williams, J.; Pöschl, U.; Hoor, P.; Fischer, H.; Warneke, C.; Holzinger, R.; Hansel, A.; Lindinger, W.; Scheeren, B.; et al. High spatial and temporal resolution measurements of primary organics and their oxidation products over the tropical forests of Surinam. *Atmos. Environ.* **2000**, *34*, 1161–1165.

(41) Paulot, F.; Crounse, J. D.; Kjaergaard, H. G.; Kurten, A.; St. Clair, J. M.; Seinfeld, J. H.; Wennberg, P. O. Supporting Online Material forUnexpected Epoxide Formation in the Gas-Phase Photooxidation of Isoprene. *Science (80-.).* **2009**, *325*, 730–733.

(42) Rivera-Rios, J. C.; Nguyen, T. B.; Crounse, J. D.; Jud, W.; St. Clair, J. M.; Mikoviny, T.; Gilman, J. B.; Lerner, B. M.; Kaiser, J. B.; de Gouw, J.; et al. Conversion of hydroperoxides to carbonyls in field and laboratory instrumentation: Observational bias in diagnosing pristine versus anthropogenically controlled atmospheric chemistry. *Geophys. Res. Lett.* **2014**, *41*, 8645–8651.

(43) Bates, K. H.; Crounse, J. D.; St Clair, J. M.; Bennett, N. B.; Nguyen, T. B.; Seinfeld, J. H.; Stoltz, B. M.; Wennberg, P. O. Gas phase production and loss of isoprene epoxydiols. *J. Phys. Chem. A* **2014**, *118*, 1237–1246.

(44) Xu, L.; Guo, H.; Boyd, C. M.; Klein, M.; Bougiatioti, A.; Cerully, K. M.; Hite, J. R.; Isaacman-VanWertz, G.; Kreisberg, N. M.; Knote, C.; et al. Effects of anthropogenic emissions on aerosol formation from isoprene and monoterpenes in the southeastern United States. *Proc. Natl. Acad. Sci. U.S.A.* **2015**, *112*, 37–42.

(45) Nguyen, T. B.; Coggon, M. M.; Bates, K. H.; Zhang, X.; Schwantes, R. H.; Schilling, K. A.; Loza, C. L.; Flagan, R. C.; Wennberg, P. O.; Seinfeld, J. H. Organic aerosol formation from the reactive uptake of isoprene epoxydiols (IEPOX) onto non-acidified inorganic seeds. *Atmos. Chem. Phys.* **2014**, *14*, 3497–3510.

(46) Liu, Y.; Kuwata, M.; Strick, B. F.; Geiger, F. M.; Thomson, R. J.; McKinney, K. A.; Martin, S. T.; Geiger, F. M.; McKinney, K. A.; Martin, S. T. Uptake of Epoxydiol Isomers Accounts for Half of the Particle-Phase Material Produced from Isoprene Photooxidation via the HO2 Pathway. *Environ. Sci. Technol.* **2015**, *49*, 250–258.

(47) Kjaergaard, H. G.; Knap, H. C.; Ørnsø, K. B.; Jørgensen, S.; Crounse, J. D.; Paulot, F.; Wennberg, P. O. Atmospheric fate of methacrolein. 2. Formation of lactone and implications for organic aerosol production. *J. Phys. Chem. A* **2012**, *116*, 5763–5768.

(48) Lin, Y.-H.; Zhang, H.; Pye, H. O. T.; Zhang, Z.; Marth, W. J.; Park, S.; Arashiro, M.; Cui, T.; Budisulistiorini, S. H.; Sexton, K. G.; et al. Epoxide as a precursor to secondary organic aerosol formation from isoprene photooxidation in the presence of nitrogen oxides. *Proc. Natl. Acad. Sci. U.S.A.* **2013**, *110*, 6718–6723.

(49) Kroll, J. H.; Ng, N. L.; Murphy, S. M.; Flagan, R. C.; Seinfeld, J. H. Secondary Organic Aerosol Formation from Isoprene Photooxidation. *Environ. Sci. Technol.* **2006**, *40*, 1869–1877.

(50) Chan, A. W. H.; Chan, M. N.; Surratt, J. D.; Chhabra, P. S.; Loza, C. L.; Crounse, J. D.; Yee, L. D.; Flagan, R. C.; Wennberg, P. O.; Seinfeld, J. H. Role of aldehyde chemistry and NOx concentrations in secondary organic aerosol formation. *Atmos. Chem. Phys.* **2010**, *10*, 7169–7188.

(51) Pankow, J. F. An absorption model of gas/particle partitioning of organic compounds in the atmosphere. *Atmos. Environ.* **1994**, *28*, 185–188.

(52) Donahue, N. M.; Robinson, A. L.; Stanier, C. O.; Pandis, S. N. Coupled partitioning, dilution, and chemical aging of semivolatile organics. *Environ. Sci. Technol.* **2006**, *40*, 2635–2643.

(53) Jokinen, T.; Sipilä, M.; Richters, S.; Kerminen, V.-M.; Paasonen, P.; Stratmann, F.; Worsnop, D.; Kulmala, M.; Ehn, M.; Herrmann, H.; et al. Rapid Autoxidation Forms Highly Oxidized RO2 Radicals in the Atmosphere. *Angew. Chemie Int. Ed.* **2014**, *53*, 14596–14600.

(54) Crounse, J. D.; Nielsen, L. B.; Jørgensen, S.; Kjaergaard, H. G.; Wennberg, P. O. Autoxidation of Organic Compounds in the Atmosphere. *J. Phys. Chem. Lett.* **2013**, *4*, 3513–3520.

(55) Nguyen, T. B.; Crounse, J. D.; Schwantes, R. H.; Teng, A. P.; Bates, K. H.; Zhang, X.; St. Clair, J. M.; Brune, W. H.; Tyndall, G. S.; Keutsch, F. N.; et al. Overview of the Focused Isoprene eXperiment at the California Institute of Technology (FIXCIT): mechanistic chamber studies on the oxidation of biogenic compounds. *Atmos. Chem. Phys.* **2014**, *14*, 13531–13549.

(56) Yatavelli, R. L. N.; Lopez-Hilfiker, F.; Wargo, J. D.; Kimmel, J. R.; Cubison, M. J.; Bertram, T. H.; Jimenez, J. L.; Gonin, M.; Worsnop, D. R.; Thornton, J. A. A Chemical Ionization High-Resolution Time-of-Flight Mass Spectrometer Coupled to a Micro Orifice Volatilization Impactor (MOVI-HRToF-CIMS) for Analysis of Gas and Particle-Phase Organic Species. *Aerosol Sci. Technol.* **2012**, *46*, 1313–1327.

(57) Junninen, H.; Ehn, M.; Petäjä, T.; Luosujärvi, L.; Kotiaho, T.; Kostiainen, R.; Rohner, U.; Gonin, M.; Fuhrer, K.; Kulmala, M.; et al. A high-resolution mass spectrometer to measure atmospheric ion composition. *Atmos. Meas. Tech.* **2010**, *3*, 1039–1053.

(58) Eisele, F.; Tanner, D. Measurement of the gas phase concentration of H2SO4 and methane sulfonic acid and estimates of H2SO4 production and loss in the atmosphere. *J. Geophys. Res.* **1993**, *98*, 9001–9010.

(59) Ehn, M.; Junninen, H.; Petäjä, T.; Kurtén, T.; Kerminen, V.-M.; Schobesberger, S.; Manninen, H. E.; Ortega, I. K.; Vehkamäki, H.; Kulmala, M.; et al. Composition and temporal behavior of ambient ions in the boreal forest. *Atmos. Chem. Phys.* **2010**, *10*, 8513–8530.

(60) Brockmann, J. E. Sampling and transport of aerosols. In *Aerosol measurement: Principles, Techniques, and Applications*; Baron, P. A.; Willeke, K., Eds.; Wiley-Interscience: New York, 2001; pp. 143–195.

(61) Hilal, S. H.; Karickhoff, S. W.; Carreira, L. A. Prediction of the Vapor Pressure Boiling Point, Heat of Vaporization and Diffusion Coefficient of Organic Compounds. *QSAR Comb. Sci.* **2003**, *22*, 565–574.

(62) Hilal, S. H.; Saravanaraj, A. N.; Whiteside, T.; Carreira, L. A. Calculating physical properties of organic compounds for environmental modeling from molecular structure. *J. Comput. Aided. Mol. Des.* **2007**, *21*, 693–708.

(63) Veres, P.; Gilman, J. B.; Roberts, J. M.; Kuster, W. C.; Warneke, C.; Burling, I. R.; de Gouw, J. Development and validation of a portable gas phase standard generation and calibration system for volatile organic compounds. *Atmos. Meas. Tech.* **2010**, *3*, 683–691.

(64) Viggiano, A.; Perry, R.; Albritton, D.; Ferguson, E.; Fehsenfeld, F. C. Stratospheric negative-ion reaction rates with H2SO4. *J. Geophys. Res. Ocean.* **1982**, *87*, 7340–7342.

(65) Mauldin, R.; Tanner, D.; Eisele, F. Measurements of OH during PEM-Tropics A. *J. Geophys. Res.* **1999**, *104*, 5817–5827.

(66) Garden, A. L.; Paulot, F.; Crounse, J. D.; Maxwell-Cameron, I. J.; Wennberg, P. O.; Kjaergaard, H. G. Calculation of conformationally weighted dipole moments useful in ion–molecule collision rate estimates. *Chem. Phys. Lett.* **2009**, *474*, 45–50.

(67) Rissanen, M. P.; Kurtén, T.; Sipilä, M.; Thornton, J. A.; Kangasluoma, J.; Sarnela, N.; Junninen, H.; Jørgensen, S.; Schallhart, S.; Kajos, M. K.; et al. The formation of highly oxidized multifunctional products in the ozonolysis of cyclohexene. *J. Am. Chem. Soc.* **2014**, *136*, 15596–15606.

(68) Decarlo, P. F.; Kimmel, J. R.; Trimborn, A.; Northway, M. J.; Jayne, J. T.; Aiken, A. C.; Gonin, M.; Fuhrer, K.; Horvath, T.; Docherty, K. S.; et al. Field-Deployable, High-Resolution, Time-of-Flight Aerosol Mass Spectrometer. *Anal. Chem.* **2006**, *78*, 8281–8289.

(69) Canagaratna, M. R.; Jimenez, J. L.; Kroll, J. H.; Chen, Q.; Kessler, S. H.; Massoli, P.; Hildebrandt Ruiz, L.; Fortner, E.; Williams, L. R.; Wilson, K. R.; et al. Elemental ratio measurements of organic compounds using aerosol mass spectrometry: characterization, improved calibration, and implications. *Atmos. Chem. Phys.* **2015**, *15*, 253–272.

(70) Paatero, P. *End user's guide to multilinear engine applications*; University of Helsinki: Helsinki, Finland, 2007.

(71) Canonaco, F.; Crippa, M.; Slowik, J. G.; Baltensperger, U.; Prévôt, a. S. H. SoFi, an IGOR-based interface for the efficient use of the generalized multilinear engine (ME-2) for the source apportionment: ME-2 application to aerosol mass spectrometer data. *Atmos. Meas. Tech.* **2013**, *6*, 3649–3661.

(72) Ulbrich, I. M.; Canagaratna, M. R.; Zhang, Q.; Worsnop, D. R.; Jimenez, J. L. Interpretation of organic components from Positive Matrix Factorization of aerosol mass spectrometric data. *Atmos. Chem. Phys.* **2009**, *9*, 2891–2918.

(73) Crounse, J.; McKinney, K.; Kwan, A. J.; Wennberg, P. O. Measurement of gas-phase

hydroperoxides by chemical ionization mass spectrometry. *Anal. Chem.* **2006**, *78*, 6726–6732.

(74) St Clair, J. M.; McCabe, D. C.; Crounse, J. D.; Steiner, U.; Wennberg, P. O. Chemical ionization tandem mass spectrometer for the in situ measurement of methyl hydrogen peroxide. *Rev. Sci. Instrum.* **2010**, *81*, 094102–094106.

(75) Barley, M. H.; McFiggans, G. The critical assessment of vapour pressure estimation methods for use in modelling the formation of atmospheric organic aerosol. *Atmos. Chem. Phys.* **2010**, *10*, 749–767.

(76) Ziemann, P. J.; Atkinson, R. Kinetics, products, and mechanisms of secondary organic aerosol formation. *Chem. Soc. Rev.* **2012**, *41*, 6582–6605.

(77) Paulot, F.; Henze, D. K.; Wennberg, P. O. Impact of the isoprene photochemical cascade on tropical ozone. *Atmos. Chem. Phys.* **2012**, *12*, 1307–1325.

(78) Seinfeld, J. H.; Pandis, S. N. *Atmospheric chemistry and physics: from air pollution to climate change*; 2nd ed.; John Wiley & Sons, Inc.: Hoboken, New Jersey, USA, 2006; Vol. 2nd.

(79) Zhang, X.; Cappa, C. D.; Jathar, S. H.; McVay, R. C.; Ensberg, J. J.; Kleeman, M. J.; Seinfeld, J. H. Influence of vapor wall loss in laboratory chambers on yields of secondary organic aerosol. *Proc. Natl. Acad. Sci. U.S.A.* **2014**, *111*, 5802–5807.

(80) McMurry, P. H.; Grosjean, D. Gas and aerosol wall losses in Teflon film smog chambers. *Environ. Sci. Technol.* **1985**, *19*, 1176–1182.

(81) Cocker, D. R.; Flagan, R. C.; Seinfeld, J. H. State-of-the-art chamber facility for studying atmospheric aerosol chemistry. *Environ. Sci. Technol.* **2001**, *35*, 2594–2601.

(82) Crump, J. G.; Seinfeld, J. H. Turbulent deposition and gravitational sedimentation of an aerosol in a vessel of arbitrary shape. *J. Aerosol Sci.* **1981**, *12*, 405–415.

(83) Keller-Rudek, H.; Moortgat, G. K.; Sander, R.; Sörensen, R. The MPI-Mainz UV/VIS spectral atlas of gaseous molecules of atmospheric interest. *Earth Syst. Sci. Data* **2013**, *5*, 365–373.

(84) Aster, R. C.; Thurber, C. H.; Borchers, B. *Parameter Estimation and Inverse Problems*; International geophysics series; Elsevier Academic Press: Boston, 2005.

(85) Middlebrook, A. M.; Bahreini, R.; Jimenez, J. L.; Canagaratna, M. R. Evaluation of Composition-Dependent Collection Efficiencies for the Aerodyne Aerosol Mass Spectrometer using Field Data. *Aerosol Sci. Technol.* **2012**, *46*, 258–271.

(86) Bahreini, R.; Ervens, B.; Middlebrook, A. M.; Warneke, C.; de Gouw, J. A.; DeCarlo, P. F.; Jimenez, J. L.; Brock, C. a.; Neuman, J. A.; Ryerson, T. B.; et al. Organic aerosol

formation in urban and industrial plumes near Houston and Dallas, Texas. *J. Geophys. Res.* **2009**, *114*, D00F16.

(87) Ng, N. L.; Canagaratna, M. R.; Jimenez, J. L.; Chhabra, P. S.; Seinfeld, J. H.; Worsnop, D. R. Changes in organic aerosol composition with aging inferred from aerosol mass spectra. *Atmos. Chem. Phys.* **2011**, *11*, 6465–6474.

(88) Gaston, C. J.; Riedel, T. P.; Zhang, Z.; Gold, A.; Surratt, J. D.; Thornton, J. A. Reactive uptake of an isoprene-derived epoxydiol to submicron aerosol particles. *Environ. Sci. Technol.* **2014**, *48*, 11178–11186.

(89) Hu, W. W.; Campuzano-Jost, P.; Palm, B. B.; Day, D. A.; Ortega, A. M.; Hayes, P. L.; Krechmer, J. E.; Chen, Q.; Kuwata, M.; Liu, Y. J.; et al. Characterization of a real-time tracer for Isoprene Epoxydiols-derived Secondary Organic Aerosol (IEPOX-SOA) from aerosol mass spectrometer measurements. *Atmos. Chem. Phys. Discuss.* **2015**, *15*, 11223–11276.

(90) Lee, B. H.; Lopez-Hilfiker, F. D.; Mohr, C.; Kurtén, T.; Worsnop, D. R.; Thornton, J. A. An iodide-adduct high-resolution time-of-flight chemical-ionization mass spectrometer: application to atmospheric inorganic and organic compounds. *Environ. Sci. Technol.* **2014**, *48*, 6309–6317.

(91) Pankow, J. F.; Asher, W. E. SIMPOL.1: a simple group contribution method for predicting vapor pressures and enthalpies of vaporization of multifunctional organic compounds. *Atmos. Chem. Phys.* **2008**, *8*, 2773–2796.

(92) Atkinson, R. Gas-Phase Tropospheric Chemistry of Volatile Organic Compounds: 1. Alkanes and Alkenes. *J. Phys. Chem. Ref. Data* **1997**, *26*, 215–290.

(93) Xie, Y.; Paulot, F.; Carter, W. P. L.; Nolte, C. G.; Luecken, D. J.; Hutzell, W. T.; Wennberg, P. O.; Cohen, R. C.; Pinder, R. W. Understanding the impact of recent advances in isoprene photooxidation on simulations of regional air quality supplementary information. *Atmos. Chem. Phys.* **2013**, *13*, 8439–8455.

(94) Matsunaga, A.; Ziemann, P. J. Gas-Wall partitioning of organic compounds in a Teflon film chamber and potential effects on reaction product and aerosol yield measurements. *Aerosol Sci. Technol.* **2010**, *44*, 881–892.

(95) Yeh, G. K.; Ziemann, P. J. Identification and yields of 1,4-hydroxynitrates formed from the reactions of C8-C16 n-alkanes with OH radicals in the presence of NO(x). *J. Phys. Chem. A* **2014**, *118*, 8797–8806.

(96) Surratt, J. D.; Murphy, S. M.; Kroll, J. H.; Ng, N. L.; Hildebrandt, L.; Sorooshian, A.; Szmigielski, R.; Vermeylen, R.; Maenhaut, W.; Claeys, M.; et al. Chemical Composition of Secondary Organic Aerosol Formed from the Photooxidation of Isoprene. *J. Phys. Chem. A* **2006**, *110*, 9665–9690.

(97) Kokkola, H.; Yli-Pirila, P.; Vesterinen, M.; Korhonen, H.; Keskinen, H.; Romakkaniemi, S.; Hao, L.; Kortelainen, A.; Joutsensaari, J.; Worsnop, D. R.; et al. The role of low volatile organics on secondary organic aerosol formation. *Atmos. Chem. Phys.* **2014**, *14*, 1689–1700.

(98) Nguyen, T. B.; Crounse, J. D.; Teng, A. P.; St. Clair, J. M.; Paulot, F.; Wolfe, G. M.; Wennberg, P. O. Rapid deposition of oxidized biogenic compounds to a temperate forest. *Proc. Natl. Acad. Sci. U.S.A.* **2015**, *112*, E392–E401.

(99) Janssen, R. H. H.; Vilà-Guerau de Arellano, J.; Ganzeveld, L. N.; Kabat, P.; Jimenez, J. L.; Farmer, D. K.; van Heerwaarden, C. C.; Mammarella, I. Combined effects of surface conditions, boundary layer dynamics and chemistry on diurnal SOA evolution. *Atmos. Chem. Phys.* **2012**, *12*, 6827–6843.

(100) Shilling, J. E.; Chen, Q.; King, S. M.; Rosenoern, T.; Kroll, J. H.; Worsnop, D. R.; McKinney, K. A.; Martin, S. T. Particle mass yield in secondary organic aerosol formed by the dark ozonolysis of α-pinene. *Atmos. Chem. Phys.* **2008**, *8*, 2073–2088.

(101) Pathak, R. K.; Stanier, C. O.; Donahue, N. M.; Pandis, S. N. Ozonolysis of α -pinene at atmospherically relevant concentrations: Temperature dependence of aerosol mass fractions (yields). *J. Geophys. Res.* **2007**, *112*, D03201.

(102) Peeters, J.; Müller, J. J.-F.; Stavrakou, T.; Nguyen, V. S. V. Hydroxyl Radical Recycling in Isoprene Oxidation Driven by Hydrogen Bonding and Hydrogen Tunneling: the Upgraded LIM1 Mechanism. *J. Phys. Chem. A* **2014**, *118*, 8625–8643.

(103) Crounse, J. D.; Paulot, F.; Kjaergaard, H. G.; Wennberg, P. O. Peroxy radical isomerization in the oxidation of isoprene. *Phys. Chem. Chem. Phys.* **2011**, *13*, 13607–13613.

(104) Riipinen, I.; Pierce, J. R.; Yli-Juuti, T.; Nieminen, T.; Häkkinen, S.; Ehn, M.; Junninen, H.; Lehtipalo, K.; Petäjä, T.; Slowik, J.; et al. Organic condensation: a vital link connecting aerosol formation to cloud condensation nuclei (CCN) concentrations. *Atmos. Chem. Phys.* **2011**, *11*, 3865–3878.

(105) Wong, J. P. S.; Zhou, S.; Abbatt, J. P. D. Changes in Secondary Organic Aerosol Composition and Mass due to Photolysis: Relative Humidity Dependence. *J. Phys. Chem. A* **2015**, *119*, 4309–4316.

(106) Hodzic, A.; Madronich, S.; Kasibhatla, P. S.; Tyndall, G.; Aumont, B.; Jimenez, J. L.; Lee-Taylor, J.; Orlando, J. Organic photolysis reactions in tropospheric aerosols: effect on secondary organic aerosol formation and lifetime. *Atmos. Chem. Phys.* **2015**, *15*, 9253–9269.

(107) Grosjean, D. Wall loss of gaseous pollutants in outdoor teflon chambers. *Environ. Sci. Technol.* **1985**, *19*, 1059–1065.

(108) Yeh, G. K.; Ziemann, P. J. Gas-Wall partitioning of oxygenated organic compounds: measurements, structure–activity relationships, and correlation with gas chromatographic retention factor. *Aerosol Sci. Technol.* **2015**, *49*, 726–737.

(109) La, Y. S.; Camredon, M.; Ziemann, P. J.; Valorso, R.; Matsunaga, A.; Lannuque, V.; Lee-Taylor, J.; Hodzic, A.; Madronich, S.; Aumont, B. Impact of chamber wall loss of gaseous organic compounds on secondary organic aerosol formation: explicit modeling of SOA formation from alkane and alkene oxidation. *Atmos. Chem. Phys.* **2016**, *16*, 1417–1431.

(110) Bian, Q.; May, A. A.; Kreidenweis, S. M.; Pierce, J. R. Investigation of particle and vapor wall-loss effects on controlled wood-smoke smog-chamber experiments. *Atmos. Chem. Phys.* **2015**, *15*, 11027–11045.

(111) Zhang, X.; Schwantes, R. H.; McVay, R. C.; Lignell, H.; Coggon, M. M.; Flagan, R. C.; Seinfeld, J. H. Vapor wall deposition in Teflon chambers. *Atmos. Chem. Phys.* **2015**, *15*, 4197–4214.

(112) Loza, C. L.; Chan, A. W. H.; Galloway, M. M.; Keutsch, F. N.; Flagan, R. C.; Seinfeld, J. H. Characterization of vapor wall loss in laboratory chambers. *Environ. Sci. Technol.* **2010**, *44*, 5074–5078.

(113) Shiraiwa, M.; Yee, L. D.; Schilling, K. A.; Loza, C. L.; Craven, J. S.; Zuend, A.; Ziemann, P. J.; Seinfeld, J. H. Size distribution dynamics reveal particle-phase chemistry in organic aerosol formation. *Proc. Natl. Acad. Sci. U.S.A.* **2013**, *110*, 11746–11750.

(114) Taylor, W. D.; Allston, T. D.; Moscato, M. J.; Fazekas, G. B.; Kozlowski, R.; Takacs, G. A. Atmospheric photodissociation lifetimes for nitromethane, methyl nitrite, and methyl nitrate. *Int. J. Chem. Kinet.* **1980**, *12*, 231–240.

(115) Mauldin, R. L.; Tanner, D. J.; Eisele, F. L. A new chemical ionization mass spectrometer technique for the fast measurement of gas phase nitric acid in the atmosphere. *J. Geophys. Res. Atmos.* **1998**, *103*, 3361–3367.

(116) Huey, L. G.; Hanson, D. R.; Howard, C. J. Reactions of SF6- and I- with Atmospheric Trace Gases. *J. Phys. Chem.* **1995**, *99*, 5001–5008.

(117) Atkinson, R.; Carter, W. P. L.; Winer, A. M.; Pitts, J. N. An experimental protocol for the determination of OH radical rate constants with organics using methyl nitrite photolysis as an OH radical source. *J. Air Pollut. Control Assoc.* **1981**, *31*, 1090–1092.

(118) Pirjola, L.; Kulmala, M.; Wilck, M.; Bischoff, A.; Stratmann, F.; Otto, E. Formation of sulphuric acid aerosols and cloud condensation nuclei: An expression for significant nucleation and model comparison. *J. Aerosol Sci.* **1999**, *30*, 1079–1094.

(119) Matsunaga, A.; Ziemann, P. J. Yields of beta-hydroxynitrates, dihydroxynitrates, and trihydroxynitrates formed from OH radical-initiated reactions of 2-methyl-1-alkenes. *Proc. Natl. Acad. Sci. U.S.A.* **2010**, *107*, 6664–6669.

(120) Lim, Y. Bin; Ziemann, P. J. Chemistry of secondary organic aerosol formation from OH radical-initiated reactions of linear, branched, and cyclic alkanes in the presence of NOx. *Aerosol Sci. Technol.* **2009**, *43*, 604–619.

(121) Atkinson, R.; Arey, J. Atmospheric degradation of volatile organic compounds. *Chem. Rev.* **2003**, *103*, 4605–4638.

(122) Yeh, G. K.; Ziemann, P. J. Alkyl nitrate formation from the reactions of C8 –C14 n -alkanes with OH radicals in the presence of NOx : measured yields with essential corrections for gas–wall partitioning. *J. Phys. Chem. A* **2014**, *118*, 8147–8157.

(123) Kroll, J. H.; Donahue, N. M.; Jimenez, J. L.; Kessler, S. H.; Canagaratna, M. R.; Wilson, K. R.; Altieri, K. E.; Mazzoleni, L. R.; Wozniak, A. S.; Bluhm, H.; et al. Carbon oxidation state as a metric for describing the chemistry of atmospheric organic aerosol. *Nat. Chem.* **2011**, *3*, 133–139.

(124) Atkinson, R.; Tuazon, E. C.; Mac Leod, H.; Aschmann, S. M.; Winer, A. M. The gas-phase reaction of chlorine nitrate with water vapor. *Geophys. Res. Lett.* **1986**, *13*, 117–120.

(125) Palm, B. B.; Campuzano-Jost, P.; Ortega, A. M.; Day, D. A.; Kaser, L.; Jud, W.; Karl, T.; Hansel, A.; Hunter, J. F.; Cross, E. S.; et al. In situ secondary organic aerosol formation from ambient pine forest air using an oxidation flow reactor. *Atmos. Chem. Phys. Discuss.* **2015**, *15*, 30409–30471.

(126) Boedeker. PTFE, FEP, and PFA Specifications http://www.boedeker.com/feppfa_p.htm (accessed Feb 1, 2016).

(127) Kuwata, M.; Zorn, S. R.; Martin, S. T. Using Elemental Ratios to Predict the Density of Organic Material Composed of Carbon, Hydrogen, and Oxygen. *Environ. Sci. Technol.* **2012**, *46*, 787–794.

(128) Mazzoleni, L. R.; Saranjampour, P.; Dalbec, M. M.; Samburova, V.; Hallar, A. G.; Zielinska, B.; Lowenthal, D. H.; Kohl, S. Identification of water-soluble organic carbon in non-urban aerosols using ultrahigh-resolution FT-ICR mass spectrometry: organic anions. *Environ. Chem.* **2012**, *9*, 285.

(129) Nozière, B.; Kalberer, M.; Claeys, M.; Allan, J.; D’Anna, B.; Decesari, S.; Finessi, E.; Glasius, M.; Grgić, I.; Hamilton, J. F.; et al. The Molecular Identification of Organic Compounds in the Atmosphere: State of the Art and Challenges. *Chem. Rev.* **2015**, *115*, 3919–3983.

(130) Gao, S.; Keywood, M.; Ng, N. L.; Surratt, J.; Varutbangkul, V.; Bahreini, R.; Flagan, R. C.; Seinfeld, J. H. Low-Molecular-Weight and Oligomeric Components in Secondary Organic Aerosol from the Ozonolysis of Cycloalkenes and α-Pinene. *J. Phys. Chem. A* **2004**, *108*, 10147–10164.

(131) Glasius, M.; Duane, M.; Larsen, B. R. Determination of polar terpene oxidation products in aerosols by liquid chromatography–ion trap mass spectrometry. *J. Chromatogr. A* **1999**, *833*, 121–135.

(132) Iinuma, Y.; Böge, O.; Gnauk, T.; Herrmann, H. Aerosol-chamber study of the α-pinene/O3 reaction: influence of particle acidity on aerosol yields and products. *Atmos. Environ.* **2004**, *38*, 761–773.

(133) Williams, B. J.; Zhang, Y.; Zuo, X.; Martinez, R. E.; Walker, M. J.; Kreisberg, N. M.; Goldstein, A. H.; Docherty, K. S.; Jimenez, J. L. Organic and inorganic decomposition products from the thermal desorption of atmospheric particles. *Atmos. Meas. Tech. Discuss.* **2015**, *8*, 13377–13421.

(134) Martinez, R. E.; Williams, B. J.; Zhang, Y.; Hagan, D.; Walker, M.; Kreisberg, N. M.; Hering, S. V.; Hohaus, T.; Jayne, J. T.; Worsnop, D. R. Development of a volatility and polarity separator (VAPS) for volatility- and polarity-resolved organic aerosol measurement. *Aerosol Sci. Technol.* **2016**, *50*, 255–271.

(135) Thomson, J. J. *Conduction of electricity through gases*; Cambridge University Press: Cambridge, 1903.

(136) Karasek, F. W. Plasma chromatography. *Anal. Chem.* **1974**, *46*, 710A–720A.

(137) Eiceman, G. A.; Karpas, Z.; Herbert H. Hill, J. *Ion Mobility Spectrometry, Third Edition*; Ion Mobility Spectrometry; Third.; CRC Press: Boca Raton, FL, 2013.

(138) McNaught, A. D.; Wilkinson, A. *IUPAC Compendium of Chemical Terminology (The "Gold Book")*; 2014.

(139) Groessl, M.; Graf, S.; Knochenmuss, R. High resolution ion mobility-mass spectrometry for separation and identification of isomeric lipids. *Analyst* **2015**, *140*, 6904–6911.

(140) Kanu, A. B.; Dwivedi, P.; Tam, M.; Matz, L.; Hill, H. H. Ion mobility-mass spectrometry. *J. Mass Spectrom.* **2008**, *43*, 1–22.

(141) Dwivedi, P.; Wu, P.; Klopsch, S. J.; Puzon, G. J.; Xun, L.; Hill, H. H. Metabolic profiling by ion mobility mass spectrometry (IMMS). *Metabolomics* **2008**, *4*, 63–80.

(142) Jarrold, M. F. Peptides and Proteins in the Vapor Phase. *Annu. Rev. Phys. Chem.* **2000**, *51*, 179–207.

(143) Kaplan, K.; Graf, S.; Tanner, C.; Gonin, M.; Fuhrer, K.; Knochenmuss, R.; Dwivedi, P.; Hill, H. H. Resistive Glass IM-TOFMS. *Anal. Chem.* **2010**, *82*, 9336–9343.

(144) Bradbury, N. E.; Nielsen, R. A. Absolute Values of the Electron Mobility in Hydrogen. *Phys. Rev.* **1936**, *49*, 388–393.

(145) Zare, R. N.; Fernández, F. M.; Kimmel, J. R. Hadamard Transform Time-of-Flight Mass Spectrometry: More Signal, More of the Time. *Angew. Chemie Int. Ed.* **2003**, *42*, 30–35.

(146) Zhang, X.; Knochenmuss, R.; Siems, W. F.; Liu, W.; Graf, S.; Hill, H. H. Evaluation of Hadamard Transform Atmospheric Pressure Ion Mobility Time-of-Flight Mass Spectrometry for Complex Mixture Analysis. *Anal. Chem.* **2014**, *86*, 1661–1670.

(147) Knochenmuss, R.; Graf, S.; Fuhrer, K.; Gonin, M. Multiplexed High Pressure Ion Mobility-TOFMS: High Resolution, Sensitivity and Structural Information in One Package. In *Proceedings of the 61st ASMS Conference on Mass Spectrometry and Allied Topics*; 2013; p. WP745.

(148) Revercomb, H. E.; Mason, E. A. Theory of plasma chromatography/gaseous electrophoresis. Review. *Anal. Chem.* **1975**, *47*, 970–983.

(149) Mason, E. A.; Schamp, H. W. Mobility of gaseous lons in weak electric fields. *Ann. Phys. (N. Y).* **1958**, *4*, 233–270.

(150) Mcdaniel, E. W.; Mason, E. A. The mobility and diffusion of ions in gases. *Book* **1973**, *10*, 1973.

(151) Siems, W. F.; Viehland, L. A.; Hill, H. H. Improved Momentum-Transfer Theory for Ion Mobility. 1. Derivation of the Fundamental Equation. *Anal. Chem.* **2012**, *84*, 9782–9791.

(152) Budisulistiorini, S. H.; Li, X.; Bairai, S. T.; Renfro, J.; Liu, Y.; Liu, Y. J.; McKinney, K. A.; Martin, S. T.; McNeill, V. F.; Pye, H. O. T.; et al. Examining the effects of anthropogenic emissions on isoprene-derived secondary organic aerosol formation during the 2013 Southern Oxidant and Aerosol Study (SOAS) at the Look Rock, Tennessee ground site. *Atmos. Chem. Phys.* **2015**, *15*, 8871–8888.

(153) Lin, Y.-H.; Budisulistiorini, S. H.; Chu, K.; Siejack, R. A.; Zhang, H.; Riva, M.; Zhang, Z.; Gold, A.; Kautzman, K. E.; Surratt, J. D. Light-absorbing oligomer formation in secondary organic aerosol from reactive uptake of isoprene epoxydiols. *Environ. Sci. Technol.* **2014**, *48*, 12012–12021.

(154) Lin, Y.; Zhang, Z.; Docherty, K. S.; Zhang, H.; Budisulistiorini, S. H.; Rubitschun, C. L.; Shaw, S. L.; Knipping, E. M.; Edgerton, E. S.; Kleindienst, T. E.; et al. Isoprene Epoxydiols as Precursors to Secondary Organic Aerosol Formation: Acid-Catalyzed Reactive Uptake Studies with Authentic Compounds. *Environ. Sci. Technol.* **2012**, *46*, 250–258.

(155) Rattanavaraha, W.; Chu, K.; Budisulistiorini, S. H.; Riva, M.; Lin, Y.-H.; Edgerton, E. S.; Baumann, K.; Shaw, S. L.; Guo, H.; King, L.; et al. Assessing the impact of anthropogenic pollution on isoprene-derived secondary organic aerosol formation in $PM_{2.5}$ collected from the Birmingham, Alabama ground site during the 2013 Southern Oxidant and Aerosol Study. *Atmos. Chem. Phys. Discuss.* **2016**, 1–43.

(156) Zhang, Z.; Lin, Y.-H.; Zhang, H.; Surratt, J. D.; Ball, L. M.; Gold, a. Technical Note: Synthesis of isoprene atmospheric oxidation products: isomeric epoxydiols and the rearrangement products *cis*- and *trans*-3-methyl-3,4-dihydroxytetrahydrofuran. *Atmos. Chem. Phys.* **2012**, *12*, 8529–8535.

(157) Horning, E. C.; Carroll, D. I.; Dzidic, I.; Lin, S.-N.; Stillwell, R. N.; Thenot, J.-P. Atmospheric pressure ionization mass spectrometry. *J. Chromatogr. A* **1977**, *142*, 481–495.

(158) McEwen, C. N.; Larsen, B. S. Ionization mechanisms related to negative Ion APPI, APCI, and DART. *J. Am. Soc. Mass Spectrom.* **2009**, *20*, 1518–1521.

(159) Kückelmann, U.; Warscheid, B.; Hoffmann, T. On-Line Characterization of Organic Aerosols Formed from Biogenic Precursors Using Atmospheric Pressure Chemical Ionization Mass Spectrometry. *Anal. Chem.* **2000**, *72*, 1905–1912.

(160) Kang, E.; Root, M. J.; Toohey, D. W.; Brune, W. H. Introducing the concept of Potential Aerosol Mass (PAM). *Atmos. Chem. Phys.* **2007**, *7*, 5727–5744.

(161) Lambe, A. T.; Ahern, A. T.; Williams, L. R.; Slowik, J. G.; Wong, J. P. S.; Abbatt, J. P. D.; Brune, W. H.; Ng, N. L.; Wright, J. P.; Croasdale, D. R.; et al. Characterization of aerosol photooxidation flow reactors: heterogeneous oxidation, secondary organic aerosol formation and cloud condensation nuclei activity measurements. *Atmos. Meas. Tech.* **2011**, *4*, 445–461.

(162) Stark, H.; Yatavelli, R. L. N.; Thompson, S. L.; Kimmel, J. R.; Cubison, M. J.; Chhabra, P. S.; Canagaratna, M. R.; Jayne, J. T.; Worsnop, D. R.; Jimenez, J. L. Methods to extract molecular and bulk chemical information from series of complex mass spectra with limited mass resolution. *Int. J. Mass Spectrom.* **2015**, *389*, 26–38.

(163) Hettiyadura, A. P. S.; Stone, E. A.; Kundu, S.; Baker, Z.; Geddes, E.; Richards, K.; Humphry, T. Determination of atmospheric organosulfates using HILIC chromatography with MS detection. *Atmos. Meas. Tech.* **2015**, *8*, 2347–2358.

(164) Riva, M.; Budisulistiorini, S. H.; Zhang, Z.; Gold, A.; Surratt, J. D. Chemical characterization of secondary organic aerosol constituents from isoprene ozonolysis in the presence of acidic aerosol. *Atmos. Environ.* **2015**, *1*, 1–9.

(165) Olson, C. N.; Galloway, M. M.; Yu, G.; Hedman, C. J.; Lockett, M. R.; Yoon, T.; Stone, E. A.; Smith, L. M.; Keutsch, F. N. Hydroxycarboxylic acid-derived organosulfates: Synthesis, stability, and quantification in ambient aerosol. *Environ. Sci. Technol.* **2011**, *45*, 6468–6474.

(166) Galloway, M. M.; Chhabra, P. S.; Chan, A. W. H.; Surratt, J. D.; Flagan, R. C.; Seinfeld, J. H.; Keutsch, F. N. Glyoxal uptake on ammonium sulphate seed aerosol: reaction products and reversibility of uptake under dark and irradiated conditions. *Atmos. Chem.*

Phys. **2009**, *9*, 3331–3345.

(167) Surratt, J. D.; Chan, A. W. H.; Eddingsaas, N. C.; Chan, M.; Loza, C. L.; Kwan, A. J.; Hersey, S. P.; Flagan, R. C.; Wennberg, P. O.; Seinfeld, J. H. Reactive intermediates revealed in secondary organic aerosol formation from isoprene. *Proc. Natl. Acad. Sci. U.S.A.* **2010**, *107*, 6640–6645.

(168) Surratt, J. D.; Gómez-González, Y.; Chan, A. W. H.; Vermeylen, R.; Shahgholi, M.; Kleindienst, T. E.; Edney, E. O.; Offenberg, J. H.; Lewandowski, M.; Jaoui, M.; et al. Organosulfate Formation in Biogenic Secondary Organic Aerosol. *J. Phys. Chem. A* **2008**, *112*, 8345–8378.

(169) Gómez-González, Y.; Surratt, J. D.; Cuyckens, F.; Szmigielski, R.; Vermeylen, R.; Jaoui, M.; Lewandowski, M.; Offenberg, J. H.; Kleindienst, T. E.; Edney, E. O.; et al. Characterization of organosulfates from the photooxidation of isoprene and unsaturated fatty acids in ambient aerosol using liquid chromatography/(−) electrospray ionization mass spectrometry. *J. Mass Spectrom.* **2008**, *43*, 371–382.

(170) Edney, E. O.; Kleindienst, T. E.; Jaoui, M.; Lewandowski, M.; Offenberg, J. H.; Wang, W.; Claeys, M. Formation of 2-methyl tetrols and 2-methylglyceric acid in secondary organic aerosol from laboratory irradiated isoprene/NOX/SO2/air mixtures and their detection in ambient PM2.5 samples collected in the eastern United States. *Atmos. Environ.* **2005**, *39*, 5281–5289.

(171) Riedel, T. P.; Lin, Y.-H.; Budisulistiorini, S. H.; Gaston, C. J.; Thornton, J. a.; Zhang, Z.; Vizuete, W.; Gold, A.; Surratt, J. D. Heterogeneous Reactions of Isoprene-Derived Epoxides: Reaction Probabilities and Molar Secondary Organic Aerosol Yield Estimates. *Environ. Sci. Technol. Lett.* **2015**, *2*, 38–42.

(172) Stone, E. A.; Yang, L.; Yu, L. E.; Rupakheti, M. Characterization of organosulfates in atmospheric aerosols at Four Asian locations. *Atmos. Environ.* **2012**, *47*, 323–329.

(173) Surratt, J. D.; Kroll, J. H.; Kleindienst, T. E.; Edney, E. O.; Claeys, M.; Sorooshian, A.; Ng, N. L.; Offenberg, J. H.; Lewandowski, M.; Jaoui, M.; et al. Evidence for Organosulfates in Secondary Organic Aerosol. *Environ. Sci. Technol.* **2007**, *41*, 517–527.

(174) St. Clair, J. M.; Rivera-Rios, J. C.; Crounse, J. D.; Knap, H. C.; Bates, K. H.; Teng, A. P.; Jørgensen, S.; Kjaergaard, H. G.; Keutsch, F. N.; Wennberg, P. O. Kinetics and Products of the Reaction of the First-Generation Isoprene Hydroxy Hydroperoxide (ISOPOOH) with OH. *J. Phys. Chem. A* **2016**, *120*, 1441–1451.

(175) Hyttinen, N.; Kupiainen-Määttä, O.; Rissanen, M. P.; Muuronen, M.; Ehn, M.; Kurtén, T. Modeling the Charging of Highly Oxidized Cyclohexene Ozonolysis Products Using Nitrate-Based Chemical Ionization. *J. Phys. Chem. A* **2015**, *119*, 6339–6345.

(176) Cubison, M. J.; Jimenez, J. L. Statistical precision of the intensities retrieved from

constrained fitting of overlapping peaks in high-resolution mass spectra. *Atmos. Meas. Tech.* **2015**, *8*, 2333–2345.

(177) Mentel, T. F.; Springer, M.; Ehn, M.; Kleist, E.; Pullinen, I.; Kurtén, T.; Rissanen, M.; Wahner, A.; Wildt, J. Formation of highly oxidized multifunctional compounds: autoxidation of peroxy radicals formed in the ozonolysis of alkenes – deduced from structure–product relationships. *Atmos. Chem. Phys.* **2015**, *15*, 6745–6765.

(178) Kulmala, M.; Kontkanen, J.; Junninen, H.; Lehtipalo, K.; Manninen, H. E.; Nieminen, T.; Petäjä, T.; Sipilä, M.; Schobesberger, S.; Rantala, P.; et al. Direct observations of atmospheric aerosol nucleation. *Science* **2013**, *339*, 943–946.

(179) Hidy, G. M.; Blanchard, C. L.; Baumann, K.; Edgerton, E.; Tanenbaum, S.; Shaw, S.; Knipping, E.; Tombach, I.; Jansen, J.; Walters, J. Chemical climatology of the southeastern United States, 1999-2013. *Atmos. Chem. Phys.* **2014**, *14*, 11893–11914.

(180) Fernández-Maestre, R.; Harden, C. S.; Ewing, R. G.; Crawford, C. L.; Hill, H. H. Chemical standards in ion mobility spectrometry. *Analyst* **2010**, *135*, 1433.

(181) Vogel, A. L.; Äijälä, M.; Corrigan, A. L.; Junninen, H.; Ehn, M.; Petäjä, T.; Worsnop, D. R.; Kulmala, M.; Russell, L. M.; Williams, J.; et al. In situ submicron organic aerosol characterization at a boreal forest research station during HUMPPA-COPEC 2010 using soft and hard ionization mass spectrometry. *Atmos. Chem. Phys.* **2013**, *13*, 10933–10950.

(182) Veres, P.; Roberts, J. M.; Warneke, C.; Welsh-Bon, D.; Zahniser, M.; Herndon, S.; Fall, R.; de Gouw, J. Development of negative-ion proton-transfer chemical-ionization mass spectrometry (NI-PT-CIMS) for the measurement of gas-phase organic acids in the atmosphere. *Int. J. Mass Spectrom.* **2008**, *274*, 48–55.

(183) Thompson, S. L.; Yatavelli, R. L. N.; Stark, H.; Kimmel, J. R.; Krechmer, J. E.; Day, D. A.; Isaacman-VanWertz, G.; Yee, L.; Goldstein, A. H.; Khan, M. A. H.; et al. Field intercomparison of the gas/particle partitioning of oxygenated organics during the Southern Oxidant and Aerosol Study (SOAS) in 2013. *Aerosol Sci. Technol.* **2015**, *Submitted*.

(184) Ruotolo, B. T.; Benesch, J. L. P.; Sandercock, A. M.; Hyung, S.-J.; Robinson, C. V. Ion mobility-mass spectrometry analysis of large protein complexes. *Nat. Protoc.* **2008**, *3*, 1139–1152.

(185) Paglia, G.; Williams, J. P.; Menikarachchi, L.; Thompson, J. W.; Tyldesley-Worster, R.; Halldórsson, S.; Rolfsson, O.; Moseley, A.; Grant, D.; Langridge, J.; et al. Ion Mobility Derived Collision Cross Sections to Support Metabolomics Applications. *Anal. Chem.* **2014**, *86*, 3985–3993.

(186) Fernandez-Lima, F. A.; Becker, C.; McKenna, A. M.; Rodgers, R. P.; Marshall, A. G.; Russell, D. H. Petroleum Crude Oil Characterization by IMS-MS and FTICR MS. *Anal.*

Chem. **2009**, *81*, 9941–9947.

(187) Rissanen, M. P.; Kurtén, T.; Sipilä, M.; Thornton, J. A.; Kausiala, O.; Garmash, O.; Kjaergaard, H. G.; Petäjä, T.; Worsnop, D. R.; Ehn, M.; et al. Effects of Chemical Complexity on the Autoxidation Mechanisms of Endocyclic Alkene Ozonolysis Products: From Methylcyclohexenes toward Understanding α-Pinene. *J. Phys. Chem. A* **2015**, *119*, 4633–4650.

(188) Yamasaki, H.; Kuwata, K.; Miyamoto, H. Effects of ambient temperature on aspects of airborne polycyclic aromatic hydrocarbons. *Environ. Sci. Technol.* **1982**, *16*, 189–194.

(189) Pankow, J. F. Review and comparative analysis of the theories on partitioning between the gas and aerosol particulate phases in the atmosphere. *Atmos. Environ.* **1987**, *21*, 2275–2283.

(190) Pankow, J. F. An absorption model of the gas/aerosol partitioning involved in the formation of secondary organic aerosol. *Atmos. Environ.* **1994**, *28*, 189–193.

(191) Camredon, M.; Aumont, B.; Lee-Taylor, J.; Madronich, S. The SOA/VOC/NO_x system: an explicit model of secondary organic aerosol formation. *Atmos. Chem. Phys.* **2007**, *7*, 5599–5610.

(192) Shrivastava, M. K.; Lane, T. E.; Donahue, N. M.; Pandis, S. N.; Robinson, A. L. Effects of gas particle partitioning and aging of primary emissions on urban and regional organic aerosol concentrations. *J. Geophys. Res.* **2008**, *113*.

(193) Metzger, S.; Dentener, F.; Pandis, S.; Lelieveld, J. Gas/aerosol partitioning: 1. A computationally efficient model. *J. Geophys. Res.* **2002**, *107*, 4312.

(194) Chung, S. H.; Seinfeld, J. H. Global distribution and climate forcing of carbonaceous aerosols. *J. Geophys. Res.* **2002**, *107*, 4407.

(195) Kanakidou, M.; Seinfeld, J. H.; Pandis, S. N.; Barnes, I.; Dentener, F. J.; Facchini, M. C.; Van Dingenen, R.; Ervens, B.; Nenes, A.; Nielsen, C. J.; et al. Organic aerosol and global climate modelling: a review. *Atmospheric Chemistry and Physics*, 2005, *5*, 1053–1123.

(196) Isaacman, G.; Kreisberg, N. M.; Yee, L. D.; Worton, D. R.; Chan, A. W. H.; Moss, J. A.; Hering, S. V.; Goldstein, A. H. Online derivatization for hourly measurements of gas- and particle-phase semi-volatile oxygenated organic compounds by thermal desorption aerosol gas chromatography (SV-TAG). *Atmos. Meas. Tech.* **2014**, *7*, 4417–4429.

(197) Holzinger, R.; Williams, J.; Herrmann, F.; Lelieveld, J.; Donahue, N. M.; Röckmann, T. Aerosol analysis using a Thermal-Desorption Proton-Transfer-Reaction Mass Spectrometer (TD-PTR-MS): a new approach to study processing of organic aerosols. *Atmos. Chem. Phys.* **2010**, *10*, 2257–2267.

(198) Isaacman-VanWertz, G.; Yee, L. D.; Kreisberg, N. M.; Wernis, R.; Moss, J. A.; Hering, S.

V.; De S??, S. S.; Martin, S. T.; Alexander, M. L.; Palm, B. B.; et al. Ambient Gas-Particle Partitioning of Tracers for Biogenic Oxidation. *Environ. Sci. Technol.* **2016**, *50*, 9952–9962.

(199) Thompson, S. L.; Yatavelli, R. L. N.; Stark, H.; Kimmel, J. R.; Krechmer, J. E.; Day, D. A.; Hu, W.; Isaacman-VanWertz, G.; Yee, L.; Goldstein, A. H.; et al. Field intercomparison of the gas/particle partitioning of oxygenated organics during the Southern Oxidant and Aerosol Study (SOAS) in 2013. *Aerosol Sci. Technol.* **2016**, 1–27.

(200) Perraud, V.; Bruns, E. a; Ezell, M. J.; Johnson, S. N.; Yu, Y.; Alexander, M. L.; Zelenyuk, A.; Imre, D.; Chang, W. L.; Dabdub, D.; et al. Nonequilibrium atmospheric secondary organic aerosol formation and growth. *Proc. Natl. Acad. Sci. U.S.A.* **2012**, *109*, 2836–2841.

(201) Vaden, T. D.; Imre, D.; Beranek, J.; Shrivastava, M.; Zelenyuk, A. Evaporation kinetics and phase of laboratory and ambient secondary organic aerosol. *Proc. Natl. Acad. Sci. U.S.A.* **2011**, *108*, 2190–2195.

(202) Virtanen, A.; Joutsensaari, J.; Koop, T.; Kannosto, J.; Yli-Pirilä, P.; Leskinen, J.; Mäkelä, J. M.; Holopainen, J. K.; Pöschl, U.; Kulmala, M.; et al. An amorphous solid state of biogenic secondary organic aerosol particles. *Nature* **2010**, *467*, 824–827.

(203) Renbaum-Wolff, L.; Grayson, J. W.; Bateman, A. P.; Kuwata, M.; Sellier, M.; Murray, B. J.; Shilling, J. E.; Martin, S. T.; Bertram, A. K. Viscosity of -pinene secondary organic material and implications for particle growth and reactivity. *Proc. Natl. Acad. Sci. U.S.A.* **2013**, *110*, 8014–8019.

(204) Shiraiwa, M.; Ammann, M.; Koop, T.; Poschl, U. Gas uptake and chemical aging of semisolid organic aerosol particles. *Proc. Natl. Acad. Sci. U.S.A.* **2011**, *108*, 11003–11008.

(205) Odum, J. R.; Hoffmann, T.; Bowman, F.; Collins, D.; Flagan Richard, C.; Seinfeld John, H.; Flagan, R. C.; Seinfeld, J. H. Gas particle partitioning and secondary organic aerosol yields. *Environ. Sci. Technol.* **1996**, *30*, 2580–2585.

(206) Pandis, S. N.; Paulson, S. E.; Seinfeld, J. H.; Flagan, R. C. Aerosol formation in the photooxidation of isoprene and β-pinene. *Atmos. Environ. Part A. Gen. Top.* **1991**, *25*, 997–1008.

(207) Griffin, J.; Cocker, D. R.; Seinfeld, H. Estimates of global atmospheric organic aerosol from oxidation of biogenic hydrocarbons. *Geophys. Res. Lett.* **1999**, *26*, 2721–2724.

(208) Odum, J. R.; Jungkamp, T. P. W.; Griffin, R. J.; Flagan, R. C.; Seinfeld, J. H. The Atmospheric Aerosol-Forming Potential of Whole Gasoline Vapor. *Science (80-.).* **1997**, *276*, 96–99.

(209) Krechmer, J. E.; Pagonis, D.; Ziemann, P. J.; Jimenez, J. L. Quantification of Gas-Wall

Partitioning in Teflon Environmental Chambers Using Rapid Bursts of Low-Volatility Oxidized Species Generated in Situ. *Environ. Sci. Technol.* **2016**, *50*, 5757–5765.

(210) Ye, P.; Ding, X.; Hakala, J.; Hofbauer, V.; Robinson, E. S.; Donahue, N. M. Vapor wall loss of semi-volatile organic compounds in a Teflon chamber. *Aerosol Sci. Technol.* **2016**, *50*, 822–834.

(211) Pound, G. M. Selected Values of Evaporation and Condensation Coefficients for Simple Substances. *J. Phys. Chem. Ref. Data* **1972**, *1*, 135–146.

(212) Cammenga, H. K. Evaporation mechanisms of liquids. In *Current topics in materials science*; 1980; pp. 335–446.

(213) Kulmala, M.; Wagner, P. E. Mass accommodation and uptake coefficients - A quantitative comparison. *J. Aerosol Sci.* **2001**, *32*, 833–841.

(214) Saleh, R.; Shihadeh, A.; Khlystov, A. Determination of evaporation coefficients of semi-volatile organic aerosols using an integrated volume-tandem differential mobility analysis (IV-TDMA) method. *J. Aerosol Sci.* **2009**, *40*, 1019–1029.

(215) Saleh, R.; Donahue, N. M.; Robinson, A. L. Time scales for gas-particle partitioning equilibration of secondary organic aerosol formed from alpha-pinene ozonolysis. *Environ. Sci. Technol.* **2013**, *47*, 5588–5594.

(216) Julin, J.; Winkler, P. M.; Donahue, N. M.; Wagner, P. E.; Riipinen, I. Near-Unity Mass Accommodation Coefficient of Organic Molecules of Varying Structure. *Environ. Sci. Technol.* **2014**, *48*, 12083–12089.

(217) Cappa, C. D.; Jimenez, J. L. Quantitative estimates of the volatility of ambient organic aerosol. *Atmos. Chem. Phys.* **2010**, *10*, 5409–5424.

(218) Grieshop, A. P.; Donahue, N. M.; Robinson, A. L. Is the gas-particle partitioning in alpha-pinene secondary organic aerosol reversible? *Geophys. Res. Lett.* **2007**, *34*, 1–5.

(219) Karnezi, E.; Riipinen, I.; Pandis, S. N. Measuring the atmospheric organic aerosol volatility distribution: a theoretical analysis. *Atmos. Meas. Tech.* **2014**, *7*, 2953–2965.

(220) Grieshop, A. P.; Miracolo, M. A.; Donahue, N. M.; Robinson, A. L. Constraining the Volatility Distribution and Gas-Particle Partitioning of Combustion Aerosols Using Isothermal Dilution and Thermodenuder Measurements. *Environ. Sci. Technol.* **2009**, *43*, 4750–4756.

(221) Sinclair, D.; La Mer, V. K. Light Scattering as a Measure of Particle Size in Aerosols. The Production of Monodisperse Aerosols. *Chem. Rev.* **1949**, *44*, 245–267.

(222) Peng, Z.; Day, D. A.; Stark, H.; Li, R.; Palm, B. B.; Brune, W. H.; Jimenez, J. L. HOx radical chemistry in oxidation flow reactors with low-pressure mercury lamps

systematically examined by modeling. *Atmos. Meas. Tech.* **2015**, *8*, 4863–4890.

(223) Palm, B. B.; Campuzano-Jost, P.; Ortega, A. M.; Day, D. A.; Kaser, L.; Jud, W.; Karl, T.; Hansel, A.; Hunter, J. F.; Cross, E. S.; et al. In situ secondary organic aerosol formation from ambient pine forest air using an oxidation flow reactor. *Atmos. Chem. Phys.* **2016**, *16*, 2943–2970.

(224) Aster, R.; Borchers, B.; Thurber, C. Parameter estimation and inverse problems. *Book* **2013**.

(225) Compernolle, S.; Ceulemans, K.; Müller, J.-F. EVAPORATION: a new vapour pressure estimation methodfor organic molecules including non-additivity and intramolecular interactions. *Atmos. Chem. Phys.* **2011**, *11*, 9431–9450.

(226) McFeely, F. R.; Somorjai, G. A. Vaporization kinetics of hydrogen-bonded liquids. *J. Phys. Chem.* **1972**, *76*, 914–918.

(227) Lednovich, S. L.; Fenn, J. B. Absolute evaporation rates for some polar and nonpolar liquids. *AIChE J.* **1977**, *23*, 454–459.

(228) Nah, T.; McVay, R. C.; Zhang, X.; Boyd, C. M.; Seinfeld, J. H.; Ng, N. L. Influence of seed aerosol surface area and oxidation rate on vapor wall deposition and SOA mass yields: a case study with α-pinene ozonolysis. *Atmos. Chem. Phys.* **2016**, *16*, 9361–9379.

(229) Trump, E. R.; Epstein, S. A.; Riipinen, I.; Donahue, N. M. Wall effects in smog chamber experiments: A model study. *Aerosol Sci. Technol.* **2016**, *50*, 1180–1200.